High-Fidelity Hydrostructural Design Optimization of Lifting Surfaces

by

Nitin Garg

A dissertation submitted in partial fulfillment
of the requirements for the degree of
Doctor of Philosophy
(Naval Architecture and Marine Engineering and Scientific Computing)
in the University of Michigan
2017

Doctoral Committee:

Professor Yin L. Young, Co-Chair
Professor Joaquim R. R. A. Martins, Co-Chair
Assistant Professor Matthew D. Collette
Associate Professor Krzysztof J. Fidkowski
Assistant Professor Kevin J. Maki

Research means to investigate something you do not know or understand.

– Neil Armstrong

gargn@umich.edu
ORCID iD : 0000-0002-7018-1746
2017

ACKNOWLEDGMENTS

I feel privileged to have had Prof. Yin Lu Young and Prof. Joaquim R. R. A. Martins as my co-advisors. Their support and guidance have been invaluable throughout the time of my dissertation. They have been extremely patient with me, while providing constructive criticism and encouragement. I am also thankful to my dissertation committee, Prof. Krzysztof Fidkowski, Prof. Matthew Collette, and Prof. Kevin Maki, for their valuable comments and suggestions on my thesis.

I would like to thank Dr. Paul Brandner and Dr. Bryce Pearce from Australian Maritime College for testing the optimized hydrofoil and also providing me an opportunity to gain experience in experimental testing. Special thanks go to Dr. Andrew Phillips from Defence Science and Technology Group, Australia for manufacturing the optimized hydrofoil and answering my numerous queries about manufacturing. I also wish to thank Mr. Robert Wrigley for his valuable help in setting up the experiments, as well as Dr. Nigel St. John and Mr. Russell Cairns for their help in manufacturing the hydrofoils. I would also like to acknowledge the support by the US Office of Naval Research (Grant No. N00014-13-1-0763 and N00014-16-1-2972 managed by Ms. Kelly Cooper).

I would like to thank my colleagues at the Naval Architecture and Marine Engineering Department and the MDOlab for their help and suggestions throughout the years. I am extremely grateful to Dr. Peter Lyu and Dr. Gaetan Kenway, without whose guidance and support this thesis would not have been possible. I would also like to acknowledge my friends, classmates, and colleagues for all the wonderful experiences.

Finally, I would like to thank my family: my beloved parents, R. P. Garg and Nisha Garg, for always encouraging and supporting me, brother Ashish, and in-laws. Most importantly, I acknowledge my wife, Swati, for her constant encouragement and support.

TABLE OF CONTENTS

LIST OF FIGURES

LIST OF TABLES

LIST OF ABBREVIATIONS

ALPSO	Augmented lagrange multiplier particle swarm optimization
AMC	Australian maritime college
CFD	Computational fluid dynamics
CFRP	Carbon fiber reinforced polymers
CP	Center of pressure
DSTG	Defence science and technology group
DV	Design variables
EA	Elastic axis
FEA	Finite element analysis
FFD	Free form deformation
FSI	Fluid structure interaction
GFRP	Glass fiber reinforced polymers
LE	Leading edge
MACH	MDO for aircraft configurations with high-fidelity
MDO	Multidisciplinary design optimization
NSGA2	Non sorting genetic algorithm II
OML	Outer mold line
RANS	Reynolds-averaged Navier–Stokes
RK	Runge–Kutta
SA	Spalart–Allmaras
SLSQP	Sequential quadratic programming method
SNOPT	Sparse nonlinear OPTimizer
TE	Trailing edge

LIST OF SYMBOLS

A	Hydrofoil planform area [m^2]
a	Speed of sound in the fluid [m/s]
b	Hydrofoil semi-chord at mid-span, $b = c/2$ [m]
c	Mean chord [m]
C_D	Drag coefficient, $C_D = \dfrac{D}{0.5\rho_f U^2 sc}$
C_f	Skin friction coefficient, $C_f = \dfrac{\tau_w}{0.5\rho_f U^2}$
C_L	Lift coefficient, $C_L = \dfrac{L}{0.5\rho_f U^2 sc}$
C_L/C_D	Lift-to-drag ratio or efficiency
C_M	Moment coefficient, $C_M = \dfrac{M}{0.5\rho_f U^2 sc^2}$
C_p	Pressure coefficient, $C_p = \dfrac{P_{\text{local}} - P_{\text{ref}}}{0.5\rho_f U^2}$
D	Hydrodynamic drag [N]
e	Distance from the elastic axis (EA) to the center of pressure (CP) non-dimensionalized by the mean chord c
I	Function of interest in optimization (objectives or constraints)
L	Hydrodynamic lift [N]
M	Hydrodynamic moment [Nm]
s	Hydrofoil loaded span [m]
U	Inflow velocity [m/s]
u	Vector of structural displacements
x	Optimization design variables

α_{BT}	Effective structural bend-twist coupling ratio, $\alpha_{BT} = K^s_{\theta\theta}/\sqrt{K^s_{hh}K^s_{\theta\theta}}$
$\mathrm{A_{cav}}$	Non-dimensional aggregated cavitation constraint
α	Geometric incidence relative to the freestream flow direction [°]
α_{eff}	Effective incidence relative to freestream flow direction, $\alpha_{\mathrm{eff}} = \alpha + 2\theta_{\mathrm{tip}}/\pi$ [°]
$\mathrm{A_{ref}}$	Reference hydrofoil area [m^2]
$\mathcal{A}$	Hydrodynamic solver residuals
$\mathcal{S}$	Structural solver residuals
$C_{p_{\mathrm{min}}}$	Minimum pressure coefficient
δ_{tip}	Tip bending deflection [mm]
K^s_{hh}	Effective structural bending stiffness [N/m]
$K^s_{h\theta}$	Effective structural bend-twist coupling stiffness [N]
KS_{σ_v}	Non-dimensional aggregated stress constraint
$K^s_{\theta\theta}$	Effective structural twisting stiffness [Nm]
M_a	Mach number, $M_a = U/a$
μ_f	Dynamic viscosity of water [$\mathrm{Ns/m}^2$]
ν_f	Fluid kinematic viscosity [m^2/s]
ν_s	Solid Poisson's ratio
ϕ	Hydrodynamic adjoint vector
P_{local}	Local fluid pressure [Pa]
P_{ref}	Reference upstream hydrostatic pressure [Pa]
ψ	Structural adjoint vector
P_{vap}	Saturated vapor pressure of the fluid [Pa]
Re	Reynolds number, $\mathrm{Re} = Uc/\nu_f$
ρ_f	Fluid density [$\mathrm{kg/m}^3$]
ρ_s	Solid density [$\mathrm{kg/m}^3$]
σ	Cavitation number, $\sigma = \dfrac{P_{\mathrm{ref}} - P_{\mathrm{vap}}}{0.5\rho_f U^2}$

$\sigma_{s,f}$ Fatigue strength [MPa]

σ_v von Mises stress [MPa]

σ_y Yield strength [MPa]

$t_{\max}/c$ Maximum thickness-to-chord ratio

θ_{tip} Tip twisting deflection [deg. or rad.]

$t_{\max}$ Local maximum hydrofoil thickness [m]

τ_w Local wall shear stress [N/m^2]

U_D Critical divergence velocity [m/s]

U_{cav} Cavitation inception speed, $U_{\text{cav}} = \sqrt{\dfrac{P_{\text{ref}} - P_{\text{vap}}}{0.5\rho_f C_{p_{\min}}}}$ [m/s]

ABSTRACT

Recent advances in high-performance computing and the efficiency of numerical solvers have made it possible to use sequential high-fidelity hydrodynamic and structural simulations to carry out design and optimization of marine lifting surfaces such as hydrofoils and propulsors. However, the design optimization of flexible hydrofoils and propellers requires coupled hydrodynamic and structural analysis to achieve a truly optimal, physically realizable, and structurally sound design. To address this need, the thesis presents an efficient high-fidelity hydrostructural design optimization with large numbers of design variables, multiple design points, as well as design constraints to avoid cavitation, avoid excessive stresses, and satisfy manufacturing tolerances. The hydrostructural solver couples a 3-D nearly incompressible Reynolds-averaged Navier–Stokes solver with a 3-D structural finite-element solver. The hydrostructural solver is validated by comparing the hydrodynamic load coefficients and tip bending deformations of a cantilevered aluminum hydrofoil with a NACA 0009 cross section and a trapezoidal planform. A coupled adjoint approach for efficient computation of the performance and constraint function derivatives with respect to 210 shape design variables is used. Using this state-of-the-art hydrostructural design optimization tool, a multipoint optimization yields improved performance over the entire range of expected operating conditions with significantly increased cavitation inception speed. The hydrostructural optimal result is compared to an equivalent hydrodynamic-only optimization, and results show that only the hydrostructural optimized design satisfies the stress constraint up to the highest expected loading condition, highlighting the need for coupled hydrostructural optimization. The proposed approach enables multipoint optimization of the hydrostructural performance for hydrofoils and marine propulsors, and it constitutes a powerful new tool for improving existing designs, and exploring new con-

cepts. The thesis also presents the first experimental validation of a numerically optimized hydrofoil designed using the developed hydrostructural optimization tool. Good agreement is observed between the predictions and measurements, where both showed that the optimized hydrofoil yielded an overall increase in the lift-to-drag ratio of 29% and significantly delayed cavitation inception compared to the NACA 0009 baseline.

In keeping up with the recent advances in material and manufacturing technology, the possibility of using composite material for marine propulsors is investigated. Combined experimental and numerical studies are presented to understand the benefits and challenges of using composite material for the maritime applications. The composite hydrofoils are manufactured by Defence Science and Technology Group (DSTG), Australia and are tested in the cavitation tunnel at Australian Maritime College (AMC), Australia. Results are presented for three composite hydrofoils with different orientations of the structural carbon layers, resulting in a different material-based bend-twist coupling. The results show that the material-based bend-twist coupling has a significant impact on the load-dependent deformation response, stall boundary, modal characteristics, susceptibility to static divergence, and cavity dynamics.

This thesis helps in advancing the understanding of the impact of load-dependent bend-twist coupling on the performance of adaptive composite hydrofoils. We also took the first step towards developing a high-fidelity hydrostructural design optimization tool for composite hydrofoils by extending our structural solver to simulate the performance of anisotropic composite hydrofoils. The high-fidelity hydrostructural solver combined with the improved understanding of the material-based bend-twist coupling has the potential to play an important role in the analysis, design, and optimization of the next generation adaptive composite marine propulsors.

CHAPTER 1

Introduction

1.1 Motivation

With recent advances in high-performance computing, computational fluid dynamics (CFD) modeling and structural modeling has become an integral part of the engineering analysis and design process of marine vessels and propulsors. In aircraft wing design, CFD and structural modeling have been integrated with numerical optimization and adjoint methods to enable high-fidelity aerostructural shape optimization with a large number of design variables. However, for maritime applications, there are additional challenges that need to be addressed to carry out high-fidelity hydrostructural optimization.

To date, most of the design optimization tool for maritime applications only considered hydrodynamic performance. Very few examples of hydrostructural shape optimization can be found in literature, and they either used low-fidelity methods or used high-fidelity methods with a few design variables (< 15). Therefore, the first goal of this thesis is to carry out high-fidelity hydrostructural optimization with a large number of design variables (of the order of 100), with constraints on cavitation inception, aggregated von Mises stress, and the manufacturing tolerances.

Recently, many researchers have been focusing on numerical optimization techniques for the aerospace, marine, and wind engineering applications, but with minimal or no experimental validation of the numerical results. Thus, the second goal of this thesis is to

validate the hydroelastic and cavitation performance of the numerically optimized hydrofoil using experimental measurements.

In the first part of the thesis, numerical design optimization tool for an isotropic (i.e., aluminum) hydrofoil is presented. With the recent advances in material and manufacturing technology, there has been an increased interest in the use of composite material for aerospace, marine, and wind applications. The next step should be to develop design optimization tool for the composite material. While in the isotropic hydrofoil optimization, only the shape of the hydrofoil is optimized to improve hydroelastic and cavitation performance, the composite hydrofoil optimization will include optimizing both the shape and the material configuration to achieve improved performance. However, to conduct composite hydrofoil optimization, we should first improve the understanding of the influence of inherent material-based bend-twist coupling of anisotropic composites on the hydroelastic and cavitation performance of hydrofoils. The third goal of this thesis is to present combined numerical and experimental studies to understand the benefits and the challenges of using composite material for future maritime applications.

Finally, to combine the efficient high-fidelity hydrostructural design optimization tool and the improved knowledge of the impact of material-based bend-twist coupling on the hydroelastic and cavitating performance of composite hydrofoils, we take the first step towards developing a hydrostructural design optimization tool capable of optimizing both the geometric shape and the material configurations of composite hydrofoils. Thus, the fourth goal of the thesis is to extend the high-fidelity hydrostructural solver to simulate the performance of anisotropic composite hydrofoils.

1.2 Hydrostructural Optimization of Marine Propulsors

Since 90% of the world trade happens by water, the energy efficiency of maritime transport is critical to global sustainability, as well as economic worldwide growth. The latest

amendments to the International Conventional for the Prevention of Pollution from Ships (MARPOL) mandate an increasingly stringent Energy Efficiency Design Index (EEDI) score for the majority of new vessels. As per the regulations adopted by International Maritime Organization (IMO) in 2011, new ships built between 2015 and 2019 need to have an EEDI of at least 10% better than the reference line (which is based on the efficiency of ships built between 1999 and 2009). After that, new ships built between 2020 and 2024 will be required to be 20% more efficient than the reference line, and then ships built from 2025 onwards will be required to be 30% more efficient [41].

The annual fuel consumption of commercial ships in 2001 was 289 million tonnes [32]. Thus, even a 1% fuel consumption reduction would lead to a fuel savings of 2.89 million tonnes annually, which would significantly reduce the operational cost and the environmental impact of maritime transportation. One of the ways to increase the efficiency of marine transportation is to improve the propulsors, so there has been an increased interest in marine propulsor design optimization.

Over the last decade, significant advances have been made in the analysis and design of marine propulsors. However, most of the approaches adopted in the literature either only considered hydrodynamic effects with low-fidelity methods or used high-fidelity methods with few design variables.

Since propulsors exhibit complex geometries and their performance is sensitive to small local shape changes, a large number of shape design variables are required to take full advantage of optimization. To evaluate propulsor performance and to accurately quantify the effect of small shape changes, computational fluid dynamics (CFD) simulations that accounts for viscous and cavitation effects is necessary. Furthermore, since propulsor blades can deform, the CFD model should be coupled to a structural model to obtain the correct shapes for each operating condition. Coupling to a structural model also enables us to enforce material yield stress or fatigue limit constraints to ensure safe and reliable operation. These needs are also applicable to hydrofoil design. Note that hydrofoils can be seen

as simplified profiles for more complex propeller or turbine blades, rudder, and control surfaces.

1.2.1 Cavitation Constraint, Large Number of Design Variables, and High-fidelity

Researchers have performed hydrodynamic shape optimization of hydrofoils using potential flow methods both without considering cavitation [57] and by enforcing cavitation [19, 40, 73, 103, 120]. Cavitation is the formation of bubbles in a liquid due to a drop in local pressure to near or below the saturated vapor pressure, and is a critical driver in marine propulsor design, because cavitation can lead to significant performance decay, erosion, vibration, and noise issues.

For at sea operations, designers should make sure that the propulsor is not only efficient but also has the desired cavitation characteristics over a range of lift coefficients. Brockett [19] presented one of the first studies for optimizing hydrofoil performance while considering cavitation. Brockett was able to find an optimized cavitation-free hydrofoil for a given design lift coefficient and minimum thickness (based on strength considerations) for a range of lift coefficients using 2-D potential flow theory, which assumes inviscid and irrotational flow. Eppler and Shen [40, 130] used an inverse wing section design method based on 2-D potential flow coupled with the turbulent boundary-layer theory to design a series of symmetrical and asymmetrical hydrofoil sections with delayed cavitation inception and separation characteristics.

Kinnas et al. [73] developed an efficient, nonlinear boundary element method (BEM) to carry out potential flow analysis of 2-D and 3-D cavitating hydrofoils. Mishima et al. [103] used the low-order BEM developed by Kinnas et al. [72] and carried out gradient-free optimization to find the optimized hydrofoil geometry that minimizes the drag coefficient for a given lift coefficient and cavitation number, with a constraint on the maximum cavity length and cavity volume. The influence of viscous effects was considered by applying a

constant friction coefficient over the wetted foil surface. Only five design variables were used in their optimization study, and the method is only valid for cases at low to moderate angles of attack due to the inviscid and irrotational flow assumption of the potential flow solver. Zeng et al. [156] developed a genetic algorithm to optimize 2-D sections with 10 shape design variables and used a potential flow-based lifting surface (LS) method to optimize the 2-D sections in the 3-D propeller blade design.

Besides potential flow-based optimization studies, some researchers also carried out high-fidelity hydrodynamic shape optimization for hydrofoils, and marine vessels [24,141]. They used gradient-free optimization algorithms, which limited the number of design variables to less than 15 due to a large number of required function evaluations, compounded with the high computational cost of high-fidelity hydrodynamic solvers.

In Chapter 4, the challenge of performing high-fidelity RANS (Reynolds-averaged Navier–Stokes)-based hydrodynamic shape optimization with respect to a large number of shape design variables (210) while enforcing cavitation constraints [43] is tackled. This is achieved through the use of gradient-based optimization algorithm together with an adjoint method that efficiently computes the required gradients. Results show that an efficient high-fidelity hydrodynamic shape optimization method capable of handling large number of design variables is necessary to find an optimal design for highly loaded conditions, where viscous effects cannot be neglected [43].

1.2.2 Coupled Hydrostructural Optimization

The optimization efforts mentioned before considered only the hydrodynamic performance and assumed the lifting surfaces to be rigid. The rigid assumption may be sufficient for relatively stiff metallic marine propulsors with zero skew or sweep, as the propeller blade or hydrofoil undergo small bending deformation with negligible twisting deformation. However, the flow-induced coupled bending and twisting deformation of propeller blades or hydrofoils with high skew or made of a lightweight and flexible material (e.g.,

fiber-reinforced composites) becomes more critical, as the twisting deformation changes the effective angle of attack, and hence the performance [147]. The deformation of the flexible lifting surface can be detrimental or beneficial for the structural performance, hydrodynamic performance, as well as cavitating performance, depending on the design. The impact of the fluid-structure interaction on performance further highlights the need for coupled hydrostructural optimization in the design of the next-generation marine propulsors using advanced lightweight materials.

Recently, Lee and Lin [79] performed hydrostructural optimization of a composite marine propeller using a 3-D coupled LS (lifting surface)-FEM solver with a genetic algorithm to optimize the stacking sequence of a 3-D composite marine propeller in steady, fully wetted conditions. They considered only 12 design variables for the stacking sequence of the composite material layers, but they did not consider the susceptibility to cavitation or the material failure in the optimization. Lin et al. [82] performed experimental studies in a cavitation tunnel for the DTNSRDC 4498 propeller design, comparing three different propellers: 1) original shape with quasi-isotropic stacking sequence, 2) original shape with the optimized stacking sequence, obtained using genetic algorithm [78, 83], and 3) pre-deformed shape with the optimized stacking sequence. The optimized propeller was designed to have a torque coefficient equal to the original shape at the design advance coefficient of 0.889. However, the experimental data showed that the design torque was not met at that advance coefficient for the original shape with the optimized stacking sequence. Thus, pre-deformed shape with the optimized stacking sequence was considered to be the true optimum. Results showed poor agreement between the experimental measurements and numerical predictions using a steady-state BEM solver (PSF-2) coupled with a commercial finite element solver (ABAQUS). They concluded that the pitch of the optimized propeller decreases as the loading decreases, resulting in reduced torque and increased efficiency. However, they did not test a no-twist or a rigid propeller for a fair comparison. Additionally, they did not consider structural integrity of the optimized propeller or cavita-

tion.

Motley et al. [105], Liu and Young [85], and Plucinski et al. [126] also performed hydrostructural optimization studies to optimize the efficiency of adaptive composite marine propellers, with consideration for cavitation, fluid-structure interaction, and material stress limits. All three studies used coupled 3-D BEM hydrodynamic solver and a 3-D finite element method (FEM) structural dynamics solver, which was validated with experimental measurement of rigid metallic and adaptive composite marine propellers [102,147,149,150, 152, 154]. While the LS method is slightly faster than the BEM [79], the BEM is better at capturing the flow details at the propulsor's leading edge and tip, the effects of nonlinear thickness-loading coupling, as well as cavitation. Motley et al. [105] presented an integrated probabilistic design approach to minimize lifetime fuel consumption subject to cavitation and stress-based material failure initiation constraints, with consideration for the probabilistic operation profile of the vessel. Liu and Young [85] and Plucinski et al. [126] used a genetic algorithm to optimize the stacking sequence to maximize the efficiency of self-twisting composite marine propellers. However, since they used a genetic algorithm as the optimizer, they only considered five design variables representing the stacking sequence for the composite propeller material layup with a discrete set of ply angles. Moreover, previous work on composite marine propellers has mostly focused on the optimization of the material layup sequence, and not the propeller shape itself.

Most of the previous work on shape optimization of marine propulsors has been based on low-to-medium-fidelity potential flow solvers–such as LS or BEM methods–with only up to 15 design variables. The multipoint aerostructural optimization with respect to large numbers of design variables using coupled CFD and FEM solver has been tackled in the aircraft wing design through the use of gradient-based algorithms together with efficient methods for computing the required gradients by Kenway et al. [67]. They carried out the coupled multipoint aerostructural optimization of a transonic transport wing with respect to 472 geometric shape and structural sizing variables, subject to 57 constraints. In a more

recent effort, Kenway et al. [69] minimized the fuel burn subject to lift, pitch moment, geometric, and structural failure constraints, yielding an 11.2% fuel burn reduction. While the approach has been successfully applied in aircraft wing design, the maritime application brings additional challenges such as higher loading, fluid structure interaction, as well as the potential susceptibility to cavitation, and hydroelastic instabilities.

In Chapter 5, the challenge of performing high-fidelity RANS-based coupled hydrostructural shape optimization while enforcing cavitation constraints, fatigue stress constraint, and the manufacturing tolerances is tackled. Results show that an efficient high-fidelity coupled hydrostructural optimization capable of handling large number of design variables is necessary to achieve a truly optimal, physically realizable, and structurally sound design. The hydrodynamic and cavitation performance improvement of the optimized hydrofoil is validated with experiments in Chapter 6.

1.2.3 Multipoint Optimization

Traditionally, marine propulsors and hydrofoils have been designed to achieve optimal performance at a single or a few operating conditions, such as the hump speed, the sustained speed, and the maximum speed. However, depending on the mission objectives, loading conditions, and sea states, a vessel may be required to operate over a wide range of operating conditions. It is also well known that the performance of fixed geometry and fixed pitch marine propulsors can decay rapidly for off-design conditions. Nevertheless, many designers still only design the propulsor geometry for optimal performance at a single design point, and then evaluate the performance at the other critical operating points to ensure satisfactory performance. Similarly, the structural performance evaluation is typically conducted only after the propulsor geometry is optimized based on the hydrodynamic performance only. This sequential design approach is adopted due to the high computational cost associated with the multipoint design using coupled fluid and structural calculations, particularly when using high-fidelity methods. However, this may not yield the best

overall design, particularly for vessels with broad operational profiles and load-dependent self-adaptive propellers [147].

Motley and Young [107] carried out performance-based analysis and design for rigid and flexible composite marine propellers across the probabilistic operational space of the vessel. They used the same 3-D coupled BEM-FEM solver as used by [85, 105, 126]. They concluded that it is critical to consider the full operational space when designing or analyzing self-adaptive composite marine propellers, due to the load-dependent blade deformation and performance. Motley and Young [107] also noted that the steady state efficiency and power requirements of the optimized rigid and adaptive propellers are similar at the design condition. However, the adaptive composite propeller achieves better performance in spatially varying wake inflow, off-design conditions, and cavitating conditions than its rigid counterpart due to the passive load-dependent pitch adaptation. They used an equivalent unidirectional fiber angle model to capture the global load-dependent hydroelastic behavior of multi-layer composite designs and to perform first-order analysis to confirm the structural integrity.

Kramer et al. [74] used a probabilistic multipoint approach to optimize the diameter of two waterjets for maximum overall system efficiency of a surface-effect ship while satisfying size and cavitation constraints. They found an increase in the lifetime fuel efficiency for the probabilistic multipoint optimized design compared to the single-point design. Blasques et al. [14] performed the design and optimization of a flexible composite marine propeller. They used the derivative-free pattern-search algorithm NOMADm as the optimization algorithm. To evaluate the performance, they used a 3-D BEM solver coupled with the commercial FEM software ANSYS. The propeller was optimized for two design points: cruise speed and maximum speed. The results showed a combined reduction of 1.25% in fuel consumption, and a decrease of 4.7% at the cruising speed condition for a controllable-pitch propeller installed on a naval vessel. However, they did not consider cavitation and studied the strength constraints separately, rather than in the optimization

model. Various other researchers also showed that the probabilistic multipoint design can lead to improved performance over the vessel's entire operation profile [107, 113, 145].

In Chapters 4 and 5, the difference in the performance as well as the computational time of the single-point optimized design and the multipoint optimized design is discussed. Results show that to achieve a design capable of performing well over the entire range of operation, multipoint optimization is necessary.

1.3 Effects of Load-dependent Bend-Twist Coupling on the Performance of Composite Hydrofoils

While Chapters 4 and 5 present a state-of-the-art high-fidelity coupled hydrostructural design optimization tool for optimizing the geometric shape of marine propulsors, the optimization of adaptive composite propulsors requires optimization of both shape and material configuration. In this section, previous studies and background on the impact of inherent material-based bend-twist coupling of the composite material on the hydroelastic performance will be presented.

1.3.1 Challenges and Benefits of Composites

Traditionally, marine propulsors are constructed of metallic alloys such as nickel aluminum bronze (NAB). NAB is preferred because of its anti-biofouling characteristics, good corrosion fatigue resistance in salt water, high resistance to cavitation erosion, and high stiffness. The abundance of available literature and extensive collective experience in the design, manufacturing, and use of metallic alloys favors its use for marine propulsors. In addition, the high stiffness of metallic alloys such as NAB allows decoupling of the hydrodynamic and structural analysis, which simplifies the design and analysis process.

With recent advances in resin and fiber materials technology, as well as the development of reliable high quality manufacturing methods, composites are now commonly used

in aerospace [50,71,118,143] and wind engineering applications [51,63,76,88,94,95,139]. Composites are also being used for many maritime applications, including propellers, turbines, pumps, hydrofoils, wings, waterjets, ducts, and control surfaces such as rudders, fins, and stern planes. However, the use of composites in marine propulsors is still not common compared to metallic alloys [13, 23, 27, 29, 52, 110, 147]. The reluctance to use composites, despite the well-known advantages (e.g., higher specific strength, higher specific stiffness, and resistance to corrosion), can be attributed to the lack of expertise and knowledge about manufacturing, design, serviceability, and reliability of composites in the harsh marine environment. Composites are also more difficult to model because of their anisotropic response (i.e., their material properties vary with respect to the load direction) and complex material failure mechanisms [9, 10, 12, 47, 56, 59, 117, 121, 129, 133]. There is also a reluctance to use composites for marine propulsors because of the lack of systematic data sets to validate design and analysis tools. Most marine propulsors are still made of metallic alloys, such as NAB, as the structural weight is not as critical a driver for maritime applications, as for aerospace or wind engineering applications.

One critical advantage of anisotropic composites that has gained significant interest in recent years is the ability to improve the hydrodynamic performance by tailoring the intrinsic material-induced bend-twist behavior to achieve passive, load-dependent shape adaptation. As shown in the previous literature, hydroelastic tailoring can be used to increase the energy efficiency and delay cavitation inception of composite marine propellers and turbines, particularly in spatially and/or temporally varying inflows and in off-design conditions [27, 85, 107, 109, 110, 147]. In addition to efficiency, another critical concern for both propulsors and turbines is flow-induced vibrations and noise, which can be passively controlled by understanding and carefully tailoring the load-dependent bend-twist coupling response of anisotropic composites.

For flexible marine propulsors and turbines, the hydrodynamic load may induce bending and twisting deformation, which will change the effective blade incidence and in turn

affect the hydrodynamic load distributions, flow separation and cavitation inception boundaries, as well as modal vibration characteristics (i.e. mode shapes, modal frequencies, and damping coefficients) and hydroelastic instability boundaries (e.g. static divergence and flutter) [147]. For isotropic and deformable lifting bodies, hydrodynamic bend-twist coupling exists when the center of pressure is away from the elastic axis (or shear center), where the twisting moment can induce a change in the effective angle of attack, and hence the hydroelastic performance and vibration characteristics [25,26]. The hollow and rib-spar structure typical of helicopter blades and wind turbines allow the designer some control of the elastic axis, but the center of pressure is difficult to control, as it is dependent on the flow condition. On the other hand, most marine propulsors and turbine blades have solid interior architecture because of the need to withstand high hydrodynamic loads (which are proportional to the fluid density), which limits the designer's ability to vary the elastic axis or the center of gravity. Moreover, practical geometric and material constraints typically limit the twisting deformation of hydrodynamic lifting devices made of homogeneous and isotropic engineering materials to be less than one degree. To achieve greater passive control of the hydroelastic response and stability of hydrodynamic lifting bodies, the intrinsic material bend-twist coupling behavior of anisotropic composites can be utilized by carefully selecting the material layup and stacking sequence, which can yield twisting deformation greater than one degree under normal hydrodynamic loads. However, the analysis and design process of adaptive composite marine propulsors introduces additional complications. The deformation and performance of passive adaptive hydrodynamic lifting bodies depend on the total load, which complicates the propeller-hull matching process, as the propeller must be able to overcome the vessel resistance, which varies with ship speed, heading, and sea states [107,147]. Moreover, a flexible lifting body designed to interact with the flow can be susceptible to flow-induced vibrations and hydroelastic instability issues. Hence, it is critical to fully understand and predict the load-dependent bend-twist coupling effects on the hydroelastic response and stability of adaptive composite marine propulsors and turbines.

1.3.2 Previous Experimental and Numerical Studies

Over the last decade, various researchers have presented coupled fluid-structure interaction (FSI) models to study the behavior of flexible marine propulsors and turbines in both sub-cavitating and cavitating flows [7, 26, 38, 85, 86, 112, 144, 145]. Lin and Lin [84] were among the first to show the effects of stacking sequence of anisotropic material layers on the hydroelastic performance of composite propeller blades. Numerical studies have shown that the load-dependent bend-twist coupling behavior of anisotropic composites can be used to improve the efficiency and reduce or delay cavitation compared to similar rigid geometry designs when operating at off-design conditions [70, 85, 106, 107, 109, 144, 152, 153]. Similar advantages have been found numerically for composite marine turbines, where adaptive blades were shown to improve performance, reduce structural loads, and reduce/delay cavitation compared to rigid blades [11, 104, 114, 115, 148]. Related numerical studies to optimize the stacking sequence of composite propellers to maximize fuel efficiency can be found in [79, 83, 85, 109, 126].

Gowing et al. [49] carried out one of the first experiments to study the effect of flexible hydrofoils on cavitation inception characteristics. They presented experimental measurements for two composite elliptic hydrofoils that were designed to reduce twist under load. They concluded that the deflections reduced the effective angle of attack, which delays cavitation inception due to the reduced tip loading. Chen et al. [27] presented results for a 24-inch model-scale adaptive pitch composite marine propeller that was designed to de-pitch under hydrodynamic load in forward operating conditions. They concluded that a properly designed flexible composite propeller can be more efficient and cavitation inception can be significantly delayed, compared to their rigid counterparts, in highly loaded off-design conditions and in spatially varying inflow. In addition to the studies conducted by Chen et al. [27], other experimental studies of composite marine propellers can be found in [82, 119]. In addition, Ducoin et al. [37–39], Akcabay et al. [6, 7], Akcabay and Young [8], and Chae et al. [25, 26] also carried out combined experimental and nu-

merical studies of the flow-induced deformation response, hydroelastic performance, and flow-induced vibration characteristics of cantilevered flexible hydrofoils in fully wetted and cavitating flow conditions. They concluded that the hydrodynamic and structural responses of the hydrofoil are strongly coupled, and the vibration characteristics of the hydrofoils can be significantly influenced by not only the structural stiffness and mass, but also the fluid inertial, damping, and disturbing forces.

Recently, Zarruk et al. [155] presented experimental measurements for six hydrofoils with similar geometry, but made up of different materials (stainless steel (steel), aluminum (AL), CFRP 00, CFRP +30). The results showed that the composite hydrofoils have significantly different hydrodynamic and hydroelastic performance, compared with the metallic hydrofoils. They also showed that the fiber orientation of the structural CFRP layers significantly affected the hydrodynamic performance. However, Zarruk et al. [155] did not fully investigate the impact of load-dependent bend-twist coupling, particularly on the stall boundaries, and did not connect the deformation response with the hydrofoil modal characteristics and hydroelastic stability boundaries, all of which are critical for the design, analysis, optimization, and safe operation of marine propulsors.

In Chapter 7, combined numerical and experimental studies are presented to understand the impact of load-dependent bend-twist coupling on the hydroelastic performance, stall boundaries, modal characteristics, static divergence speeds, and the cavitating performance of composite hydrofoils. Finally, in Chapter 8, we take the first step towards developing an efficient high-fidelity design optimization tool for composite hydrofoils by extending the FSI solver to simulate the behavior of unidirectional anisotropic composite hydrofoils.

1.4 Thesis Objectives

The objective of this thesis can be listed as:

- Extend a state-of-the-art aerodynamic design optimization tool to carry out the CFD-

based hydrodynamic shape optimization of a hydrofoil, with a large number of design variables and a constraint on cavitation inception, over a wide range of operating conditions.

- Extend the design optimization tool to carry out the coupled hydrostructural shape optimization of a hydrofoil, with a large number of design variables and a constraint on cavitation inception and fatigue stress, over a wide range of operating conditions.
- Validate the hydroelastic and cavitation performance improvement of an optimized hydrofoil with experimental measurements.
- Present combined experimental and numerical studies to improve the understanding of the governing physics behind load-dependent bend-twist coupling of composite hydrofoils.
- Extend the high-fidelity FSI solver to simulate the performance of unidirectional anisotropic composite hydrofoils.

1.5 Thesis Outline

This thesis presents a state-of-the-art high-fidelity hydrostructural shape optimization tool with a capability to handle a large number of design variables and constraints on cavitation inception, fatigue stress, and the manufacturing tolerances. The thesis can be divided into three major parts: (1) the coupled hydrostructural design optimization tool, (2) the combined experimental and numerical studies to understand the influence of the inherent bend-twist coupling of composites on the hydroelastic and cavitation performance of composite hydrofoils, and (3) coupled hydrostructural solver to predict the behavior of composite hydrofoils.

In Chapters 2, we discuss the hydrostructural design optimization framework. Chapter 2 gives an overview of each component in the framework, i.e., CFD solver, structural

solver, fluid-structure coupling algorithm, geometry and mesh perturbation, optimization algorithms, and cavitation constraint. Chapter 3 describes the experimental setup used for the experimental measurements presented in the following chapters. The experimental study presented in this thesis are conducted in Australian maritime College (AMC). The need for a large number of design variables and high-fidelity solver (i.e., RANS-based fluid solver over the Euler-based fluid solver) in the optimization process is described in Chapter 4. Chapter 4 also presents the multipoint hydrodynamic shape optimization of a hydrofoil, with a constraint on cavitation inception. In Chapter 5, we present the validation study of the hydrostructural solver. In addition, the multi-point hydrostructural optimization of an aluminum hydrofoil is presented with constraints on cavitation inception, fatigue stress, and the manufacturing tolerances. In Chapter 5, we also discuss the difference between the hydrodynamic-only optimized design and the hydrostructural design, in terms of performance as well as the computational time. In Chapter 6, experimental validation of the performance improvement through the numerical optimization techniques is presented.

Chapter 7 focuses on improving the understanding of underlying physics behind load-dependent bend-twist coupling of composite hydrofoils. We present combined experimental and numerical studies to understand the influence of inherent material-based bend-twist coupling on the hydroelastic response and the cavitation performance of composite hydrofoils. In Chapter 8, we extend the high-fidelity structural solver to simulate the performance of anisotropic composites. The modal characteristics (i.e., mode shapes and frequencies), static stress, and deformation verification studies against a commercial structural solver, Abaqus, is presented. The conclusions are summarized in Chapter 9.

CHAPTER 2

Hydrostructural Design Optimization Framework

To achieve the overall goal of performing hydrostructural optimization of marine lifting surfaces, the previously developed framework, MACH (MDO of Aircraft Configurations with High-fidelity) [66, 67] was extended. The MACH framework has the capability of performing static aeroelastic (aerostructural) optimization of lifting surfaces, which consists of simultaneously optimizing the aerodynamic shape and structural sizing while accounting for structural flexibility [21, 65, 69, 80]. The MACH framework is adapted for hydrostructural shape optimization of lifting surfaces in viscous and nearly incompressible flows, with a constraint to avoid cavitation inception, aggregated von Mises stress, and the manufacturing tolerances. We now briefly describe the components of the hydrostructural optimization framework: CFD solver, structural solver, fluid-structure coupling algorithm, geometry perturbation algorithm, optimization algorithm, adjoint gradient computation, and cavitation constraint.

2.1 CFD Solver

The flow is assumed to be governed by the 3-D compressible RANS equations without body forces, which can be written as,

$$\begin{aligned} \frac{\partial \rho_f}{\partial t} + \frac{\partial}{\partial x_j}[\rho_f v_j] &= 0 \\ \frac{\partial \rho_f v_i}{\partial t} + \frac{\partial}{\partial x_j}[\rho_f v_i v_j + p\delta_{ij} - \tau_{ij}] &= 0 \\ \frac{\partial E}{\partial t} + \frac{\partial}{\partial x_j}[E v_j + p v_j + q_j - v_i \tau_{ij}] &= 0 \end{aligned} \tag{2.1}$$

where the subscript indices $i, j = 1, 2, 3$ correspond to the x, y, and z directions, respectively; v is the velocity; ρ_f is the fluid density; p_f is the fluid pressure; E is the fluid energy; τ_{ij} is the fluid shear stress tensor; δ_{ij} is the Kronecker delta; and q_i is the fluid heat flux vector. These equations can be written in discrete form as a set of residual equations for the flow states $w = [\rho_f, \rho_f v_1, \rho_f v_2, \rho_f v_3, \rho_f E]^T$,

$$\mathcal{A}(w) = 0 \tag{2.2}$$

The CFD solver used herein is ADflow, which is a 3-D finite-volume, cell centered multi-block solver for the compressible flow equations [137]. The Jameson–Schmidt–Turkel [62] scheme augmented with artificial dissipation is used for spatial discretization. An explicit multi-stage Runge–Kutta method is used for the temporal discretization. The one-equation Spalart–Allmaras (SA) [131] turbulence model is used. ADflow includes a discrete adjoint solver developed by Lyu et al. [90] (explained briefly in Section 2.6) that computes gradients suitable for shape optimization studies [28, 68, 89, 91].

The focus of this thesis is on incompressible flows. The compressible flow equations can be used to solve incompressible flows, where the Mach number ($M_a = U/a$; where U is the fluid speed, and a is the speed of sound in the fluid) is very close to zero, say less than 0.01. As explained in Turkel et al. [136], when solving compressible equations for

such low Mach numbers, numerical issues arise because of the large disparity between the acoustic wave speed, i.e., $v + a$, and the waves convection speed, i.e., v, resulting in an ill-conditioned system.

There are two basic approaches available in the literature to solve compressible flow equations for nearly incompressible flows: 1) Dual-time stepping approach [17, 101, 140]: This approach is used for time-accurate solutions. In this approach, flow-field at each level is treated as a steady-state problem in pseudo-time, with appropriate source terms to provide an influence on the flow history at the current time level. However, they are relatively difficult to implement due to the addition of pseudo-time variable. 2) Pseudo-compressibility approach [30, 135, 136]: This approach damages the time-accuracy of the solution. In this approach, the time derivatives of a flow governing equation are pre-multiplied by a preconditioner matrix which slows down the speed of the acoustic waves towards the fluid speed to make the system well-conditioned. Since, in this thesis, we are not interested in the time-accurate solutions, we use the pseudo-compressibility approach. Turkel et al. [136] describe pseudo-compressibility approach using two algorithms: in the first algorithm, conversation variables, i.e., $[\rho_f, \rho_f v_1, \rho_f v_2, \rho_f v_3, \rho_f E]$, are used for all the updates and the major change is the multiplication of the time derivatives by a nonphysical matrix. In the second algorithm, instead of updating the conservation variables, the new variables are used (as specified in Turkel et al. [136]). Second algorithm basically changes the dependent variable from density to pressure, since density becomes constant in the incompressible limit. With the second algorithm, inflow Mach number of zero results in an effectively incompressible code. Zero Mach number is not possible with the first algorithm since density appears in the equation, but a low enough Mach number, e.g. $M_a = 0.01$, can be achieved efficiently by preserving the integrity of the solution since the flow compressibility effects are negligible for $M_a < 0.1$. However, to avoid updating the variables and significantly reducing the amount of work required, we chose the first algorithm. The disadvantage of the first algorithm is that it runs into numerical problems for Mach numbers

below 0.01. Details of the first algorithm implemented in ADflow is presented below.

The condensed compressible RANS equation (non-conservative form of the Eq. (2.1)), for the 3-D viscous flows with the preconditioner matrix can be written as,

$$\mathbf{D^{-1}w_t + Aw_x + Bw_y + Cw_z} = 0 \tag{2.3}$$

where $\mathbf{w_t}$ is the time derivative of the state variables; $\mathbf{w_x}$ (or $\mathbf{w_y}$ and $\mathbf{w_z}$) is the x (or y and z)-derivative of the state variables; and $\mathbf{A}$ (or $\mathbf{B}$ and $\mathbf{C}$) is the flux Jacobian. To accommodate the compressible formulation in ADflow, the preconditioner matrix, $\mathbf{D}$, is defined as,

$$\mathbf{D} = \frac{\partial \mathbf{w_c}}{\partial \mathbf{w_0}} \mathbf{D_0} \frac{\partial \mathbf{w_0}}{\partial \mathbf{w_c}} \tag{2.4}$$

where $\mathbf{w_0}$=$[p, u, v, w, E]^T$; $\mathbf{w_c}$=$[\rho_f, \rho_f v_1, \rho_f v_2, \rho_f v_3, \rho_f E]^T$; and $\mathbf{D_0}$ is defined as,

$$\mathbf{D_0} = \begin{bmatrix} \frac{\beta M_T^2}{a^2} & 0 & 0 & 0 & 0 & -\frac{\beta M_T^2 \zeta}{a^2} \\ -\frac{\gamma v_1}{\rho_f a^2} & 1 & 0 & 0 & 0 & \frac{\gamma v_1 \zeta}{\rho_f a^2} \\ -\frac{\gamma v_2}{\rho_f a^2} & 0 & 1 & 0 & 0 & \frac{\gamma v_2 \zeta}{\rho_f a^2} \\ -\frac{\gamma v_3}{\rho_f a^2} & 0 & 0 & 1 & 0 & \frac{\gamma v_3 \zeta}{\rho_f a^2} \\ 0 & 0 & 0 & 0 & 1 & 0 \\ 0 & 0 & 0 & 0 & 0 & 1 \end{bmatrix} \tag{2.5}$$

$$\beta M_T^2 = \min[\max(K_1(v_1^2 + v_2^2 + v_3^2), K_2(v_{1\text{inf}}^2 + v_{2\text{inf}}^2 + v_{3\text{inf}}^2)), a^2] \tag{2.6}$$

$$K_1 = K_3\left[1 + \frac{(1 - K_1 M_0^2)}{K_1 M_0^4} M_a^2\right] \tag{2.7}$$

where a is the speed of sound; ρ_f is the density of the fluid; $v_{1\text{inf}}$,$v_{2\text{inf}}$, $v_{3\text{inf}}$ are the free-stream velocities along x, y, and z, respectively. M_a is the free stream Mach number; M_0 is a constant set by the user to decide the specific Mach number to activate the preconditioner;

for $M_a > M_0, \beta M_T^2 = a^2$.

The main function of this preconditioner matrix, **D**, is to reduce the stiffness of the eigenvalues. The acoustic wave speed, $v + a$, is replaced by a pseudo-wave speed of the same order of magnitude as the fluid speed. To be efficient, the selected preconditioning is valid for inviscous computations as well as for viscous computations.

There are various low-speed preconditioners available in the literature. Some of the most common ones are Turkel [136], Choi–Merkle [30] and Van leer [138]. A general preconditioner with two free parameters, γ and ζ is presented in Eq. (2.5). If $\zeta = 1$ and $\gamma = 0$, then we have the preconditioner suggested by Choi and Merkle [30]. With $\zeta = 0$ and $\gamma = 0$, the Turkel [136] preconditioner is recovered. In the present method, the Turkel preconditioner is used. M_0 is fixed as 0.2 in the current solver, such that the preconditioner is active only when the Mach number is below 0.2. K_3 was set as 1.05 and K_2 as 0.6, which are within the range suggested by Turkel [136]. Note that the preconditioning matrix shown in Eq. (2.5) becomes singular at $M_a = 0$. Thus, the preconditioner will not work for Mach number very close to 0. The preconditioner was tested for Mach number as low as 0.01. For $M_a < 0.01$, the preconditioner runs into some numerical difficulties depending on the problem. Typically, in marine applications, the Mach number ranges from 0.001 to 0.05. The higher end of the range can be easily solved using the modified solver, but numerical issues are encountered near the lower end. However, for $M_a < 0.01$, compressibility effects are negligible, and hence the actual solution would be practically the same as the $M_a = 0.01$ case.

Additionally, to simulate the same dynamic viscosity and temperature as used in the experiments, the Sutherland's law [132] is used,

$$\mu_f = \mu_{\text{ref}} \left[\frac{T}{T_{\text{ref}}} \right]^{3/2} \frac{T_{\text{ref}} + S_{\text{ref}}}{T + S_{\text{ref}}}, \tag{2.8}$$

where T_{ref} is the reference temperature, μ_{ref} is the dynamic viscosity at T_{ref}, and S_{ref} is

the Sutherland temperature. Since Sutherland's law is not valid for water, we modified the Sutherland's law parameters (T_{ref}, S_{ref}) to get $\mu_f = \mu_{\text{ref}}$ by setting $T = T_{\text{ref}}$. Thus, for any value of S_{ref} we have,

$$\left[\frac{T}{T_{\text{ref}}}\right]^{3/2} \frac{T_{\text{ref}} + S_{\text{ref}}}{T + S_{\text{ref}}} = 1. \tag{2.9}$$

To replicate the experimental conditions used by Zarruk et al. [155], we set $T = T_{\text{ref}} = 15^{\text{o}}$ C, so $\mu_f = 1.140 \times 10^{-3}$ Ns/m^2.

2.1.1 Convergence Behavior of the Low-Speed Preconditioner Solver

As shown in previous literature [136], the low-speed preconditioners typically reduces the speed of the system significantly and thus the convergence speed also reduces. The slow convergence rate makes it difficult to be used for analysis, and thus optimization. To overcome the slow convergence issue, the spectral radius method used to calculate the time step size in the Runge–Kutta 4^{th} order (RK4) solver was modified to reflect the state variables after preconditioning. The spectral radius, r, of a matrix can be defined as the maximum absolute value of its eigenvalues (λ_i), as shown in Eq. (2.10). The modified time step size is calculated by finding the spectral radius of the preconditioned flux Jacobians, **A**, **B**, and **C**, as shown in Eq. (2.11).

$$r(\mathbf{A}) = \max|\lambda_i| \tag{2.10}$$

$$\triangle t = CFL \times \forall \times \frac{1}{r(\mathbf{A}) + r(\mathbf{B}) + r(\mathbf{C})} \tag{2.11}$$

where $|\lambda_i|$ are the eigenvalues of the respective matrices. $r(\mathbf{A})$ represents the spectral radius of **A**, and similarly for $r(\mathbf{B})$ and $r(\mathbf{C})$. CFL is the CFL (Courant–Friedrichs–Lewy) number [33] and $\forall$ is the volume of the particular cell.

Table 2.1 shows the comparison of the time and iterations taken by ADflow at the Mach number of 0.8, and ADflow at the Mach number of 0.05. Both the simulations were carried

out for a tapered NACA 0009 hydrofoil (as shown later in Section 4.1.1) using RANS equations, at Re = 1×10^6 and angle of attack (α) of 6°. The computational time and number of iterations required for convergence for the two cases are compared in Table 2.1. Both simulations used a 515,520 cell mesh (shown later in Figure 4.2) with a y^+ of 1.1. The solutions were converged until the residuals were less than 1×10^{-6}. The simulations were carried out with 64 processors (2.80 GHz Intel Xeon E5-2680V2 processors at the University of Michigan High Performance Computing (HPC) flux cluster. As observed from Table 2.1, the ADflow at Mach number of 0.05 takes approximately 2.2 times the computational time taken by the ADflow at the Mach number of 0.8, which is acceptable to carry out optimization studies.

Table 2.1: Comparison of computational time and the number of iterations required for convergence for the RANS-simulation results using the ADflow at $M_a = 0.8$ and $M_a = 0.05$ for a tapered NACA 0009 hydrofoil at Re = 1.0×10^6 and α of 6°. The simulations were carried out with 64 processors (2.80 GHz Intel Xeon E5-2680V2 processors).

	M_a=0.8	M_a=0.05
Computational time (s)	343	743
No. of Iterations	2559	6144

2.2 Structural Solver

The structural solver used in the MACH framework is the Toolkit for the Analysis of Composite Structures (TACS) [64]. TACS is a parallel, general 3-D finite-element solver for structural analysis. The steady-state structural governing equation residuals can be written as,

$$\mathcal{S}(u) = Ku - F = 0, \tag{2.12}$$

where u is the vector of structural displacements, K is the linear structural stiffness matrix, and F is the hydrodynamic load vector. TACS is also able to compute gradients using an adjoint method (explained in Section 2.6), making the cost of the gradient calculation

nearly independent of the number of structural design variables. In the present research, the hydrofoil is assumed to be made of a solid homogeneous isotropic material with the linear elastic response. In addition to the displacements, TACS computes the stress for each finite element.

2.3 Fluid-Structure Coupling Algorithm

The CFD and the structural solvers described above are coupled in a hydrostructural solver capable of predicting the hydrofoil deflections and forces for a given flow condition. The hydrodynamic loads (pressure and shear stresses) computed by ADflow are transferred to the structural solver, and the displacements from the structural solver, in turn, dictate the deformation of the CFD mesh. Kenway et al. [66] implemented the load and displacement transfer scheme used in this work based on the methodology presented by Brown [20]. Rigid links are computed between each CFD surface mesh point and the closest point on the structural model surface. The rigid links are then used to extrapolate the displacements from the structural surface to the CFD surface. The consistent force vector is determined by employing the method of virtual work, ensuring that the force transfer is conservative. The integration of the forces is performed on the CFD mesh, and forces are then transferred to the structure through the rigid links. The two major advantages of using this scheme are that (1) it is consistent and conservative by construction, and (2) it may be used to transfer loads and displacements between CFD and structural meshes that are not coincident.

To solve the coupled hydrostructural equations, the hydrodynamic analysis is first partially converged, and the forces are evaluated. These forces are then transferred to the structural analysis, and the corresponding displacements are computed. Thereafter, the displacements are transferred back to the hydrodynamic analysis, the geometry, and the corresponding mesh is deformed, and a new CFD solution is found. This iterative loop continues until the coupled convergence criterion is satisfied (when the relative decrease in

both the hydrodynamic and structural residuals compared to the free-stream values is less than 10^{-5}).

2.4 Geometry Perturbation Algorithm

The free-form deformation (FFD) volume approach is used to parametrize the geometry [66]. To obtain a more efficient and compact set of geometric design variables, the FFD volume approach parametrizes the geometric changes rather than the geometry itself. All the geometric changes are performed on the outer boundary of the FFD volume. Changes to this outer boundary modify the objects embedded in the volume, including the foil and the structural mesh. Deformation of the structural mesh cause changes in the stiffness matrix of the structural model, resulting in a change in the stiffness, resonance frequencies, and internal stress distribution. The examples of the FFD control points used for hydrofoil optimization are presented in Chapters 4 and 5.

Since the geometry is modified during the optimization using the FFD volume approach, the CFD mesh needs to be perturbed to carry out the hydrostructural solution for the modified geometry. The mesh perturbation scheme is a hybridization of algebraic and linear-elasticity methods [66]. In the hybrid warping scheme, a linear-elasticity-based warping algorithm is used for a coarse approximation of the mesh to account for large, low-frequency perturbations; the algebraic warping algorithm is used to attenuate small, high-frequency perturbations. For the results shown in this thesis, the hybrid approach is not required, and the algebraic algorithm is used because only small mesh perturbations were needed to optimize the geometry.

2.5 Optimization Algorithm

The CFD and structural FEM solutions are the most expensive components in the hydrostructural shape optimization. Thus, for large-scale optimization problems, the chal-

lenge is to solve the problem to the desired level of optimality with as few hydrostructural function evaluations as possible. There are two broad categories of optimization algorithms: gradient-free algorithms and gradient-based algorithms. Gradient-free algorithms, such as genetic algorithms and particle swarm optimization, have a higher probability of getting close to the global minima for problems with multiple local minima. However, the gradient-free algorithms exhibit low convergence rates and require large numbers of function calls, especially for large numbers of design variables, making it impossible to optimize with respect to hundreds of design variables [92] (as shown in Figure 2.1 from [92]). Additionally, Lyu et al. [89] carried out a series of fixed planform shape aerodynamic optimizations for three random geometries. Lyu et al. [89] concluded that the optimized designs have similar pressure coefficient (C_p) distributions, cross-sectional shapes, and the drag between the three designs is very close to each other. They also concluded that the design space for that optimization problem is mostly convex, but has a small multimodal flat region. Thus, for the problems presented in this thesis, the gradient-based algorithms should be able to converge very close to the global minima, if not at the global minima.

To reduce the number of function evaluations for cases with large numbers of design variables, we used the gradient-based optimization algorithm SNOPT (sparse nonlinear optimizer) [48]. SNOPT utilizes a sequential quadratic programming algorithm and is capable of solving large-scale nonlinear optimization problems with thousands of constraints and design variables.

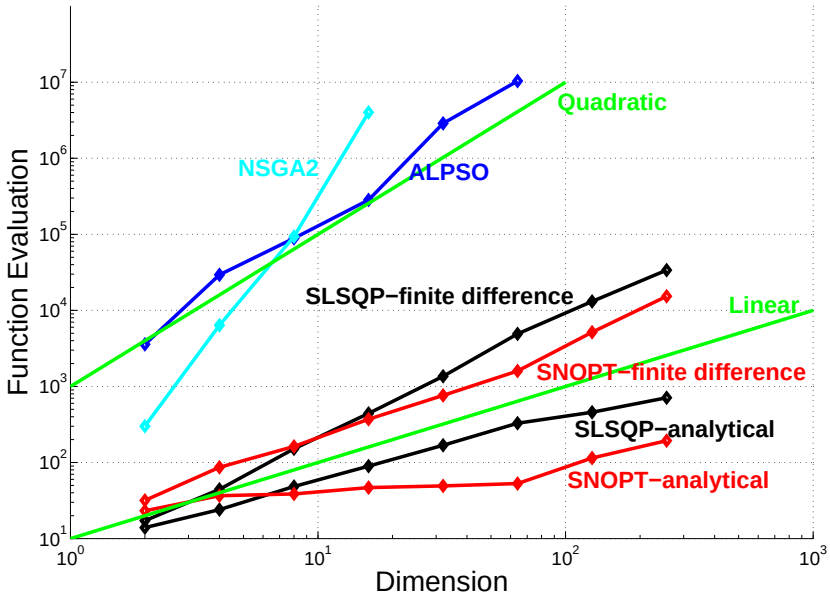

Figure 2.1: While the gradient-free methods (NSGA2, ALPSO) scale poorly, the gradient based methods (SNOPT, SLSQP) scale linearly with the number of design variables. The function used for this study is multi-dimensional Rosenbrock function. The figure is originally presented in Lyu et al. [92].

2.6 Adjoint Gradient Computation

Effective gradient-based optimization requires accurate and efficient gradient calculations. The finite-difference provides a straightforward way to compute gradients, but they are neither accurate nor efficient [99]. The finite-difference methods are sensitive to the step size used for the difference: If the step size is higher or lower than the optimal step size, the errors can be significant. The complex-step method yields accurate gradients, but it is not efficient for large numbers of design variables [98, 99]. Therefore, we use the adjoint method for gradient calculations, which can efficiently and accurately compute gradients with respect to large numbers of design variables [91, 93, 98].

The adjoint method has been extensively used in aerodynamic shape optimization [61, 89, 116, 123], as well as structural design optimization [34, 35]. The flow adjoint solver used in this work was developed by linearizing the discretized PDEs (partial differential

equations) using automatic differentiation [90, 93]. This approach significantly reduces the implementation time by removing the requirement for hand differentiation and the derivation of the adjoint boundary conditions.

For problems where the flow and structural equations are coupled, a coupled adjoint approach is required. Martins et al. [97] proposed this coupled adjoint approach and applied it to the aerostructural design optimization of a supersonic business jet [96]. Kenway et al. [66, 67] implemented the coupled adjoint used in this work, which is summarized below.

The residual equations from the hydrodynamic and structural disciplines—presented earlier as Eqs. (2.2) and (2.12)—can be combined, and the resultant residual of the multidisciplinary system can be written as,

$$\mathcal{R} = \begin{bmatrix} \mathcal{A}(w, u; x) \\ \mathcal{S}(u, w; x) \end{bmatrix} = 0 \tag{2.13}$$

where, x is the vector of design variables.

For gradient-based optimization, we require the derivatives of an objective or constraint function (i.e., the function of interest) I with respect to the design variables x. Given the dependence on the states of the flow (w), the states of the structure (u), and the design variables (x), the total derivative of the function of interest is

$$\frac{\mathrm{d}I}{\mathrm{d}x} = \frac{\partial I}{\partial x} + \begin{bmatrix} \dfrac{\partial I}{\partial w} & \dfrac{\partial I}{\partial u} \end{bmatrix} \begin{bmatrix} \dfrac{\mathrm{d}w}{\mathrm{d}x} \\ \\ \dfrac{\mathrm{d}u}{\mathrm{d}x} \end{bmatrix}. \tag{2.14}$$

Note that the total derivatives ($\mathrm{d}w/\mathrm{d}x$ and $\mathrm{d}u/\mathrm{d}x$) require the solution of the governing equations, while the partials do not.

To avoid the calculation of the total derivatives, we can use the derivatives of the resid-

uals:

$$\begin{bmatrix} \dfrac{\mathrm{d}\mathcal{A}}{\mathrm{d}x} \\ \\ \dfrac{\mathrm{d}\mathcal{S}}{\mathrm{d}x} \end{bmatrix} = \begin{bmatrix} \dfrac{\partial \mathcal{A}}{\partial x} \\ \\ \dfrac{\partial \mathcal{S}}{\partial x} \end{bmatrix} + \begin{bmatrix} \dfrac{\partial \mathcal{A}}{\partial w} & \dfrac{\partial \mathcal{A}}{\partial u} \\ \\ \dfrac{\partial \mathcal{S}}{\partial w} & \dfrac{\partial \mathcal{S}}{\partial u} \end{bmatrix} \begin{bmatrix} \dfrac{\mathrm{d}w}{\mathrm{d}x} \\ \\ \dfrac{\mathrm{d}u}{\mathrm{d}x} \end{bmatrix} = 0, \tag{2.15}$$

where $\mathcal{A}$ represent the flow residuals and $\mathcal{S}$ represent the structural residuals. Substituting Eq. (2.15) into Eq. (2.14), we can eliminate the total derivatives and obtain

$$\frac{\mathrm{d}I}{\mathrm{d}x} = \frac{\partial I}{\partial x} - \underbrace{\begin{bmatrix} \dfrac{\partial I}{\partial w} & \dfrac{\partial I}{\partial u} \end{bmatrix} \begin{bmatrix} \dfrac{\partial \mathcal{A}}{\partial w} & \dfrac{\partial \mathcal{A}}{\partial u} \\ \\ \dfrac{\partial \mathcal{S}}{\partial w} & \dfrac{\partial \mathcal{S}}{\partial u} \end{bmatrix}^{-1}}_{\Psi^T} \begin{bmatrix} \dfrac{\partial \mathcal{A}}{\partial x} \\ \\ \dfrac{\partial \mathcal{S}}{\partial x} \end{bmatrix}. \tag{2.16}$$

The adjoint method consists in solving for the coupled adjoint vector, $\Psi = [\psi^T \quad \phi^T]^T$. From Eq. (2.16) we can obtain the linear system,

$$\begin{bmatrix} \dfrac{\partial \mathcal{A}}{\partial w} & \dfrac{\partial \mathcal{A}}{\partial u} \\ \\ \dfrac{\partial \mathcal{S}}{\partial w} & \dfrac{\partial \mathcal{S}}{\partial u} \end{bmatrix}^T \begin{bmatrix} \psi \\ \\ \phi \end{bmatrix} = \begin{bmatrix} \dfrac{\partial I}{\partial w} & \dfrac{\partial I}{\partial u} \end{bmatrix}^T. \tag{2.17}$$

These are the coupled adjoint equations governing the fluid and structural response, which need to be solved for each function of interest, irrespective of the number of design variables. This makes the adjoint method computationally more efficient, as usually there are large number of design variables (> 100), particularly for problems with complex geometry and structural or material configurations, but only a limited number of functions of interest (e.g., drag coefficient, lift coefficient, efficiency, and maximum stress).

Once the adjoint variables are obtained by solving the coupled adjoint equations Eq. (2.17),

we can substitute the adjoint vector into Eq. (2.16) to obtain the gradient of the function of interest with respect to the design variables:

$$\frac{\mathrm{d}I}{\mathrm{d}x} = \frac{\partial I}{\partial x} - \psi^T \left(\frac{\partial \mathcal{A}}{\partial x} \right) - \phi^T \left(\frac{\partial \mathcal{S}}{\partial x} \right). \tag{2.18}$$

Kenway et al. [66] provide a more detailed derivation, including explanations of how all the partial derivatives are computed, and how the coupled linear system is solved.

Since our structural model has thousands or more of finite elements, there are potentially as many stress constraints. Enforcing stress constraints for each element would require the computation of thousands or more of coupled adjoint vectors, which would be prohibitive. To reduce the number of required adjoint solutions, we use the Kreisselmeier–Steinhauser (KS) constraint aggregation technique [127, 142], which provides a conservative estimate of the maximum stress in a smooth and differentiable manner. The KS constraint used in this thesis is presented in Lambe et al. [77]. For the sake of completeness, KS constraint is briefly explained here. Consider a set of constraints $\vec{C}(\vec{x}) \leq 0$, where $\vec{C} : \mathbb{R}^n \rightarrow \mathbb{R}^m$ and the maximum-value function $\max_i\{C_i(\vec{x})\} \leq 0$ aggregates the constraint set. Since we are using gradient-based optimization algorithm, the non-smooth maximum-value function is not compatible. Thus, a smooth aggregation KS technique replaces $\vec{C}(\vec{x}) \leq 0$ with

$$KS\left(\vec{C}(\vec{x})\right) = c_{\max} + \frac{1}{\rho_{KS}} \ln\left(\sum_{i=1}^{m} exp\left(\rho_{KS}\left(C_i(\vec{x} - c_{\max})\right)\right) \right) \leq 0, \tag{2.19}$$

where $c_{\max} = \max_i\{C_i(\vec{x})\}$, x are the design variables, and ρ_{KS} is the user-specified parameter. ρ_{KS} is used to balance the smoothness of the KS function and the accuracy of the feasible region. For the results presented in this thesis, $\rho_{KS} = 80$. As explained in Lambe et al. [77], KS is a conservation aggregation technique, i.e., if a given design point $\vec{x}$ is feasible with respect to the KS constraint, then it will be feasible for original set of constraints.

Using the KS technique, we aggregate the von Mises stresses to obtain a single con-

straint for the entire volume of the hydrofoil, for which the corresponding adjoint vector is computed.

2.7 Cavitation Constraint

To enforce a CFD-based cavitation constraint, we developed a formulation inspired by the work of Kenway and Martins [69], who developed a constraint for flow separation and applied it to aircraft wing design. Papoutsis–Kiachagias et al. [120] also developed a similar technique to constrain cavitation in hydraulic turbomachines. First, we determine if there is cavitation at a given location on the surface by checking if the minimum pressure is lower than or equal to the vapor pressure, i.e., when

$$-C_p \geq \sigma \tag{2.20}$$

where,

$$\begin{aligned} C_p &= \frac{P_{\text{local}} - P_{\text{ref}}}{0.5\rho_f U^2} \\ \sigma &= \frac{P_{\text{ref}} - P_{\text{vap}}}{0.5\rho_f U^2} \\ P_{\text{ref}} &= P_{\text{atm}} + \rho_f g h, \end{aligned} \tag{2.21}$$

where P_{local} is the absolute local pressure, P_{atm} is the atmospheric pressure, ρ_f is the fluid density, g is the gravitational acceleration, h is the submerged depth, and P_{vap} is the vapor pressure of water at 15°C (1706 Pa).

In this work, we use $\sigma = 1.6$, which represents the cavitation inception condition for a vessel with an advance speed of 25 knots (12.9 m/s) for a submerged depth of 1.0 m. We define a cavitation sensor as,

$$\chi = \begin{cases} 1 & \text{if} \quad -C_p \geq \sigma \\ 0 & \text{if} \quad -C_p < \sigma \end{cases} \tag{2.22}$$

The sensor χ is defined for each and every surface location and is equal to one when there is cavitation, and zero when there is no cavitation, which is essentially a Heaviside function. Since a gradient-based optimizer is used, the discontinuity of this function needs to be addressed [69]. Thus, we use a smooth Heaviside function to blend the discontinuity across the CFD cells, yielding

$$\overline{\chi} = \frac{1}{1 + e^{2k(C_p + \sigma)}} \tag{2.23}$$

The cavitation constraint is formulated as the integral of $\overline{\chi}$ over the hydrofoil surface to determine the total surface area susceptible to cavitation, i.e.,

$$A_{\text{cav}} = \frac{1}{A_{\text{ref}}} \iint_A \overline{\chi} \mathrm{d}A \tag{2.24}$$

where A_{ref} is the planform hydrofoil area, and k is a free parameter used to determine the sharpness of the transition. We use $k = 10$ for the results presented in this thesis, which yields the desired behavior. In theory, A_{cav} should be zero, but due to the inevitable discretization errors, we used $A_{\text{cav}} \leq 5 \times 10^{-4}$. Note that A_{cav} is non-dimensional, thus, it is not dependent on the hydrofoil or blade area.

2.7.1 Cavitation Inception Speed

The delay of cavitation inception increases the cavitation inception speed, which can be estimated from the definition of pressure coefficient with the value for the vapor pressure of water,

$$U_{\text{cav}} = \sqrt{\frac{P_{\text{ref}} - P_{\text{vap}}}{0.5 \rho_f C_{p_{\text{min}}}}} \tag{2.25}$$

For example, a reduction in $-C_{p\text{min}}$ from 2.1 to 1.0 corresponds to a cavitation inception speed increase from 10.6 m/s to 15.4 m/s, for an assumed submerged depth of 1 m.

CHAPTER 3

Experimental Setup and Techniques

To validate the numerical design optimization framework presented in the previous chapter, we use the experimental studies carried out at the Australian Maritime College. The experimental measurements are used to validate the hydrodynamic and hydrostructural results shown later in Chapters 4 and 5, respectively [155]. In addition to the validation study, we collaborated with Australian Maritime College (AMC) and Defence Science Technology Group (DSTG), Australia to conduct experiments on the optimized hydrofoil (presented in Chapter 6) and the composite hydrofoils (presented in Chapter 7). The hydrofoils are manufactured by DSTG, Australia and are tested in Cavitation Research Laboratory (CRL) variable pressure tunnel (or cavitation tunnel) at AMC, Australia. In this chapter, details of the experimental facility, the hydrofoil setup, and the experimental techniques will be discussed.

3.1 Experimental Facility

The experimental measurements presented in this work are conducted in the cavitation tunnel at the AMC. The tunnel test section is 0.6 m square by 2.6 m long. The operating velocity and pressure ranges are respectively, 2–12 m/s and 4–400 kPa absolute. The tunnel volume is 365 m^3, which is filled with demineralized fresh water (conductivity of order 1 μS/cm). The tunnel has ancillary systems for rapid degassing and for continuous injection and removal of nuclei and large volumes of incondensable gas. The test section velocity is

measured from one of the two (low and high range) Siemens Sitrans P differential pressure transducer models 7MF4433-1DA02-2AB1-Z and 7MF4433-1FA02-2AB1-Z (measuring the calibrated contraction differential pressure) with estimated precisions of 0.007 m/s and 0.018 m/s, respectively. The velocity and pressure in the test section are controlled to maintain a constant Reynolds numbers and cavitation numbers. The test section velocity is spatially uniform to within 0.5%, has temporal variations of less than 0.2%, and the freestream turbulence intensity at the inlet of the test section is about 0.5%. The blockage ratio, defined as the quotient of the planform area of the hydrofoils and the tunnel test section cross-sectional area, is 0.075. For the range of testing conditions, the blockage effect on the results is expected to be negligible [53, 111]. Detailed descriptions of the facility are given in [15, 36, 155].

3.2 Hydrofoil Setup

The hydrofoil geometry and properties have been selected based on the requirements for modeling of static and dynamic conditions typical of those experienced by propellers and hydrofoils operating in ship or submarine wakes. The hydrofoil geometry has an unswept trapezoidal planform with a loaded span of s = 300 mm, a base chord of 120 mm, and a tip chord of 60 mm. An unswept geometry was deliberately chosen to focus on the material bend-twist coupling effects on the hydroelastic response of the composite hydrofoils (as presented in Chapter 7). The hydrofoil is rigidly mounted from the ceiling of the test section via a six-component force balance as described in Section 3.4. The effective aspect ratio of the hydrofoil, considering the cantilevered condition at the root, is AR = $2s/c$ = 6.67, where c = 90 mm is the mean chord. The model size of the hydrofoil has been chosen as a trade-off between the Re and instrumentation limits, such that confinement effects are negligible [46, 53].

All the hydrofoil models have identical planform and a NACA 0009 cross section. The

4 digit NACA 0009 profile is used, as their pre-stall hydrodynamic performance is relatively independent of the Reynolds number [60], which helps to highlight the load (or Re)-dependent effects of the composite hydrofoils. The experimental hydrodynamic characteristics of the NACA 0009 profiles are comprehensively described in the literature [3, 128]. The hydrofoils are made up of either standard or modified section profiles and are referred to as type I or type II hydrofoils, respectively (as shown in Figure 3.1). The modified NACA 0009 profile is used to provide a thicker trailing edge for improved manufacturability for the type II hydrofoils. The hydrofoil trailing edge was made thicker by adjusting the coefficient of the last term in the NACA 4 digit equation, i.e.,

$$\zeta = 5t(0.2969\eta^{0.5} - 0.126\eta - 0.3516\eta^2 + 0.2843\eta^3 - 0.08890\eta^4) \tag{3.1}$$

where η and ζ are the chordwise coordinate and the half thickness, respectively, non-dimensionalized by the chord; t is the thickness to chord ratio, which is 0.09 for NACA 0009. In the original geometry, i.e., the type I hydrofoils, the coefficient of η^4 is 0.1015, instead of 0.08890.

Two type I hydrofoils were manufactured and tested: one made of solid stainless steel (SS 316L alloy, presented in Chapter 4) and one made of solid aluminum (6061 T6 alloy, presented in Chapter 5). Five type II hydrofoils were manufactured: stainless steel (steel), aluminum, and three composite hydrofoils. Based on the construction and attachment assembly of the hydrofoil shown in Figures 3.2 and 3.3, the structural span is effectively 320 mm and 316 mm (as opposed to the 300 mm loaded span) for the type I and type II hydrofoils, respectively. The discrepancy in the span is due to the mounting arrangement, as illustrated in Figures 3.2 and 3.3. The three composite hydrofoils have the different orientation for the structural unidirectional carbon fiber reinforced polymers (CFRP) layers: 0^o, $+30^o$, and -30^o relative to the spanwise axis of the hydrofoil. Details of the composite hydrofoils are presented in Chapter 7. All the stainless steel, aluminum, and the composite

hydrofoils were manufactured to a ± 0.1 mm surface tolerance and a 0.8 μm surface finish. No roughness was added to induce turbulent flow, as the laminar flow region should be limited for the NACA 0009 section used and for the Re range tested [60].

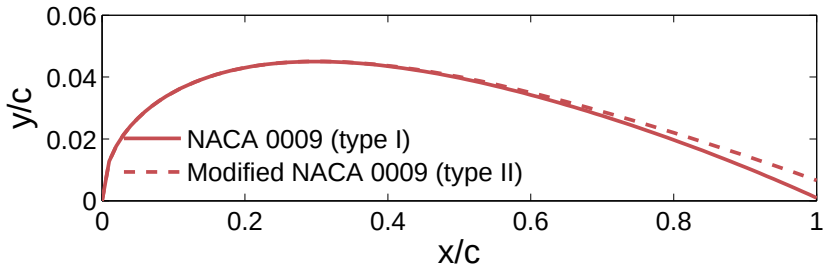

Figure 3.1: Half cross-section of the standard NACA 0009 (type I hydrofoils) and modified NACA 0009 hydrofoil (type II hydrofoils) geometry showing the thickened trailing edge.

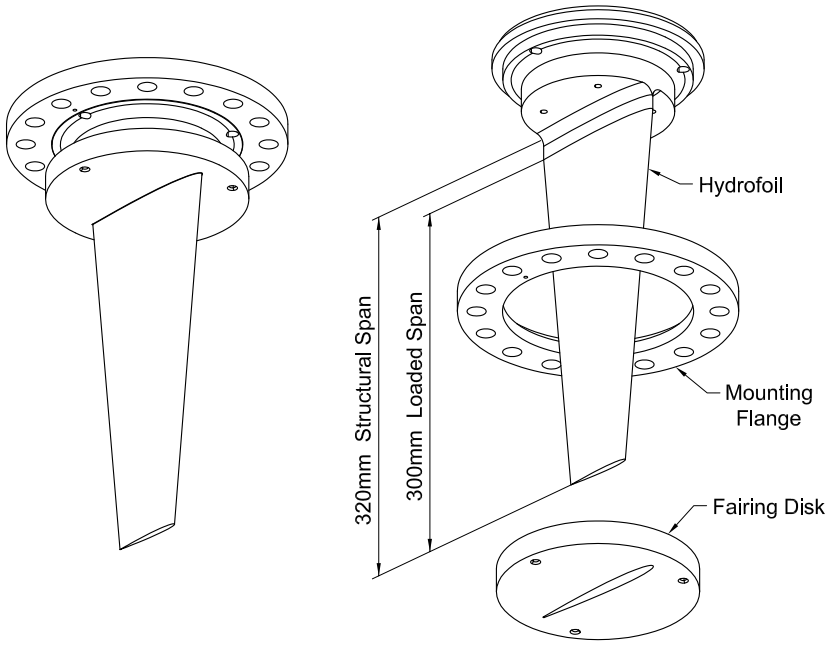

Figure 3.2: Details of the hydrofoil mounting arrangement for the type I hydrofoil. The figure illustrates the difference between the loaded span length (300 mm) and the structural span length (320 mm). This figure is originally presented in [155].

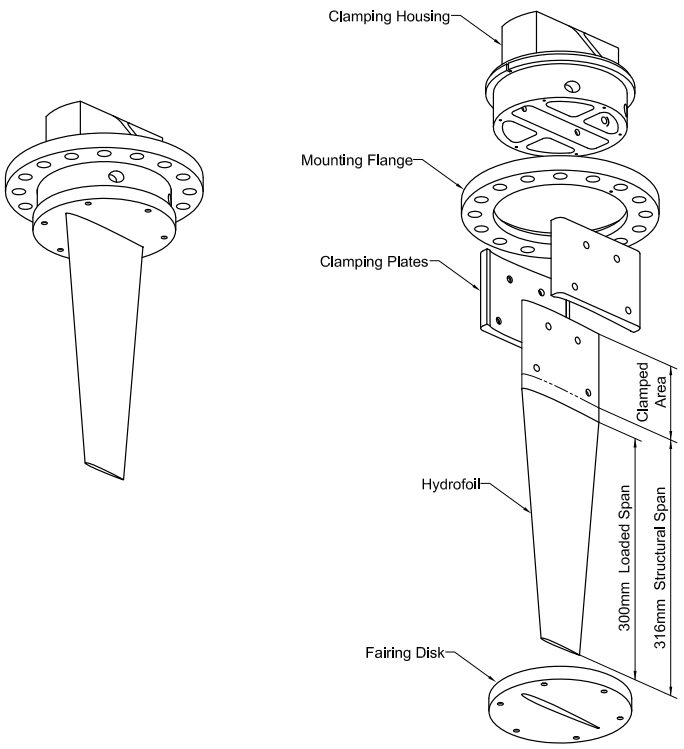

Figure 3.3: Details of the hydrofoil mounting arrangement for the type II hydrofoil. The figure illustrates the difference between the loaded span length (300 mm) and the structural span length (316 mm). This figure is originally presented in [146].

3.3 Maximum Allowable Loads for the Hydrofoils

In order to assess the load capacity of the composite hydrofoils, an additional CFRP 00 model was manufactured and tested under the same cantilever loading conditions and subjected to concentrated point loads near the tip, until failure was detected. The loading near the tip represents an extreme case, due to higher moment arm than a realistic load location of expected center of pressure under hydrodynamic loading at mid-span. For the extreme case, the failure occurred at a load of 2.49 kN by non-catastrophic delamination near the root of the CFRP 00 hydrofoil. The failure site correlated to a region of high interlaminar stress observed at the same position by finite element analysis (FEA), which was presented in Ibrahim et al. [58]. To ensure elastic structural behavior and to avoid structural failure inside the cavitation tunnel, the maximum mean side or normal load permissible was set at

1 kN for all the hydrofoils presented in this thesis, which gives a maximum stress of about 0.4 of the failure strength for the composite hydrofoils. Hence, as shown later, the maximum angle of attack was limited for the high flow velocity conditions to avoid exceeding the 1 kN load limit.

3.4 Experimental Techniques

The hydrofoils were mounted via a six-component force balance through a 0.16 m diameter penetration on the tunnel test section ceiling 0.7 m downstream of the test section entrance. The 0.16 m diameter penetration was made fair (to 50 μm) using a disk mounted on the hydrofoil as shown in Figures 3.2 and 3.3. There is a nominal radial clearance of 0.5 mm between the fairing disk and the test section ceiling penetration to avoid interference with the force measurement. From the total load vector measured using the force balance, mean components of the lift, drag and pitching moments are presented. Data were sampled at 1 kHz for 30 s for all the Re values. The spanwise force, roll moment, and yaw moment is also measured, but are not presented here as they are not pertinent to the present topic.

The force balance is calibrated by the least squares fit between a basis vector loading cycle and the six outputs giving a 6×6 matrix from which estimated precision on all components has less than a 0.5% uncertainty. The uncertainty of the absolute position of the indexing system is less than 0.1° and the incremental precision is less than 0.001°. To avoid cavitation, the water tunnel was pressurized up to 200 kPa for all the subcavitating runs. Some preliminary cavitation results for the optimized and the composite hydrofoil are presented in Chapter 6 and 7, respectively.

3.5 Bend and Twist Deflection Measurements

The bend and twist deflections at the free hydrofoil tip in Chapters 6 and 7 were measured by processing the high-speed images of the hydrofoil tip section in unloaded and

loaded conditions. At each incidence, still photographs of the hydrofoil tip section were first acquired with the hydrofoil in still water (i.e. unloaded) condition, and then in flowing water (i.e. loaded condition) after steady-state condition is reached. To facilitate the deflection measurements, two contrasting targets (2.3 mm circular dots) were placed near the leading and trailing edges on the tip face of the hydrofoil. Using the diameter of the contrasting targets, the worst case uncertainty is calculated as 1.08% of the tip chord, i.e. 0.65mm, for the bending deflection and 0.45° for the twist deformation. Photographs were taken using a Canon EOS 50D 35 mm digital SLR camera with a Canon EF 24-70 mm lens using the bright LED lights (image resolution 4752×3168 pixels). The images were calibrated using the known tip chord of the hydrofoil.

The Matlab [100] 'imfindcircles' algorithm was used to detect the target near the leading and trailing edges at the tip face. The tip deflections are computed at the elastic axis (EA) of the tip section. The angle between the line joining the two targets for the deformed and undeformed shape gives the tip twist. The tip deflection is considered positive in direction of the lift force and the twist is considered positive nose-up, which leads to an increase in the effective angle of attack. The specific examples of the deflection measurement are presented in Chapters 6 and 7.

CHAPTER 4

Hydrodynamic Optimization of a Hydrofoil

Using the optimization framework explained in Chapter 2, high-fidelity hydrodynamic shape optimization of a hydrofoil will be presented in this chapter. As explained in Chapter 1, the majority of the hydrodynamic shape optimization problems in literature are either handled with low-fidelity or high-fidelity with less than 15 design variables. In this chapter, CFD-based hydrodynamic shape optimization for a hydrofoil over a wide range of operating conditions with a large number of design variables (order of 100) is presented, with constraints on cavitation inception. The need for a large number of design variables is demonstrated by comparing the optimized design obtained using a different number of shape design variables. The need for a high-fidelity hydrodynamic optimization tool is also demonstrated by comparing RANS-based optimized design with the Euler-based optimized design. This work is based on previous papers presented by the author [43, 45].

4.1 Validation and Formulation

4.1.1 Model Setup

For the results presented in this chapter, an unswept, linearly tapered type I NACA 0009 hydrofoil was studied with a span length of 0.3 m and a mean chord length of 0.09 m, with a maximum chord length of 0.12 m at the root and a minimum chord length of 0.06 m at the tip, Re = 1.0×10^6. The nominal freestream velocity is 12.4 m/s. The effective aspect ratio

of the hydrofoil is AR = $2s/c$ = 6.67, where c (=90 mm) is the mean chord. A photograph of the type-I stainless steel baseline is shown in Figure 4.1. The mesh used for all the optimization and validation results is shown in Figure 4.2. The mesh used is a structured O-grid with 515,520 cells and a y^+ of 1.1. There are approximately 20 elements in the normal direction from the hydrofoil surface to encapsulate the boundary layer. The domain size is 30 chord lengths in all the directions.

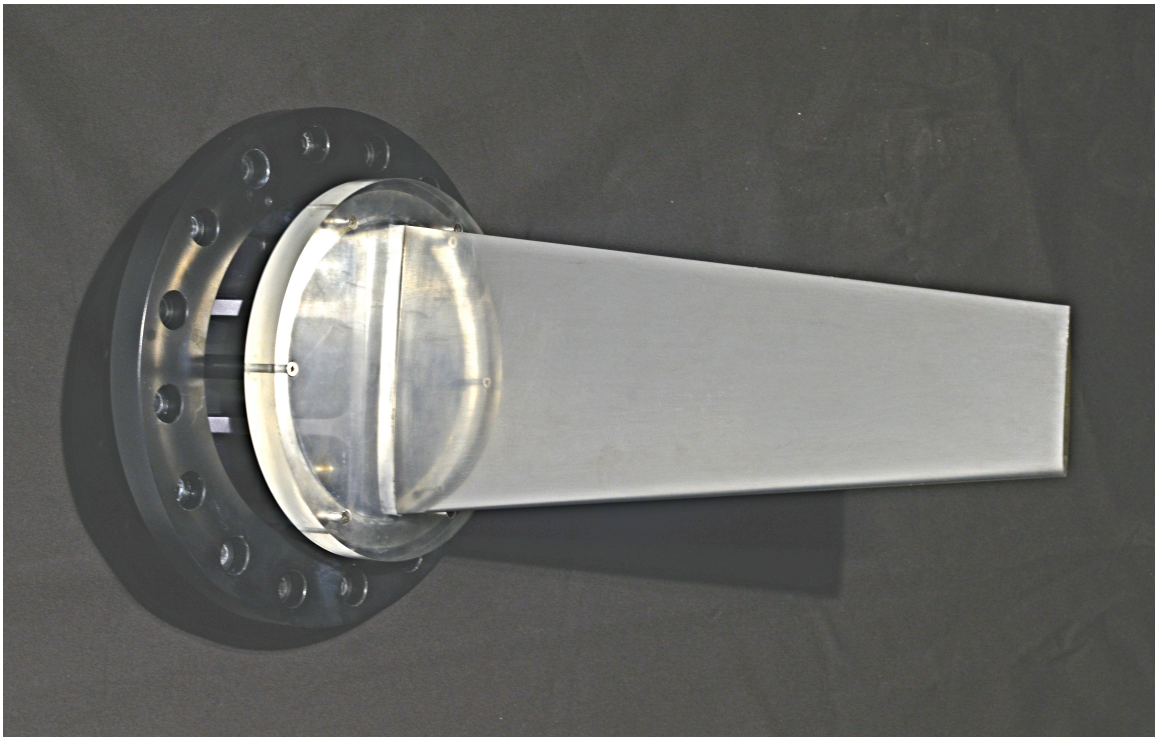

Figure 4.1: Type I stainless steel NACA 0009 baseline hydrofoil used in experiments, along with the mounting arrangement [155] (image courtesy of Dr. Paul Brandner and Dr. Bryce Pearce of the Australian Maritime College, Tasmania).

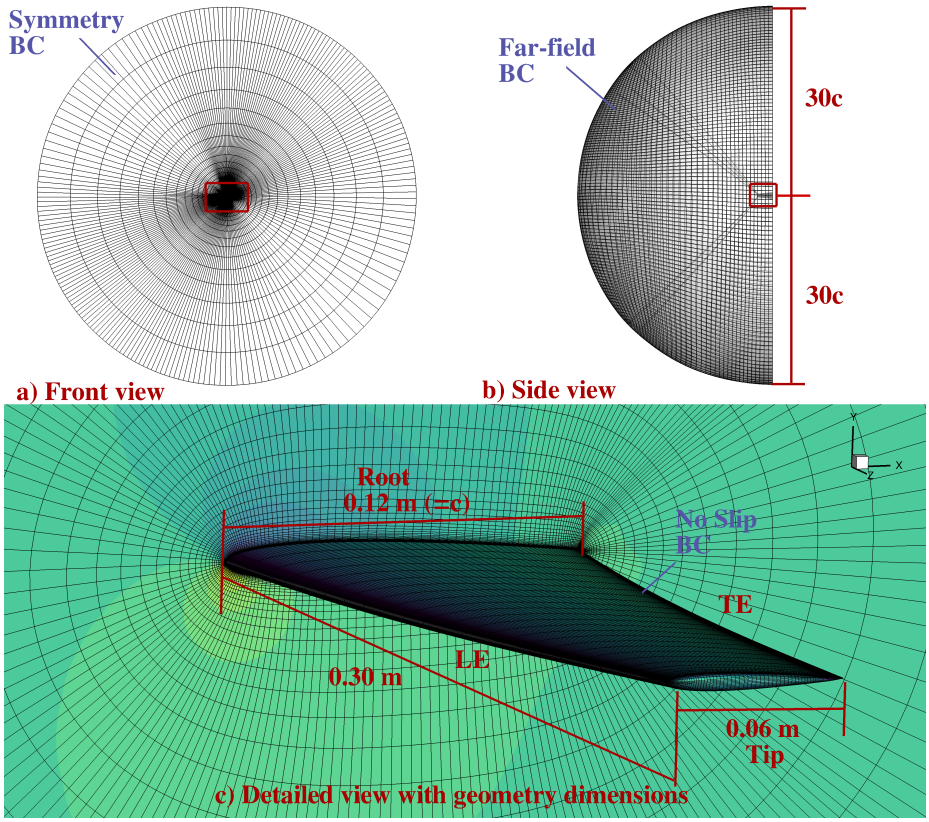

Figure 4.2: Baseline cantilevered NACA 0009 hydrofoil showing the computational domains for the CFD mesh (a,b,c), and dimensions (c).

4.1.2 Accuracy of the ADflow

To validate the CFD prediction with the low-speed preconditioner, same tapered NACA 0009 hydrofoil (as shown in section 4.1.1), with Re = 1.0×10^6 and U = 12.4 m/s was studied. For the validation study presented in this chapter, the type I stainless steel-316L hydrofoil is selected as it behaves practically as a rigid hydrofoil with negligible deformation.

Table 4.1 shows the comparison of the parameters used in the experiment and in the numerical solution. All the parameters were matched (including the Reynolds number), except for the Mach number. However, as the compressibility effects are almost negligible for Mach number less than 0.1, this discrepancy in Mach number should not affect the solution. To get the same dynamic viscosity as in the experiments, the constants were modified in Sutherland's law (as mentioned in Section 2.1 and Eq. (2.8)).

A 515,520 cell mesh, as shown in Figure 4.2, was used for the RANS solution with a y^+ of 1.1. To validate the ADflow solver, the results were compared to the experimental measurements of C_L and C_D for the type I stainless steel hydrofoil from Zarruk et al. [155] at Re = 1.0×10^6. As can be observed from Figure 4.3, there is a good agreement between the predicted and measured lift coefficient (C_L) and drag coefficient (C_D) values for a wide range of angles of attack. The ADflow (with the SA turbulence model), over predicts the C_D value by 14.37%, and under-predicts the C_L value by 3.3%, at $\alpha = 6^\circ$, when compared with the experimental results [155]. The discrepancy in the force coefficients is due to the coarseness of the CFD mesh, as will be shown later in detail in Section 5.2.3 for the type I aluminum hydrofoil. However, C_D follow the same trend as the experimental measurements and in hydrodynamic shape optimization, we are generally more interested in the change in drag coefficient due to optimization, rather than the actual grid converged value. Thus, in the interest of computational efficiency, we used a CFD mesh with 515,520 cells for optimization studies presented later in this chapter. Results were also compared with solution from the commercial CFD software (ANSYS) with a 21.3 million element mesh at an $\alpha = 6^\circ$ (displayed as an open black diamond in Figure 4.3), using the URANS (unsteady RANS) method with the k-omega shear stress transport ($k-\omega$ SST) turbulence model. The difference was 2.9% in C_L and 1.7% in C_D at $\alpha = 6^\circ$ between the ADflow and CFX predictions, in spite of the different turbulence models. For Re = 1.0×10^6, experiments were only conducted until a maximum angle of attack of 6°, to avoid excessive forces on the hydrofoil.

Table 4.1: Data for the hydrodynamic validation against the experimental results [155].

Cross section	NACA 0009
Effective aspect ratio	6.67
Re	1×10^6
ρ_f	999 Kg/m^3
M_a	0.008
U_f	12.4 m/s
Material	Stainless steel (SS-316L)
Fluid	Water
T_f	15^{o}C
μ_f	1.140×10^{-3} Ns/m^2

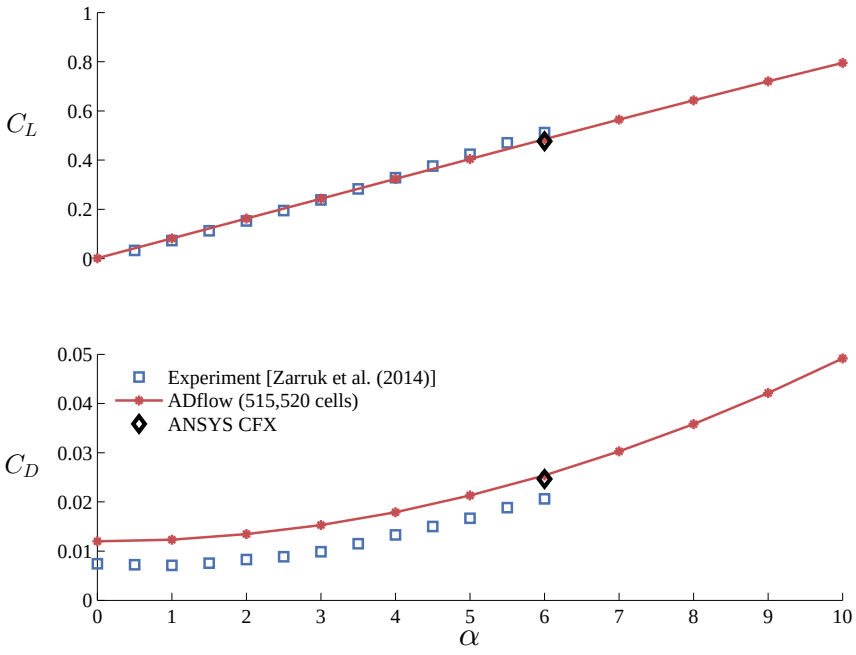

Figure 4.3: Comparison between the predicted lift coefficient (C_L) and drag coefficient (C_D) values at various angle of attack (α) obtained using ADflow with the experimental measurements from [155] for a tapered type I NACA 0009 hydrofoil. The open black diamond symbols represent the solution from the commercial CFD solver, ANSYS, with the k-ω SST model with a 21.3 million cell mesh ($y^+ \approx 1.0$).

4.1.3 CFD Grid Convergence Study

To ensure that the results are independent of the mesh size, the grid convergence was studied with three different mesh sizes: 515,520 cells, 4,124,160 cells, and 32,993,280 cells for the tapered NACA 0009 hydrofoil (as shown in section 4.1.1), with Re = 1.0×10^6, U = 12.4 m/s, and $\alpha = 6^\circ$. As shown in Table 4.2, there is a difference of 0.19% in C_L values and 2.63% in C_D values for the coarsest mesh and the finest mesh. Figure 4.4 shows the comparison of C_p variation along the chordwise direction for the three meshes at mid-span position ($z/s = 0.50$), and they all seem to lie on top of each other with an only slight difference near the leading edge. Thus, to balance computational cost and accuracy, the mesh size of $515,520$ cells was used for the optimization study shown in the next section.

Table 4.2: Comparison of y^+, C_L, and C_D values from RANS-simulation for the tapered type I NACA 0009 hydrofoil at Re = 1.0×10^6, U = 12.4 m/s, and $\alpha = 6^\circ$ using different mesh sizes with the ADflow solver.

Mesh Size	y^+	C_L	C_D
515520	1.1	0.4767	0.0234
4124160	0.8	0.4753	0.0233
32993280	0.5	0.4758	0.0228

4.1.4 Optimization Problem Formulation

The optimization problem setup is described in Table 4.3. The design optimization problem involves minimizing the drag coefficient by changing the hydrodynamic shape. Constraints are imposed on lift coefficient, minimum pressure coefficient to avoid cavitation, and minimum local thickness based on the original thickness. The drag coefficient, C_D, is minimized for a given C_L and a given cavitation number, σ (as defined in Section 2.7), for the results shown in Section 4.2. The lift coefficient is constrained to be equal to a target value, which varies depending on the case. The leading edge position and chord length are fixed to be the same as the baseline NACA 0009 hydrofoil values.

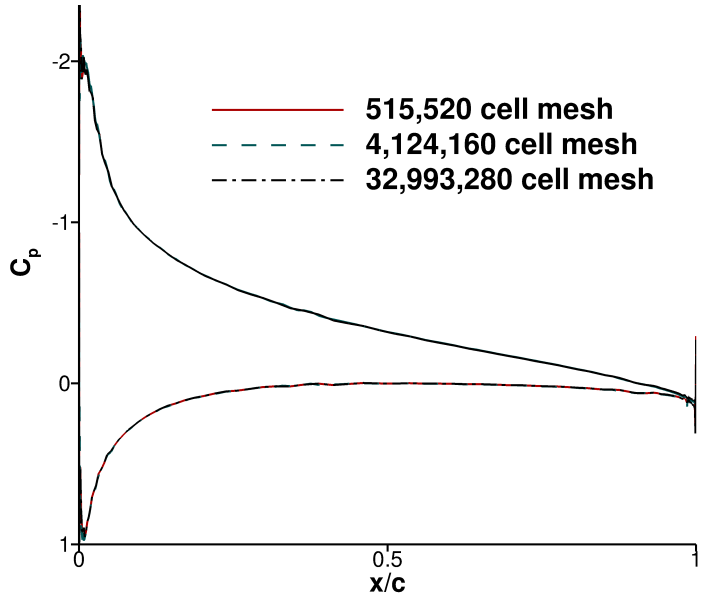

Figure 4.4: C_p variations along the chord for the three different meshes is displayed at mid-span ($z/s = 0.50$) location. They all lie on top of each other with only slight difference at the leading edge.

Figure 4.2 shows the mesh used for the RANS based optimization, with 515,520 cells.

Figure 4.5 depicts the FFD volume used for optimization.

Table 4.3: Optimization problem for a tapered type I NACA 0009 hydrofoil.

	Function variables	Description	Qty.
minimize	C_D	Drag coefficient	1
Design variables	x	FFD control points	200
		Twist design variables	10
Constraint	$C_L = C_L^*$	Lift coefficient constraint	1
	$t_i \geq 0.8 \times t_{\text{base}}$	Minimum thickness constraint	400
		Fixed leading edge constraint	10
	$A_{\text{cav}} \leq 5 \times 10^{-4}$	Non-dimensional aggregated cavitation constraint	1

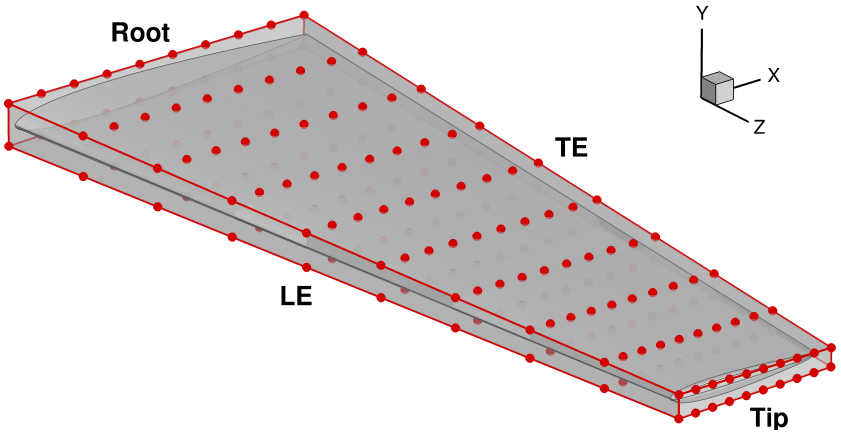

Figure 4.5: Coordinate system and hydrofoil shape design variables using 200 FFD control points (10 spanwise × 10 chordwise × 2 thickness), as indicated by the circles.

The twist design variables are defined as the angle of a given section relative to the root section, and the angle of attack is the angle of the root cross section relative to the free stream. To ensure a consistent definition of the angle of attack when comparing the performance of the baseline and the optimized hydrofoils at a given lift, the twist at the root is subtracted from all the outboard sections. An example of spanwise twist distribution is presented in Figure 4.6, where the top plot represent the spanwise twist distribution and the angle of attack without subtracting the twist at the root section. The bottom figure presents the updated spanwise twist distribution and the angle of attack after subtracting the twist at the root section, i.e., 2.93°, from all the outboard sections of the optimized design. Hence, all the twist angles shown in next section are defined relative to the root section, and the twist at the root section is taken as zero. Table 4.4 shows the angle of attack (α) required to produce the desired C_L of 0.3, 0.5, and 0.75 for the baseline hydrofoil. These angle of attacks were used as the reference angle of attacks for the optimization. Thus, the optimization presented in Section 4.2 are for fixed α, where the desired C_L at each α is achieved by optimizing the FFD control points and the twist design variables to minimize C_D.

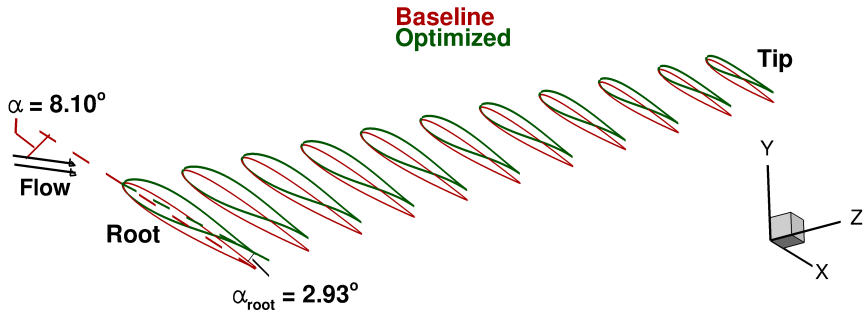

(a) The baseline and the optimized hydrofoil without the subtraction of twist at root section

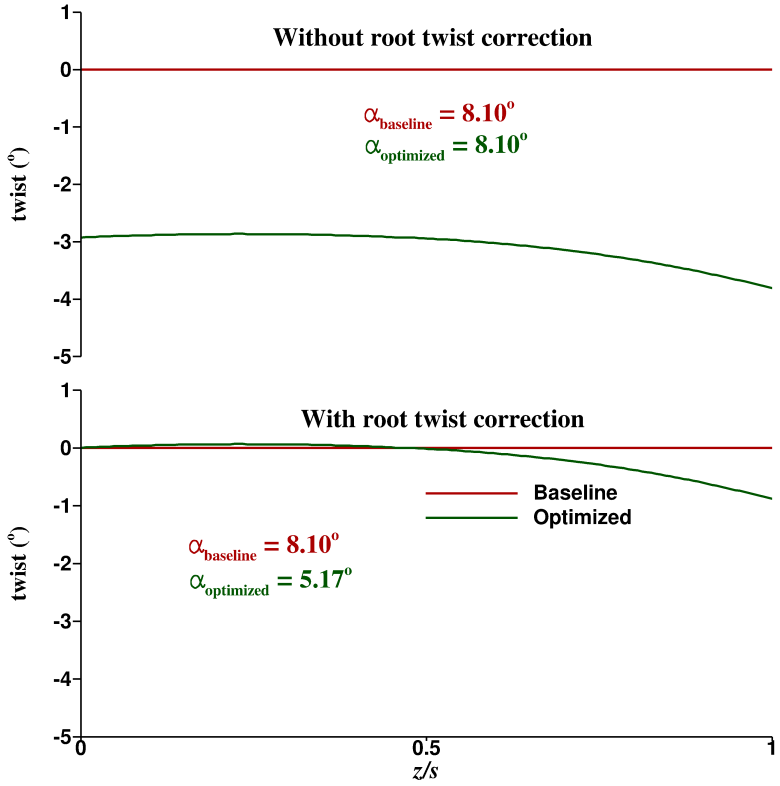

(b) Top: Spanwise twist distribution and the angle of attack without subtracting the twist at the root section. Bottom: Spanwise twist distribution and the angle of attack after subtracting the twist at the root section from all the outboard sections of the optimized design.

Figure 4.6: The twist angle in this thesis is defined relative to the root section, with the twist at the root section as zero.

Table 4.4: Angle of attack required to produce the desired lift coefficient for the baseline hydrofoil at Re = 1.0×10^6 and U = 12.4 m/s.

C_L	α
0.3	3.75°
0.5	6.30°
0.75	9.50°

The influence of the number of design variables will be studied in Section 4.2.1. For the results shown in Section 4.2.2 and after, a total of 210 design variables were used with 200 FFD control points (10 spanwise $\times$ 10 chordwise $\times$ 2 thickness) and 10 spanwise twist design variables.

4.2 Results

4.2.1 Effect of Number of Design Variables

In this section, the effect of the number of design variables on the hydrodynamic optimized design is investigated. The results are presented for optimization of a tapered NACA 0009 hydrofoil for a design C_L of 0.75, at Re = 1.0×10^6 and U = 12.4 m/s, using the optimization problem setup shown in Table 4.3. Figure 4.8 depicts the FFD volume with the 18, 48, 200, and 720 FFD control points. Note that only the FFD control points were varied, while the number of twist design variables (i.e., 3) remained fixed in each case. The number of twist design variables is decided to match with the maximum number of spanwise FFD control points in the 18 FFD control points case. The spanwise twist design variables are defined at the root, the mid-span and at the tip of the hydrofoil. As explained earlier, the maximum number of design variables used in the previous high-fidelity gradient-free hydrodynamic optimization studies are typically restricted to 15 or less, due to more than quadratic increase in computational cost with the increase in number of design variables [92]. For the SNOPT adjoint-based algorithm, however, the increase in computational time with increase in number of design variables is approximately linear [92], and hence, a larger number of design variables can be used.

A comparison of the total CPU time and optimized C_D values for the single-point optimization at C_L = 0.75 for the different number of design variables are shown in Figure 4.7. The computational time mentioned in Figure 4.7 is distributed over 192 processors (2.80 GHz Intel Xeon E5-2680V2) on the University of Michigan High performance Computing

(HPC) flux cluster, operated by Advanced Research Computing. As shown in Figure 4.9, the optimizations converged to similar geometries in terms of the twist and camber distribution, but with significant differences in the sectional C_p profile.

To present a consistent definition of angle of attack between the optimized and baseline hydrofoils, the twist at the root of the optimized hydrofoils is subtracted from the optimized twist distribution, resulting in an reduced angle of attack of $\alpha \approx 5.5^{\circ}$ (exact α for each optimized hydrofoil is mentioned in Figure 4.9) for the optimized hydrofoils, as compared to $\alpha = 9.50^{\text{o}}$ for the baseline hydrofoil to achieve $C_L = 0.75$.

While the difference in C_D values was only 0.7% between the case with 21 and 723 design variables, there were differences in the optimized geometry and pressure profile, as observed from Figure 4.9B. Figure 4.9B shows finer control in the optimization problem is needed to achieve better optimized design. For the cases with 203 and 723 design variables, the optimal solutions are practically the same, except the region very close to the root section. The results in Figure 4.9 suggest that at least 203 design variables (200 FFD control points and 3 twist variables) are needed for a simple, unswept, and tapered hydrofoil to get a properly converged optimal solution. As the complexity of the problem increases, such as, if the problem of interest is a marine propeller instead of a hydrofoil, significantly higher number of design variable will be required to parametrize the geometry. Thus, the capability of the current design optimization tool to handle a large number of design variables will be very beneficial in case of the actual marine propellers.

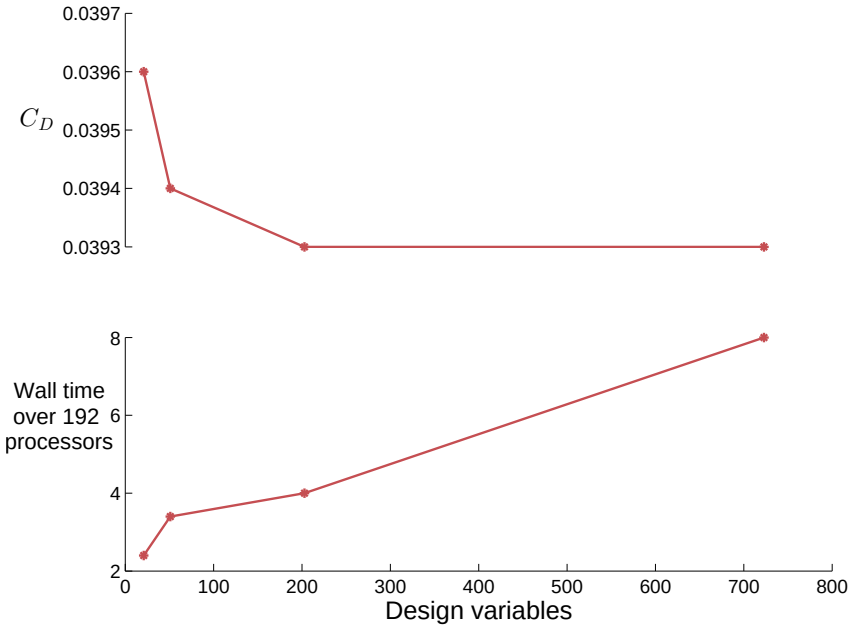

Figure 4.7: Comparison of the wall time (spread over 192 processors) and C_D for the optimization problem with different number of design variables for hydrodynamic-only optimization at $C_L = 0.75$.

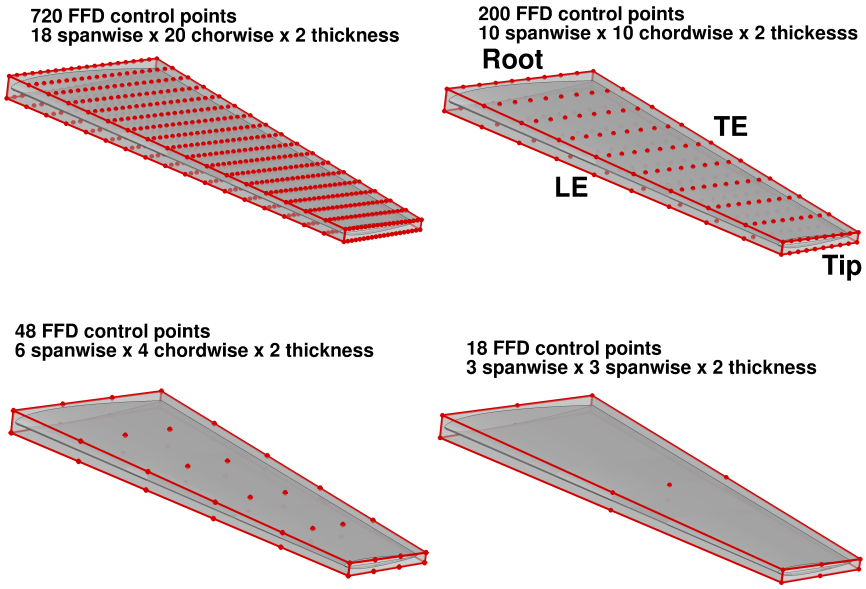

Figure 4.8: The different FFD volumes used to study the effect of number of FFD design variable on the RANS-based optimization. The circles denotes the FFD control points. Note that the total number of design variables is equal to the number of FFD control points plus the three twist variables.

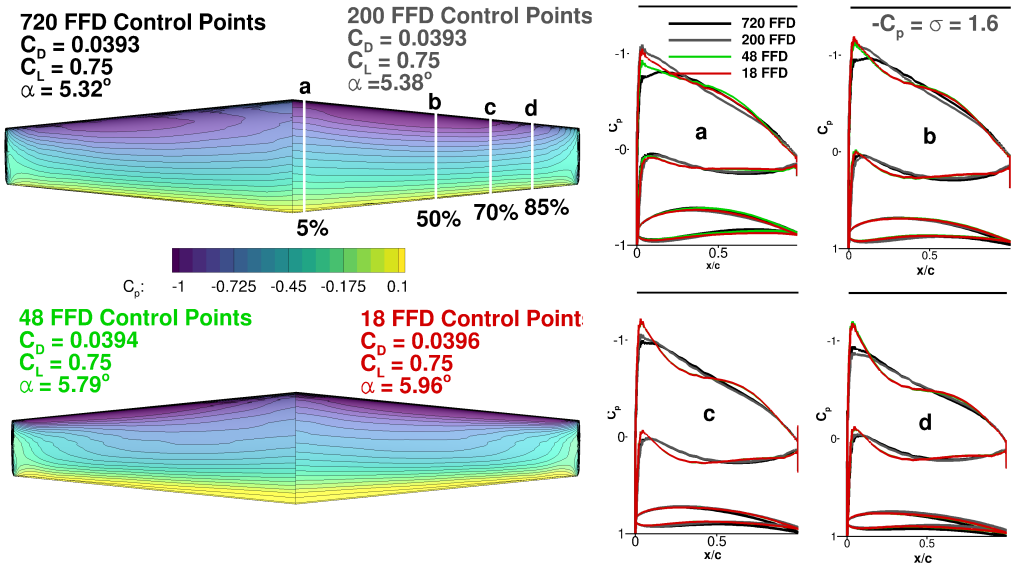

Figure 4.9: Results show the difference in optimization with 18, 48, 200, and 720 FFD control points for a simple, unswept, hydrofoil at Re = 1.0×10^6 and U = 12.4 m/s. A) The maximum difference in C_D values was less than 0.7%. B) The optimization results converged to similar geometries (particularly in terms of the twist and camber distribution), but with significant differences in the sectional pressure profile noticed for the case with 18 FFD control points and 720 FFD control points. Black horizontal line represents the constraint on cavitation number. The optimized solution are practically the same for 200 and 720 FFD control points, except the region very close to the root section.

4.2.2 Importance of Considering Viscous Effects

In this section, the advantage of using high-fidelity solver (RANS equations) over a lower fidelity solver (Euler equations) is demonstrated. The Euler solver used for this study is a purely inviscid solver, with no external correction for viscosity. For pre-stall cases and with low to moderate loading conditions, viscous effects are negligible, so the Euler-based and RANS-based optimization will lead to similar optimized geometry and performance. In this section, a high loading case ($C_L = 0.75$) is presented to illustrate the need for the high-fidelity RANS solver at high C_L values, where impending stall and flow reversal make the effects of viscosity critical.

Similar to the previous results, the results are for optimization of a tapered NACA 0009 hydrofoil at Re = 1.0×10^6 and U = 12.4 m/s, using the problem setup shown in Table 4.3. The optimization was carried out for $C_L = 0.75$ using both the Euler and the RANS solver. The problem setup for both the Euler and the RANS optimization cases is the same, including geometry and mesh size, with the only difference being the flow solver. 210 shape design variables (200 FFD design variables and 10 spanwise twist variables) were used in both the cases. Figure 4.10 A – D depicts the C_p contour plots on the left side and the skin friction coefficient (C_f) contours on the right side for the (1) Euler-based optimized hydrofoil for $\alpha = 5.15^\circ$ and $C_L = 0.75$, (2) the RANS analysis of the Euler-based optimized hydrofoil at $\alpha = 5.15^\circ$ (which yield a C_L of 0.66), (3) the RANS analysis of the Euler-based optimized hydrofoil at $C_L = 0.75$ (which required an α of 6.16°), and (4) the RANS-based optimized hydrofoil at $C_L = 0.75$ and $\alpha = 5.38^\circ$. As observed from Figure 4.10, the predicted drag coefficient obtained from the Euler optimization at $\alpha = 5.15^\circ$ is less than that from the RANS optimization, which is expected since the Euler solver assumes inviscid flow. When the RANS analysis was carried out on the Euler-optimized hydrofoil, the result was significantly different. At $\alpha = 5.15^\circ$, the RANS analysis shows that Euler-based optimized hydrofoil only produces C_L of 0.66 and C_D of 0.0364. To obtain the desired C_L of 0.75, an α of 6.16° is required for the Euler-based optimized hydrofoil, and the resultant C_D

with RANS analysis of the Euler-optimized hydrofoil was 11.7% higher than the C_D from the RANS-based optimized hydrofoil. The above mentioned differences are due to viscous effects, which are not considered in the Euler solver. Significant differences in the sectional optimized geometry and the pressure profile, between the Euler-based optimized hydrofoil, the RANS-based optimized hydrofoil, and the RANS analysis of the Euler-optimized hydrofoil, can be noted from Figure 4.10E. The pressure distribution on the RANS-based optimized hydrofoil and the Euler-based optimized hydrofoil are significantly different because the different solvers result in different converged optimal geometries, as shown in Figure 4.10E. The result clearly illustrates the need of high-fidelity solver to carry out hydrodynamic optimization, especially for off-design points with high C_L values, where the flow might separate.

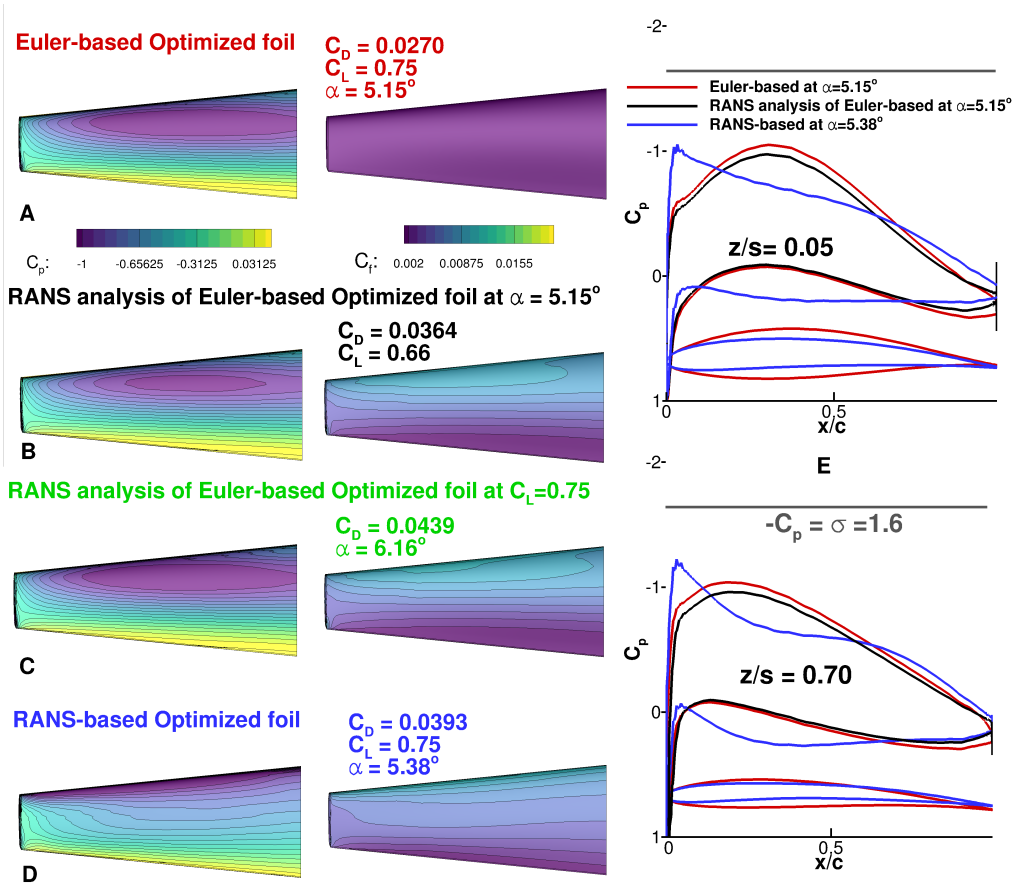

Figure 4.10: Optimization of the type I NACA 0009 hydrofoil at Re = 1.0×10^6 and U = 12.4 m/s for a given C_L of 0.75 using the Euler and RANS solver. A) The predicted drag of the Euler-based optimized hydrofoil is less than the RANS-based optimized hydrofoil, as an Euler solver assumes inviscid flow. B) At $\alpha = 5.15^\circ$, the RANS-analysis of Euler optimized hydrofoil produces C_L of 0.66 with $C_D = 0.0364$. C) To produce $C_L = 0.75$, the Euler-optimized hydrofoil will require an α of 6.16° and the corresponding C_D is 0.0439, which is 11.7% higher than the RANS-optimized hydrofoil at $C_L = 0.75$. D) RANS-optimized results for $C_L = 0.75$ and $\alpha = 5.38^\circ$. E) Significant differences can be observed in the pressure profile and sectional geometry profile (at $z/s = 0.05$ and $z/s = 0.70$).

4.2.3 Single-Point Hydrodynamic Shape Optimization

In this section, the baseline hydrofoil was optimized to achieve the minimum drag coefficient (C_D) for a target lift coefficient (C_L) and a cavitation number (σ) of 1.6. The optimization was carried out with 210 shape design variables (200 FFD design variables and 10 spanwise twist variables). Note that the NACA 0009 hydrofoil is already a very

efficient hydrofoil to begin with, which makes the optimization problem more challenging. The single-point optimization took 4.2 hours (over 192 processors, 2.80 GHz Intel Xeon E5-2680V2) on the University of Michigan HPC flux cluster.

To investigate how the optimal geometry changes with the design C_L, the single-point optimization were carried out for various target C_L values. To demonstrate the case at the highest design C_L, Figure 4.11 shows a detailed comparison of the baseline hydrofoil and the optimized hydrofoil at a C_L of 0.75. As shown in Figure 4.11B, the spanwise sectional lift distribution for the optimized hydrofoil is much closer to the ideal elliptical distribution. The gradient of the sectional lift distribution is also reduced near the tip region for the optimized hydrofoil, which translates to a reduction in the strength of the tip vortex. The maximum negative pressure coefficient, $-C_p$, reduces from 3.1 for the NACA 0009 hydrofoil to 1.2 for the optimized hydrofoil, as shown in Figure 4.11C, which will help to significantly delay cavitation inception. In order words, cavitation inception speed for the optimized hydrofoil will increase from 8.4 m/s to 13.50 m/s, for an assumed submergence depth of 1 m (using Eq. (2.25)). The results indicate that partial leading edge cavitation (as indicated by the white contour region with $-C_p \geq \sigma$) will develop around the baseline hydrofoil at $C_L = 0.75$ and $\sigma = 1.6$, but no cavitation is observed for the optimized hydrofoil. As observed from Figure 4.11C, the optimized hydrofoil has a higher camber and a non-zero spanwise twist/pitch distribution compared to the baseline hydrofoil, which reduced the effective angle of attack and shifted the loading more towards the mid-chord of the hydrofoil.

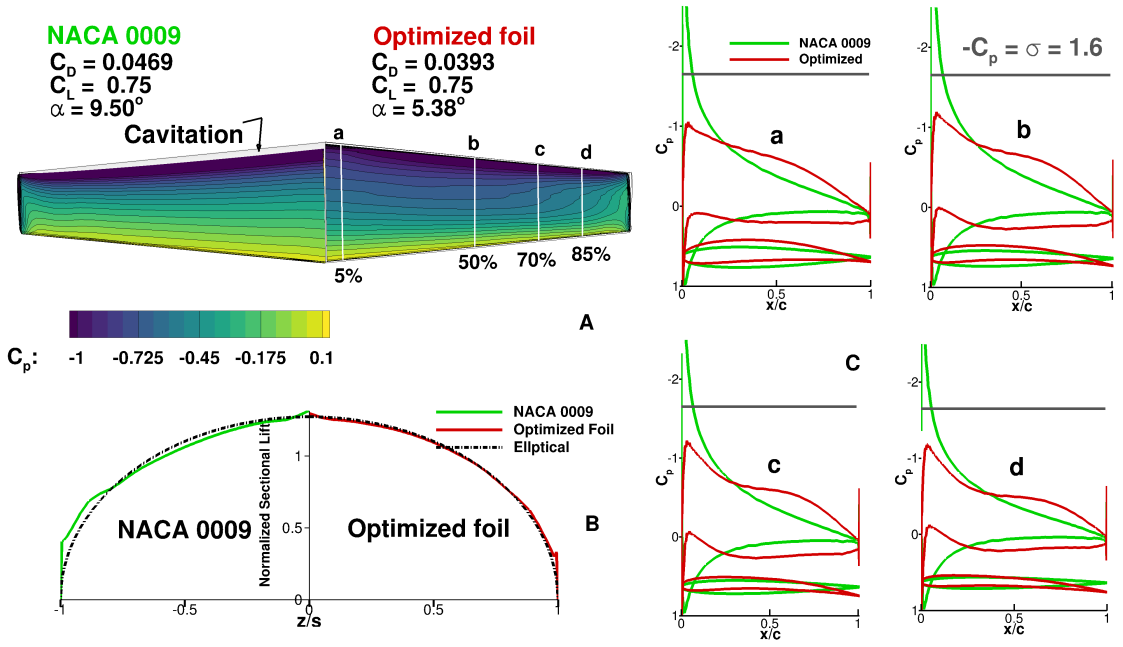

Figure 4.11: A reduction in C_D of 14.4% is noted for the optimized hydrofoil. A) White contour region along the leading edge of the tapered NACA 0009 hydrofoil shows the area with $-C_p \geq \sigma$. B) Comparison of the normalized sectional lift distribution with the ideal elliptical lift distribution for the baseline hydrofoil and for the optimized hydrofoil. There is a reduction in the gradient at the tip region for the optimized hydrofoil, which also results in reduced tip vortex strength. C) Note that there is a significant decrease in maximum $-C_p$ from the baseline to the optimized hydrofoil. Differences between the sectional shape of the original and optimized hydrofoil are also shown in the bottom of each subplot on the right.

Figure 4.12 shows the comparison of the lift-to-drag ratio (i.e. C_L/C_D) at the various design C_L values for the baseline hydrofoil, the single-point optimized hydrofoil at each C_L value, and the single-point optimized hydrofoil at $C_L = 0.75$ only. It should be noted that the single-point optimized hydrofoil at each C_L requires a different geometry at each C_L, thus it can only be achieved if there is a robust active morphing capability. Assuming that there is an active morphing capability, with the single-point optimization at each C_L value, the best possible performance is achieved; there is a minimum increase in lift-to-drag ratio of 6.4% throughout the operating regime, and the increase in lift-to-drag ratio is 19% at the C_L value of 0.75, over the baseline hydrofoil. With the single-point optimized hydrofoil at $C_L = 0.75$ only, due to fixed geometry; degraded performance was noted when

operating away from design C_L of 0.75; in particular, at $C_L = 0.3$, the single-point optimized hydrofoil for $C_L = 0.75$ only resulted in a higher C_D value than the baseline hydrofoil. Thus, the results show that, unless there is a robust active morphing capability available, there is a need for the multipoint optimization to achieve a globally optimal design using fixed geometry, as demonstrated next in Section 4.2.4.

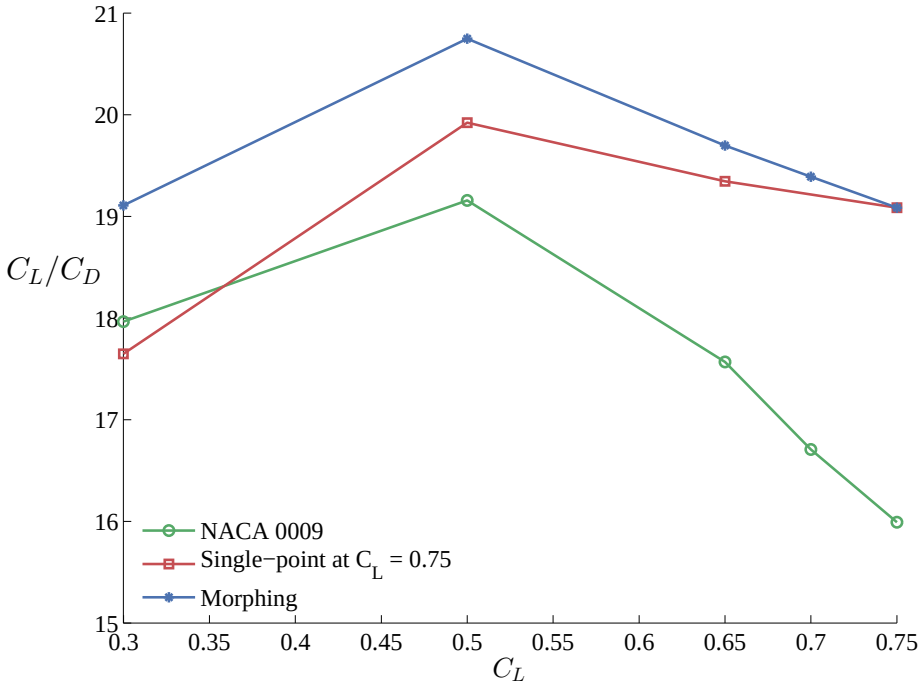

Figure 4.12: Comparison of lift-to-drag ratio (i.e. C_L/C_D) versus C_L for the baseline hydrofoil with the single-point optimized hydrofoil at each C_L, and the single-point optimized hydrofoil at $C_L = 0.75$ only. All the results were obtained using RANS solver with Re = 1.0×10^6 and U = 12.4 m/s.

4.2.4 Comparison of Multipoint Optimization and Single-point Optimization

As shown in Section 4.2.3, the single-point optimization does not necessary result in a globally optimal solution with the best efficiency possible over the entire range of operating conditions. The design optimized for $C_L = 0.75$ lead to a higher C_D than the baseline

hydrofoil at $C_L = 0.3$. Such a design would lead to low overall efficiency, particularly if the probability of operating at $C_L = 0.75$ is low compared to $C_L = 0.3$. Hence, a probabilistic multipoint optimization study is needed.

To achieve this, a probabilistic multipoint approach is proposed, similar to that presented by Motley et al. [105] and Kramer et al. [74], where we seek to minimize the expected drag coefficient over a range of lift coefficients, defined as

$$\mathbb{E}[C_D] = \int_{\Omega} C_D(C_L)\, p(C_L)\, \mathrm{d}C_L, \tag{4.1}$$

where $p(C_L)$ is the probability density function (PDF) for the flow conditions expected in operation. In this case, we only consider C_L to vary in the flow condition domain Ω, where each C_L is associated with variation in the angle of attack, and Reynolds number effects are neglected.

The expected value of drag coefficient can be computed using numerical integration with m quadrature points using midpoint integration as follows,

$$\mathbb{E}[C_D] \approx \sum_{k=1}^{m} C_D\left(C_{L_k}\right) p\left(C_{L_k}\right) \Delta C_L, \tag{4.2}$$

This approach results in a similar objective to the previous work done in multipoint aerodynamic shape optimization [68, 81], and in hydrodynamic optimization of propeller and hull systems [74, 105], and can be written as,

$$\bar{C}_D = \sum_{k=1}^{m} w_k C_{D_k} \tag{4.3}$$

where the weights w_k can be computed based on the PDF, i.e. $w_k = p\left(C_{L_k}\right) \Delta C_L$. Then, the

overall hydrodynamic efficiency is

$$\bar{\eta} = \sum_{k=1}^{m} w_k \frac{C_{L_k}}{C_{D_k}}. \tag{4.4}$$

To compare the difference between a single-point and a probabilistic multipoint optimization, a simple three point probability distribution, as shown in Table 4.5, was chosen. Since our hydrofoil is a canonical case, there is no specific targeted application and a real PDF of the operating conditions does not exist. Therefore, the operating conditions and corresponding weights in Table 4.5 are based on engineering experience.

The objective function is to minimize the sum of the drag coefficient at the three target C_L values weighted by the probability of operating at the particular C_L value, as shown in Eq. (4.3). The cavitation number (σ) was fixed at 1.6. The problem setup remains same as shown in Table 4.3. However, to make sure that the problem is well-posed, the angle of attack (defined with respect to the original undeformed FFD volume) for $C_L = 0.75$ was fixed at 9.50° (without consideration for the root twist), and the angle of attacks for the other C_L values in the multipoint problem are allowed to be design variables. The multipoint optimization took 12.5 hours (over 192 processors) on the University of Michigan HPC flux cluster.

Table 4.5: The probabilistic multipoint profile used for the multipoint optimization in the current chapter.

C_L	Weight, w_k
0.30	0.15
0.50	0.25
0.75	0.60

The bar-chart in Figure 4.13 shows a comparison of the C_D values for the baseline hydrofoil, the single-point optimized hydrofoil at $C_L = 0.75$, the multipoint optimized hydrofoil, and the single-point optimized hydrofoil at each C_L value (which indicates the hypothetical best performance scenarios with active morphing capability, as explained in Sec-

tion 4.2.3). All the results were obtained using the RANS solver. As expected, the single-point design for $C_L = 0.75$ and the morphing hydrofoil performed the best at $C_L = 0.75$; the multi-point design showed the next best performance at $C_L = 0.75$, with only 1.4% reduction in efficiency compared to the single-point optimized design at $C_L = 0.75$. Note that while the performance of single-point optimized hydrofoil for $C_L = 0.75$ only is even worse than the original tapered NACA 0009 hydrofoil for $C_L = 0.3$, the probabilistic multipoint design performs better than the baseline hydrofoil over the entire range of operating conditions.

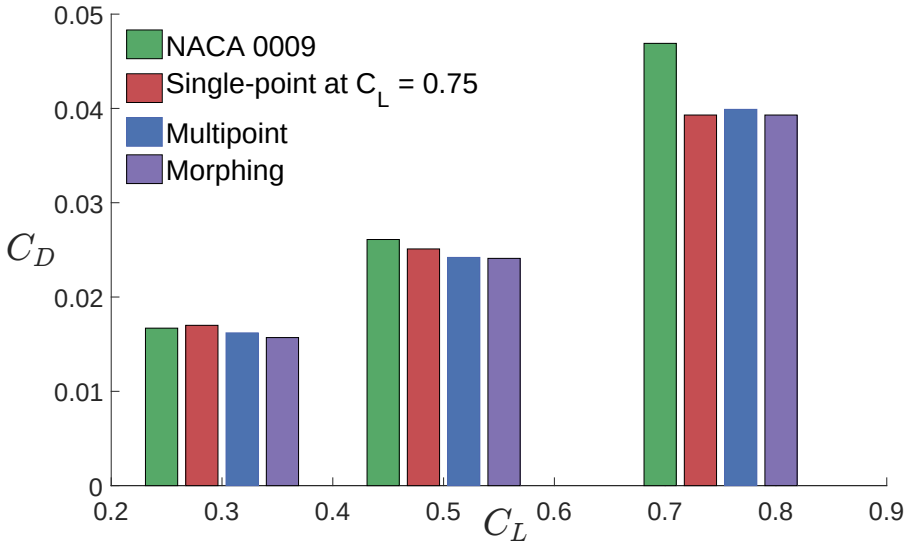

Figure 4.13: The comparison of C_D at different C_L values of 0.3, 0.5, and 0.75 for the baseline hydrofoil, single-point optimized hydrofoil at $C_L = 0.75$ only, probabilistic multipoint optimized hydrofoil with fixed geometry, and single-point optimized hydrofoil at each C_L, with varying geometry at each C_L (morphing).

A comparison of the detailed performance of baseline hydrofoil, the single-point optimization at $C_L = 0.75$, and the probabilistic multipoint optimization is shown in Figure 4.14. Columns 2–4 in Figure 4.14 shows the predicted C_p contours for the hydrofoils at the C_L values specified in the first column. The last column in Figure 4.14 shows the difference in geometry for the baseline hydrofoil, the single-point optimized hydrofoil, and the multipoint optimized hydrofoil at $z/s = 0.5$. The maximum negative pressure coef-

ficient, $-C_p$, reduces from 2.9 and 3.1 for the baseline hydrofoil to 1.3 and 1.5 for the multipoint optimized hydrofoil, at $C_L = 0.5$ and $C_L = 0.75$, respectively. Figure 4.14 Column 2–4 show that the partial leading edge cavitation will develop around the baseline hydrofoil for $C_L \geq 0.5$ and $\sigma = 1.6$, but no cavitation is observed for both optimized hydrofoils (the single-point optimized hydrofoil and the multipoint optimized hydrofoil). Note that the single-point optimized hydrofoil at $C_L = 0.75$ has a much higher camber and a more negative twist compared to the original hydrofoil and the multipoint design; hence, the single-point optimized hydrofoil at $C_L = 0.75$ behaves poorly at the lower C_L values. As $C_L = 0.75$ has the highest probability in the probabilistic multipoint optimization, the performance of the multipoint optimized hydrofoil and single-point optimized hydrofoil at design C_L of 0.75 is almost same with respect to C_D values. However, at other C_L points in the multipoint optimization, the multipoint design showed better performance, as expected.

The results show that while the single-point optimization can achieve the best efficiency at the design C_L, the single-point optimized hydrofoil showed reduced performance at the off-design conditions, namely, $C_L = 0.3$ and $C_L = 0.5$. The probabilistic multipoint optimized hydrofoil will result in an overall increase in the efficiency by 14.4% (based on Eq. (4.4)) over the baseline hydrofoil. Note that the overall efficiency of the multipoint design (with a fixed geometry) is only 1.5% less than the best possible solution from the hypothetical morphing hydrofoil (i.e. with varying geometry at each C_L). The increase in the cavitation inception speed compared to the baseline hydrofoil, is 49% at $C_L = 0.50$, and 39% at $C_L = 0.75$, for an assumed submergence depth of 1 m. This improvement in overall efficiency would be even more obvious if the probability of operating at the highest C_L is lower, which is often the case for many marine propulsors as they seldom operate at the highest loading condition. Thus, it is necessary to carry out the probabilistic multipoint optimization using realistic mission/operation profiles at an intermediate design stage to achieve a design that performs well throughout the entire range of operating conditions.

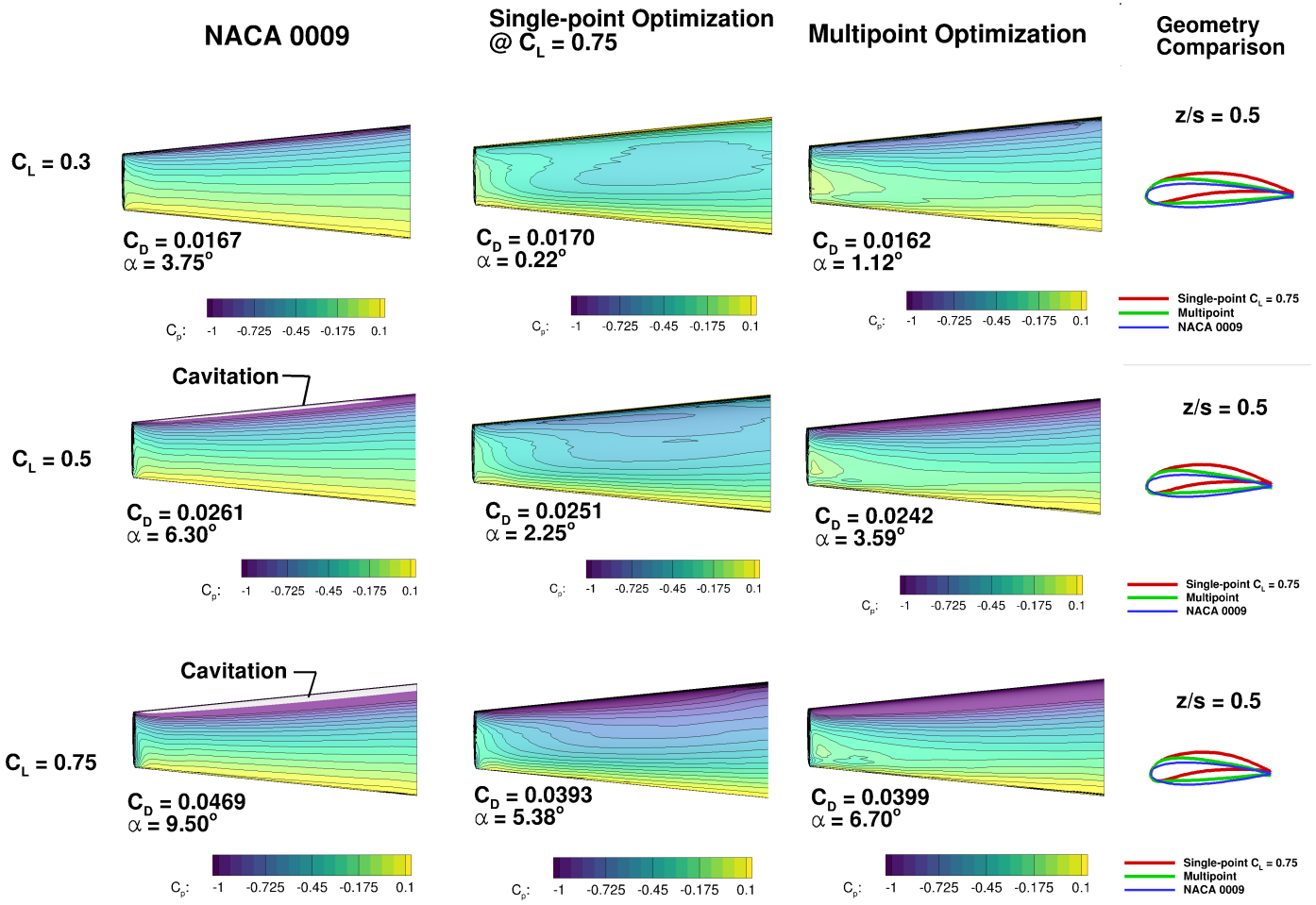

Figure 4.14: Comparison of the baseline hydrofoil, the single-point optimized hydrofoil at $C_L = 0.75$, and the multipoint optimized hydrofoil. Note that the white contour region along the leading edge for the baseline hydrofoil indicates the region with $-C_p \geq \sigma$. The figures in the last column are not plotted to scale, to show the difference in geometries more prominently. As can be seen from the predicted C_D values, while the single-point optimized hydrofoil only performs well at the optimized point and performs poorly at the off-design points, the multipoint optimized design performs well over the entire range of operating conditions.

4.3 Conclusions

In this chapter, the ADflow RANS solver was validated against experimental data [155] and verified against commercial CFD software results for the case of a type I tapered stainless steel NACA 0009 hydrofoil. The ADflow, over predicts the C_D value by 14.37% (because of the limited number of cells in CFD mesh) and under-predicts the C_L value by 3.3%, when compared with experimental results [155]. However, when ADflow results were compared with commercial CFD software (ANSYS CFX), the difference was 2.9% in C_L and 1.7% in C_D values, in spite of the different turbulence models.

The effect of the number of shape design variables was studied. The results show that while the change in C_D values was not significant, the pressure distribution (particularly near the hydrofoil leading edge) and geometry varies significantly with the number of shape design variables. The results concluded that a minimum of 203 design variables (200 FFD control points and 3 twist variables) was needed to achieve an acceptable optimal solution.

The need for RANS-based design optimization, as opposed to Euler-based design optimization, was demonstrated. This was evidenced by the fact that 1) the RANS-based and Euler-based design optimizations for the same C_L lead to significantly different geometry, and 2) the RANS analysis of the Euler-based optimized hydrofoil showed that it cannot deliver the required lift unless the angle of attack is increased; moreover, to deliver the same C_L, RANS-analysis of the Euler-based optimized hydrofoil will lead to a 11.7% higher drag coefficient compared to the RANS-optimized hydrofoil.

To demonstrate the power of the RANS-based shape optimization methodology, a series of optimizations were performed for a tapered hydrofoil. A single-point optimization was conducted at five C_L values with 210 design variables, where the optimized geometry was significantly different for each C_L, and hence a robust active morphing method would be needed to realize this design. Nevertheless, such an actively morphed hydrofoil would lead to an increase in the lift-to-drag ratio of 6.4% throughout the operating profile, and the increase in lift-to-drag ratio would increase to 19% for $C_L = 0.75$. The optimized

hydrofoil at $C_L = 0.75$ would also lead to an increase in the cavitation inception speed by 60%, compared to the baseline hydrofoil. However, the performance of the single-point optimized hydrofoil degrades when operated away from the design C_L value. In particular, the hydrofoil optimized for the highest lift coefficient ($C_L = 0.75$) shows inferior performance even when compared to the baseline hydrofoil at the lowest lift coefficient ($C_L = 0.3$) condition.

To overcome the issue of degraded performance of the single-point optimized design at off-design conditions, a multipoint optimization was carried out for a fixed geometry design. The multipoint optimization was found to perform better than the baseline hydrofoil over the entire operation profile, where the overall efficiency (i.e., the lift-to-drag ratio) was improved by 14.4% compared to the baseline hydrofoil. The increase in the cavitation inception speed compared to the baseline hydrofoil, was 49% at $C_L = 0.50$ and 39% at $C_L = 0.75$, for an assumed submergence depth of 1 m. For the multipoint optimized hydrofoil, the geometry remains fixed throughout the operation range and the overall efficiency was only 1.5% less than the hypothetical actively morphed hydrofoil with the optimal varying geometry at each C_L. The results show that the proposed high-fidelity hydrodynamic optimization tool can be used to carry out the probabilistic multipoint optimization, using realistic operation profiles at an intermediate design stage to achieve a design that performs well throughout the entire range of operating conditions.

CHAPTER 5

Hydrostructural Optimization of an Aluminum Hydrofoil

In this chapter, the CFD-based hydrodynamic shape optimization presented in previous chapter is developed further to perform coupled hydrostructural optimization of marine lifting surfaces. To achieve this goal, the deflected shape for each operating condition is computed by coupling the CFD solver to a high-fidelity structural FEM solver. In addition to the cavitation constraint presented in the previous chapter, the fatigue strength constraint based on the structural solution is enforced. Prior to performing coupled hydrostructural optimization of marine lifting surfaces, the hydrostructural solver is first validated using the experimental measurements. The validation of the hydrostructural solver is performed against experiments performed on an aluminum version of the type I NACA 0009 hydrofoil, which yields measurable bending deformations [155], and is thus more suitable for hydrostructural studies. The hydrostructural coupling in the analysis allows us to account for the different deflected shapes at each operating condition, instead of assuming fixed geometry. Results show that the hydrostructural coupling is essential to ensure structurally sound designs with the best possible hydrodynamic performance, and that hydrodynamic-only optimization (presented in previous chapter) and coupled hydrostructural optimization leads to very different geometries. This work is based on previous paper presented by the author [44].

5.1 Baseline Hydrofoil Model

Similarly to Chapter 4, the results presented in this chapter are based on a cantilevered trapezoidal type I NACA 0009 hydrofoil made of solid aluminum with an aspect ratio of 6.67 that has no sweep and a taper ratio of 0.5. The geometry and dimensions of this foil are shown in Figure 4.2. We chose this hydrofoil because high-quality experimental data for the hydrodynamic forces and structural displacements is available from Zarruk et al. [155]. We present the validation of our hydrostructural solver against these experimental results in Section 5.2. This NACA 0009 hydrofoil provides the baseline design for all the optimizations presented in Section 5.3.

5.1.1 Fluid Model

Similar to the previous chapter, the nominal freestream velocity is 12.4 m/s, resulting in a Reynolds number of 1.0×10^6 based on the mean chord. The flow is assumed to be fully turbulent and the SA turbulence model is used in ADflow. The CFD mesh used for all the optimization results—shown in Figure 4.2—is a structured O-grid with 515,520 cells and $y^+ = 1.1$. The domain size is 30 chord lengths in all directions, with boundary conditions applied as shown in Figure 4.2.

5.1.2 Structural Model

Figure 5.1(a) shows the structural mesh used for the optimization results, which has 44,800 linear 8-node brick elements, with 7 elements along the thickness direction, 40 elements in the chordwise direction, and 160 elements in the spanwise direction. A clamped boundary condition is enforced at the root, i.e., the displacements and rotations are set to zero for all the nodes at the root. The red lines in Figure 5.1 highlight the edges of the outer mold line that is in contact with the water. The clamped boundary condition actually extends 20 mm beyond the wetted boundary at the root in the experimental setup due to

the use of an acrylic fairing disk to seal the load cell from the tunnel and the associated mounting design [155], as shown in Figure 3.2. Hence, the root of the structural mesh is also offset 20 mm relative to the CFD mesh, as shown in Figure 5.1.

While the CFD mesh has rounded tip, the tip of the structural mesh is modeled in a square shape. To avoid zero thickness leading and trailing edges, less than 2% of the chord is cut off on the solid FEM model at each end. This has a negligible contribution to the structural stiffness and hence should not affect the structural response. Although the flow domain boundaries do not coincide with the structural surfaces at the leading and trailing edges, the fluid-structure coupling is still possible due to the use of rigid links in the load and displacement transfer algorithm, as explained in Section 2.3.

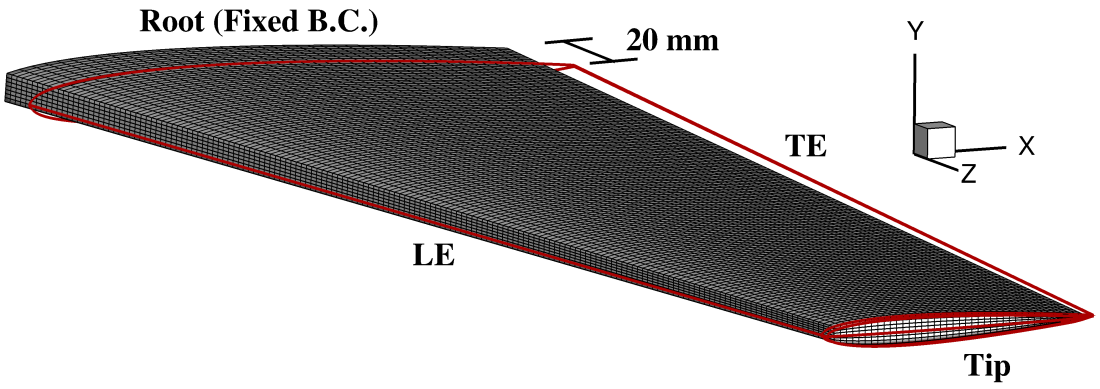

Figure 5.1: Baseline cantilevered NACA 0009 hydrofoil showing the structural mesh.

5.2 Validation and Formulation

5.2.1 Experimental Setup

Similar to the hydrodynamic validation in the previous chapter, the hydrostructural solutions are compared to the experimental measurements conducted at the variable pressure water tunnel at the Cavitation Research Laboratory (CRL) of the University of Tasma-

nia [36].

Only the results from the type I aluminum hydrofoil are used to validate the results shown in this chapter, since it is the most flexible of the metal foils. A worst case uncertainty of 13% is reported for the tip bending deflections measurements.

Table 4.1 lists the parameters used for the experiment. Similar to hydrodynamic-only validation presented in the previous chapter, all the parameters (dimensions, Reynolds number, fluid density, velocity, the material of the hydrofoil) from the experiments were matched in the numerical model, except for the Mach number. However, because compressibility effects are negligible for Mach numbers lower than 0.1, this discrepancy in Mach number does not affect the solution. Structurally, the hydrofoil has a solid cross section and is made of homogeneous 6061-T6 aluminum alloy, whose material properties are listed in Table 5.1.

5.2.2 Natural Frequency Validation

To ensure the accuracy of the coupled hydrostructural calculations, it is important that the effective stiffness of the structure be the same as in the experiment, which can be verified by comparing the natural frequencies since the mass is known. The natural frequencies are also important to understand the vibration characteristics of the hydrofoil, and to avoid unwanted vibration, noise, accelerated fatigue, and hydroelastic instability [147].

Table 5.1: 6061-T6 aluminum alloy material properties.

Symbol	Description	Value	Units
ρ_s	Solid density	2700	Kg/m^3
E_s	Elastic modulus	69	GPa
ν_s	Poisson's ratio	0.33	–
σ_y	Yield strength	276	MPa
$\sigma_{s,f}$	Fatigue strength	97	MPa

Table 5.2 compares the experimental value for the first (spanwise bending) mode nat-

ural frequency of the hydrofoil, which was obtained in-air [155], to that of two numerical computations: one using our structural solver TACS, and the other using the commercial structural analysis software NASTRAN [1]. The two numerical results differ only by 0.1%, while the discrepancy relative to the experimental results is 1.6%.

Table 5.2: Comparison between first mode in-air natural frequency of the type I aluminum hydrofoil from experimental results [155], and numerical results from NASTRAN and TACS (current FEM solver). A structural mesh with 44,800 elements—as shown in 5.1—is used for both NASTRAN and TACS.

	Experiment [155]	NASTRAN	TACS (current FEM solver)
Frequency (Hz)	100.0	98.5	98.4

5.2.3 Hydrostructural Solver Validation

To validate the coupled hydrostructural solver, we compare our numerical results with the experimental measurements. For Re = 1.0×10^6, experiments were only conducted up to an angle of attack of 6^o to keep the maximum lift force to be less than 1 kN. Figure 5.2 compares the mean predicted C_L (lift coefficient), C_M (pitch moment coefficient), C_D (drag coefficient), and δ_{tip}/b (normalized tip bending deflection, where $b = c/2$ is the semi-chord at midspan) at various angles of attack with the experimental measurements of the type I aluminum hydrofoil presented in reference [155]. We used a fine CFD mesh with 4,124,160 cells and a structural mesh with 179,200 elements (shown in the red line and star symbol in Figure 5.2). Good agreement between the numerical predictions and the experimental measurements is observed in Figure 5.2: the average difference in the lift force and moment coefficient predictions is 3.5%. The average difference in the drag coefficient is 5.4%.

The computed tip bending deflection is non-dimensionalized with respect to the mid-span half-chord (δ_{tip}/b), where $b = 45$ mm. The predicted deflection is compared to the experimental values in the last plot in Figure 5.2. The average difference in the tip deflections is 5.5%, which is lower than the maximum experimental uncertainty (13.0%). For

$\mathrm{Re} = 1.0 \times 10^6$, the experimentally measured tip bending deflection is 13.36 mm at an angle of attack of 6^{o}, while the numerical prediction is 13.44 mm. Tip twist deflections are not compared, since the twist deflections for the aluminum hydrofoil were too small to measure.

In Figure 5.2, we also compare C_L, C_M, C_D, and δ_{tip}/b from a coarser CFD mesh (515,520 cells) and a coarser structural mesh (44,800 elements); while Figure 5.2 shows that the C_D is over-predicted compared to the measured value. On the other hand, the fine mesh predictions, C_L, C_M, and δ_{tip}/b, show excellent agreement with experimental measurements. Additionally, C_D from the coarser mesh (515,520 cells) follow the same trend as the finer mesh (4,124,160 cells) and the experimental measurements.

Note that the similar trend (i.e., over-prediction of C_D) with the coarser CFD mesh (515,520 cells) for the type I stainless steel hydrofoil was also presented in the previous chapter. In hydrostructural shape optimization, we are generally more interested in the gradient of the drag coefficient due to the use of the adjoint-based optimization, rather than the actual grid converged value. Thus, in the interest of computational efficiency, we used a CFD mesh with 515,520 cells and a structural mesh with 44,800 elements for optimization studies presented later in this chapter. Additionally, as noted in the previous chapter, the ADflow predictions with a CFD mesh of 515,520 cells were verified with predictions obtained using the commercial CFD solver, ANSYS CFX, using an incompressible uRANS (unsteady RANS) method with the $k-\omega$ shear stress transport ($k-\omega$ SST) turbulence model with a finer mesh, and the difference in C_D for the type I stainless steel hydrofoil between the two codes was only 1.7%.

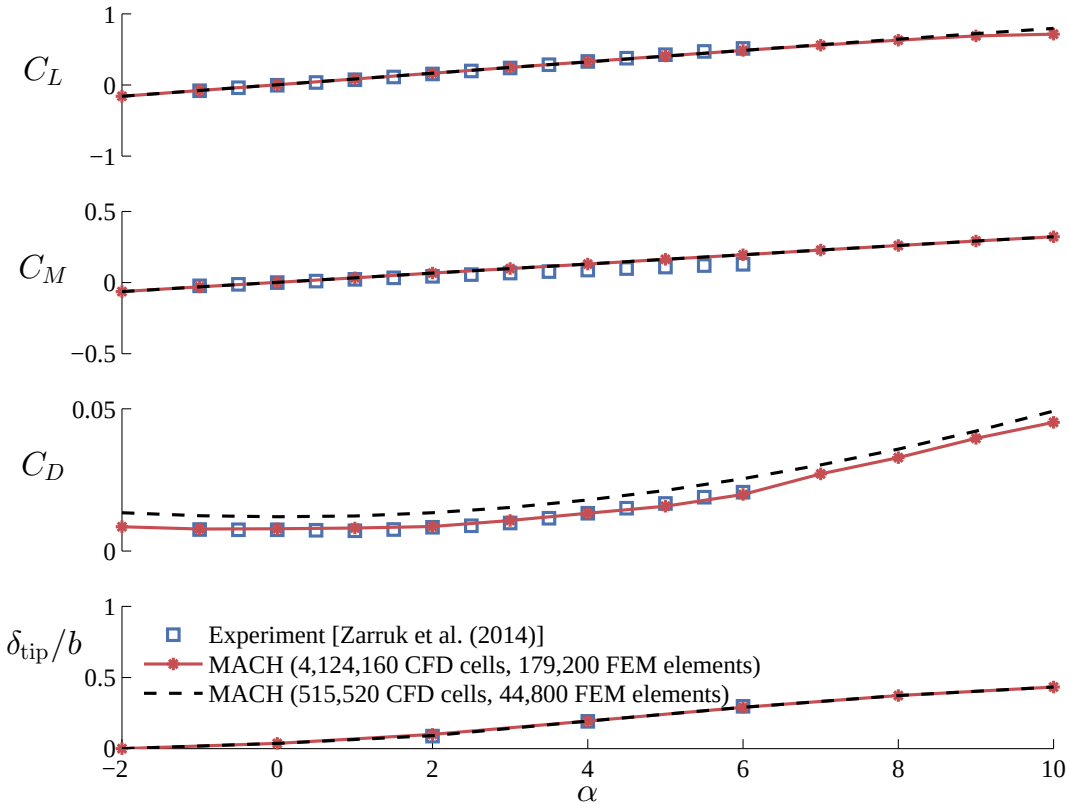

Figure 5.2: Comparison between computed force and moment coefficients, and dimensionless tip bending deformation values from two meshes, and experimental results of the type I aluminum NACA 0009 hydrofoil at Re = 1.0×10^6 [155]. Red line represents results from finer meshes (used for validation study) and black dashed line represents results from coarser meshes (used for the optimization studies).

5.2.4 Grid Convergence Study

To study the effect of fluid and structural mesh sizes on the hydrostructural results, we carry out a fluid model grid convergence study with a consistent structural mesh, and structural model grid convergence study with a consistent fluid mesh.

5.2.4.1 Fluid Grid Convergence Study

The convergence of the drag coefficient with number of fluid cells (N) for Re = 1.0×10^6 at $C_L = 0.48$ and $\alpha = 5.5^{\text{o}}$ is shown in Figure 5.3. As ADflow is second order accurate for a three-dimensional mesh, we use grid factor as $N^{(-2/3)}$ to study the fluid grid convergence.

To ensure that there is no discrepancy in hydrodynamic coefficients resulting from the structural mesh, we used a fine structural mesh of 179,200 for all the cases. We found that 4,124,160 fluid mesh cells are needed to reach convergence of the drag calculation, while the lift coefficient already converged with 515,520 cells.

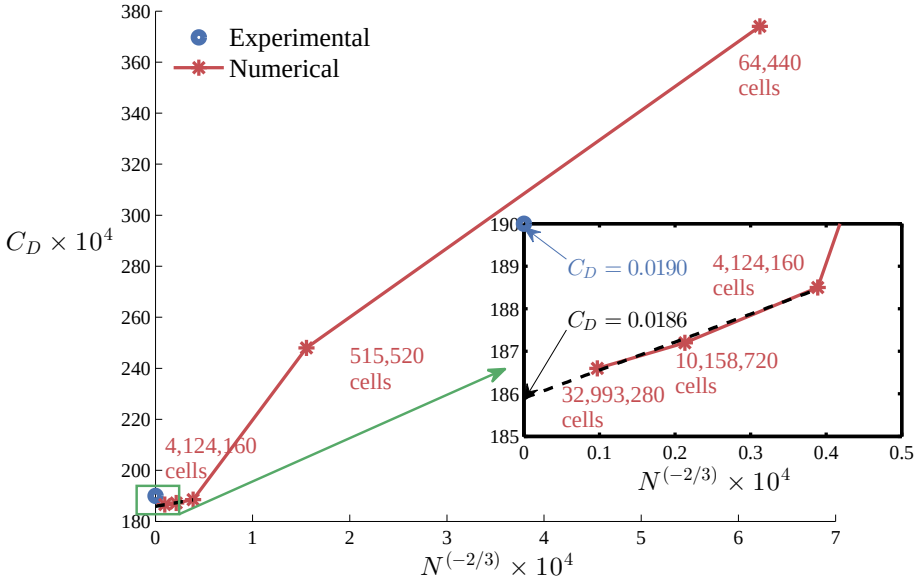

Figure 5.3: The drag coefficient plotted against the grid factor ($N^{-2/3}$) is approximately linear (shown in the subplot with the black dashed line) for the three finest CFD meshes, indicating second order convergence for the type I aluminum NACA 0009 hydrofoil at Re = 1.0×10^6 and $C_L = 0.48$. 179,200 FEM elements structural mesh is used in all the cases. The error in C_D with the finest grid is 1.57%.

5.2.4.2 Structural Grid Convergence Study

A structural grid convergence study is performed using six different structural mesh sizes ranging from 25,200 to 1,638,400 linear 8-noded brick elements. To be consistent, a fine CFD mesh of 4,124,160 cells is used for all the structural grid convergence studies. Table 5.3 compares lift coefficient, lift force, first mode in-air natural frequency, and tip bending deformation values for the hydrostructural solutions.

The difference in tip deformation between the medium mesh with 44,800 FEM elements (highlighted in gray in Table 5.3) results and the experimental results is only 0.6%,

which is well within the experimental uncertainty. Thus, to balance accuracy and computational efficiency, a CFD mesh with 515,520 cells and a structural mesh with 44,800 elements are selected to carry out the hydrostructural optimizations in the remainder of this chapter.

Table 5.3: Structural grid convergence study for a fixed CFD mesh with 4,124,160 cells.

Elements	C_L	Lift force (N)	Dry natural frequency (Hz)	Tip deflection (mm)
25,200	0.4880	1012.98	99.5	12.01
44,800	0.4892	1015.47	98.4	13.28
100,800	0.4891	1015.26	97.6	13.22
179,200	0.4898	1016.72	97.4	13.44
691,200	0.4896	1016.31	97.3	13.48
1,638,400	0.4896	1016.30	97.3	13.50

5.2.5 Optimization Problem Formulation

Similar to the hydrodynamic optimization presented in the previous chapter, the design optimization problem involves minimizing the drag coefficient by changing the hydrodynamic shape. In addition to the constraints on lift coefficient, and minimum pressure coefficient to avoid cavitation, constraints are also imposed on maximum von Mises stresses to avoid fatigue failure, and minimum cross-sectional profile thicknesses at the hydrofoil trailing edge to ensure manufacturability and ease of handling. The optimization problem formulation is detailed in Table 5.4. The lift coefficient is constrained to be equal to a target value, which varies depending on the case. The leading edge position and chord length are fixed to be the same as the baseline NACA 0009 hydrofoil values.

The von Mises stresses are aggregated using the aggregation function KS_{σ_v}, as previously explained in Section 2.6. The von Mises stress is constrained from exceeding the fatigue strength ($\sigma_{s,f}$) of the aluminum alloy with a safety factor of 1.1. The fatigue strength is used because of a large number of load cycles in real-world operations. However, in the model scale testing, the duration for each flow condition is limited, so the hydrofoil was

Table 5.4: Coupled hydrostructural optimization problem setup for the type I tapered NACA 0009 hydrofoil.

	Function/ variables	Description	Quantity
minimize	C_D	Drag coefficient	1
with respect to	x	FFD control points	200
		Twist design variables	10
subject to	C_L^*	Lift coefficient constraint	1
		Fixed leading edge constraint	10
	$A_{\text{cav}} \leq 5 \times 10^{-4}$	Non-dimensional aggregated cavitation constraint	1
	$KS_{\sigma_v} \leq 1$	Stress constraint	1
	$t_{\text{TE}_i} \geq 1.1 t_{\text{TE}_{\text{base}}}$	Trailing edge thickness constraint	20

tested to much higher loads in Zarruk et al. [155]. The fatigue strength of the aluminum alloy is approximately one-third of its yield strength.

The CFD and FEM meshes used for the coupled hydrostructural optimization were previously shown in Figure 4.2 and 5.1, respectively. As mentioned in the previous section, we use a CFD mesh with 515,520 cells and a structural mesh with 44,800 elements for the optimization studies presented in this chapter. Figure 5.4 shows the FFD control points used for optimization. We previously studied the influence of the number of design variables on the optimized values and concluded that the optimal solution converged with 200 FFD control points (Chapter 4). Thus, for the results shown in Section 5.3, we use a total of 210 design variables—200 FFD control points (10 spanwise $\times$ 10 chordwise $\times$ 2 thickness), and 10 spanwise twist design variables—as shown on the right hand side of Figure 5.4. The angle of attack definition remains consistent with the definition presented in the last chapter. Hence, all the twist angles presented in the next section are defined relative to the root section, and the twist at the root section is taken as zero, as explained in Figure 4.6. The undeflected and deflected NACA 0009 baseline hydrofoil at $C_L = 0.65$ with the von Mises stress constraints are shown on the left side of Figure 5.4 while the optimization problem setup is shown on the right.

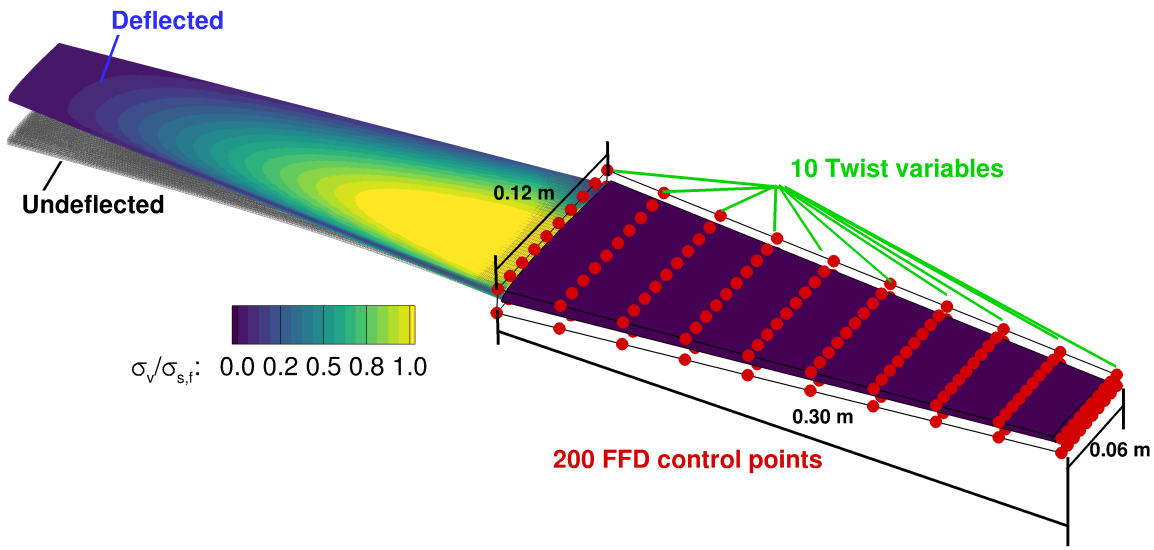

Figure 5.4: Type I aluminum NACA 0009 baseline hydrofoil undeflected and deflected shapes (left), showing von Mises stress contours at $C_L = 0.65$; the hydrostructural optimization design variables (right) consist of FFD control points (red spheres) and section twist variables.

The trailing edge of the NACA 0009 baseline and all the optimized designs is blunt due to physical constraints, terminating in a back-facing edge of finite thickness. To make sure that the optimized geometry can be manufactured and easily handled, we constrained the trailing edge thickness to be no less than 10% higher than the baseline NACA 0009 hydrofoil thickness at 20 points distributed spanwise along the trailing edge. This absolute trailing edge thickness constraint value varies linearly from 0.242 mm at the root to 0.121 mm at the tip.

5.3 Results

We now present single-point and multipoint optimized hydrofoils, and compare their performance and geometries. We demonstrate the importance of performing coupled hydrostructural optimization over hydrodynamic-only optimization. We also present the optimization results for a hypothetical morphing hydrofoil to quantify the best possible gain

in performance assuming active shape morphing can be achieved.

5.3.1 Single-point Hydrostructural Optimization

For the single-point hydrostructural optimization, the hydrofoil was obtained by minimizing the drag coefficient for a single flow condition corresponding to a target lift coefficient. The design variables and constraints are as previously described in Section 5.2.5 and are listed in Table 5.4. This optimization took 12 h of wall time using 192 processors (2.60 GHz Intel Xeon E5-2680V2).

Figure 5.5 compares the optimized hydrofoil at $C_L = 0.65$ to the NACA 0009 baseline. The hydrostructural optimization reduced C_D by 11.04% relative to the NACA 0009 baseline. This figure shows the C_p distributions on the suction side 5.5(a), where the C_p contour for the baseline NACA 0009 geometry is shown on the left, and the contour for the optimized geometry is shown on the right. To complement this visualization, we also show cross-sectional profiles at three spanwise sections ($z/s = 0.05$, 0.5, and 0.85) and the corresponding chordwise C_p distributions on the bottom 5.5(d), where the baseline sectional shapes and the C_p distributions are shown in green, and the optimized ones are shown in red.

The optimization added camber to the originally symmetric profile, which is expected for an efficient hydrofoil at $C_L = 0.65$. This added camber should reduce the angle of attack necessary to achieve the same lift. However, since the angle of attack is fixed in the optimization, the optimizer decreased the twist of all sections instead (including the root). As mentioned earlier, to present a consistent definition of angle of attack between the optimized and baseline hydrofoils, the twist at the root of the optimized hydrofoil (5.02^{o} for $C_L = 0.65$) is subtracted from the optimized twist distribution, resulting in an angle of attack of $\alpha = 3.08^{\text{o}}$, compared to $\alpha = 8.10^{\text{o}}$ for the baseline hydrofoil to achieve $C_L = 0.65$. The resulting twist distribution after subtracting the root twist is plotted in Figure 5.5(g).

Figure 5.5(a) shows that the baseline hydrofoil exhibits partial leading edge cavitation

(where $-C_p \geq \sigma$), as indicated by the gray area near the leading edge in the planform view, which is consistent with the high suction peak observed in the sectional $-C_p$ distribution in Figure 5.5(d). However, the optimized hydrofoil exhibits no cavitation. The optimizer is able to satisfy the cavitation constraint by re-shaping the cross section to drastically reduce the leading edge pressure peak and avoid cavitation. The re-shaping involves adding camber, changing twist distribution, reducing the angle of attack, and increasing the leading edge radius. As shown in Figure 5.5(d), the maximum negative pressure coefficient reduces from 2.1 to 1.0 for the optimized hydrofoil, which significantly delays cavitation inception. The cavitation inception speed increases from 10.6 m/s to 15.4 m/s, for an assumed submerged depth of 1 m (using Eq. (2.25)).

As we can see in the sectional C_p plots in Figure 5.5(d) and the cavitation constraint convergence history in Figure 5.6, the cavitation constraint was only active in the first six iterations, but not in the subsequent iterations. Thus, we would end up with the same design even without the cavitation constraint in this particular optimization case. The lower leading edge suction peak (or the higher cavitation inception speed) in this case was driven by the drag minimization, and the overall design was driven by the stress constraint.

Figure 5.5(b) compares the fatigue stress constraint distribution, i.e., $1.1 \times \sigma_v / \sigma_{s,f}$, between the NACA 0009 baseline (left) and the optimized geometry (right). The yellow region on the normalized stress contours for NACA 0009 baseline (left) indicates that the stress constraints are violated. The hydrostructural optimization is able to start with this infeasible design and yield an optimized design that satisfies the stress constraints by thickening the profile where needed. However, the mass of the optimized hydrofoil is still reduced by 2.5%. This is because the optimizer increased the thickness only where needed (near the root, where the internal stresses are the highest), and reduced the thickness where the stress constraints were not active (towards the tip), as shown in Figure 5.5(f) and also in Figure 5.10.

Figure 5.5(c) compares the skin friction coefficient distributions on the pressure side.

The NACA 0009 baseline exhibits higher skin friction, especially at the leading edge.

Figure 5.5(e) compares the lift distribution of NACA 0009 baseline and the optimized hydrofoil with the ideal elliptical distribution, which would have the lowest induced drag according to linear potential flow theory. The lift distributions for the two designs are close to the elliptical distribution, with increased tip loading in the optimized hydrofoil case. Note that the current problem setup did not include any constraints on the tip loading condition. Figure 5.5(g) compares the twist distribution (defined relative to the root section) of the NACA 0009 baseline and the optimized hydrofoil. While the NACA 0009 baseline has no twist, the optimized hydrofoil has nose up twist from the root to 75% of the span, and nose down twist near the tip. Hence, the required angle of attack is lower for the optimized hydrofoil than for the NACA 0009 baseline, as noted in Fig. 5.5(a).

Figure 5.6 shows the convergence history of the cavitation constraint, stress constraint, and the objective function. This convergence history shows that the stress constraint is critical in determining the optimized design while the cavitation constraint is not.

Figure 5.7 compares the stress constraint values for the NACA 0009 baseline and the optimized hydrofoil. While the baseline NACA 0009 hydrofoil violates the stress constraint for $C_L \geq 0.35$, the optimized hydrofoil satisfies the stress constraint up to the design lift coefficient ($C_L = 0.65$).

Figure 5.8 compares the variation of the lift-to-drag ratio (C_L/C_D) versus lift coefficient for both the baseline and the single-point optimized hydrofoils. The hydrostructural optimized hydrofoil performs better than the baseline hydrofoil for $C_L > 0.3$, while for $C_L < 0.3$, the optimized hydrofoil performance becomes worse than the baseline hydrofoil. Since the optimization was performed only for $C_L = 0.65$, the added camber reduced the performance at the lower C_L values. There is an increase in C_L/C_D of 12.4% at the design point ($C_L = 0.65$). The camber is detrimental at lower angles of attack due to the susceptibility to leading edge flow separation and cavitation on the pressure side of the optimized hydrofoil.

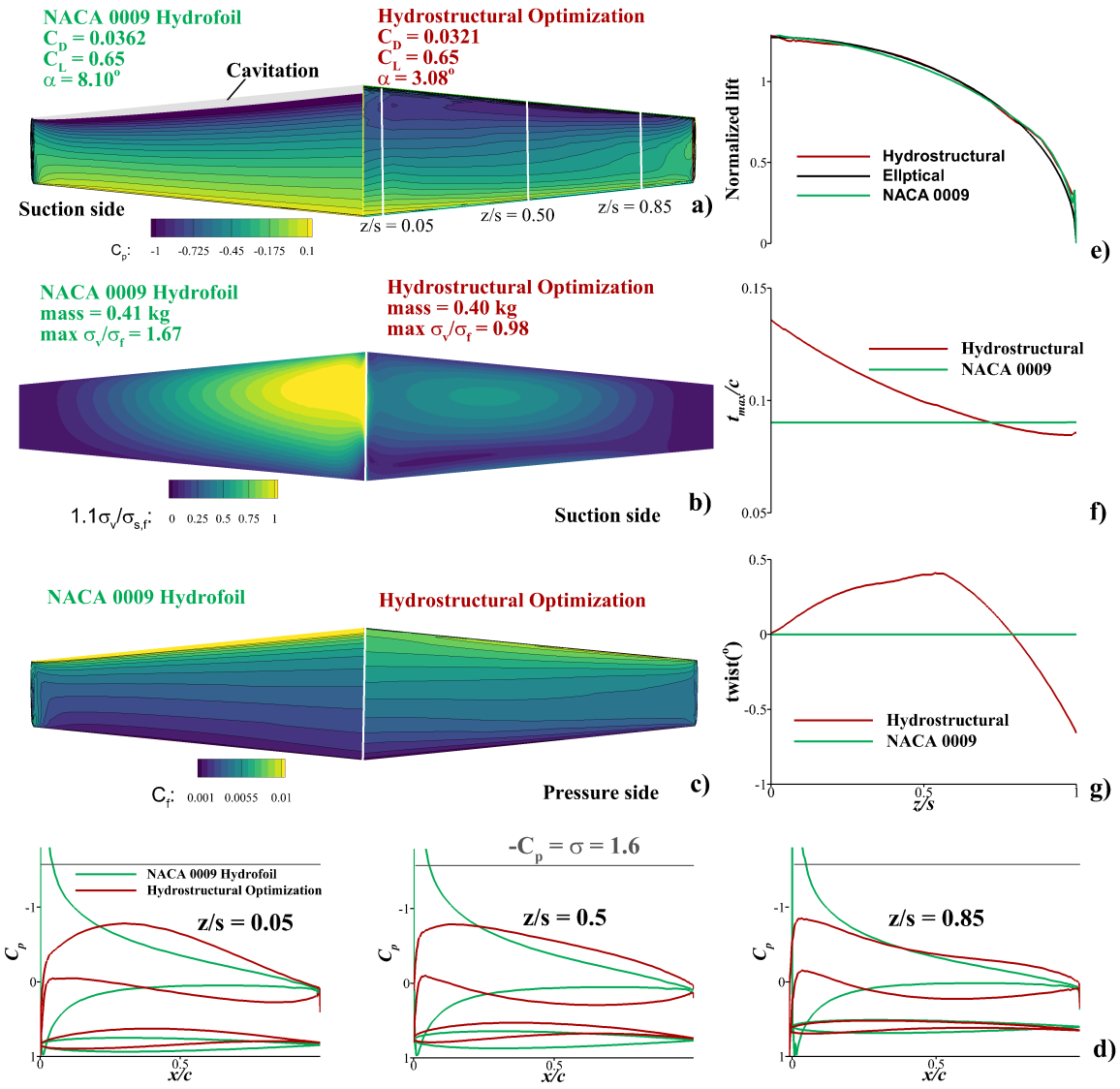

Figure 5.5: Comparison between the single-point hydrostructural optimization result (right/red) and the NACA 0009 baseline (left/green). The optimized hydrofoil added camber (as shown in subplots (d)), reducing the angle of attack required to achieve the same lift (as indicated by the text in subplot(a)), and increasing the leading edge radius and maximum thickness ($t_{\max}$) of the inbound portion (as shown in (f)), resulting in a drag reduction of 11.04% and the elimination of cavitation (a). The optimization satisfied the strength constraints by increasing the maximum thickness-to-chord ratio near the root of the hydrofoil and changing the twist distribution (as shown in subplot(g)), while decreasing the mass by 2.5% by reducing the outboard thickness (f). The sectional pressure distribution (C_p) and geometric profile at three spanwise section (z/s = 0.05, 0.5, and 0.85) are shown in subplot (d).

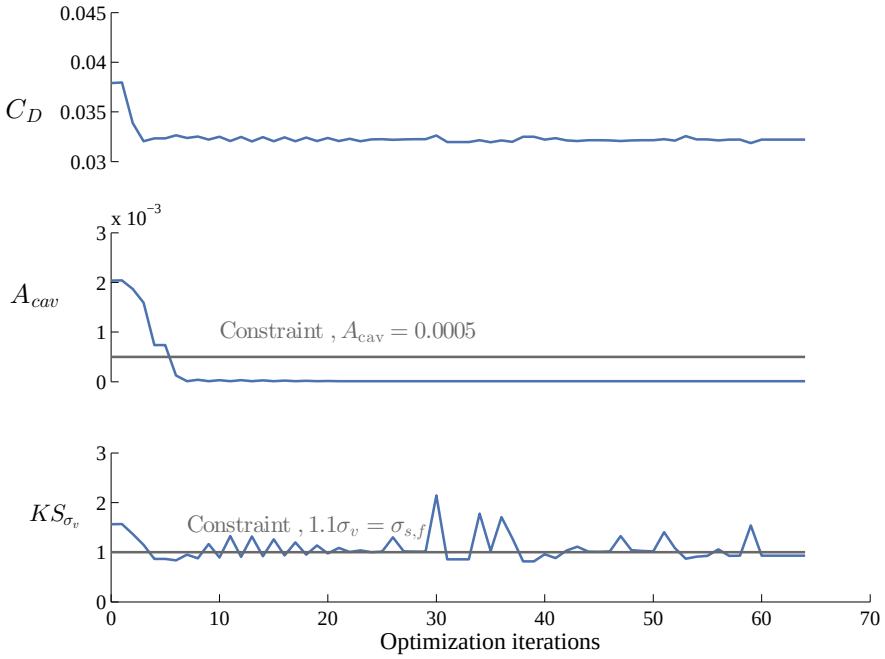

Figure 5.6: Optimization history of objective function and constraints for single-point case at $C_L = 0.65$. While the cavitation constraint was not active for this particular design optimization after the initial 6 iterations, the stress constraint was active for the optimized design.

5.3.2 Multipoint Hydrostructural Optimization

In the previous section, we showed that the single-point optimization does not achieve a design that performs well over a wide range of operating conditions. Therefore, a different approach is required to obtain a design that is robust with respect to operating conditions. To achieve this, a probabilistic multipoint approach explained in Chapter 4 is used.

To illustrate the advantage of probabilistic multipoint optimized approach over the single-point one, we perform a five-point optimization using the points and weights listed in Table 5.5. As mentioned earlier, our hydrofoil is a canonical case and a real probability density function (PDF) of the operating conditions does not exist. Therefore, the operating conditions and corresponding weights in Table 5.5 are based on engineering experience. With respect to the multipoint optimization case presented in the previous chapter, we also

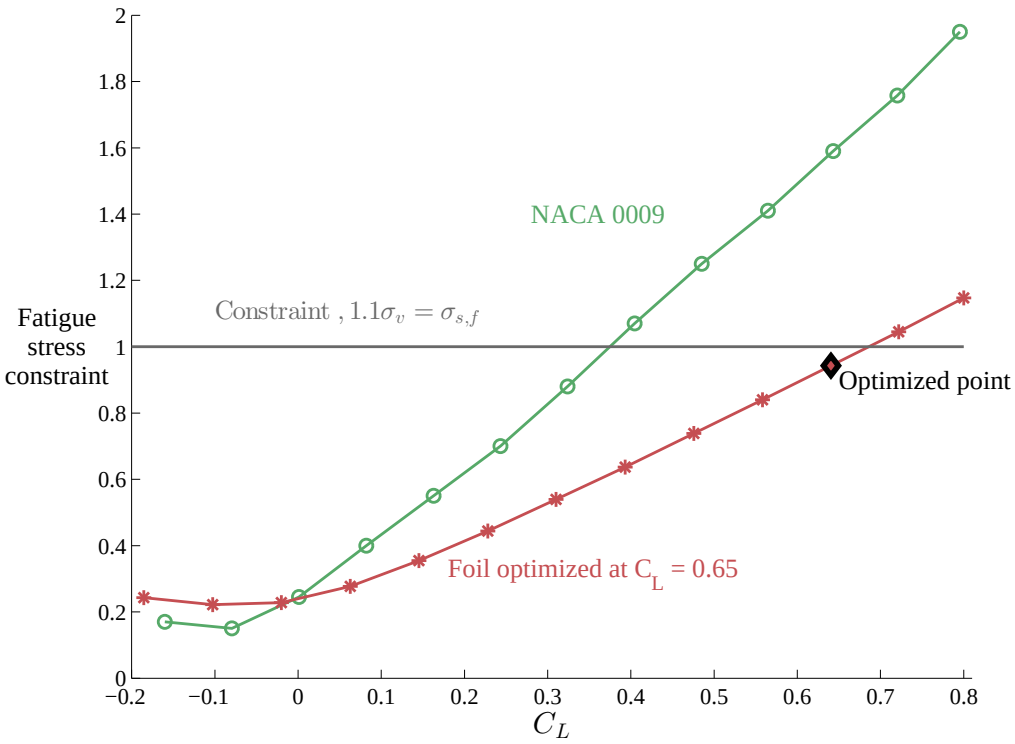

Figure 5.7: Comparison of the stress constraint for the NACA 0009 baseline and the single-point optimized foil for varying lift coefficient. While the NACA 0009 baseline violates the stress constraint for $C_L \geq 0.356$, the optimized design satisfies the stress constraint up to $C_L = 0.65$.

added a negative C_L operating condition, as both positive and negative C_L are relevant for at sea operation of hydrofoils and rudders due to varying incidence angles in waves, and for propellers due to forward and reverse operations. With the exception of the objective function, the rest of the problem formulation for the multipoint case remains the same as detailed in Table 5.4. The hydrostructural calculations and coupled adjoint calculations are carried out for each condition in the multipoint design, and the cavitation and stress constraints are enforced for all the design points.

Since the twist variables include the root twist, it is necessary to fix the angle of attack for one of the design conditions, otherwise, the problem would be under-defined. The angle of attack is defined as the angle of the root section with respect to the original undeformed NACA 0009, which is the same as for the optimized hydrofoil with zero twist at the root.

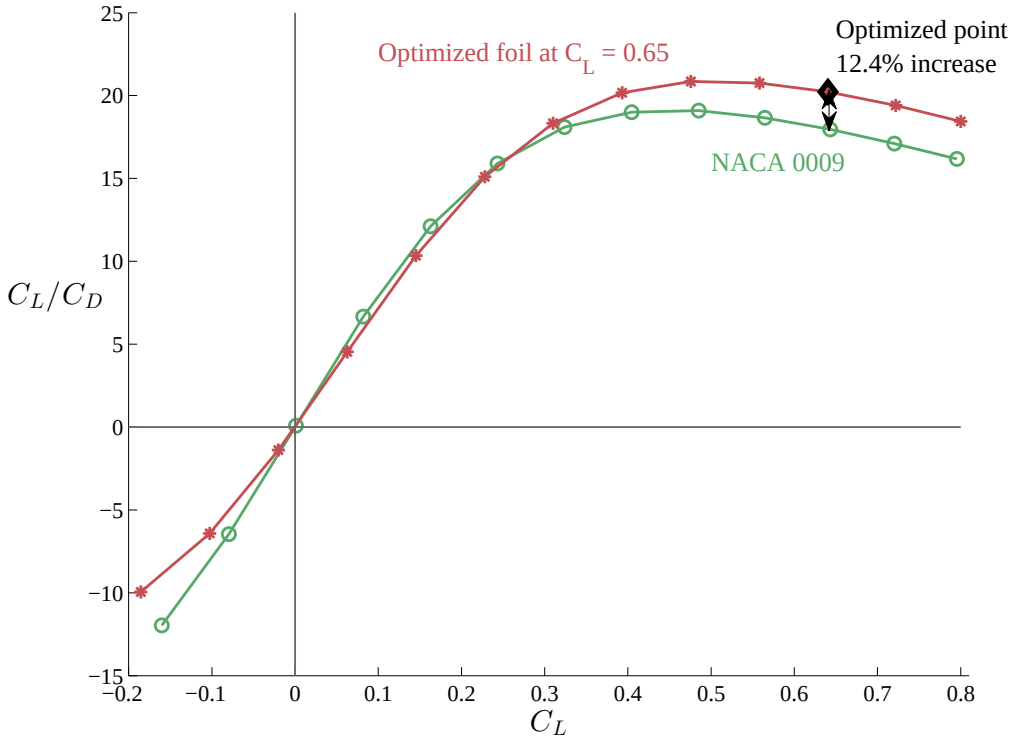

Figure 5.8: Lift-to-drag ratio of the single-point optimized hydrofoil compared to the baseline NACA 0009. The lift-to-drag ratio of the optimized hydrofoil is higher than the baseline for $C_L > 0.3$, but lower for $C_L < 0.3$.

The angle of attack was fixed at 8.10° for $C_L = 0.65$, which is the same value used for the single-point optimization. Note that the 8.10° is the angle of attack prior to the root twist angle is subtracted for a consistent definition of angle of attack with the NACA 0009 baseline. The angles of attack for the other C_L values in the multipoint problem are design variables. Similarly to the single-point optimization case, we subtracted the root twist from optimized twist distributions and incorporated the root twist in the angle of attack. The multipoint optimization took 51 h of wall time using 192 processors.

Figure 5.9 compares the multipoint hydrostructural optimized hydrofoil to the single-point hydrostructural optimized hydrofoil at $C_L = 0.65$. The multipoint optimization leads to an increase in overall efficiency (Eq. (4.4)) of 8.53% over the NACA 0009 baseline and 5.06% over the single-point hydrostructural optimized hydrofoil. Similarly to the single-

Table 5.5: Operating conditions and corresponding weights used in the probabilistic multipoint objective (Eq. (4.3)).

C_L	Weight, w_k	Critical metric
-0.15	0.10	Cavitation on pressure side
0.30	0.15	Drag
0.50	0.25	Drag
0.65	0.45	Drag at most frequent operating condition
0.75	0.05	Stress, cavitation on suction side

point results in Figure 5.5, three sets of contours are shown: the C_p distribution on the suction side for $C_L = 0.65$ (the performance-critical condition), the stress constraint value on the suction side for $C_L = 0.75$ (the strength and cavitation-critical condition), and the C_p contour on the pressure side for $C_L = -0.15$ (the pressure side cavitation-critical condition). The $C_L = 0.65$ pressure contours show that none of the optimized designs exhibits suction side cavitation. As before, the optimizer eliminates cavitation in the process of reducing the drag by increasing the leading edge radius, as shown in the comparison of the cross-sectional shape in Figure 5.10.

The multipoint optimized hydrofoil thickens considerably to satisfy the stress constraints. Unlike the single-point optimized hydrofoil, the multipoint optimized hydrofoil mass is higher than the baseline. The single-point optimization was able to reduce the mass of the baseline by thinning the outboard sections where the stress is lower. However, the multipoint optimization has to satisfy the stress and cavitation constraint at a higher loading ($C_L = 0.75$), which requires thickening both the inboard and outboard portions of the hydrofoil, leading to a 45% increase in mass over the single-point optimized design and a 41% mass increase over the NACA 0009 baseline.

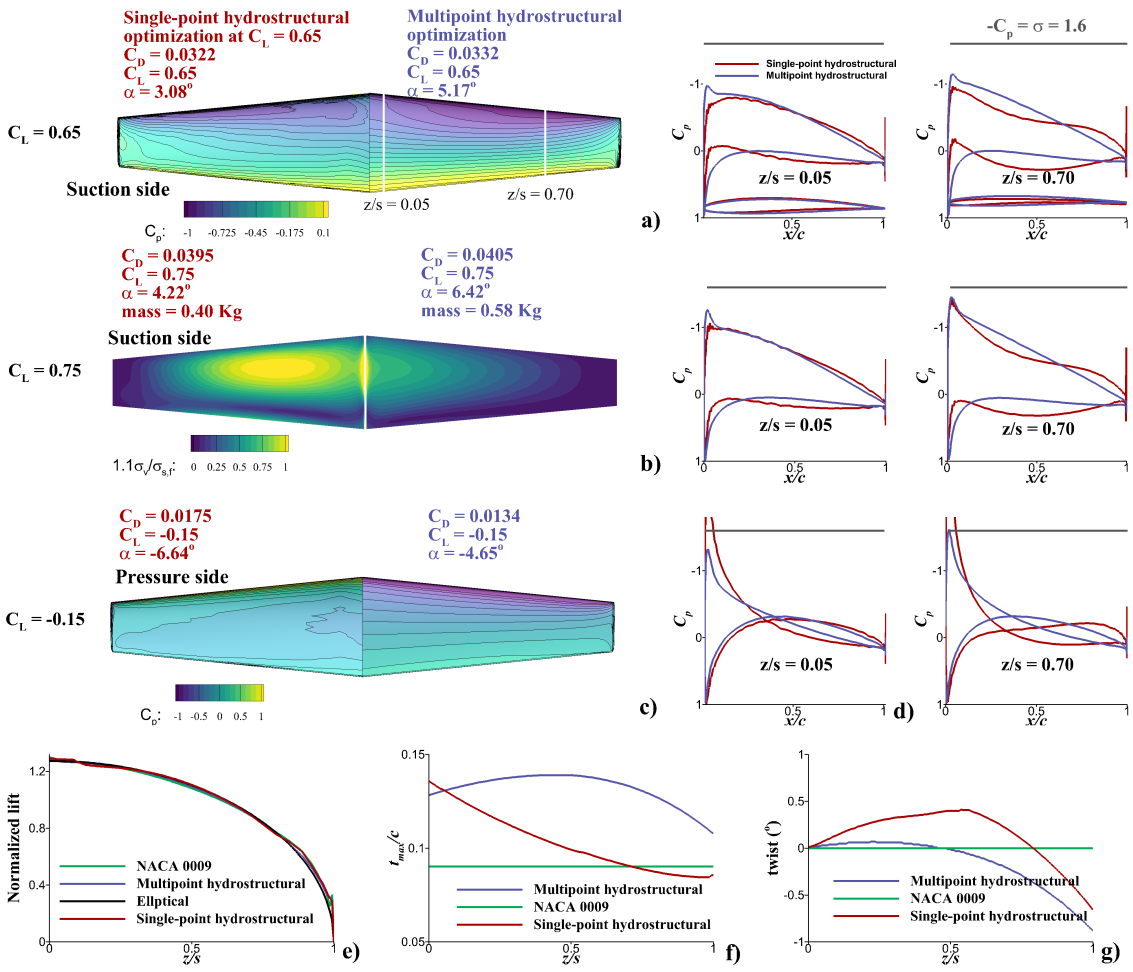

Figure 5.9: Comparison between the multipoint hydrostructural optimization result (right/blue) and the single-point hydrostructural optimized (at $C_L = 0.65$) hydrofoil (left/red). The overall efficiency increased by 5.06% (as indicated in the text in subplot (a)), with a mass increase of 45% as compared to single-point optimized hydrofoil (at $C_L = 0.65$). The single-point optimized hydrofoil violates the stress constraint at $C_L > 0.68$ (as shown in subplot (b) and Figure 5.7). The maximum thickness-to-chord ratio ($t_{\max}/c$) for the single-point optimized hydrofoil is significantly lower than the multipoint optimized hydrofoil, except at the root (as shown in subplot (f)), resulted in single-point optimized hydrofoil not meeting stress constraint. The difference in twist distribution and normalized lift distribution can also be noted from subplot (g) and (e), respectively. The suction peaks were reduced in the multipoint optimized hydrofoil to eliminate cavitation at $C_L = -0.15$ (as shown in the sectional pressure distributions on the right (in subplot (d)) for two span-wise locations, $z/s = 0.05$, and 0.70).

In Figure 5.9(d), the $C_L = -0.15$ condition, we can see that the suction peak is just under the $\sigma = 1.6$ line for the outer profile ($z/s = 0.7$) in the multipoint optimized design, indicating that the cavitation constraint at this condition is active and has a direct effect on

the design. This is in contrast with the single-point optimum case at $C_L = 0.65$, where the cavitation constraint is not active. Additionally, since single-point optimized hydrofoil was not designed for $C_L = -0.15$, it exhibits small leading edge cavitation on the pressure side at that loading condition. Similar to the single-point optimized result, there is an increase in cavitation inception speed by 38% at $C_L = 0.65$ for an assumed submerged depth of 1 m over the NACA 0009 baseline. At $C_L = -0.15$, while the suction peak for the multipoint optimized foil is lower than the single-point optimized hydrofoil, the suction peak for the multipoint optimized foil is higher than the baseline, resulting in an increase of the drag coefficient at $C_L = -0.15$ by 2.2%. This increase in C_D of the multipoint hydrostructural optimized hydrofoil over the NACA 0009 baseline at $C_L = -0.15$ can be attributed to: (1) the need for thicker sections from root to tip to withstand the highest and lowest loading condition at $C_L = 0.75$ and $C_L = -0.15$, respectively, (2) the low probability associated with this operating condition (see Table 5.5), and (3) the fact that it is more challenging to decrease the drag of a cambered hydrofoil at a negative lift condition than for a hydrofoil with a symmetric profile.

Figure 5.10 compares the sectional geometry for the NACA 0009 baseline, multipoint optimized design, and single-point optimized design at ten sections along the span. As the single-point design was optimized for $C_L = 0.65$, i.e., high loading or high angle of attack scenario only, and did not consider the performance at the lower angles of attack, the single-point optimized hydrofoil has slightly higher camber than the multipoint optimized hydrofoil (Figure 5.10). Also, since the loading near the tip is low, the optimizer reduced the thickness of the single-point optimized design to a point below the NACA 0009 baseline (which helped lower the mass of the single-point optimized design and increase the lift-to-drag ratio), but it would not meet the stress constraint for $C_L \geq 0.68$, as indicated in the Figure 5.7. Additionally, the single-point and multipoint hydrostructural optimized hydrofoil resulted in a similar suction side geometry (see Figure 5.10), because the suction side geometry is primarily dictated by the cavitation constraint and drag minimization. To sat-

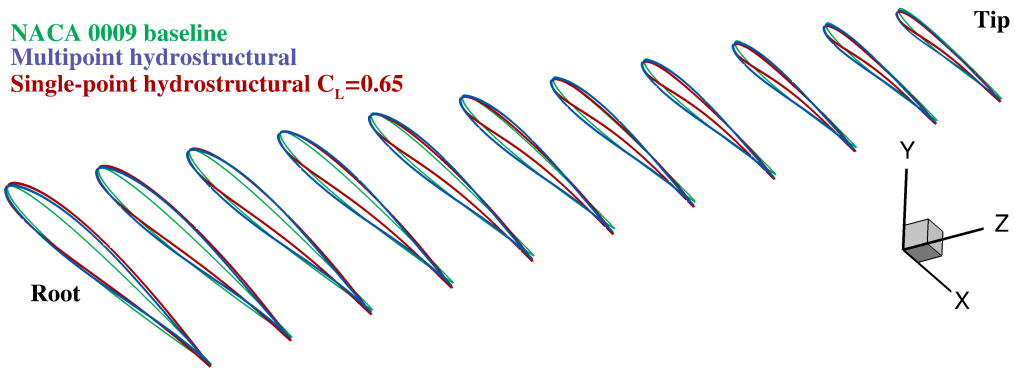

Figure 5.10: Comparison of sectional geometries for the NACA 0009 baseline, the multipoint optimized design, and the single-point optimized design at ten sections along the span.

isfy the more stringent stress constraint at $C_L = 0.75$ and to avoid pressure side cavitation at $C_L = -0.15$, the thickness was added to the pressure side to minimize the resultant increase in drag. Note that although the $C_L = 0.75$ and $C_L = -0.15$ conditions have a significantly lower probability of operation, they have a non-negligible impact on the final optimized design because of the need to satisfy the stress and cavitation constraints at those extreme operating points.

To provide one more set of comparisons, we computed the in-air natural frequencies for the multipoint optimized hydrofoil and compared them to those of the NACA 0009 baseline hydrofoil. This comparison is shown in Table 5.6, where we see that the frequencies for the optimized hydrofoil are significantly higher. This is expected, since the optimized hydrofoil is thicker, which results in higher stiffness and hence higher frequencies. Figure 5.11 shows the first four in-air modes of the multipoint optimized hydrofoil.

Table 5.6: Comparison of the in-air natural frequency (Hz) for the first four modes.

Mode	NACA 0009	Optimized
1	98.4	147.8
2	414.2	602.5
3	784.7	1072.1
4	947.1	1108.4

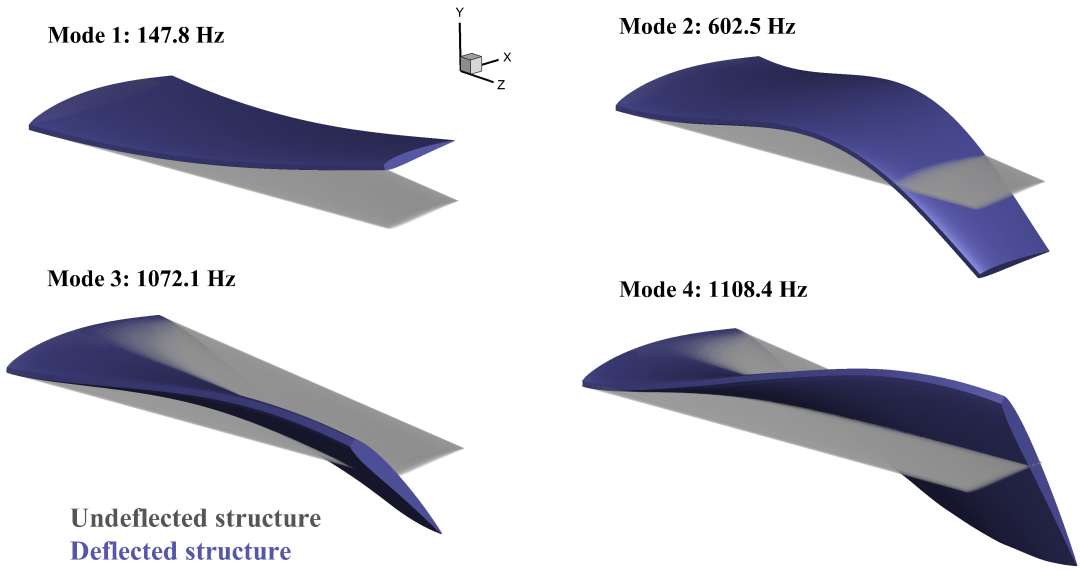

Figure 5.11: First four in-air natural vibration modes and frequencies for the multipoint optimized hydrofoil.

Figure 5.12 shows the evolution of various quantities throughout the optimization. Converged cavitation constraint values show that the cavitation critical conditions are $C_L = 0.75$ and -0.15, for the suction side and pressure side, respectively. The converged aggregated strength constraint values (KS_{σ_v}) show that $C_L = 0.75$ is the strength critical condition.

5.3.3 Multipoint Hydrostructural versus Multipoint Hydrodynamic Optimization

To demonstrate the need for coupled hydrostructural optimization instead of just hydrodynamic optimization (as presented in Chapter 4), we performed a multipoint hydrodynamic shape optimization for comparison. The problem formulation is the same as the one described in the previous section, except now we only solve for the hydrodynamics. This means that hydrofoil flexibility is ignored and no strength constraints are enforced. In Figure 5.13, we compare the multipoint hydrostructural optimized hydrofoil and the hydrostructural analysis of the multipoint hydrodynamic optimized hydrofoil. The multipoint

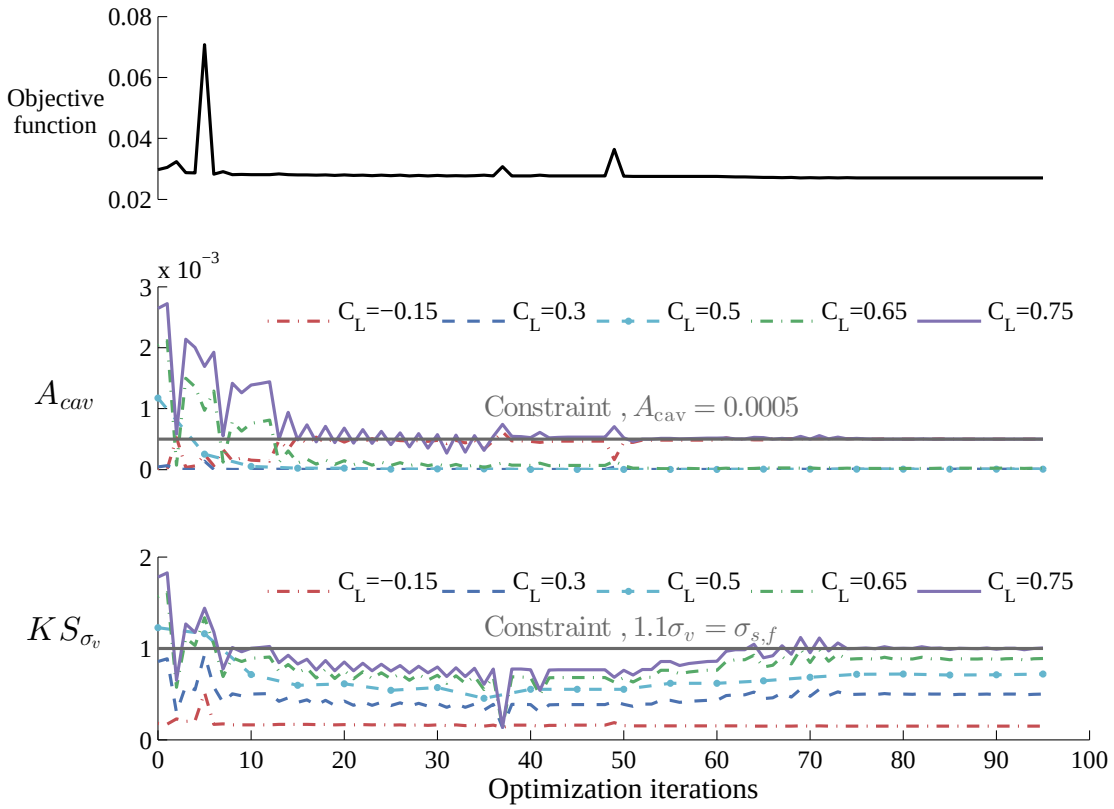

Figure 5.12: Evolution of overall efficiency (objective function), cavitation constraints (A_{cav}), and stress constraints (KS_{σ_v}) throughout the multipoint hydrostructural optimization. The design is driven by the cavitation constraints at $C_L = 0.75$ and -0.15, as well as the strength constraint at $C_L = 0.75$.

hydrodynamic optimized hydrofoil shows an overall efficiency (Eq. (4.4)) that is 1.17% higher than the multipoint hydrostructural optimized hydrofoil. This higher hydrodynamic efficiency is due to the thinner hydrofoil, which also results in a 27.6% lower mass compared to the multipoint hydrostructural optimized design. However, as shown in the second row of Figure 5.13, the stress constraint for the multipoint hydrodynamic optimized design is violated at $C_L = 0.75$, which makes this design impractical. In Figure 5.13(f) and (g), we compare the spanwise twist and maximum thickness-to-chord distributions for the multipoint hydrostructural optimized design, with the multipoint hydrodynamic optimized design.

To further analyze the difference between the various hydrofoils, we compare the fa-

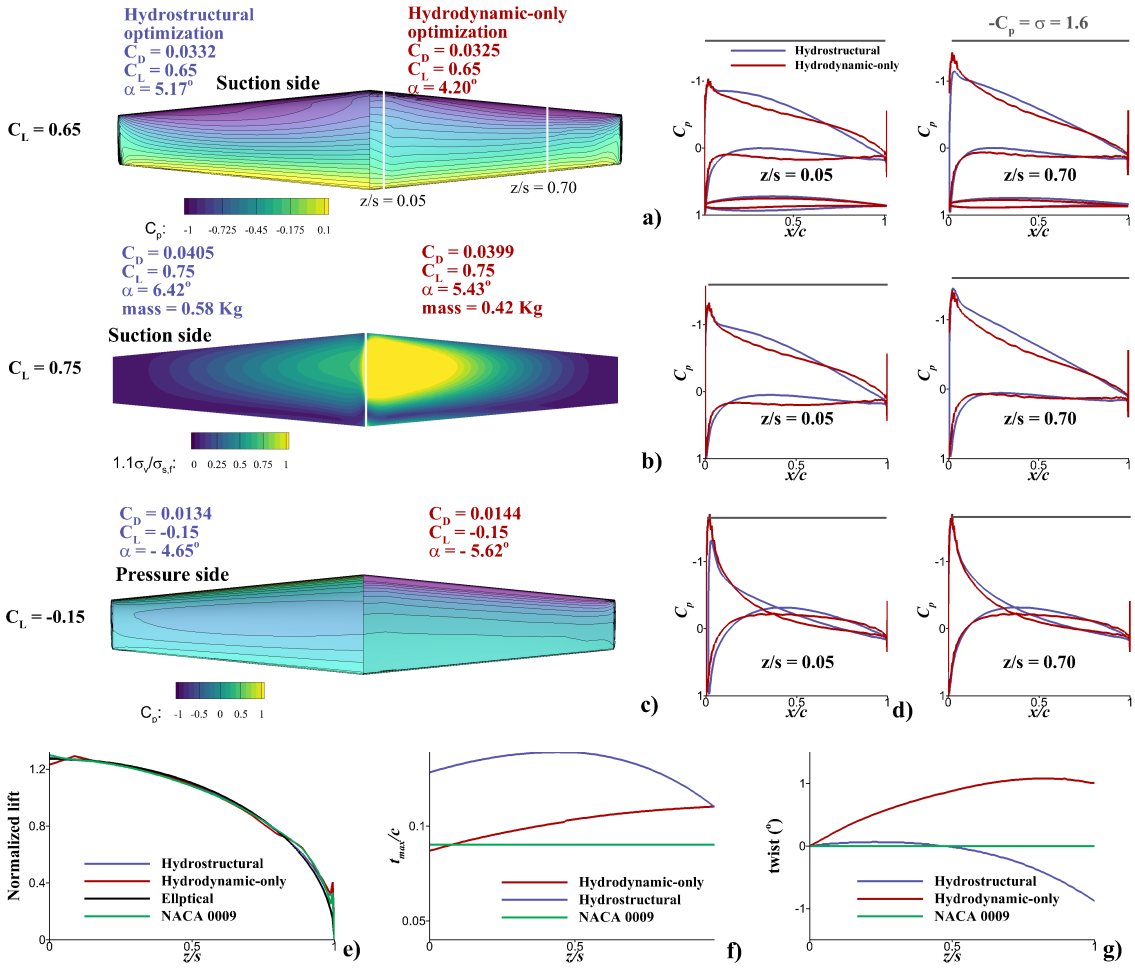

Figure 5.13: Comparison between multipoint hydrostructural optimization (left/blue) and multipoint hydrodynamic optimization (right/red). While the hydrodynamic-only optimized hydrofoil has a higher overall efficiency (as indicated in the text in subplot (a)) and lower mass, it violates the stress constraint at $C_L > 0.35$ (as shown in subplot (b) and Figure 5.14). The maximum thickness-to-chord ratio ($t_{\max}/c$) for the hydrodynamic-only hydrofoil is significantly lower than the hydrostructural optimized hydrofoil (as shown in subplot (f)), resulted in hydrodynamic-only hydrofoil not meeting the stress constraint for $C_L \geq 0.30$. The difference in twist distribution and normalized lift distribution can also be noted from subplot (g) and (e), respectively. The sectional pressure distribution (C_p) and geometric profile at two spanwise section ($z/s = 0.05$, and 0.70) are shown in subplot (d).

tigue stress constraint ($1.1\sigma_v/\sigma_{s,f}$) and hydrofoil tip bending displacement (δ_{tip}/b) in Figure 5.14 over the range of operation conditions for the NACA 0009 baseline, multipoint hydrostructural design, and the multipoint hydrodynamic design. The solid gray line represents the fatigue stress constraint. While the original tapered NACA 0009 hydrofoil violates

the stress constraint for $C_L > 0.35$, the multipoint hydrostructural optimized hydrofoil satisfies the stress constraint for up to $C_L = 0.75$, the highest loading condition. Since the multipoint hydrodynamic optimized hydrofoil does not enforce stress constraints, it results in a thinner foil that violates the stress constraint for $C_L \geq 0.30$. This makes the hydrodynamic design impractical for actual operation.

In the bottom of Figure 5.14, we plot the maximum tip bending deformation (δ_{tip}) normalized by the mid-span half chord length ($b = 45$ mm) over the range of operational conditions for the various designs. The multipoint hydrostructural optimized design exhibits much lower bending deformations, which is consistent with the fact that it has thicker cross sections and hence higher stiffness and frequencies, as observed in Figure 5.11 and Table 5.6.

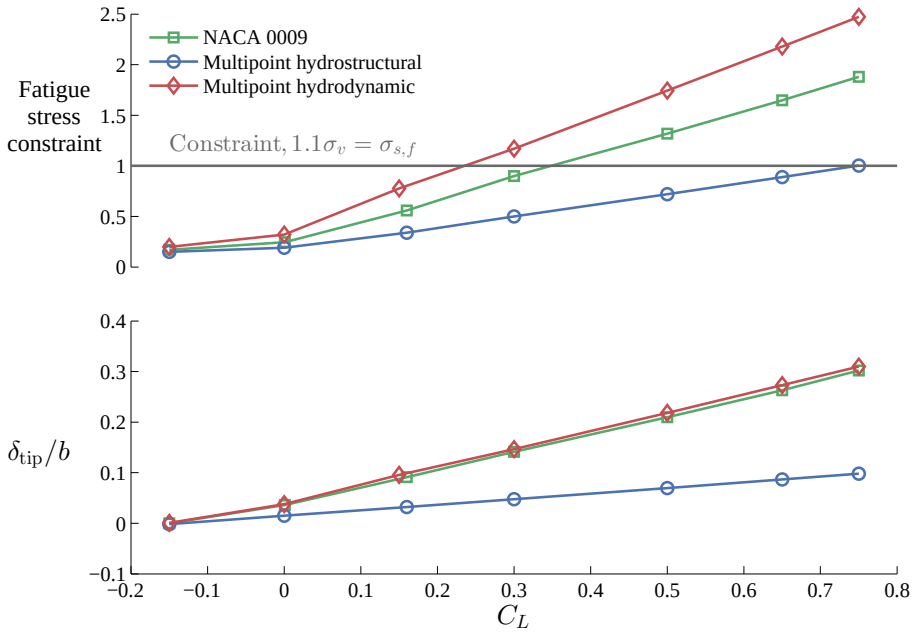

Figure 5.14: Comparison between the fatigue stress constraint and the non-dimensional tip bending deformation for the various designs versus C_L. While the NACA 0009 baseline and the multipoint hydrodynamic optimized design does not meet the stress constraint for $C_L \geq 0.35$ and $C_L \geq 0.3$, respectively, the multipoint hydrostructural optimized design meets the stress constraint up to $C_L = 0.75$, the highest expected loading condition.

5.3.4 Optimization of a Morphing Hydrofoil

The capability to morph the shape of a hydrofoil has the potential to further increase the overall efficiency. To evaluate the best theoretical performance that could be achieved, we assume a morphing technology with the ability to change its shape with complete freedom. This is currently impossible, since for our solid hydrofoil, it would imply a change in mass. However, the motivation of this comparison is to evaluate an upper bound of the benefits due to morphing, and not necessarily to obtain a practical result.

The design optimization of such a hypothetical morphing hydrofoil corresponds to performing independent single-point hydrostructural optimization at multiple lift coefficients. We chose the same five C_L values used in the multipoint optimization problem $(-0.15, 0.30, 0.50, 0.65, 0.75)$ to be able to do a more direct comparison. Similar to previous results, in addition to the lift constraint, aggregated stress constraint on the von Mises stress, and cavitation constraint is also imposed for the five C_L values. Additionally, as mentioned earlier, mass is allowed to vary and we do not have a constraint on the mass between different C_L values to illustrate the best possible performance that can be achieved at each C_L point.

Table 5.7 reports the improvement in the lift-to-drag ratio for the morphing hydrofoil compared to the NACA 0009 baseline and the multipoint hydrostructural optimized hydrofoil. The lift-to-drag ratio improvement compared to the baseline ranges from 10.03% at $C_L = -0.15$ to a maximum improvement of 14.77% at $C_L = 0.75$. However, note that the improvements in lift-to-drag ratio are only slightly better than the multipoint hydrostructural optimized hydrofoil with a fixed geometry, except for $C_L = -0.15$, where the probability of operation is low.

Figure 5.15 compares the twist and thickness distribution for the NACA 0009 baseline and the morphing hydrofoil at various C_L values. The thickness increases with increasing C_L, particularly near the root, to satisfy the stress constraints at the particular C_L.

Figure 5.16 shows that the leading edge radius and camber of the morphing hydrofoil

Table 5.7: Lift-to-drag ratio improvement for the hypothetical morphing optimized hydrofoil compared to multipoint hydrostructural fixed-geometry design, and the NACA 0009 baseline.

C_L	NACA 0009 C_L/C_D	Morphing C_L/C_D	Multipoint hydrostructural improvement (%)	Morphing improvement (%)
-0.15	-11.36	-12.50	-1.70	10.03
0.30	17.34	19.10	7.70	10.19
0.50	19.01	21.18	10.10	11.44
0.65	17.95	20.18	9.02	12.46
0.75	16.67	19.13	13.32	14.77

increased with increasing C_L to achieve the highest efficiency while avoiding cavitation, and satisfying the stress constraint. The results illustrate that the drastic changes in the hydrofoil camber, thickness, and twist distributions are needed for the morphing hydrofoil with varying C_L, which is not achievable with today's technology.

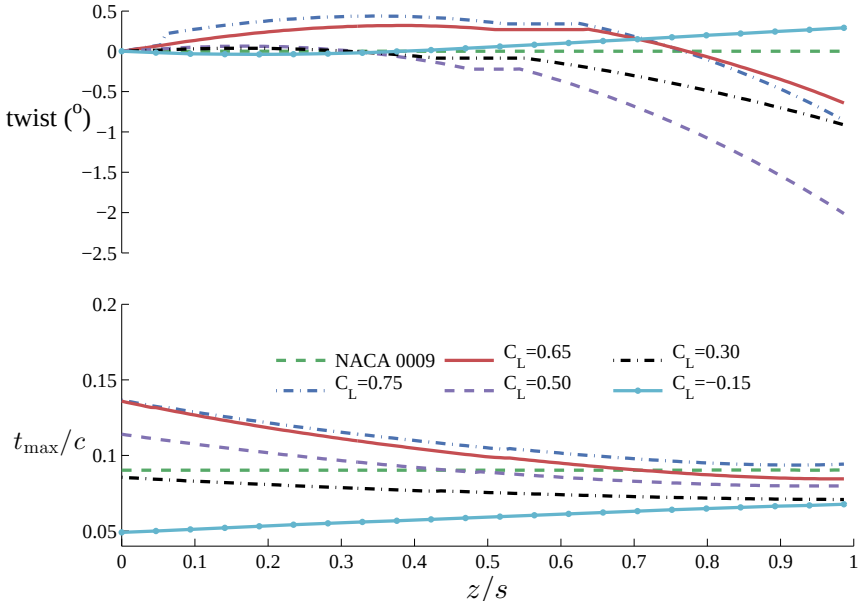

Figure 5.15: Comparison of twist and maximum thickness-to-chord ratio ($t_{\max}/c$) distribution for the NACA 0009 baseline and the morphing hydrofoil at various C_L values.

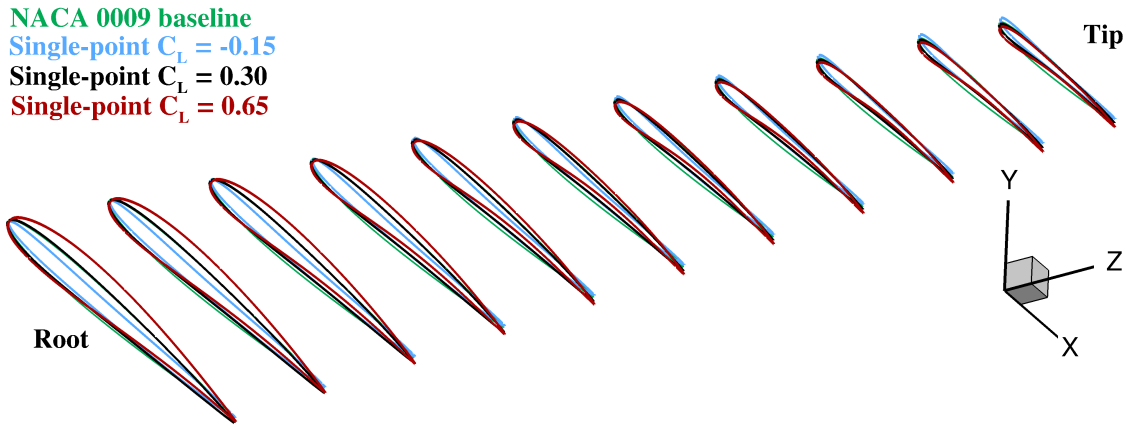

Figure 5.16: Comparison of sectional geometries for the NACA 0009 baseline and morphing hydrofoil. Twist and thickness increase with increasing C_L for the morphing hydrofoil.

5.3.5 Performance Comparison between Morphing and Fixed Geometry Designs

In Figure 5.17, we plot the lift-to-drag ratio over a wide range of lift coefficients for the previously presented designs: the NACA 0009 baseline, the single-point hydrostructural design optimized at $C_L = 0.65$, the multipoint hydrostructural design, and the morphing hydrofoil obtained using single-point hydrostructural optimized design at each C_L. We do not show the multipoint hydrodynamic design, because it violates the strength constraint for $C_L \geq 0.30$ and is thus an impractical design. As expected, the morphing hydrofoil optimized at each C_L shows the best possible performance at each point. Nevertheless, the multipoint hydrostructural optimized hydrofoil with fixed geometry follows this best case scenario closely. As shown earlier, the single-point optimized hydrofoil at $C_L = 0.65$ has the poorest performance for $C_L \leq 0.3$. Additionally, single-point optimized do not meet the stress constraint for $C_L \geq 0.68$.

As explained earlier, the hypothetical morphing hydrofoil is not currently achievable. Thus, we focus on the multipoint hydrostructural optimized hydrofoil with fixed geometry. This multipoint optimum hydrofoil performs better than the NACA 0009 baseline for the

whole range of operating conditions except for a small range just below $C_L = 0.1$, where the performance is similar. As shown in Table 5.8, the multipoint hydrostructural design leads to 8.53% increase in overall efficiency compared to the NACA 0009 baseline.

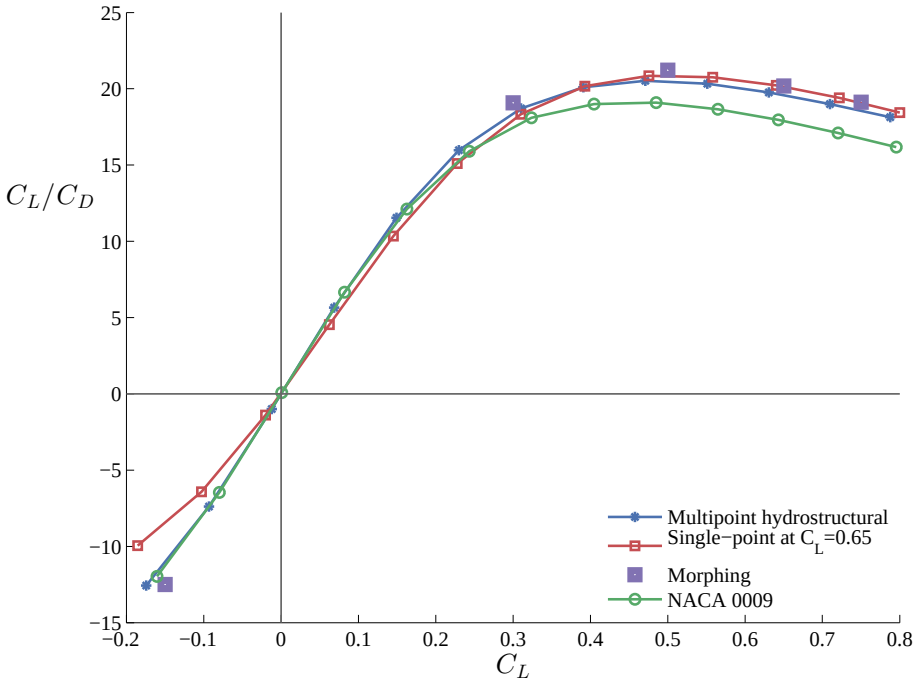

Figure 5.17: Lift-to-drag ratio over a range of operational conditions (C_L) for the NACA 0009 baseline and the various optimized hydrofoils. The multipoint hydrostructural design with fixed geometry provides a good performance over the whole range, but the hypothetical morphing hydrofoil performance is even better for the optimized points.

Table 5.8 compares the overall efficiency increase over the NACA 0009 baseline and the CPU time required when using 192 processors (2.80 GHz Intel Xeon E5-2680V2). The benefit of multipoint hydrostructural optimization over the single-point optimization can be seen in this table.

As explained earlier, the hypothetical morphing hydrofoil with optimized geometry at each C_L is the most efficient, but it is impossible to achieve unless there is a robust active morphing capability.

In Table 5.8 we also compared the CPU time required for each optimization. The time

required by the multipoint optimization is approximately equal to the time taken by one single-point optimization times the number of design points. The time required for the hydrostructural optimization is about 30% higher than the hydrodynamic optimization, but it is worthwhile because hydrostructural optimization is needed to achieve a structurally sound design.

Table 5.8: Overall efficiency increase compared to the NACA 0009 baseline for the various designs (Eq. (4.4)) and CPU wall time.

	Single-point hydrostructural	Multipoint hydrostructural	Multipoint hydrodynamic	Morphing hydrostructural
Overall efficiency increase	6.59%	8.53%	9.54%	11.78%
Stress constraint satisfied	Yes	Yes	No	Yes
Wall time (192 cores)	12 h	51 h	36 h	60 h

5.4 Conclusions

In this chapter, we presented an efficient high-fidelity hydrostructural design optimization approach capable of optimizing the hydrofoil shape while considering multiple operating conditions, fluid-structure interaction response, stress constraints, minimum thickness constraints (for ease of manufacturing and handling), and cavitation constraints. The hydrostructural optimization was performed with 210 design variables, enabling the full shape optimization in 3-D, and opening the door to a variety of hydrofoil and marine propulsor design applications.

We demonstrated and validated the approach on a cantilevered aluminum NACA 0009 tapered hydrofoil with no sweep at Re = 1.0×10^6 and U = 12.4 m/s. The coupled hydrostructural solver was validated against experimental measurements for in-air natural frequencies, hydrodynamic load coefficients, and tip bending deformations. Good agreement was achieved between the numerical predictions and the experimental measurements: Using a converged CFD of 4,124,160 cells and structural mesh of 179,200 elements, the

average difference in the C_L and C_M predictions was 3.5%, the average difference in C_D predictions was 5.4%, the average difference in tip bending deflection was 5.5%, and the difference in the first in-air natural frequency was 1.6%.

To demonstrate the RANS-based hydrostructural design optimization approach, we started from the NACA 0009 baseline and performed a series of shape optimizations. We started with an optimization considering a single operating condition ($C_L = 0.65$). This resulted in an increase in overall efficiency of 12.4%, a mass reduction of 2.5%, and an increase in the cavitation inception speed by 45%, when compared to the original NACA 0009 baseline. The simultaneous increase in efficiency and reduction in mass are significant considering that the hydrostructural optimized foil was much thicker than the NACA 0009 baseline, particularly near the root, in order to satisfy the stress constraint (which the NACA 0009 did not satisfy). However, the single-point optimized hydrofoil was found to perform worse than the NACA 0009 baseline away from the design C_L.

A five-point hydrostructural optimization was carried out, with 210 design variables and constraints on cavitation, manufacturing thicknesses, and maximum stress. The results show that the multipoint optimized geometry leads to an overall increase in efficiency of 8.53%, and an increase in cavitation inception speed by 38% (at $C_L = 0.65$), when compared to the NACA 0009 baseline hydrofoil. Moreover, the multipoint optimized geometry was able to satisfy the stress constraint up to the highest loading at $C_L = 0.75$, while the NACA 0009 baseline violates the stress constraint for $C_L \leq 0.3$.

We also carried out a hydrodynamic-only multipoint optimization, similar to the results presented in Chapter 4, to demonstrate the need for including structural flexibility and stress constraints. The results show that the hydrodynamic-only optimized foil leads to a completely different geometry than that obtained with the hydrostructural optimized hydrofoil, and that the hydrodynamic-only optimized foil violates the stress constraints. Therefore, it is necessary to carry out hydrostructural optimization to achieve a truly optimal, physically realizable, and structurally sound design.

Through the various optimization cases, we showed that the proposed hydrostructural design optimization can consider a variety of objectives and constraints while optimizing with respect to a large number of shape design variables (210) and over a range of expected operating conditions. Other work based on this same approach applied to aircraft design has shown that planform shape variables (such as sweep and span) and structural sizing variables can also be considered [68]. Given the computational wall time for the multipoint hydrostructural optimizations (around 50 h using 192 processors), it is possible to perform such optimizations overnight using 1,000 processors. With such a short design cycle, the proposed approach has the potential to revolutionize the design of the next generation of advanced hydrofoils and marine propulsors.

CHAPTER 6

Experimental Testing of the Optimized Aluminum Hydrofoil

As mentioned in the introduction (Chapter 1), there has been an increased interest in the use of numerical optimization techniques for designing aerospace, maritime, and wing engineering applications. However, validation of the numerically optimized results using experimental measurements has been scarce [55, 82]. To trust the numerical optimization results in the design and optimization process, it becomes necessary to validate the numerical results with experimental measurements. In this chapter, the numerical predictions of the hydrodynamic forces, deformations, and cavitation performance of numerically optimized hydrofoil are presented and validated against the experimental measurements. The results shown in this chapter correspond to the optimized multipoint hydrostructural hydrofoil with constraints on lift coefficient, cavitation number, von Mises stress, and manufacturing tolerances, as presented in Chapter 5, Table 5.4. The design variables are shown in Figure 5.4.

6.1 Experimental Setup and Techniques

The experimental facility, hydrofoil setup, and the experimental techniques, including the tip bending deflection measurements, used in this chapter are discussed in Chapter 3. Similar to the previous chapter, the type I aluminum NACA 0009 hydrofoil is used as

baseline for study in this chapter. Similarly to the baseline hydrofoil, the optimized hydrofoil was also made of aluminum and manufactured by DSTG, Australia, and tested in the cavitation tunnel at AMC, Tasmania.

6.1.1 Optimized Hydrofoil Manufactured by DSTG

A picture of the optimized hydrofoil manufactured by DSTG is shown in Figure 6.1. In line with the material used for the numerical optimization, the manufactured hydrofoil is built of aluminum alloy (6061-T6) (properties are listed earlier in Table 5.1). The camber and thickness variations of the optimized hydrofoil are replicated in the manufactured hydrofoil. However, even with the manufacturing constraints implemented in the optimization problem (presented in Chapter 5, Table 5.4), the manufactured hydrofoil has some discrepancies when compared to the numerically optimized hydrofoil. As depicted by the red boxes in Figure 6.1, the manufactured optimized hydrofoil differs from the numerically optimized hydrofoil due to small chips in two locations: one in the tip trailing edge, and another near the mid-span.

These discrepancies emphasize the importance of including manufacturing tolerances and uncertainty due to manufacturing in the optimization algorithm. In the present case, the differences between the numerical hydrofoil and the manufactured one are not significant enough to result in changes in hydroelastic performance of the hydrofoil, as shown in the next section.

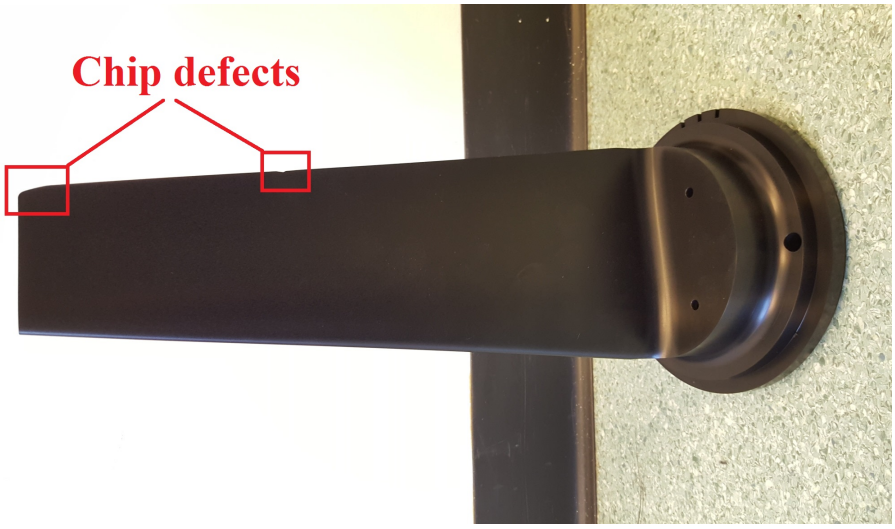

Figure 6.1: The aluminum multipoint optimized hydrofoil used in experiments with discrepancies from the numerically optimized hydrofoil, depicted in the red boxes.

6.1.2 Bending Deflection Measurements

We now use the high-speed images (as presented earlier in Section 3.5) to measure the tip bending deflections for the optimized hydrofoil.

Figure 6.2 presents sample tip deflection for one of the cases, i.e. $\alpha = 3.03^{\circ}$, Re = 1.0×10^6, for the optimized aluminum hydrofoil. The red dot and red dashed lines correspond to the undeformed shape; the green dot and green solid lines correspond to the deformed shape under the hydrodynamic load. As mentioned earlier, the tip bending deflection is considered positive in direction of the lift force. The tip twist deflections for the aluminum hydrofoil were too small to measure with this setup.

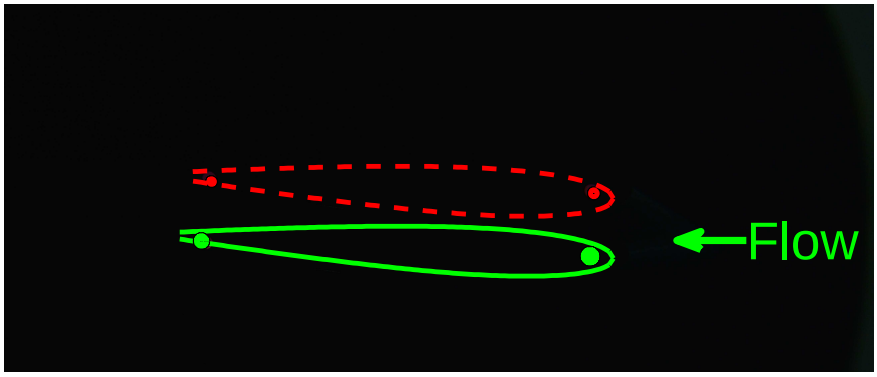

Figure 6.2: The images are taken looking up from below the free tip of the hydrofoil towards the cantilevered root. While red dots are the targets placed near the leading and trailing edges of the tip faces (as outlined by the red dashed line) during the unloaded or undeformed configuration, green dots are the target position on the loaded or deformed geometry (as outlined by the green solid line).

6.2 Results

6.2.1 Comparison of Hydrodynamic Coefficients

In this section, the validation of the numerically predicted (MACH framework) hydrodynamic coefficients, i.e., lift coefficient, drag coefficient, moment coefficient and the tip bending deformations will be compared against the experimental measurements. Figures 6.3, 6.4, and 6.5 compare the numerical predictions and the experimental measurements for C_L, C_D, and C_M, respectively at various angles of attack. The open square symbols and circle symbols represent the experimental measurements and the lines are the numerical predictions. While the red square symbols and red solid lines represent the optimized hydrofoil, the blue circle symbols and blue dashed lines represent the baseline hydrofoil. Since the absolute values of C_L and C_D are critical for the validation studies, the numerical predictions shown in this section are carried out with the finer CFD and structural mesh of 4,124,600 cells and 179, 200 elements, respectively, using the design variables from the multipoint hydrostructural optimized hydrofoil with CFD and structural mesh of 515,200 cells and 44,800 elements, respectively. Good agreement between the numerical predictions and the experimental measurements is observed: the maximum,

minimum, and the mean errors in C_L for the optimized hydrofoil are 6.12%, 0.33%, and 2.96%, respectively. The maximum, minimum, and the mean errors in C_D are 10.44%, 0.30%, and 5.10%, respectively. The maximum, minimum, and the mean errors in C_M are 9.72%, 0.35%, and 3.0%, respectively. Figure 6.6 compares the drag polar for the baseline NACA 0009 hydrofoil and the optimized hydrofoil. The results show that for a given C_L, the optimized hydrofoil has smaller C_D than the NACA 0009 baseline hydrofoil over the entire range of operating conditions.

Similarly to previous results, the predicted and measured tip bending deflection is non-dimensionalized with respect to the midspan semi chord (δ_{tip}/b), where $b = 45$ mm, and are shown in Figure 6.7. The mean difference in the tip deflections is 3.45%. As mentioned earlier, the tip twists are not compared, since the twist for the aluminum hydrofoil was too small to measure.

Figure 6.8 compares the predicted and measured lift-to-drag values for the baseline and the optimized hydrofoil. Both numerical predictions and experimental measurements show that the optimized hydrofoil performs better than the baseline hydrofoil over the entire range of operating conditions. The overall increase in the lift-to-drag ratio is 29%, as per Eq. (4.4). Note that the numerically predicted increase in the lift-to-drag ratio is higher than the one presented in Chapter 5. This increase is due to the difference in the predicted C_D values with the CFD used for the optimization compared to the CFD mesh used for the analysis. The convergence of the C_D value with the number of CFD cells is consistent with the behavior shown in Chapters 4 and 5. Figure 6.8 shows good agreement between the numerical predictions and experimental measurements for both the baseline and the optimized hydrofoil.

6.2.2 Cavitation Performance Comparison

In this section, we compare the cavitating performance of the optimized hydrofoil against the experimental measurements and observations. Ideally, cavitation performance

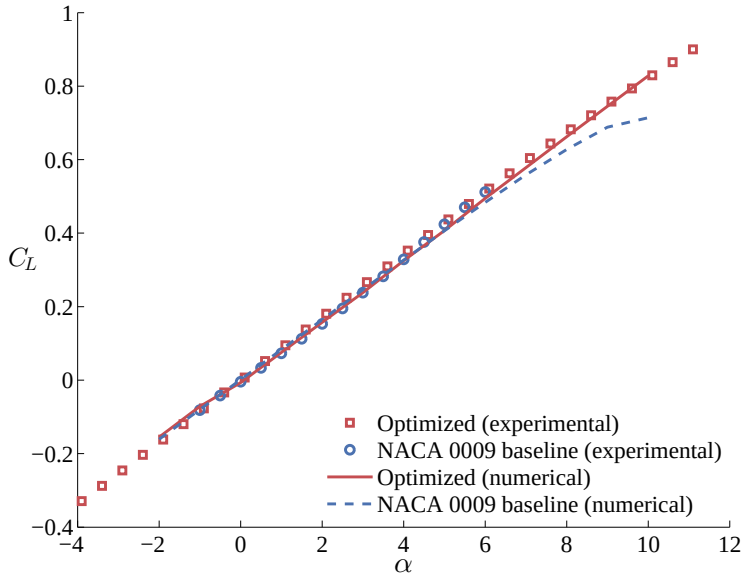

Figure 6.3: Predicted and measured values of the mean C_L for the baseline hydrofoil and the optimized hydrofoil. The maximum, minimum, and the mean errors in C_L for the optimized hydrofoil are 6.12%, 0.33%, and 2.96%, respectively.

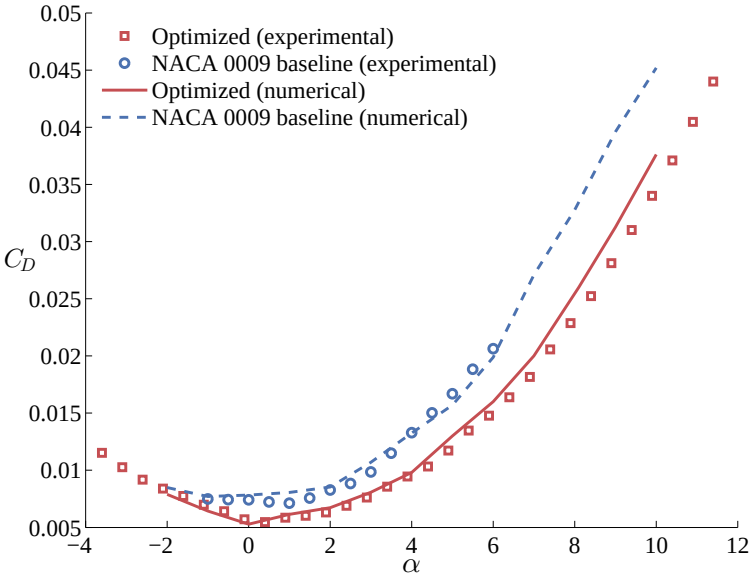

Figure 6.4: Predicted and measured values of the mean C_D for the baseline hydrofoil and the optimized hydrofoil. The maximum, minimum, and the mean errors in C_D are 10.44%, 0.30%, and 5.10%, respectively.

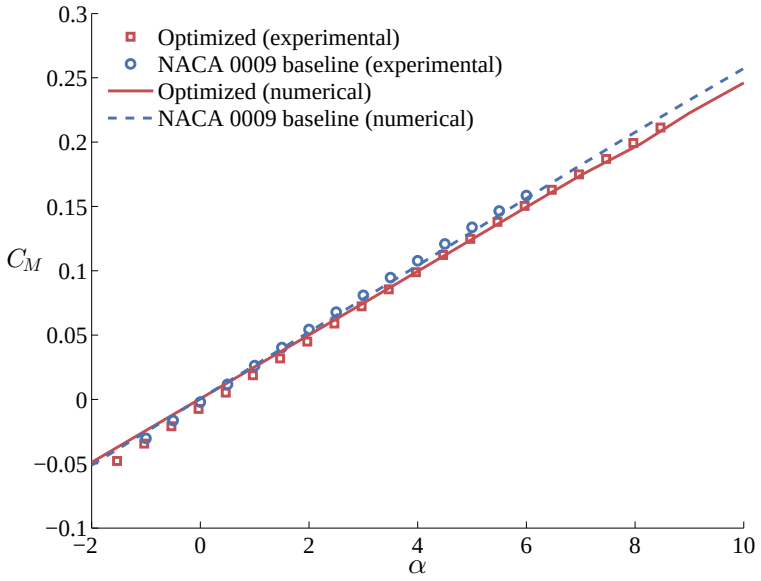

Figure 6.5: Predicted and measured values of the mean C_M for the baseline hydrofoil and the optimized hydrofoil. The maximum, minimum, and the mean errors in C_M are 9.72%, 0.35%, and 3.0%, respectively.

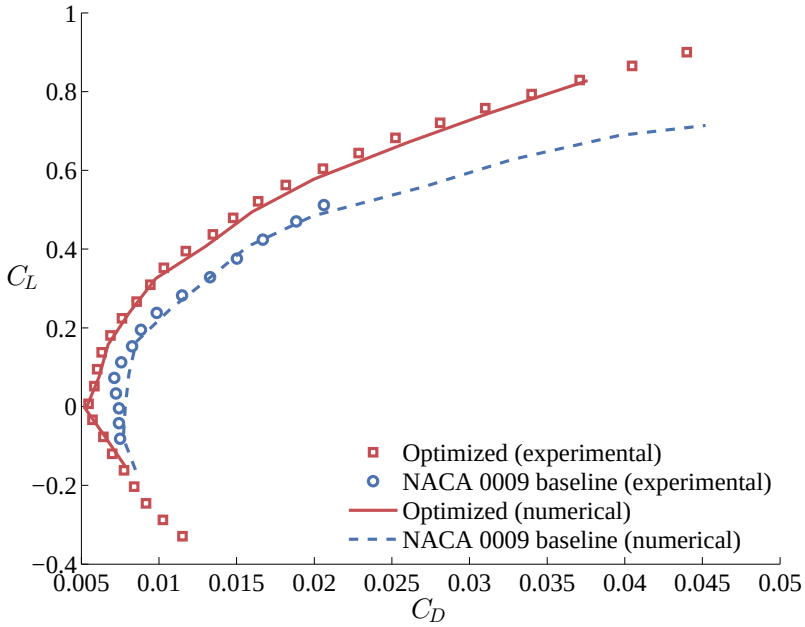

Figure 6.6: Predicted and measured drag polar for the baseline NACA 0009 hydrofoil and the multipoint optimized hydrofoil.

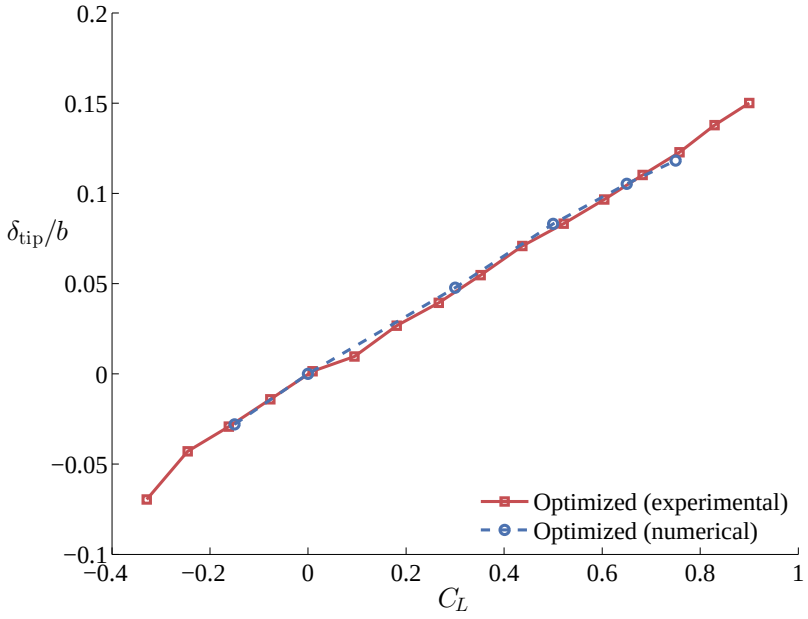

Figure 6.7: Predicted and measured values of the mean δ_{tip} for the baseline NACA 0009 hydrofoil and the multipoint optimized hydrofoil. The mean difference in the tip deflections is 3.45%.

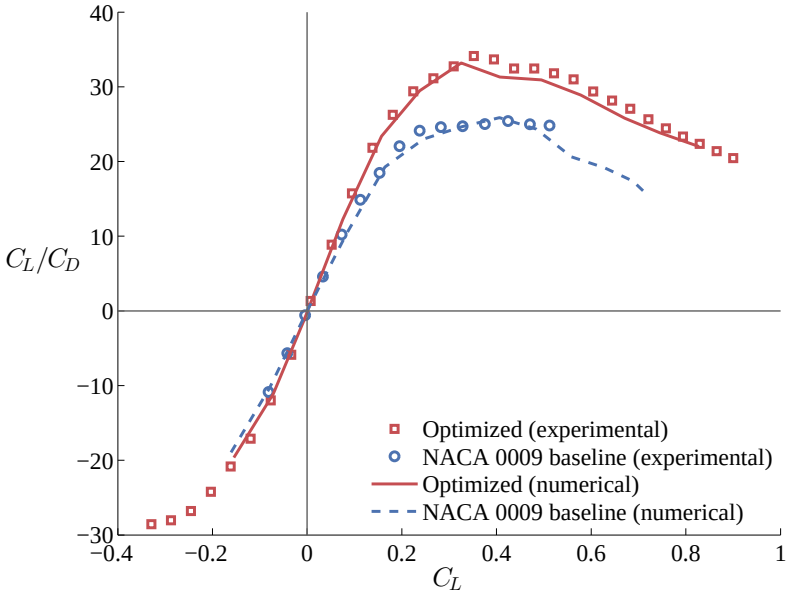

Figure 6.8: Predicted and measured values of the mean lift-to-drag ratio (C_L/C_D) for the baseline NACA 0009 hydrofoil and the optimized hydrofoil. The overall increase in lift-to-drag ratio of 29%, as defined using Eq. (4.4), was achieved.

should be compared at the same σ value, the same C_L value, and at the same Re of 1.0×10^6. However, due to the limited preliminary cavitation experimental runs, only qualitative study of the cavitation performance is presented in this section. Further cavitation testing is required to do a proper quantitative analysis of cavitation performance. Similarly to the results presented earlier in this chapter, the results presented in this section are for type I hydrofoils. Figures 6.10 and 6.11 show the optimized hydrofoil and the baseline stainless steel hydrofoil at Re = 0.8×10^6, $C_L \approx 0.5$, and $\sigma \approx 1.0$ and $\sigma \approx 0.8$, respectively. The use of baseline stainless steel hydrofoil at Re = 0.8×10^6 instead of the aluminum hydrofoil at Re = 1.0×10^6 should not impact the results significantly, as both stainless steel and aluminum hydrofoil are rigid in nature, and both exhibit negligible twist deformation (as shown in Figure 6.9). For cavitating results, Re = 0.8×10^6 was used instead of Re = 1.0×10^6, since the geometric incidence angle of 6^o at Re = 1.0×10^6 approaches the experimental load limit of 1 kN for the baseline hydrofoil. Figure 6.10 shows that while the baseline hydrofoil will experience cavitation at σ = 1.0 and C_L = 0.52, the optimized hydrofoil does not experience cavitation even at σ = 0.95 and C_L = 0.49. Figure 6.10 confirms that the baseline hydrofoil will start cavitating earlier than the optimized hydrofoil. Figure 6.11 compares the extent of cavitation for the optimized hydrofoil and the baseline hydrofoil at σ of 0.75 and 0.8, respectively. Results show greater cavitation extent for the baseline stainless steel hydrofoil as compared to the optimized hydrofoil.

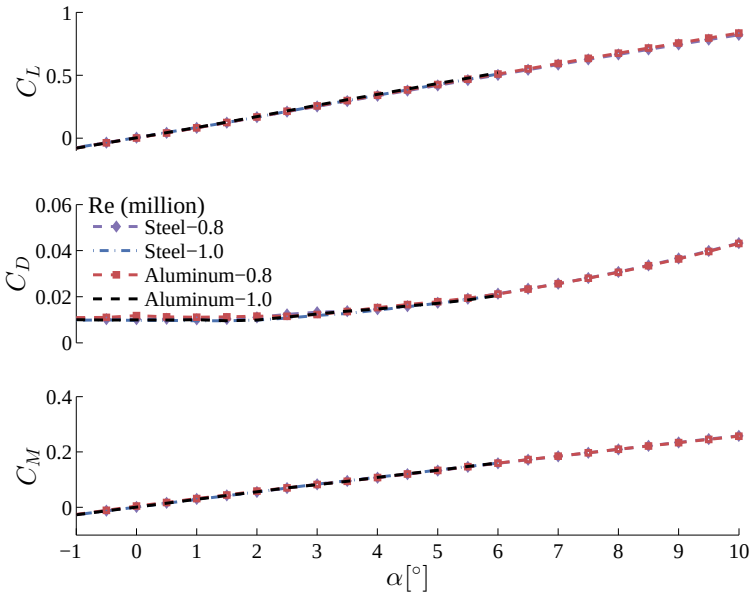

Figure 6.9: Comparison of the measured values of the mean C_L, C_D, and C_M for the stainless steel and aluminum baseline hydrofoil at Re = 0.8×10^6 and Re = 1.0×10^6. Note the similar performance for all the four cases.

In addition to noticing the cavitation from the images, the cavitation performance can also be quantified using the lift calculation. In Figure 6.12, the maximum, mean, and minimum values of the $C_L/C_{L\text{wet}}$ values are plotted against σ at $\alpha = 6^\circ$ for the baseline stainless steel hydrofoil and the optimized aluminum hydrofoil. $C_{L\text{wet}}$ is the mean lift coefficient for the fully-wetted condition, i.e., no cavitation. $C_L/C_{L\text{wet}}$ is plotted to remove differences in C_L. Note that for a given α, C_L should be constant with negligible fluctuations in the fully wetted regime, i.e., higher σ values. As shown in the previous literature [54], the mean C_L increases marginally with the onset of cavitation and then eventually reduces significantly with the further reduction in σ. The increase of difference in maximum and minimum mean values highlight the onset of cavitation. Figure 6.12 show that for similar $C_L/C_{L\text{wet}}$ values, fluctuations of the hydrodynamic loads for the baseline hydrofoil starts at $\sigma = 1.0$, which is a good indication of cavitation development, while fluctuations is not observed for the optimized hydrofoil until $\sigma = 0.75$. To examine the exact cavitation onset σ value for the baseline and optimized hydrofoils, more experiments at finer σ data points and C_L

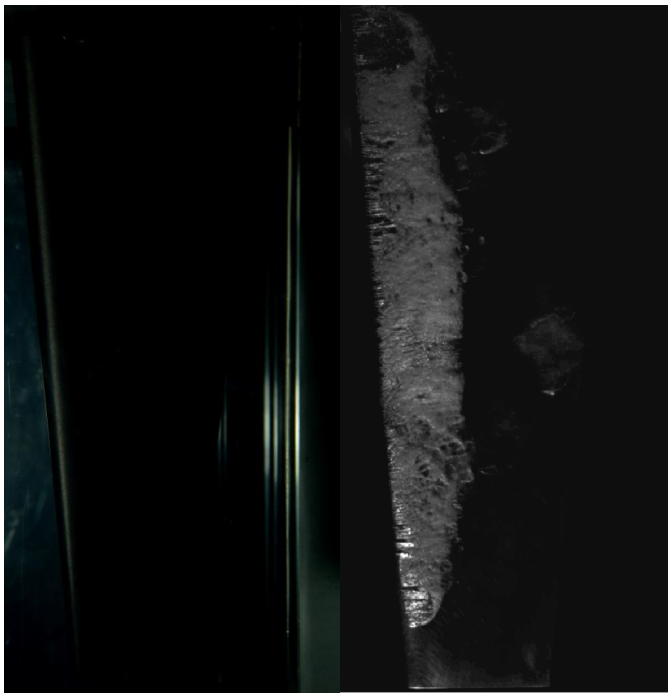

Figure 6.10: Left: optimized hydrofoil; $\alpha = 3.03^{o}$; $\sigma = 0.95$; $C_L = 0.49$. Right: baseline NACA 0009 hydrofoil; $\alpha = 6.0^{o}$; $\sigma = 1.0$; $C_L = 0.52$. Re = 0.8×10^6. While the baseline hydrofoil shows cavitation, no cavitation is observed for the optimized hydrofoil at similar σ and C_L values.

Figure 6.11: Left: optimized hydrofoil; $\alpha = 3.03^{o}$; $\sigma = 0.75$; $C_L = 0.49$. Right: baseline NACA 0009 hydrofoil; $\alpha = 6.0^{o}$; $\sigma = 0.8$; $C_L = 0.52$. Re = 0.8×10^6. For a similar σ and C_L value, there is much less cavitation in the optimized hydrofoil compared to the baseline one.

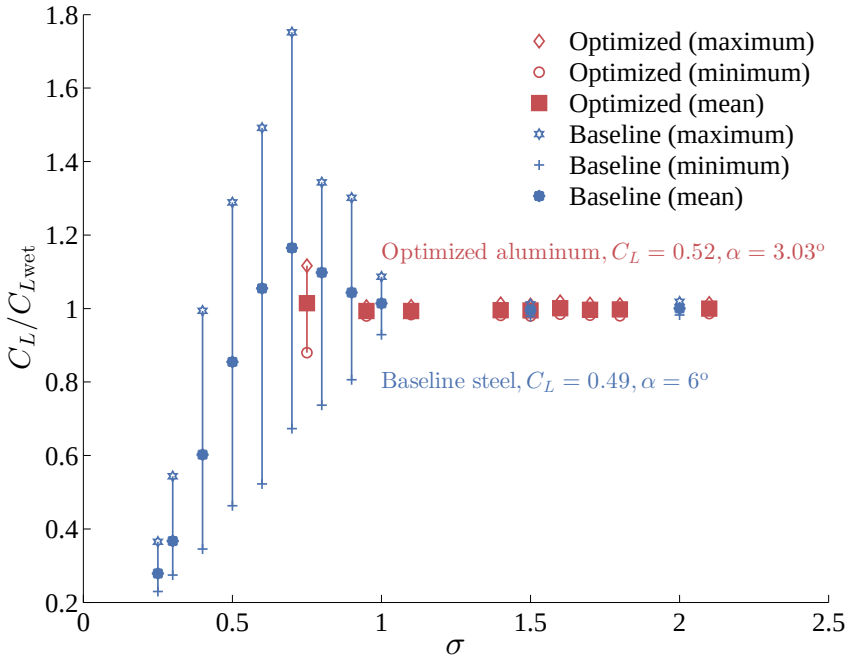

Figure 6.12: Comparison of maximum, minimum, and mean values of $C_L/C_{L\text{wet}}$ as a function of the cavitation number (σ) for the baseline stainless steel hydrofoil (blue) and the optimized hydrofoil (red). Note that the for a similar $C_L/C_{L\text{wet}}$, load fluctuations due to cavitation inception occurs earlier for the baseline hydrofoil compared to the optimized hydrofoil.

values need to be carried out in future. With the results presented so far, it can be deduced that the optimized hydrofoil shows delayed cavitation inception compared to the baseline hydrofoil; however, to quantify the exact improvement, more cavitation experiments are needed.

6.3 Conclusions

In this chapter, the numerically optimized aluminum hydrofoil (multipoint hydrostructural) presented in Chapter 5 is manufactured and tested experimentally. Similarly to previous validation studies, the experimental measurements were conducted in the variable pressure tunnel at the Australian Maritime College. The numerically predicted hydrodynamic coefficients (C_L, C_D, and C_M) and the tip bending deflection (δ_{tip}) are validated against the

experimental measurements. For the optimized hydrofoil, the average difference between the predicted and measured values for mean C_L, C_D, and C_M is 2.96%, 5.10%, and 3.0%, respectively. The average difference in the tip bending deflections is 3.45%. Results also confirm the improvement in the lift-to-drag ratio from numerical optimization across the full range of C_L. The measured overall increase in the lift-to-drag ratio compared to the NACA 0009 baseline hydrofoil is 29%.

The cavitation performance of the optimized hydrofoil is also investigated experimentally. While the experimental cavitation results are mostly qualitative, this study shows significantly delayed cavitation for the optimized hydrofoil compared to the baseline hydrofoil. For a more quantitative study of cavitating performance, more experimental runs are needed. The results shown in this chapter confirms the improvement in the hydroelastic and cavitation performance of the optimized aluminum hydrofoil experimentally.

CHAPTER 7

Bend-Twist Coupling Effects in Composite Hydrofoils

In the previous chapters, a design optimization tool is used to carry out high-fidelity hydrostructural optimization of a homogeneous and isotropic (i.e., aluminum) hydrofoil. The performance improvement of the optimized aluminum hydrofoil was also validated with experimental measurements. With recent advances in the material technology and high quality manufacturing methods, composite materials are now being commonly used in the aerospace and wind engineering applications, with limited use in marine engineering. Thus, the obvious next step is to develop a high-fidelity hydrostructural design optimization tool to carry out optimization of a composite hydrofoil. While for an isotropic hydrofoil, the performance improvement can only be achieved by changing its geometric shape, for the composite material, performance improvement can be achieved both by changing its material configurations as well as the geometric shape.

Before carrying out the composite hydrofoil optimization, it is crucial to understand the inherent load-dependent bend-twist coupling response of anisotropic composite hydrofoils. Previous work on the material-based load-dependent bend-twist coupling is described earlier in Section 1.3. In the current chapter, the load-dependent bend-twist coupling effects on the steady-state hydroelastic response and stability boundary of composite hydrofoils is investigated via combined experimental and numerical studies. In addition to the hydroelastic response, the impact of load-dependent bend-twist coupling on the vibration

response and cavity dynamics of composite hydrofoils will be presented for a range of cavitating conditions. The focus is on the understanding the underlying influence of material bend-twist coupling on the load-dependent deformation response, stall boundary, modal characteristics, static divergence, and cavity dynamics.

The hydrofoil construction, and experimental measurement and testing are carried out by DSTG, Australia, and AMC, Tasmania, respectively. The work in this chapter is presented in the papers co-authored by the author [122, 146].

7.1 Experimental Setup and Techniques

The experimental facility, hydrofoil setup, and experimental techniques, including the tip bending and twist deflection measurements are discussed in Chapter 3. Unlike previous chapters, the type II hydrofoils are used for study in this chapter. As explained in Chapter 3, the type II hydrofoils differ from the type I hydrofoils in the trailing edge thickness and effective structural span of 316 mm (instead of 320 mm for type I hydrofoils). In this chapter, results are shown for Re = Uc/ν_f ranging from 0.25×10^6 to 1.2×10^6, where U is the free stream velocity, and ν_f is the kinematic viscosity of the water. The results are presented for three composite and a stainless steel type II hydrofoils. The stainless steel hydrofoil serves as the rigid baseline. To examine the influence of material bend-twist coupling effects, the three composite hydrofoils have different orientations for the structural unidirectional carbon fiber reinforced polymers (CFRP) layers: 0^o, $+30^o$, and -30^o relative to the spanwise axis of the hydrofoil.

In this section, we discuss composite hydrofoil construction along with the material properties.

7.1.1 Composite Hydrofoil Construction

The composite hydrofoils are manufactured by DSTG, Australia and are tested in the cavitation tunnel at AMC. The details of the construction can be found in [124, 125, 146, 155]. The details of the hydrofoil construction are presented here for the sake of completeness. As stated by Young et al. [146], the three composite hydrofoils were manufactured using a closed mold resin transfer molding (RTM) process. The hydrofoils are made with layers of T700 unidirectional carbon fiber (Carbon-UD), non-crimp biaxial E-glass fabrics (Glass-(0/90)), E-glass fabric (Glass-Basket), and glass mat fabric (Glass-Mat). The properties of each layer are listed in Table 7.1. While Carbon-UD and Glass-(0/90) are the structural components of the hydrofoil, the glass-basket is the outermost ply to provide improved surface finish, protect the structural layers from handling damage, and account for any unwanted galvanic effects. The glass mat fabric is used in the hydrofoil center.

Young et al. [146] explains the coupon tests performed to determine the in-plane longitudinal and transverse tensile modulus (E_{11} and E_{22}), shear modulus (G_{12}) and Poisson's ratio (ν_{12}) of the constituent materials. The in-plane material properties of the materials used in the composite hydrofoils are listed in Table 7.2, along with the stainless steel properties for comparison.

Figure 7.1 from Young et al. [146] depicts the cross-section of the hydrofoil root, midspan, and the tip regions, with the exploded view to show the arrangement of layers. Figure 7.1b) show the orientation of the CFRP layers in the composite hydrofoils. The details of the stacking sequence can be found in [124, 146]. Figure 7.2 shows the three composite hydrofoils and the stainless hydrofoil used in the experiments, where the four holes are for the bolts used to clamp the hydrofoil between the profiled plates (presented in Figure 3.3) to achieve a fixed root boundary condition. Note that it is difficult to see the structural unidirectional carbon layer fiber angle in the picture, as it is only visible to the naked eye when viewed at a particular angle. The last 10% of the chord of the composite hydrofoil only contains glass layers (as evident by the transparent appearance), i.e., no carbon layers.

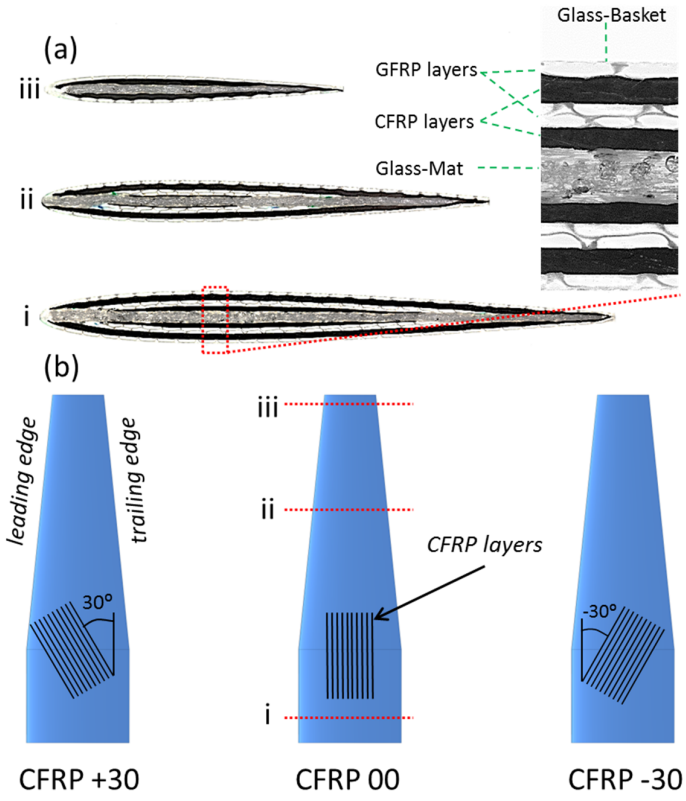

Figure 7.1: (a) Cross sections of the layered glass fiber (GFRP) and carbon fiber (CFRP) reinforced polymer hydrofoils at (i) the root, (ii) the mid span and (iii) the tip. The insert shows a close up of the cross section at the thickest part of the hydrofoil at the root. (b) Orientation of the CFRP layers in the three composite hydrofoils. The figure is originally presented in [146].

Table 7.1: Properties of the fabric layers used to manufacture the composite hydrofoils.

	Carbon-UD	Glass-(0/90)	Glass-Basket	Glass-Mat
Material	12k T-700 non-crimp unidirectional (0°)	E-Glass non-crimp biaxial (0°/90°)	E-Glass basket weave	E-Glass/polyolefin continuous filament glass skins/ polyolefin scaffold core
Fabric weight (g/m^2)	300	600	130	780
Cured ply thickness (mm)	0.26	0.58	0.15	2.4

Table 7.2: In-plane material properties of the composite materials used in the construction of the composite hydrofoils. The corresponding values for the stainless steel hydrofoil are shown at the bottom of the table as a reference.

Material	ρ_s (g/cm^3)	E_{11} (GPa)	E_{22} (GPa)	ν_{12}	G_{12} (GPa)
Carbon-UD	1.59	117.8	13.4	0.25	3.9
Glass-(0/90)	1.75	15.1	19.3	0.03	4.2
Glass-Basket	1.66	15.3	12.8	0.13	3.0
Glass-Mat	1.37	6.8	5.0	0.30	2.5
Epoxy resin	1.20	3.3	3.3	0.30	N/A
Stainless steel	7.90	193.0	193.0	0.25	77.0

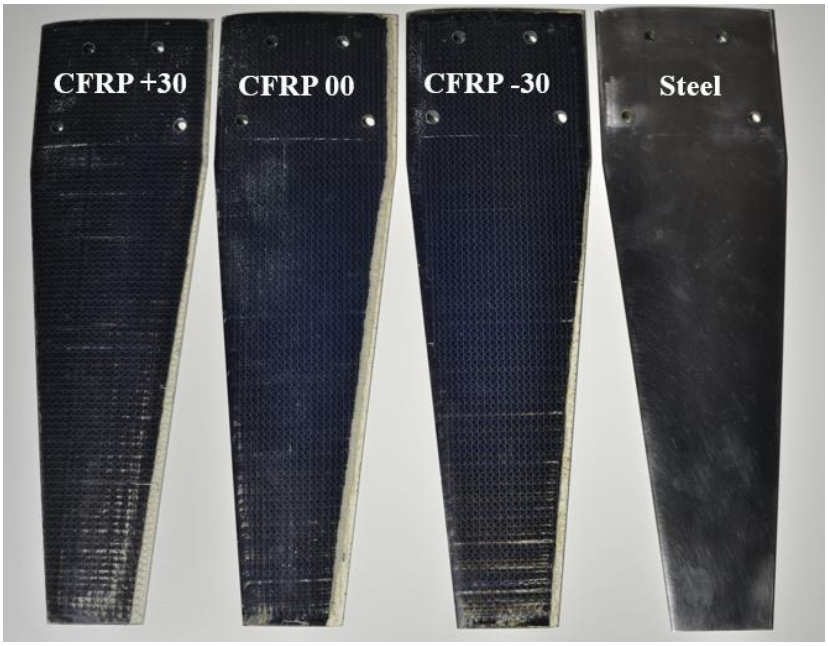

Figure 7.2: The three type II composite hydrofoils and the type II stainless steel hydrofoil used in experiments.

7.1.2 Bend and Twist Deflection Measurements

Similarly to the previous chapter, we use the high-speed images (as presented earlier in Section 3.5) to measure the tip bending and twist deformation for the composite hydrofoils.

Figure 7.3 presents sample tip deflections for one of the cases, i.e. $\alpha = 5^\circ$, Re = 1.0×10^6, for the CFRP +30 and CFRP -30 hydrofoils. The red open dot and red dashed lines correspond to the undeformed shape; the green filled dot and green solid lines correspond to

the deformed shape under the hydrodynamic load. As mentioned earlier, the tip deflection is considered positive in direction of the lift force, and the twist is considered positive nose-up, which leads to an increase in the effective angle of attack. As shown in Figure 7.3, both hydrofoils experienced spanwise bending deformation towards the suction side. While the CFRP +30 hydrofoil experience a decrease in effective angle of attack due to the negative or nose-down twist, the CFRP -30 hydrofoil experience an increase in effective angle of attack due to the positive or nose-up twist. The disparity in the twisting deformation is purely due to the differences in material bend-twist coupling caused by the orientation of the structural CFRP layers, which in turn results in differences in the hydrodynamic load coefficients, stall angle, and static divergence speed limit, as will be shown in Section 7.4.

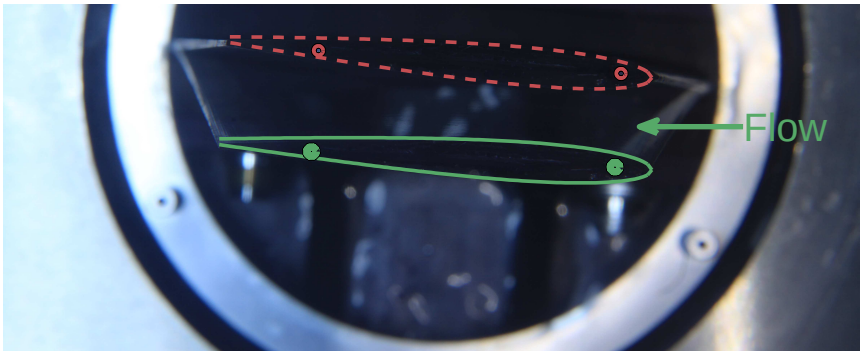

(a) CFRP +30 hydrofoil. $\delta_{tip} = 13.5$ mm, $\theta_{tip} = -1.04°$.

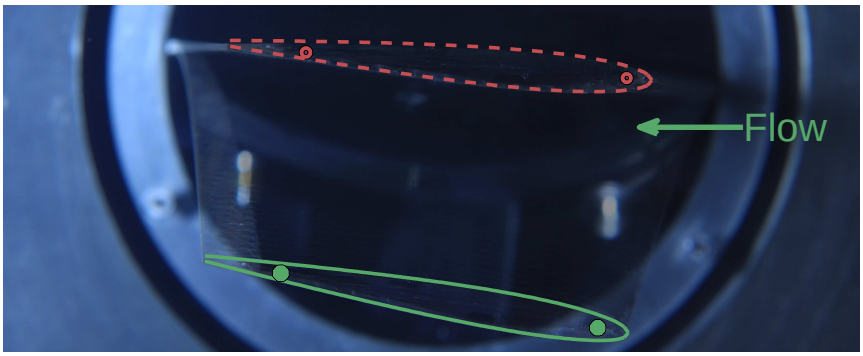

(b) CFRP -30 hydrofoil. $\delta_{tip} = 32.8$ mm, $\theta_{tip} = 5.1°$.

Figure 7.3: The images are taken looking up from below the free tip of the hydrofoil towards the cantilevered root. The red open dots are the targets placed near the leading and trailing edges of the tip faces (as outline by the red dashed line) during the unloaded or undeformed configuration. The green filled dots are the target position on the loaded or deformed geometry (as outlined by the green solid line). Both hydrofoils experienced spanwise bending deformation, with negligible chordwise deformation. While the CFRP +30 hydrofoil experienced negative twist (leading edge deformation less than the trailing edge), the CFRP -30 hydrofoil experienced positive twist, resulting in differences in effective angle of attack and hydrodynamic load coefficients for the two hydrofoils at the same flow conditions of $\alpha = 5°$ and $\mathrm{Re} = 1.0 \times 10^6$.

7.2 Modal Characteristics

The experimental modal frequencies and shapes presented in this chapter are obtained by DSTG, using the AMC cavitation tunnel. The detailed experimental procedure is explained in Young et al. [146] and are briefed here for the sake of completeness. The experimental modal analysis was carried out using the step relaxation forcing method in air. In step relaxation forcing method, the tip of the hydrofoil is loaded via a quick release

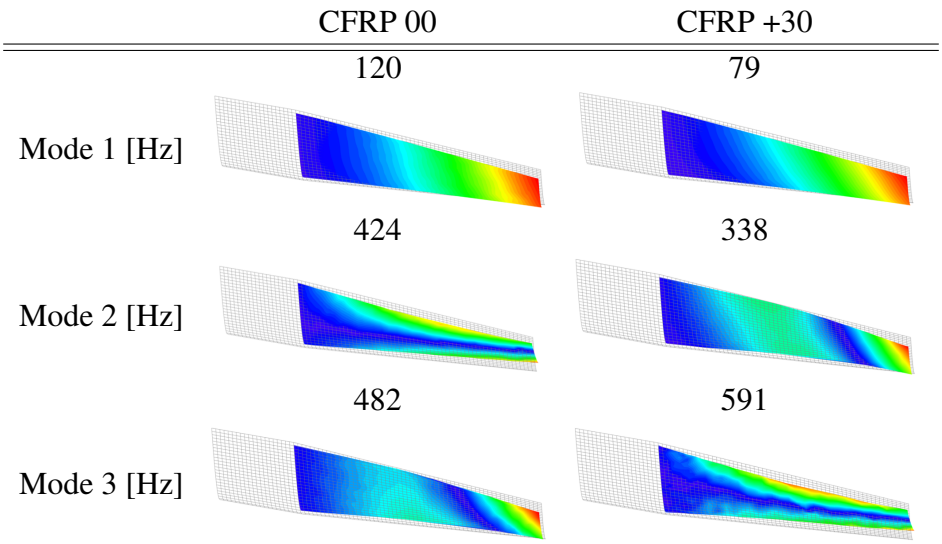

Figure 7.4: Measured mode shape estimates for the CFRP 00 hydrofoil and CFRP +30 hydrofoil in air. The experimental modal shapes are obtained by collaborators at DSTG.

hook in the drained cavitation tunnel at AMC. The cavitation tunnel was drained to get the modal frequencies in air. The displacement of the hydrofoils is measured using the Digital Image Correlation (DIC) method [31], the mode shapes and frequencies are computed using Frequency Domain Decomposition (FDD) technique [18]. Due to the time limitations, only CFRP 00 and CFRP +30 hydrofoils are tested using the DIC technique. The modal frequencies of the CFRP-30 are computed using the hammer excitation and FFT analysis of a lightweight accelerometer attached at the trailing edge at the tip of the hydrofoil. The measured mode shapes for the CFRP 00 and CFRP +30 hydrofoils and the measured frequencies for the first three modes of the three composite hydrofoils in air are presented in Figure 7.4 and Table 7.3, respectively.

To complement the experimental measurements, numerical predictions of the in-air modal response are obtained using the commercial FEA solver, Abaqus [2]. The FEA mesh used for the three composite hydrofoils is presented in Figure 7.5. The mesh has 12 elements through the thickness for a total of 307,944 linear hexahedral elements (C3D8) for the entire model. As explained earlier, the structural span of the cantilevered hydrofoil is 316 mm. A fixed boundary condition is implemented at the clamped root portion as

shown in Figure 7.5. The predicted mode shapes for the first three in-air modes for the three composite hydrofoils are shown in Figure 7.6, and comparisons of the predicted and measured natural frequencies are shown in Table 7.3. The maximum difference between the predicted and measured modal frequencies is 7.98%.

As shown in Table 7.2, the density of the stainless steel hydrofoil is almost five times that of composites, and the E_{11} for the dominant Carbon-UD layer in composites is more than half the value of the stainless steel. Thus, the first in-air modal frequency of the CFRP 00 hydrofoil is higher than the stainless steel hydrofoil, as shown in Table 7.3. As expected, the first modal frequency of the CFRP +30 and CFRP -30 hydrofoils are similar, and are lower than the CFRP 00 hydrofoil because of the lower bending stiffness caused by the orientation of the structural Carbon-UD layers away from the spanwise axis. The second modal frequencies are similar for the stainless steel and the CFRP 00 hydrofoil, with lower values for the CFRP +30 and CFRP -30 hydrofoils. Due to the higher twisting stiffness of the CFRP +30 and CFRP -30 hydrofoils, the third mode frequencies for CFRP +30 and CFRP -30 hydrofoil are higher than the CFRP 00 hydrofoil.

As mentioned in Young et al. [147], the first mode shape is often a good indicator of the deformation response. Figures 7.4 and 7.6 show that the CFRP 00 hydrofoil experiences mostly bending for the first mode, with a small degree of twist because of the fore-aft asymmetry of the modified NACA 0009 cross section. On the other hand, the CFRP +30 and CFRP -30 hydrofoils experienced combined bending and twisting for the first mode, which is evident by the deformation contours at the tip. As shown in Figure 7.6, the CFRP +30 and CFRP -30 hydrofoils exhibit opposite twist directions, which is a result of the opposite signs of the material bend-twist coupling caused by the $+30^\circ$ and -30° orientation of the structural CFRP layers. Similarly, while the second mode of the CFRP 00 hydrofoil is primarily twisting, the second mode of the CFRP +30 and CFRP -30 hydrofoils is primarily second bending mode with some twisting. Again, the CFRP +30 and CFRP -30 hydrofoils show opposite twist directions for the second mode. The third mode of the CFRP 00

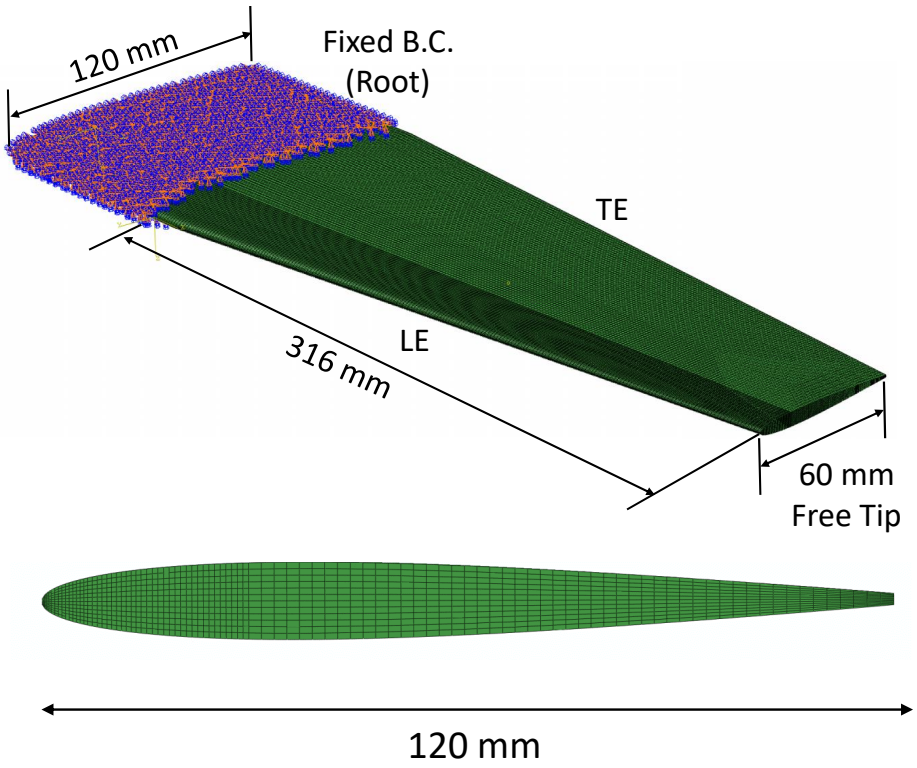

Figure 7.5: Perspective view (top) and through thickness view at the hydrofoil root (bottom) of the FEA mesh used for the eigenvalue analysis for all three composite hydrofoils.

hydrofoil is primarily second bending mode with some twisting, and the CFRP +30 and CFRP -30 hydrofoils is primarily twisting.

Note that the mode shapes and modal frequencies presented in Figures 7.4 and 7.6, and Table 7.3, correspond to in-air conditions. Previous literature show that due to the added mass effects, in-air frequencies are much higher than the in-water natural frequencies [26, 75, 108, 124, 146, 147]. Compared to the stainless steel hydrofoil, added mass effect is more apparent in composite hydrofoils due to the lower solid-to-fluid density ratio of the composite hydrofoils. Additionally, the mode shapes and their order in-water may be different from the mode shapes in-air. As noted in Phillips et al. [124], the in-water frequencies are only 40% and 90% of their respective in-air frequencies, depending on the mode and the fiber orientation of the composite hydrofoils. The experimental measurements agree with the analytical trends predicted by Motley et al. [108] and Kramer

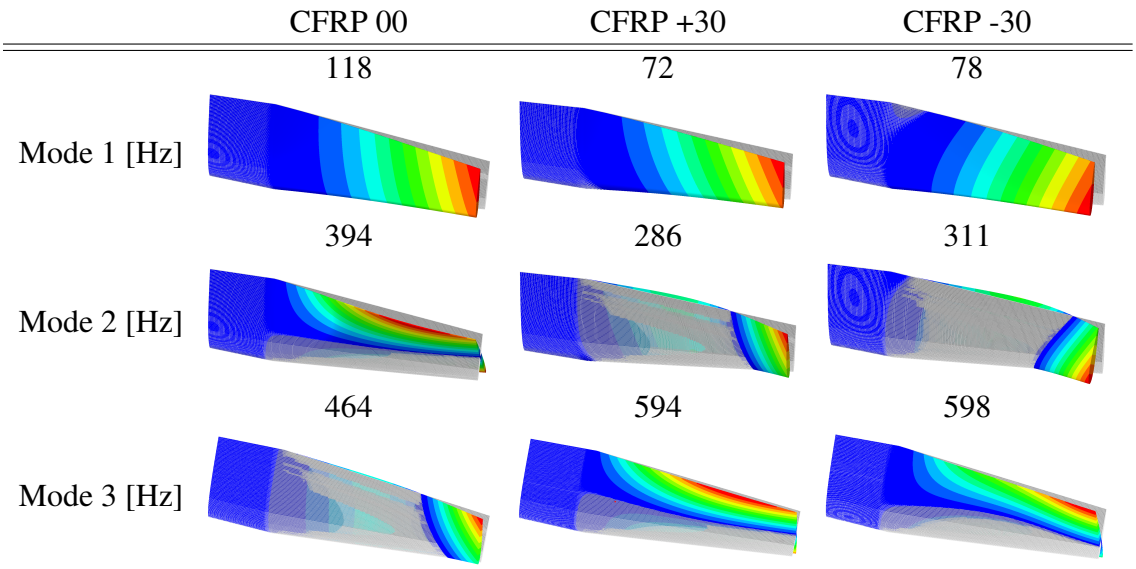

Figure 7.6: The first three predicted in-air mode shapes of the three composite hydrofoils obtained using the FEA. The gray dotted mesh represents the undeformed hydrofoil and the contours represent the deformed shape.

et al. [75]. Phillips et al. [124] also observed frequency coalescence for some modes for in-water condition. Thus, the designer must consider the modal response in-water to avoid modal coalescence [22, 75, 108, 124, 146, 147, 151].

Table 7.3: Comparison of the predicted (using Abaqus) and measured in-air natural frequencies of the three type II composite hydrofoils and the stainless steel type II NACA 0009 hydrofoils.

Mode	Stainless steel			CFRP 00			CFRP +30			CFRP -30		
	FEM	Exp.	Error	FEM	Exp.	Error	FEM	Exp.	Error	FEM	Exp.	Error
f_1 (Hz)	98	93	5.37%	118	120	1.66%	72	74	2.70%	78	79	1.26%
f_2 (Hz)	408	379	7.65%	394	428	7.94%	286	305	6.23%	311	338	7.98%
f_3 (Hz)	733	703	4.26%	464	482	3.73%	594	611	2.78%	598	591	1.18%

7.3 Steady-state 2-DOF FSI Model Formulation

To complement and help explain the experimental results, a simple FSI model is developed. The numerical model assumes that the hydrofoils undergo negligible chordwise deformation, which is supported by experimental observations. The discrete generalized equation of motion (EOM) for a 3-D rectangular, cantilevered hydrofoil can be written as,

$$M_s\ddot{X} + C_s\dot{X} + K_sX = F_{ex} + F_h \tag{7.1}$$

where M_s, C_s, and K_s are respectively the solid inertial, damping, and stiffness matrices. F_{ex} is the external excitation force vector, and F_h is the hydrodynamic fluid force vector, i.e., lift and moment. In the present work, only the steady-state solution with no external excitation is considered. Thus, $\ddot{X}$, $\dot{X}$, and F_{ex} are neglected.

By considering the spanwise bending and twisting deformations only, and integrating the mode shapes along the span, the steady-state EOM can be simplified to a two degree-of-freedom (DOF) system for the tip bending, δ_{tip}, and tip twisting, θ_{tip}, deformations at the elastic axis (EA). θ_{tip} is defined positive in the clockwise (nose-up) direction. The simplified 2-DOF can be written as,

$$\begin{bmatrix} K^s_{hh} & K^s_{h\theta} \\ K^s_{h\theta} & K^s_{\theta\theta} \end{bmatrix} \begin{bmatrix} \delta_{\text{tip}} \\ \theta_{\text{tip}} \end{bmatrix} = \begin{bmatrix} L \\ M \end{bmatrix} \tag{7.2}$$

where K^s_{hh}, $K^s_{\theta\theta}$, and $K^s_{h\theta}$ are the effective structural bending, twisting, and coupled bend-twist stiffness values, respectively. $\alpha_{BT} = K^s_{h\theta}/\sqrt{K^s_{hh}K^s_{\theta\theta}}$ is the solid bend-twist coupling ratio, and it has a value between -1 and 1 (as mentioned in [87]). α_{BT} is indicative of the effective anisotropy of the hydrofoil. $\alpha_{BT} = 0$, i.e. no material bend-twist coupling, for isotropic hydrofoils. As noted in Section 7.4, $\alpha_{BT} > 0$ will lead to nose-down twist, while $\alpha_{BT} < 0$ will lead to nose-up twist, when the hydrodynamic lift causes the hydrofoil to bend towards the suction side. L and M are the 3-D lift force and twisting moment at the EA,

respectively, and M is defined positive in the nose-up direction.

Figure 7.7 shows the equivalent 2-DOF model for the free tip section of a cantilevered hydrofoil with spanwise bending and twisting degrees of freedom. L is the resultant hydrodynamic lift acting on the hydrofoil at the Center of Pressure (CP), which is at distance $ec = 2eb$ from the EA. $b = c/2$ is the mean semi-chord.

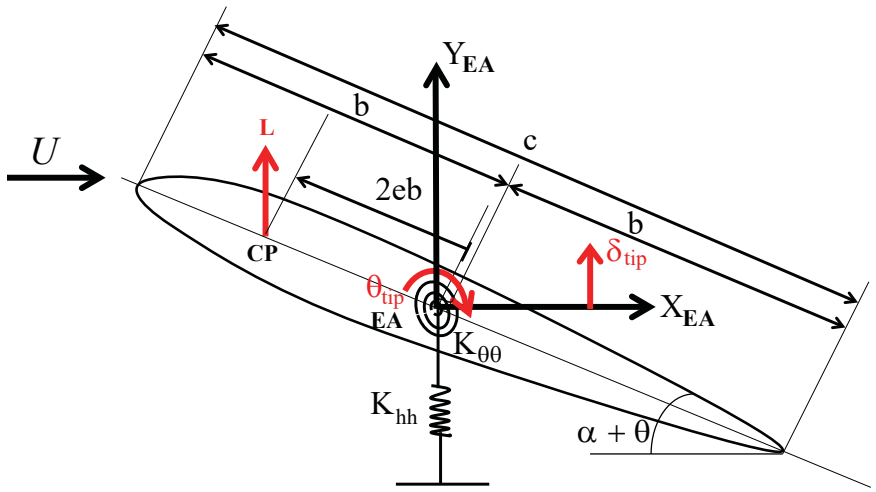

Figure 7.7: An equivalent 2-DOF mechanical model representing the free tip section of a cantilevered hydrofoil with spanwise bending and twisting degrees of freedom. The figure is edited from original figure presented in [6]. Note that the elastic axis (EA) and mid chord is at $0.45c$ and $0.5c$, respectively, from the hydrofoil leading edge, where c is the mean chord.

To compute the tip bending and twisting deformation, Eq. (7.2) is solved for δ_{tip} and θ_{tip}:

$$\delta_{\text{tip}} = \frac{L}{K^s_{hh}(1-\alpha^2_{BT})} + \frac{M\alpha^2_{BT}}{K^s_{h\theta}(\alpha^2_{BT}-1)} \tag{7.3}$$

$$\theta_{\text{tip}} = \frac{L\alpha^2_{BT}}{K^s_{h\theta}(\alpha^2_{BT}-1)} + \frac{M}{K^s_{\theta\theta}(1-\alpha^2_{BT})} \tag{7.4}$$

For $\alpha_{BT} = 0$, Eqs. (7.3) and (7.4) reduce to $\delta_{\text{tip}} = L/K^s_{hh}$ and $\theta_{\text{tip}} = M/K^s_{\theta\theta}$.

It is very challenging to construct small-scale composite hydrofoils. There may be slight differences between the designed and as-built material layup and drop-off location, which may lead to differences in the material and sectional properties. Hence, the experimental data was used to determine the effective stiffness values, i.e., K^s_{hh}, $K^s_{\theta\theta}$, and $K^s_{h\theta}$ (or

α_{BT}). Since the total hydrodynamic loads (L and M) are known via force balance measurements, and δ_{tip} and θ_{tip} are known via the tip deflection measurements, K^s_{hh}, $K^s_{\theta\theta}$, and α_{BT} can be determined using the slope and the intercept of the load versus deformation equations, as evident via Eqs. (7.3) and (7.4). An example of tip twist deflection versus moment curve for the CFRP -30 hydrofoil, along with the corresponding slope and intercept, is presented in Figure 7.8. Similarly, using slope and intercept from the tip bending deflection versus lift curve, we can calculate the stiffnesses and the bend-twist coupling coefficient.

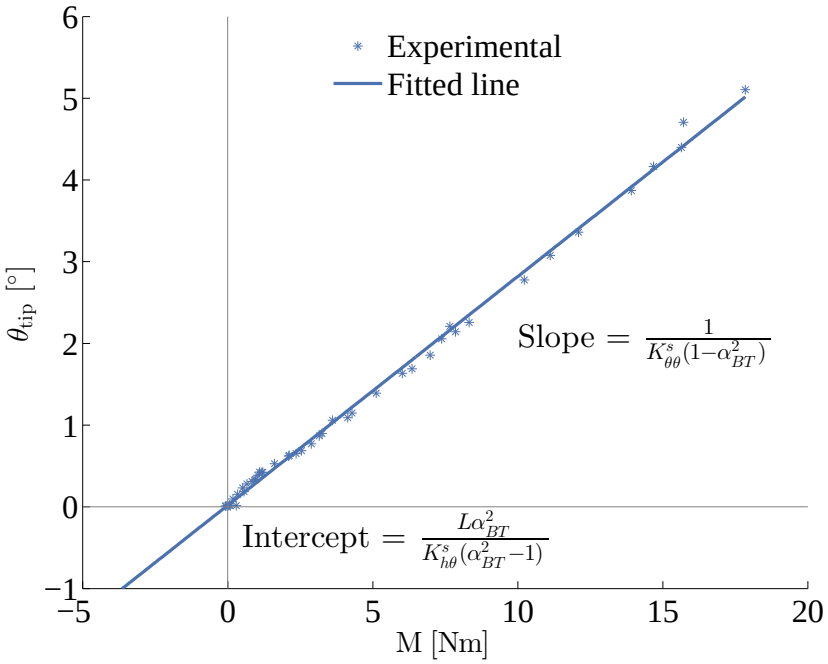

Figure 7.8: Measured tip twist deflection (in °) versus the measured moment (in Nm) for the CFRP -30 hydrofoil for all the measured Re values in the linear range.

The 3-D lift and moment on the right-hand-side of Eq. (7.2) can be obtained using classic relations between the steady-state lift and moment coefficients, C_L and C_M, and the effective angle of attack, $\alpha_{\text{eff}} = \frac{2}{\pi}\theta_{\text{tip}} + \alpha$:

$$C_L = \frac{L}{\rho_f U^2 b S} = a_o\left(\frac{2}{\pi}\theta_{\text{tip}} + \alpha\right) \tag{7.5}$$

$$C_M = \frac{M}{2\rho_f U^2 b^2 S} = a_o e\left(\frac{2}{\pi}\theta_{\text{tip}} + \alpha\right) \tag{7.6}$$

where α is the initial or undeformed geometric angle of attack, θ_{tip} is the tip twist deflection. $a_o = \partial C_L/\partial\alpha_{\text{eff}}$ is the slope of the lift curve, and $\alpha_{\text{eff}} = \alpha + 2\theta_{\text{tip}}/\pi$ is the effective angle of attack. The $2/\pi$ factor for the tip twist deflection is obtained by integrating the analytical twisting mode shape for a rectangular hydrofoil, $g(\bar{z}) = \sin(\pi\bar{z}/2)$, over the span, where $\bar{z} = z/S$ is the non-dimensional spanwise coordinate. Note that the taper of the hydrofoil was not considered in this simplified 2-DOF FSI model. e is the distance from EA to the CP non-dimensionalized by the mean chord c, as shown in Figure 7.7. Note that the NACA 0009 cross-section has zero camber, and hence the zero lift angle of attack is zero.

If there is no material bend-twist coupling, i.e., $\alpha_{BT} = 0$; substitution of Eq. (7.6) into Eq. (7.4), and Eq. (7.5) into Eq. (7.3), yields:

$$\theta_{\text{tip},0} = \frac{4ea_oqb^2S\alpha}{K^s_{\theta\theta} - \frac{8}{\pi}ea_oqb^2S} = \frac{q\alpha\frac{\pi}{2}}{q_{D,0} - q} \tag{7.7}$$

$$\delta^*_{\text{tip},0} = \frac{\delta_{\text{tip},0}}{b} = \frac{2a_oqS\alpha}{K^s_{hh}}\left[\frac{K^s_{\theta\theta}}{K^s_{\theta\theta} - \frac{8}{\pi}ea_oqb^2S}\right] = \frac{2a_oqS}{K^s_{hh}}\left(\frac{2}{\pi}\theta_{\text{tip}} + \alpha\right) \tag{7.8}$$

where $q = 0.5\rho_f U^2$ is the fluid dynamic pressure. $q_{D,0}$ is the fluid dynamic pressure at the static divergence speed $U_{D,0}$ without bend-twist coupling:

$$q_{D,0} = \frac{1}{2}\rho_f U^2_{D,0} = \frac{K^s_{\theta\theta}}{\frac{8}{\pi}ea_ob^2S} \tag{7.9}$$

The subscript "0" used in Eqs. (7.7) to (7.9) corresponds to the $\alpha_{BT} = 0$ case.

As evident in Eq. (7.7), at the critical static divergence speed, $U = U_{D,0}$, the fluid disturbing moment is equal to the solid restoring moment, i.e., the effective total torsional stiffness becomes zero, and the twist deformation goes to infinity.

If there is material bend-twist coupling, i.e. $\alpha_{BT} \neq 0$, the non-dimensional tip deforma-

tions can be written as follows:

$$\theta_{\text{tip}} = \frac{q\alpha\frac{\pi}{2}\left(1-\frac{\alpha_{BT}}{2eb}\sqrt{\frac{K^s_{\theta\theta}}{K^s_{hh}}}\right)}{q_{D,0}(1-\alpha^2_{BT})-q\left(1-\frac{\alpha_{BT}}{2eb}\sqrt{\frac{K^s_{\theta\theta}}{K^s_{hh}}}\right)} = \frac{q\alpha\frac{\pi}{2}}{q_D-q} \tag{7.10}$$

$$\delta^*_{\text{tip}} = \frac{\delta_{\text{tip}}}{b} = \frac{2a_o qS}{K^s_{hh}}\frac{\left(1-2eb\alpha_{BT}\sqrt{\frac{K^s_{hh}}{K^s_{\theta\theta}}}\right)}{1-\alpha^2_{BT}}\left(\frac{2}{\pi}\theta_{\text{tip}}+\alpha\right) \tag{7.11}$$

where q_D is the fluid dynamic pressure at the static divergence speed U_D with bend-twist coupling:

$$q_D = \frac{1}{2}\rho_f U_D^2 = q_{D,0}\frac{1-\alpha^2_{BT}}{\left(1-\frac{\alpha_{BT}}{2eb}\sqrt{\frac{K^s_{\theta\theta}}{K^s_{hh}}}\right)} \tag{7.12}$$

Eqs. (7.7) to (7.12) show the influence of the effective stiffness and material bend-twist coupling coefficient, α_{BT}, on the hydroelastic response and stability. Specifically, Eqs. (7.10) and (7.12) show that tip twist increases for $\alpha_{BT} < 0$ with increasing q (or Re), resulting in an increase in lift and moment, and reduction in static divergence speed.

7.4 Results

The results are presented in the following order: experimental measurements of the hydrodynamic forces and deformations, steady state 2-DOF FSI model predictions and comparison with measured values, study of the susceptibility to static divergence, and preliminary cavitation performance. The forces and moments presented in this chapter are defined in a body-fixed coordinate system. The origin of the coordinate system lies at the hydrofoil elastic axis at the root of the hydrofoil, where the foil intersects with the top tunnel boundary. The lift and drag forces, and pitch moments, are presented as dimensionless coefficients: lift coefficient $\left(C_L = L/(0.5\rho_f U^2 sc)\right)$, drag coefficient $\left(C_D = D/(0.5\rho_f U^2 sc)\right)$,

and moment coefficient $\left(C_M = M/(0.5\rho_f U^2 sc^2)\right)$, respectively. The moment coefficient, C_M, is defined about the EA and is positive in the nose-up direction.

7.4.1 Experimental Measurements

7.4.1.1 Hydrodynamic Load Coefficients

As explained in Chapter 3, the hydrodynamic forces and moments acting on the hydrofoil are measured using a six component force balance and the bending and twist deformations are measured using the technique presented in Section 3.5. As only the still images were captured, only steady-state deformations corresponding to the pre-stall region are presented in this chapter. As mentioned earlier, the maximum allowable lift force is restricted to 1kN for all hydrofoils, thus limiting the data for higher Re, i.e., higher flow speeds.

The mean lift, drag, and moment coefficients, as well as non-dimensional tip bending ($\delta^*_{\text{tip}} = \delta_{\text{tip}}/b$) for the stainless steel hydrofoil is presented in Figure 7.9. The stainless steel hydrofoil is presented as a rigid reference in this chapter. The rigid behavior of the stainless steel hydrofoil is confirmed by the higher natural frequencies (presented in Table 7.3), and the maximum measured non-dimensional tip bending deflection (shown in the bottom most plot of Figure 7.9) is 0.1. Additionally, the tip twist for the stainless steel hydrofoil was much lower than the measurement uncertainty of 0.45°. As expected of rigid hydrofoils in the turbulent flow, the stainless steel hydrofoil experiences delayed stall with increasing Re. The drag coefficient decrease with increasing Re due to the reduction in friction-induced (viscous) drag. When comparing with the composite hydrofoil results, only the stainless steel hydrofoil results at Re = 0.6×10^6 are presented to keep the plots clean.

Similarly to Figure 7.9, the Figures 7.10 to 7.12 presents the mean lift, drag, moment coefficients, and non-dimensional tip bending (δ_{tip}/b) and twist (θ_{tip}) of the three composite hydrofoils (i.e., CFRP 00, CFRP +30, and CFRP -30) as a function of the angle of attack (α) over a range of Reynolds numbers. As explained earlier, all the three composite hydro-

foils have the same unloaded geometry, thus, the only difference being the orientation of structural CFRP layers, causing the composite hydrofoils to have different material-based bend-twist coupling.

The results for the CFRP 00 hydrofoil, i.e., the hydrofoil with zero bend-twist coupling, is presented in Figure 7.10. As expected, the CFRP 00 results are very similar to those for the stainless steel hydrofoil. The hydrodynamic load results in the hydrofoil bending towards the suction side, as shown in the fourth plot in Figure 7.10. A slight increase in the slope of the lift curve with increasing Re can be observed for the CFRP 00 hydrofoil. The slight increase in the slope is due to the twist in the nose-up direction (as shown in the bottom-most plot of Figure 7.10), resulting in an increase in effective angle of attack. Note that the positive twist is due to the hydrodynamic bend-twist coupling (and not the material bend-twist coupling), as the center of pressure (CP) is upstream of the elastic axis (EA). As seen from the Figure 7.10, the flow-induced twist increases with increasing load, and hence higher C_L for higher Re. The higher C_L results in higher lift-induced drag, which offsets the reduction in friction drag due to increasing Re. Note that the C_D for the CFRP 00 hydrofoil is even less Re dependent than the stainless steel hydrofoil. The CFRP 00 hydrofoil is the stiffest of the three composite hydrofoils, as shown in the natural frequencies presented in Table 7.3, resulting in maximum normalized tip deflection of $\delta_{\text{tip}}/b \approx 0.3$, and the maximum twist of $\theta_{\text{tip}} \approx 1^\circ$.

The CFRP +30 with positive bend-twist coupling results in a reduction in lift and increase in stall angle with increasing Re, as shown in Figure 7.11. The reduction in lift and delayed stall is due to the negative or nose-down twist, resulting in a reduction in effective angle of attack. The twist results indicate that the negative twist caused by the material bend-twist coupling ($\alpha_{BT} > 0$) is much more significant than the positive twist from the hydrodynamic bend-twist coupling. Note that the tip bending deformation and the negative twist increases with increasing Re. The results show that the maximum normalized tip bending deflection is $\delta_{\text{tip}}/b \approx 0.65$ and the maximum negative twist is $\theta_{\text{tip}} \approx -3^\circ$. The lower

C_L also results in lower lift-induced drag, which complements the lower friction-induced drag with higher Re, resulting in a significant reduction in C_D with higher Re for the CFRP +30 hydrofoil.

As opposed to CFRP +30 hydrofoil, CFRP -30 hydrofoil has $\alpha_{BT} < 0$, which results in nose-up or positive twist. Thus, for CFRP -30 hydrofoil, both the material and hydrodynamic bend-twist coupling lead to positive twist and hence, the higher effective angle of attack. The higher effective angle of attack results in an increase in C_L and C_M, and decrease in the stall angle, with higher Re, as shown in Figure 7.12. Note that the C_D also increases with increasing Re, as the increase in lift-induced drag is higher than the reduction in friction-induced drag. The results show that the CFRP -30 hydrofoil exhibit the most significant dependence on Re, along with the highest deformation, i.e., the maximum $\delta_{\text{tip}}/b \approx 0.7$ and the maximum $\theta \approx 5^\circ$.

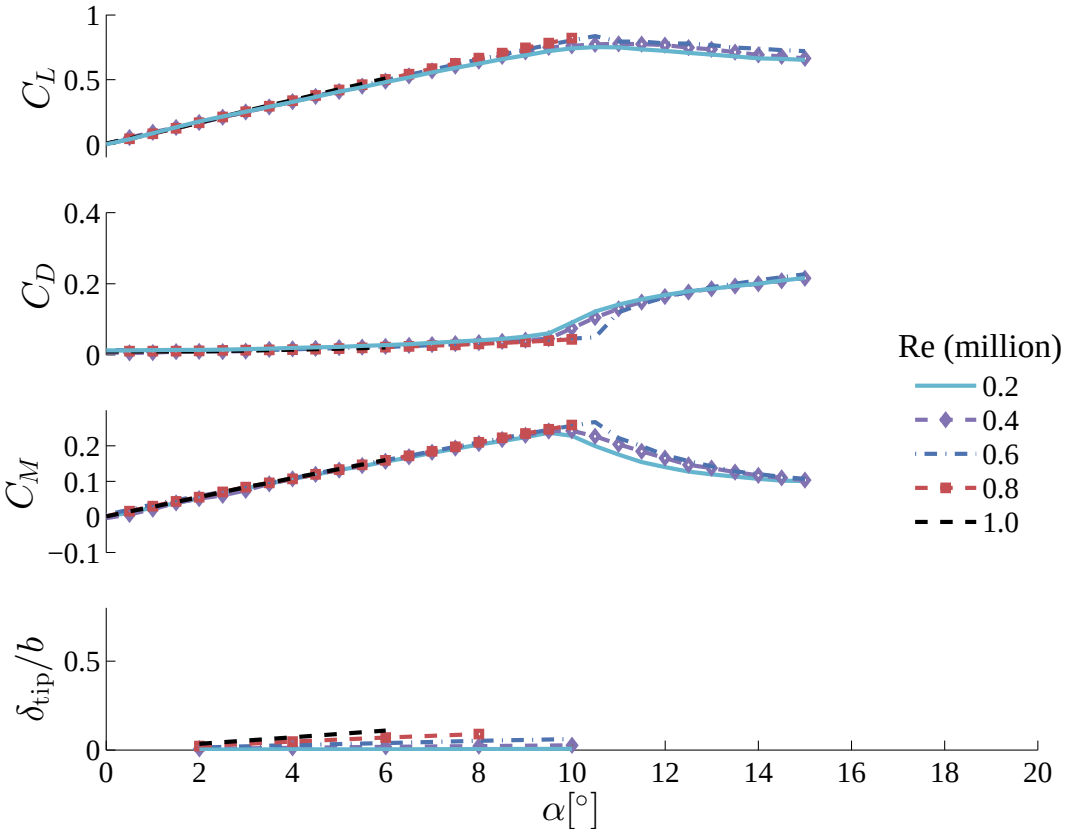

Figure 7.9: Experimental measurements of the mean lift (C_L), drag (C_D), and pitch moment (C_M) coefficients with angle of incidence for the type II stainless steel hydrofoil, for several Re values. Note that there is practically no Re dependence on the lift and moment coefficients until near stall, but the drag coefficient reduces with higher Re due to reduction in friction-induced drag.

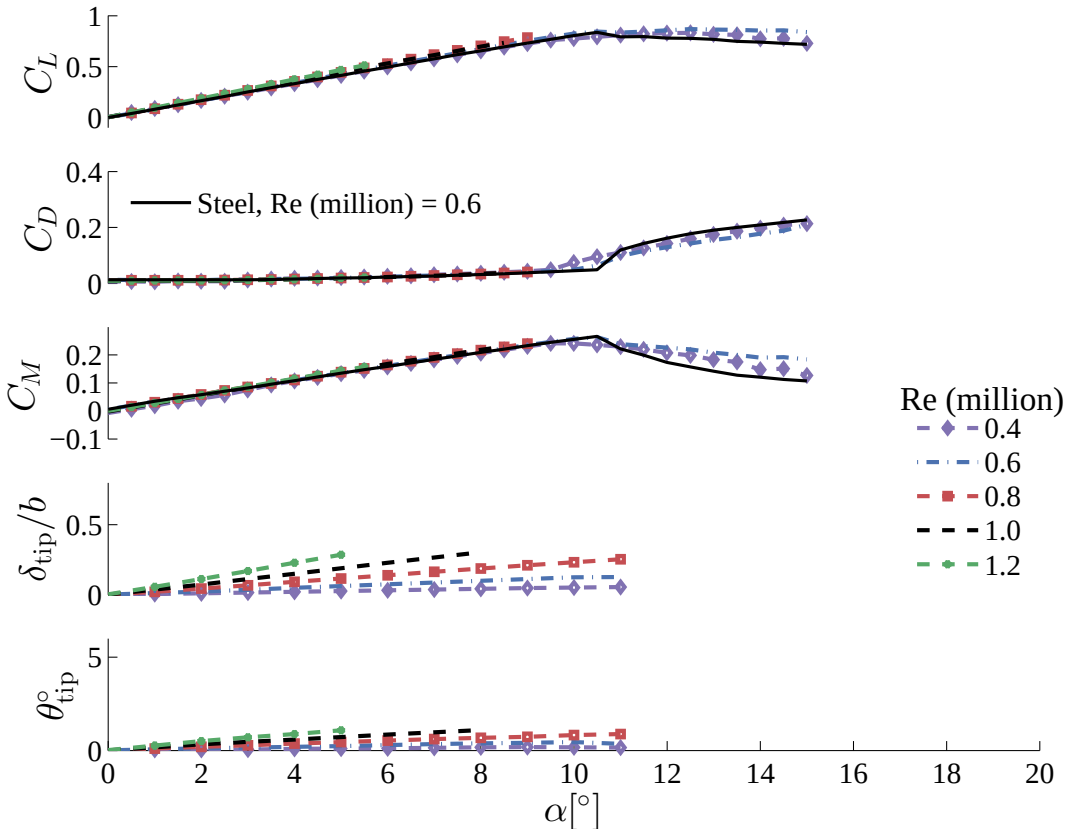

Figure 7.10: Top to bottom: Experimental measurements of the mean lift (C_L), drag (C_D), pitch moment (C_M), non-dimensional tip bending deflection, and twisting deformations with angle of incidence for the type II CFRP 00 hydrofoil, for several Re values. The CFRP 00 hydrofoil experiences a slight increase in lift and moment with increasing Re because of the small nose-up twist caused by the center of pressure acting upstream of the EA. There is no material induced bend-twist coupling because $\alpha_{BT} \approx 0$. The drag coefficient is practically independent of Re. The deformations are only reported for the flow conditions with lift force below 1 kN.

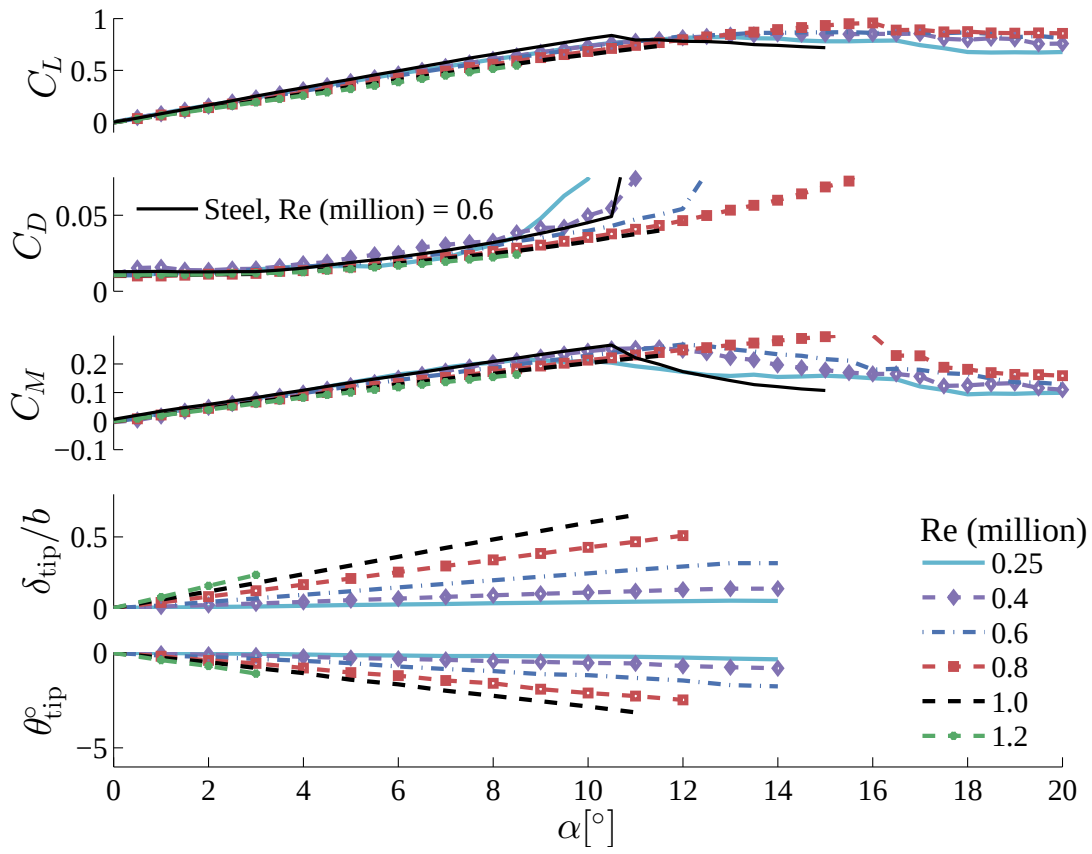

Figure 7.11: Type II CFRP +30 hydrofoil experiences a reduction in the mean lift and moment coefficients, and increase in the stall angle, with increasing Re because of the nose-down twist caused by the material-induced bend-twist coupling with $\alpha_{BT} > 0$. The drag coefficient reduces with higher Re because of reduction in both the lift-induced drag and the friction-induced drag.

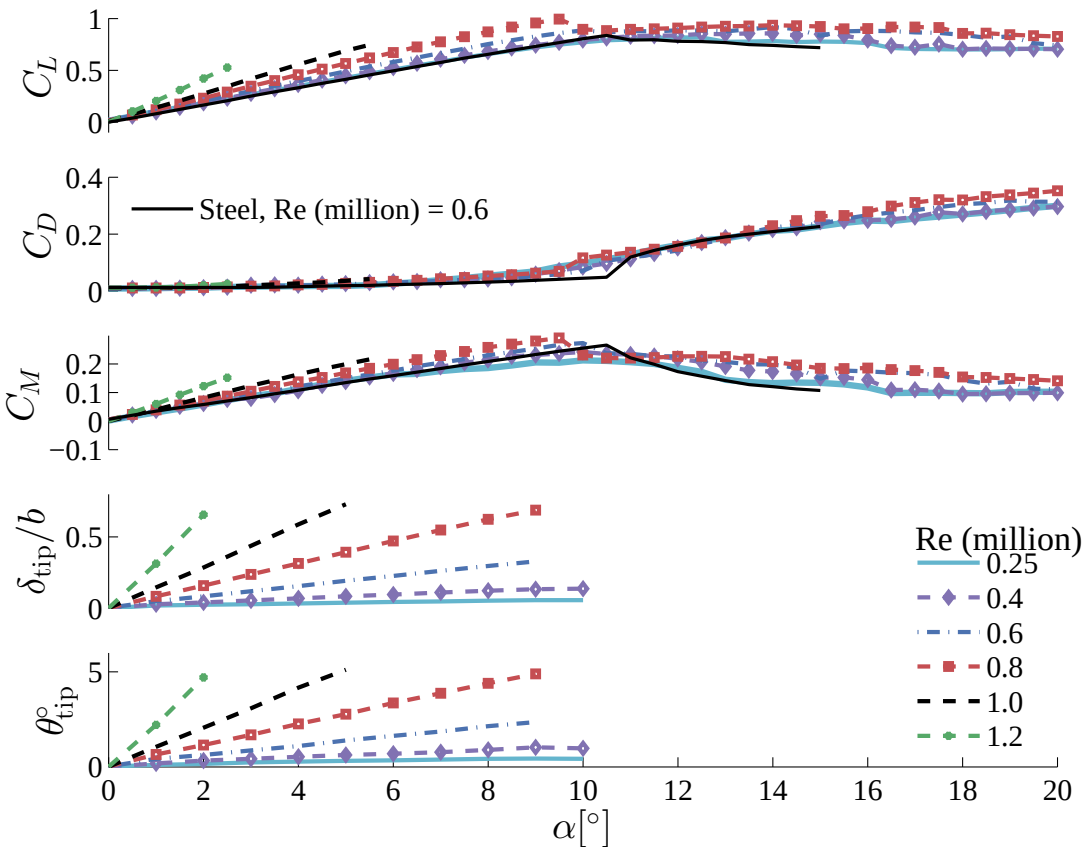

Figure 7.12: Type II CFRP -30 hydrofoil experiences an increase in the mean lift and moment coefficients, and reduction in the stall angle, with increasing Re because of the nose-up twist caused by the material-induced bend-twist coupling with $\alpha_{BT} < 0$. The drag coefficient increases with higher Re because the increase in lift-induced drag is greater than the reduction in friction-induced drag.

7.4.1.2 Efficiency and Lift Capacity

The designers for marine propulsors are more concerned with the effective lift-to-drag ratio, C_L/C_D, or efficiency, rather than the individual C_L and C_D values. Hence, Figures 7.13 and 7.14 presents the lift-to-drag ratio, C_L/C_D, against the geometric angle of attack and C_L for all four hydrofoils at Re = 0.6×10^6 and Re = 1.0×10^6, respectively.

The variation of C_L/C_D against the α (presented in Figure 7.13) show different trends for Re = 0.6×10^6 and Re = 1.0×10^6. The difference is due to influence of load-dependent bend-twist coupling of composite hydrofoils on the drag coefficient and stall angle with Re. The results show that while the stainless steel hydrofoil has highest overall efficiency

for Re = 0.6×10^6, the CFRP 00 and CFRP -30 hydrofoils exhibit higher efficiency than the stainless steel hydrofoil for $\alpha < 5^\circ$ and $\alpha < 2.5^\circ$, respectively, for Re = 1.0×10^6. Note that the CFRP -30 hydrofoil experiences earliest lift-to-drag ratio drop for both the Re, due to the accelerated stall.

In addition to variation of C_L/C_D with α, the variation of C_L/C_D with C_L is presented in Figure 7.14 for Re = 0.6×10^6 and Re = 1.0×10^6. Note the different trends as compared to the plots against α, as the angle of attack required to achieve a given C_L is different for each hydrofoil. Generally, for a given C_L, the stainless steel hydrofoil has the best overall efficiency, except for a brief range of C_L for both the Re when the composite hydrofoils are more efficient.

In Figure 7.15, we plot the measured lift force L (in N) against the speed U (in m/s) of the stainless steel hydrofoil at $\alpha = 2^\circ$ as a reference. Figure 7.15 also compares the difference in the required α for the CFRP +30 and CFRP -30 hydrofoils to achieve the same L profile. Due to the inherent bend-twist coupling, while the CFRP +30 hydrofoil requires higher α than the stainless steel hydrofoil, the CFRP -30 hydrofoil requires lower α than the stainless steel hydrofoil to produce the same L. The results are consistent with the differences in the required rotational speed (or advanced coefficient) to meet the same thrust capacity as a function of U for adaptive marine propellers, as explained in [106, 107, 147].

7.4.1.3 Stall Angle and Post-stall Behavior

The material bend-twist coupling has a significant impact on the stall and post stall behavior, in addition to the hydrodynamic loads and efficiency. The hydrofoil stall leads to significant flow separation on the suction side, reduction in mean lift and moment, increase in mean drag, and increase in load fluctuations due to unsteady vortex shedding. In Figures 7.16 to 7.18, we present the ratio of the measured standard deviation of the unsteady lift and moment coefficients, σ_{C_L} and σ_{C_M}, to their respective mean values, C_L and C_M, for the three composite hydrofoils. Figures 7.16 to 7.18 also present the non-dimensional

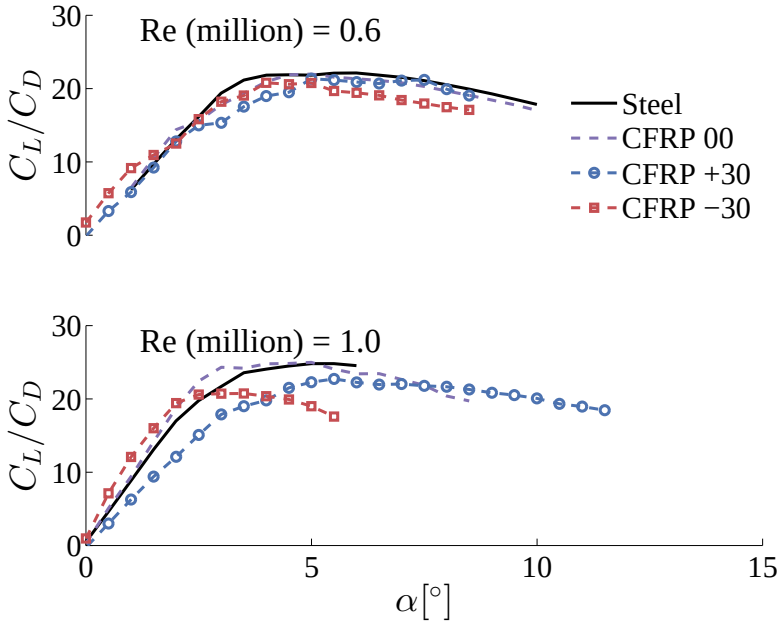

Figure 7.13: Comparison of difference in the mean lift-to-drag ratio as a function of geometric angle of attack α for the three composite hydrofoils and the stainless steel hydrofoil at Re = 0.6×10^6 and Re = 1.0×10^6.

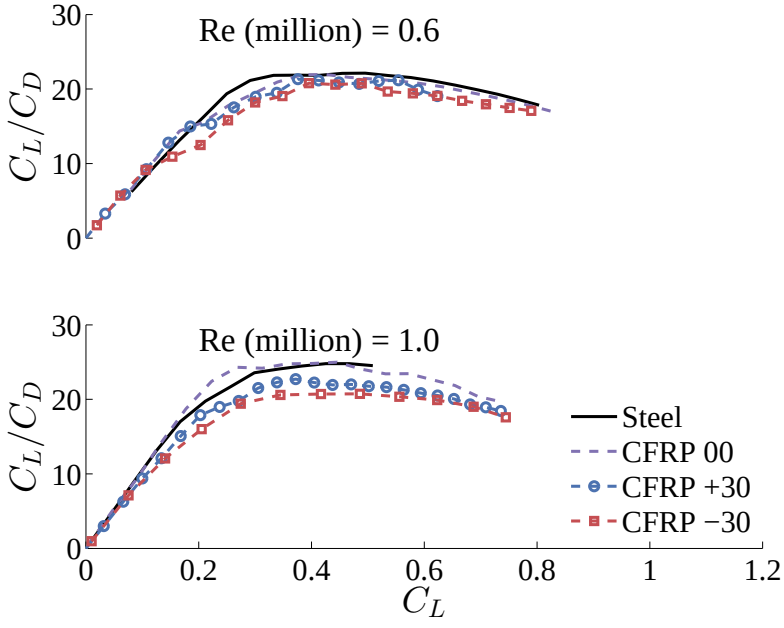

Figure 7.14: Comparison of difference in the mean lift-to-drag ratio as a function of lift coefficient C_L for the three composite hydrofoils and the stainless steel hydrofoil at Re = 0.6×10^6 and Re = 1.0×10^6.

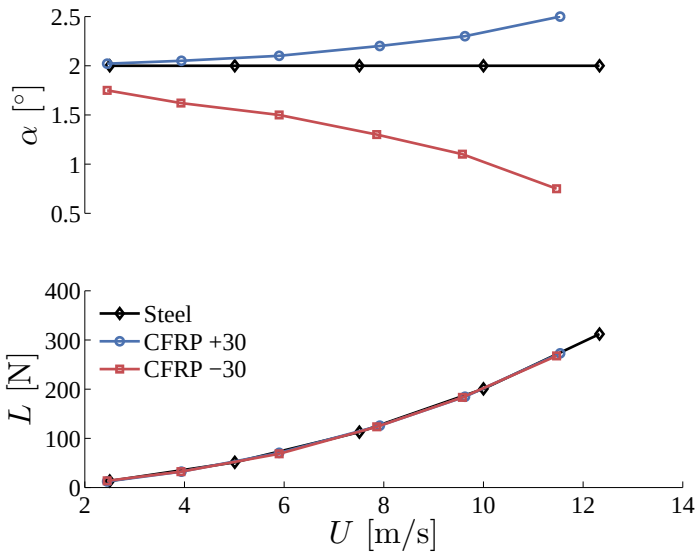

Figure 7.15: Comparison of difference in required incidence angle, α, for the CFRP +30 and CFRP -30 hydrofoils in order to achieve the same required dimensional lift L as a function of the speed U for the stainless steel hydrofoil with $\alpha = 2^\circ$. The results are based on the measured performance of the hydrofoils.

distance between the CP and the EA, i.e., $(X_{CP} - X_{EA})/c$ or e, as defined in Eq. (7.6). The results show that when stall develops, the standard deviation in the hydrodynamic load coefficients increases sharply due to unsteady load fluctuations, and the CP shifts towards the mid-chord (i.e., closer to EA). Note that the fluctuations in the moment coefficients are much more severe than the lift coefficients, since moment coefficient is dependent both on the movement of CP and the changes in C_L values. Hence, the critical stall angle in this section is defined as the angle of attack beyond which the mean moment coefficient begins to decrease. Table 7.4 presents the comparison of the moment stall angle of the four hydrofoils with different Re. Note that the maximum loading was limited to 1 kN for all the foils, and hence the stall angle was not reached for the higher Re cases.

The results show only a slight increase in the stall angle for the stainless steel hydrofoil, with increasing Re. As the composite hydrofoils have lower torsional stiffness compared to the stainless steel hydrofoil, a more distinguished increase in the stall angle can be observed

for the CFRP 00 hydrofoil compared to the stainless steel hydrofoil. As explained earlier, positive α_{BT} for CFRP +30 hydrofoil results in increasing negative twist, and negative α_{BT} for CFRP -30 hydrofoil results in increasing positive twist, with increasing α and Re. The difference in the load-dependent twist for the CFRP +30 and CFRP -30 hydrofoils, results in a dramatic increase and decrease in the moment stall angle for the CFRP +30 and CFRP -30 hydrofoils with increasing Re, respectively. For Re = 0.8×10^6, there is a difference of 6° in the stall angle for the CFRP +30 and the CFRP -30 hydrofoils. Figure 7.19 clearly demonstrate the difference in stall angle for the three composite hydrofoils at Re = 0.8×10^6.

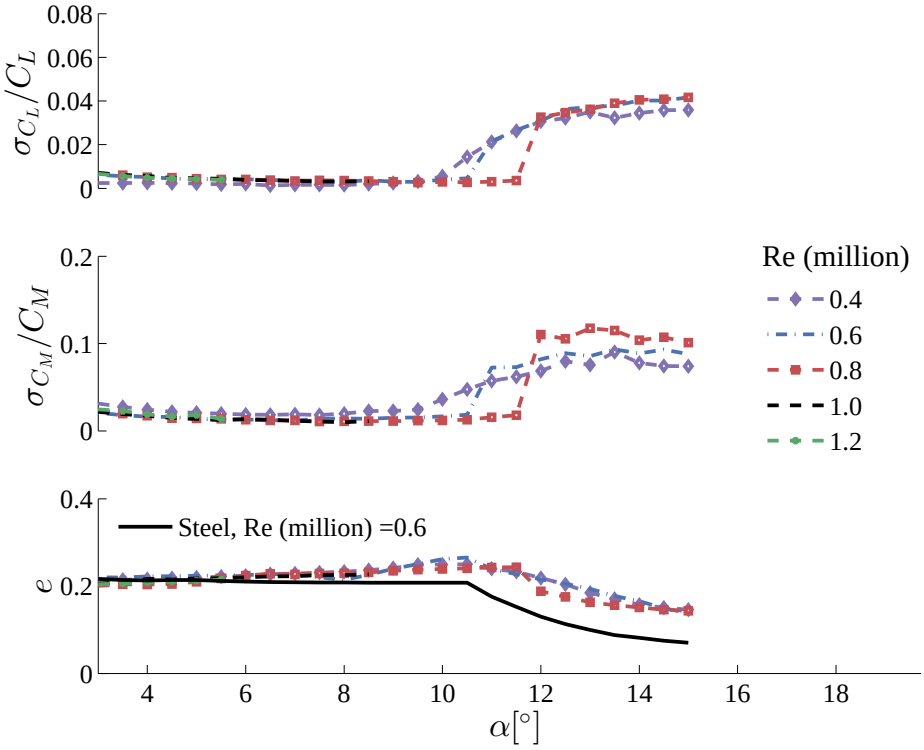

Figure 7.16: Comparison of standard deviation of the instantaneous lift and moment coefficients, σ_{C_L} and σ_{C_M}, normalized by their respective mean values, C_L and C_M, and the relative distance between the CP and the EA normalized by the mean chord, e, for the CFRP 00 hydrofoil.

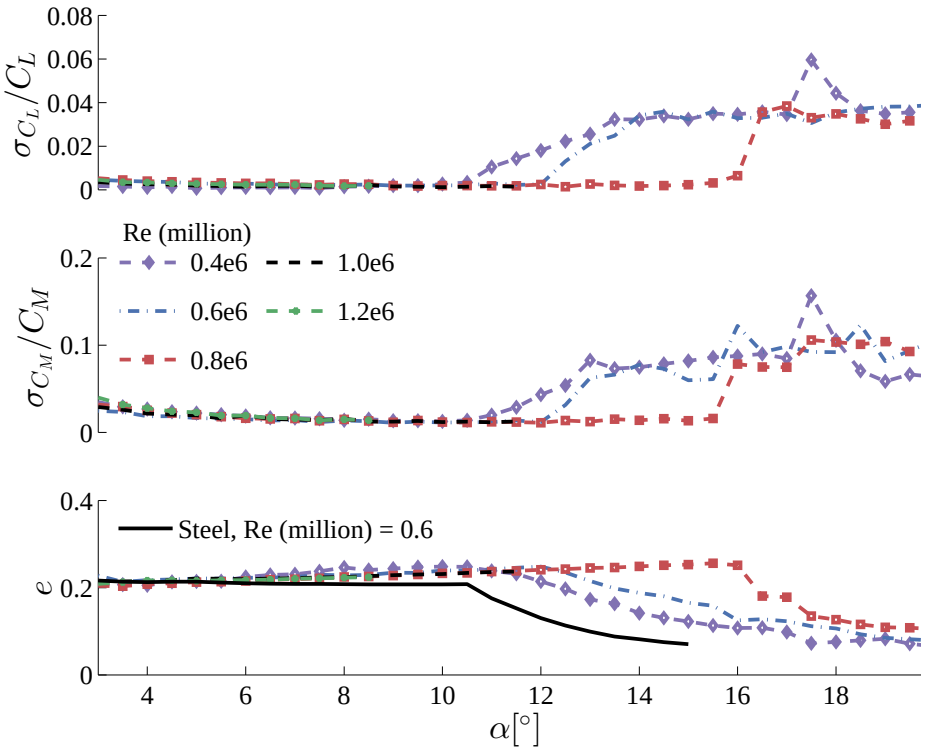

Figure 7.17: Comparison of standard deviation of the instantaneous lift and moment coefficients, σ_{C_L} and σ_{C_M}, normalized by their respective mean values, C_L and C_M, and the relative distance between the CP and the EA normalized by the mean chord, e, for the CFRP +30 hydrofoil.

Table 7.4: Comparison of moment stall angle, α_{stall}, for the stainless steel hydrofoil, and the three composite hydrofoils, for different Re. The results show that while the nose-down twist of the CFRP +30 hydrofoil leads to a significant increase in the stall angle with increasing Re, the nose-up twist of the CFRP -30 hydrofoil leads to a slight decrease in the stall angle with increasing Re.

Re	Stainless steel (α_{stall})	CFRP 00 (α_{stall})	CFRP +30 (α_{stall})	CFRP -30 (α_{stall})
0.4×10^6	10.0°	9.5°	10.5°	10.0°
0.6×10^6	10.5°	10.5°	12.0°	10.0°
0.8×10^6	N/A	11.5°	15.5°	9.5°

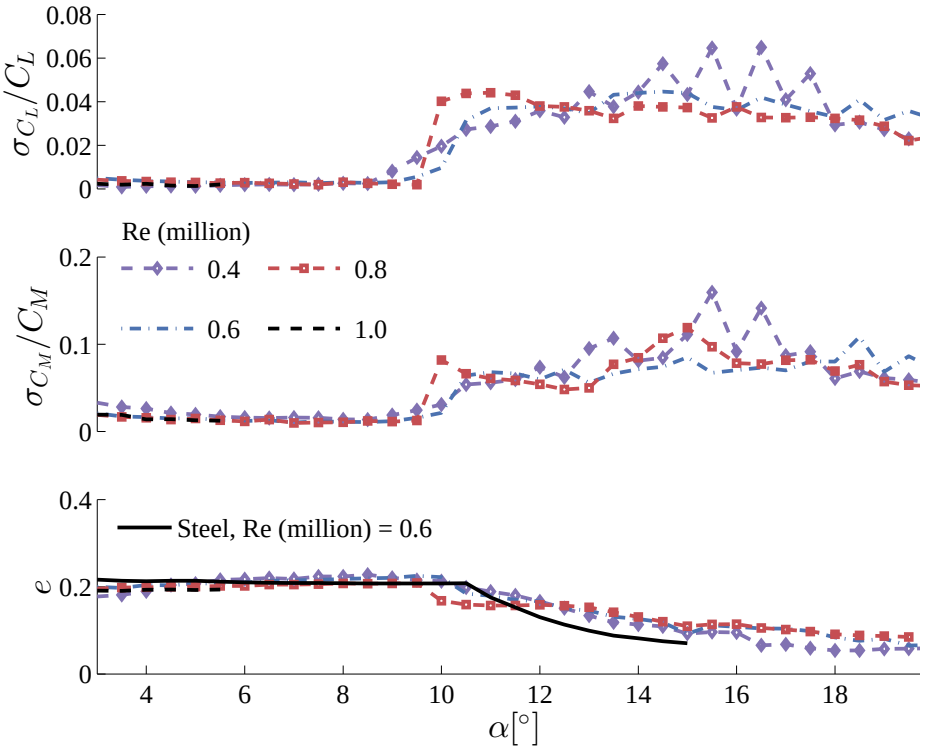

Figure 7.18: Comparison of standard deviation of the instantaneous lift and moment coefficients, σ_{C_L} and σ_{C_M}, normalized by their respective mean values, C_L and C_M, and e for the CFRP -30 hydrofoil.

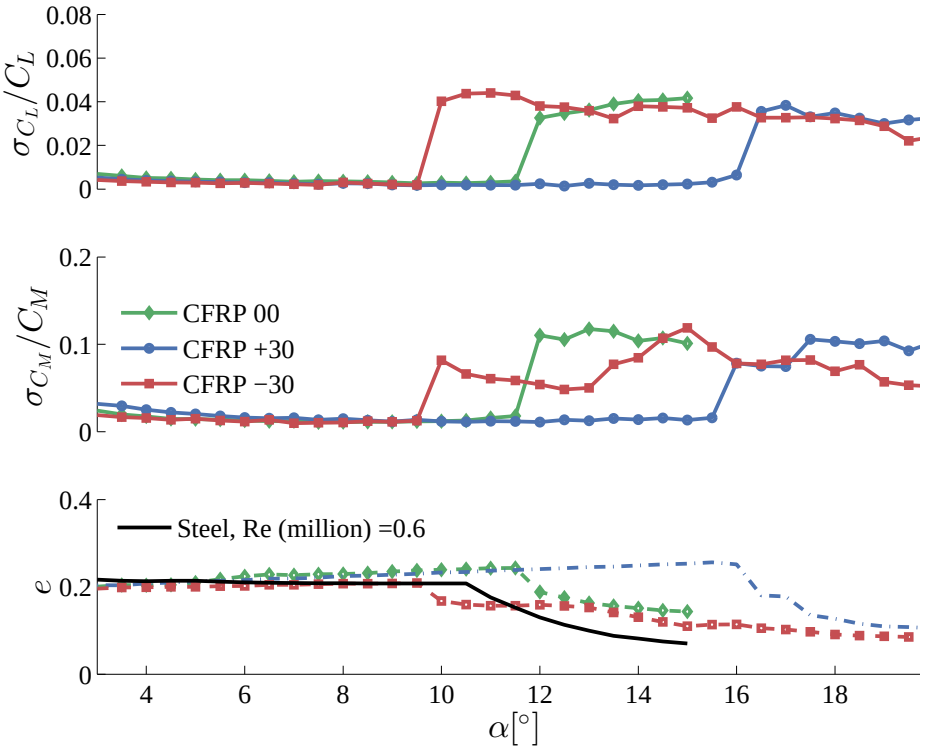

Figure 7.19: Comparison of standard deviation of the instantaneous lift and moment coefficients, σ_{C_L} and σ_{C_M}, normalized by their respective mean values, C_L and C_M, and e for all the three composite hydrofoils at Re = 0.8×10^6.

7.4.2 Steady-state 2-DOF FSI Model Predictions

The results presented in Section 7.4.1 emphasize the challenges with analysis and design of adaptive composite hydrofoils, due to the inherent material bend-twist coupling of composite materials. In this section, validation of the steady-state 2-DOF FSI model presented in Section 7.3 will be carried out. The numerical model can be used to reduce the number of experimental testing, and also facilitate rapid design and optimization.

As evident from Section 7.3, the 2-DOF model requires information of the hydrofoil bending, twisting, and bend-twist coupled stiffness values. In this work, the effective stiffness values are computed using the slope and intercept of the load deformation curves, i.e., measured lift versus tip bending deflection and moment versus the tip twist angle. The effective stiffness values for the four hydrofoils are summarized in Table 7.5. Since the 2-DOF model only considers the linear elastic behavior, only the linear portion of lift and moment are considered. Based on the material properties presented in Table 7.2, the stainless steel hydrofoil has the highest bending stiffness (K^s_{hh}), followed by CFRP 00, CFRP +30, and CFRP -30 hydrofoils. Note that the bending stiffness and the twisting stiffness ($K^s_{\theta\theta}$) of the CFRP +30 and CFRP -30 hydrofoils are similar, and are approximately equal to half of the value of the CFRP 00 hydrofoil. The twisting stiffness for the stainless steel hydrofoil could not be computed with the current setup, since the twist of the stainless steel hydrofoil was much less than 0.45°, which is the uncertainty in the twist measurement. As expected, the bend-twist coupling for the stainless steel and CFRP 00 hydrofoil is zero. Since the CFRP +30 hydrofoil resulted in the negative (nose-down) twist with the positive twisting moment, while the CFRP -30 hydrofoil resulted in the positive (nose-up) twist with the positive twisting moment, the bend-twist coupled stiffness ($K^s_{h\theta}$) of the CFRP +30 and CFRP -30 hydrofoils have opposite signs. Similarly, the bend-twist coupling coefficient, α_{BT}, of the CFRP +30 and CFRP -30 hydrofoils have opposite signs.

The accuracy of the effective stiffness are confirmed using the Figures 7.20 and 7.21. In Figures 7.20 and 7.21, lift force (N) is plotted against δ_{tip} (mm), and the pitching moment

(Nm) is plotted against θ_{tip} ($^{\text{o}}$), for the three composite hydrofoils. The symbols represent the experimental measurements at all the measured Re in the linear range, and the numerical results are computed using Eqs. (7.3) and (7.4), respectively, and the stiffness values are from the Table 7.5. The results clearly illustrate the accuracy of the stiffness values. The minor discrepancies in the result is due to the error in measuring the tip bending and twist deformations.

Table 7.5: Comparison of the effective stiffnesses and the corresponding bend-twist coupling coefficient for the four hydrofoils based on the measured load and deformation response. The twisting deformation of the stainless steel hydrofoil was too small to measure using the current image processing technique.

Hydrofoil	K^s_{hh} (N/m)	$K^s_{\theta\theta}$ (Nm)	$K^s_{h\theta}$ (N)	α_{BT}
Stainless steel	208.52 $\times 10^3$	N/A	0.00	0.00
CFRP 00	65.35 $\times 10^3$	1051.00	0.00	0.00
CFRP +30	32.19 $\times 10^3$	410.69	1398.78	0.38
CFRP -30	27.67 $\times 10^3$	411.73	-569.74	-0.17

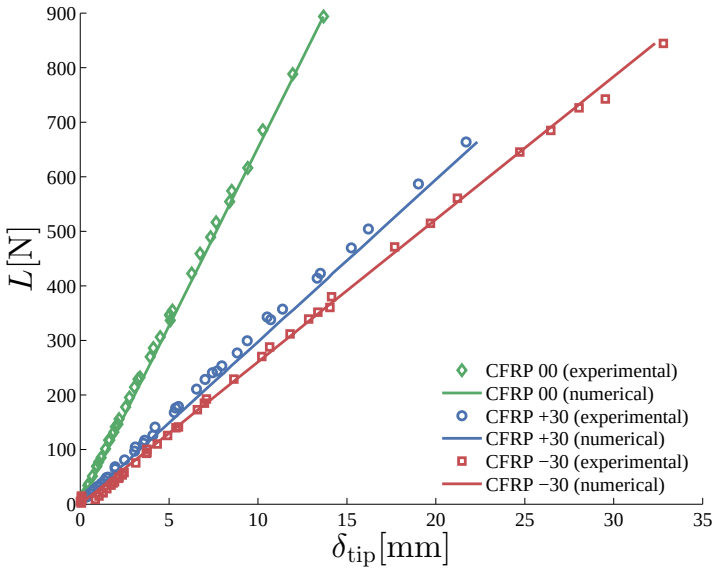

Figure 7.20: Experimental and numerically computed lift force against the tip bending deformation for the CFRP 00, CFRP +30, and CFRP -30 hydrofoils for all the measured Re values. The lines represent the numerical solution based on Eq. (7.3).

Other than the effective stiffness values, the 2-DOF model needs accurate information

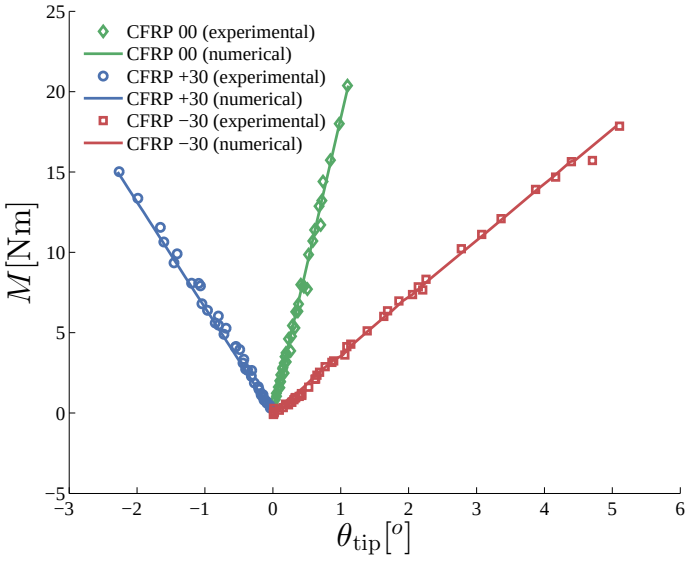

Figure 7.21: Experimental and numerically computed pitching moment against the tip twist deformation for the CFRP 00, CFRP +30, and CFRP -30 hydrofoils for all the measured Re values. The lines represent the numerical solution based on Eq. (7.4).

about the slope of the lift curve, $a_o = \partial C_L/\partial \alpha_{\text{eff}}$ and the lift eccentricity, e. The a_o value should be same for all the four hydrofoils, when plotted against the effective angle of attack, $\alpha_{\text{eff}} = \alpha + 2\theta_{\text{tip}}/\pi$. Similarly, the e value should also be same for all four hydrofoils in the linear range, as evident from Figures 7.16 to 7.18. The results presented in Figures 7.22 and 7.23 show that all four hydrofoils share the same lift slope of 1.53π and e of 0.25. Only the linear portion of the experimental measurement is presented due to the linear elastic assumption of 2-DOF model. Note that the lift slope is less than the theoretical 2-D value of 2π because of 3-D effects, including induced downwash, cross flow, and losses through the tip and root vortices.

Comparisons of the experimental measurements (which are the same as presented in Section 7.4.1) and the 2-DOF model predictions (using Eqs. (7.10) and (7.11)) of the load-dependent deformation response of the three composite hydrofoils are shown in Figures 7.24 to 7.26. The mean error in the tip bending deflection for CFRP 00, CFRP +30, and CFRP -30 hydrofoils is 0.01%. The mean error in the twist deflection for CFRP 00,

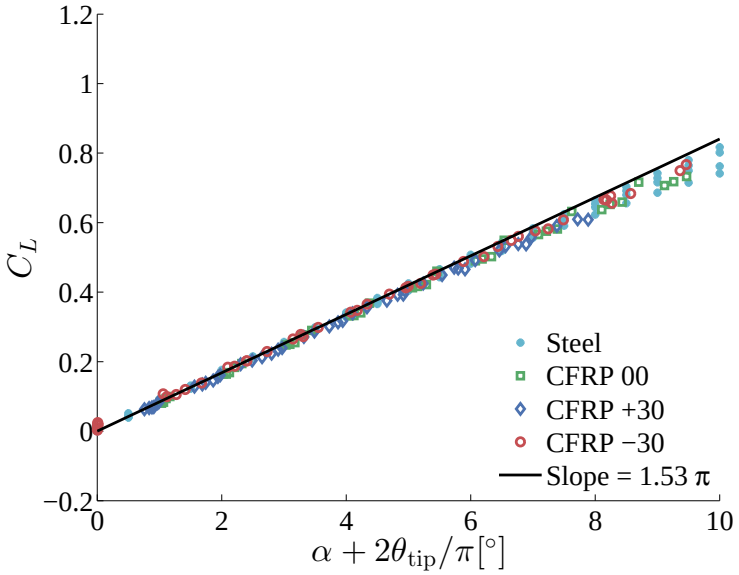

Figure 7.22: Measured mean lift coefficient (C_L) against the effective angle of attack ($\alpha + 2\theta_{\text{tip}}/\pi$) for the stainless steel, CFRP 00, CFRP +30, and CFRP -30 hydrofoils for all the measured Re values in the linear range. The black solid line represent the lift slope of $a_o = 1.53\pi$. Note that the measured data for all the four hydrofoils collapse on to one line, which validates the relation shown in Eq. (7.5).

CFRP +30, and CFRP -30 hydrofoils is 19.67%, 25.53%, and 23.19%, respectively. As mentioned earlier, the worst case uncertainty in measurements is calculated as 1.08% of the tip chord for the bending deflection and 0.45° for the twist deformation. Note that the predicted bending and twist deformations are generally within the worst case uncertainty of the measurements. While the mean error in the twist deflection is significant, the predicted values follow the same trend as experimental measurements and thus provides a good tool for the initial studies.

7.4.3 Static Divergence Analysis

The inherent material-induced bend-twist coupling of the composite hydrofoils also impacts the static divergence speed, as shown in Eq. (7.12). The static divergence occurs when the fluid disturbing moment exceeds the structural elastic restoring moment, resulting in an increase in twist deformation without bound, causing structural failure. Thus, the

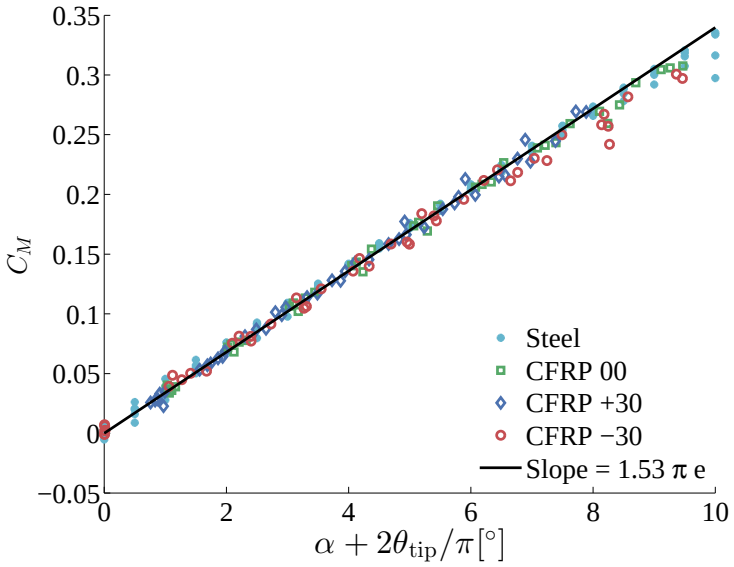

Figure 7.23: Measured mean moment coefficient (C_M) against the effective angle of attack ($\alpha + 2\theta_{\text{tip}}/\pi$) for the stainless steel, CFRP 00, CFRP +30, and CFRP -30 hydrofoils for all the measured Re values in the linear range. The black solid line represent the moment slope of $a_o e = 1.53\pi e$ with $e = 0.25$. Note that the measured data for all the four hydrofoils collapse on to one line, which validates the relation shown in Eq. (7.6).

hydrofoils experiencing increased twist with increasing load are susceptible to the static divergence. Of the three composite hydrofoils presented in this work, only the CFRP 00 and the CFRP -30 hydrofoils experiences increased twist with increasing load for $\alpha > 0^\circ$. Thus, results are only presented for CFRP 00 and CFRP -30 hydrofoil. The CFRP +30 hydrofoil is not susceptible to static divergence for cases with $\alpha > 0^\circ$, as the effective angle of attack decreases with increasing load due to the nose-down twist. However, this condition changes for $\alpha < 0^\circ$, i.e., at $\alpha < 0^\circ$, while CFRP +30 hydrofoil will be susceptible for static divergence, CFRP -30 will not be susceptible. Note that both positive and negative angles of attack are relevant for at sea operations of hydrofoils and rudders due to varying incidence angles in waves, and for propellers due to forward and reverse operations.

Table 7.6 summarizes the static divergence velocity, U_D, for the CFRP 00 and CFRP -30 hydrofoils, computed using Eqs. (7.9) and (7.12). The results show that the U_D for the CFRP -30 hydrofoil (i.e., $\alpha_{BT} < 0$) will be much lower than the CFRP 00 hydrofoil

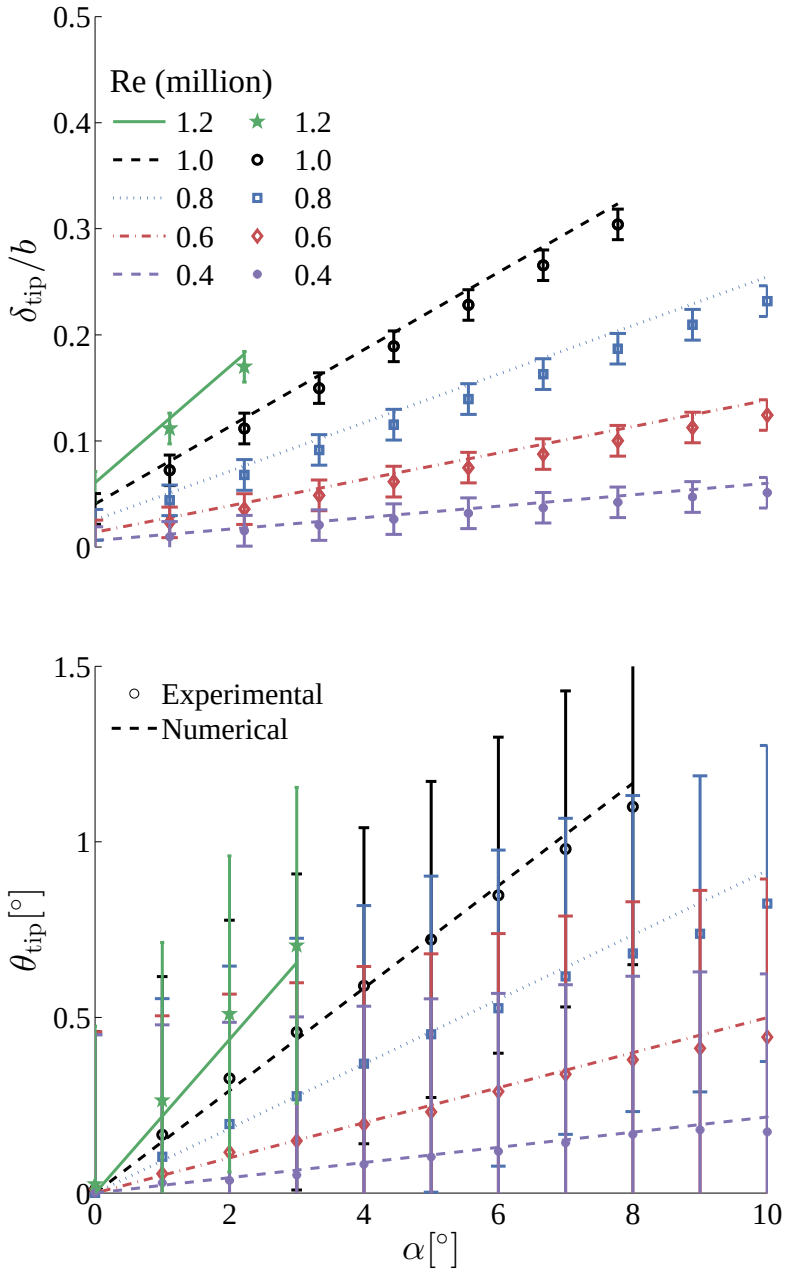

Figure 7.24: Experimental measurements (symbols) and the 2-DOF FSI model prediction (lines) of the CFRP 00 hydrofoil for a range of Re in the linear range. From top to bottom: a) δ_{tip}/b and b) θ_{tip}. The error bars represent the maximum measurement uncertainty of 0.65 mm in δ_{tip} and 0.45° in θ_{tip}.

($\alpha_{BT} = 0$). Table 7.6 also presents the critical inflow speed, $U_{critical}$, corresponding to the maximum allowable bending force of 1 kN for $C_L = 0.50$. As explained earlier, there was a 1 kN load limit to give a factor of safety of 2.5 against material failure, as delamination

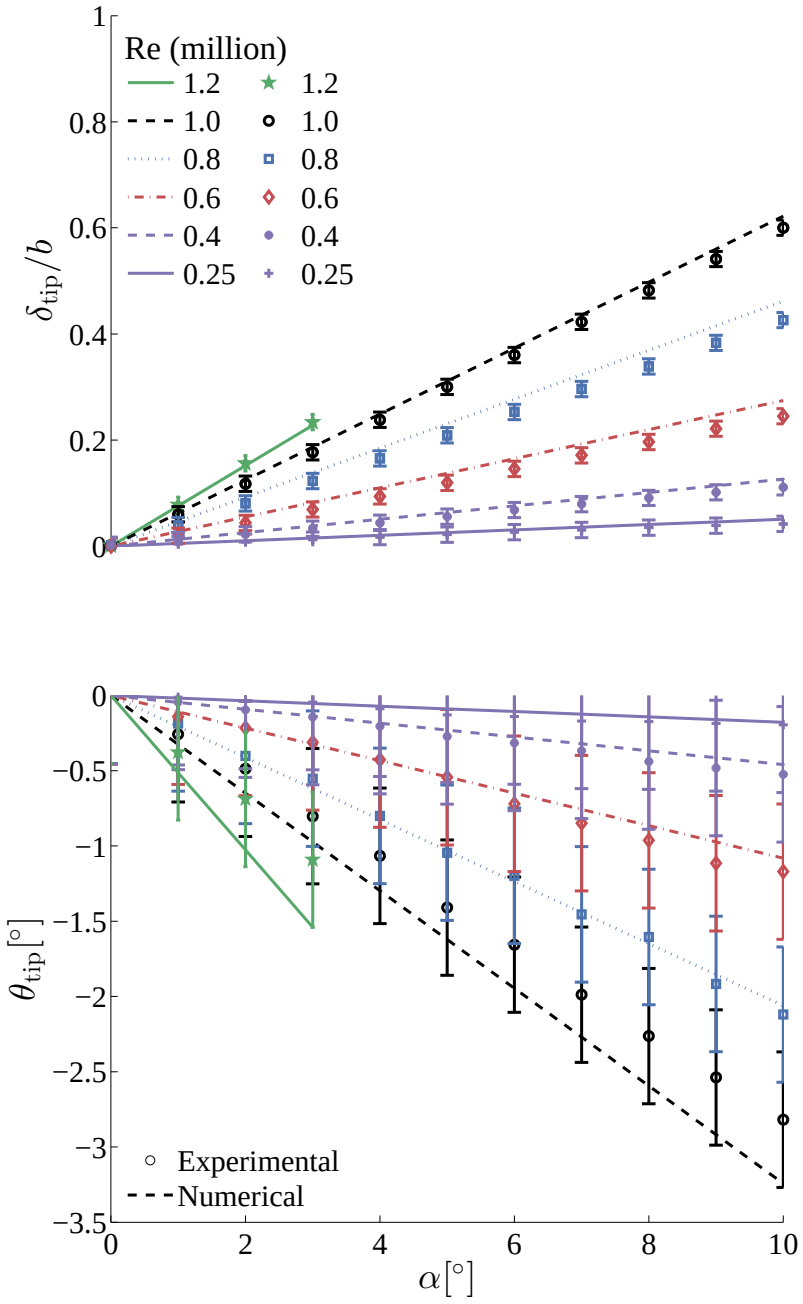

Figure 7.25: Experimental measurements (symbols) and the 2-DOF FSI model prediction (lines) of the CFRP +30 hydrofoil for a range of Re in the linear range. From top to bottom: a) δ_{tip}/b and b) θ_{tip}. The error bars represent the maximum measurement uncertainty of 0.65 mm in δ_{tip} and 0.45° in θ_{tip}.

near the root of the CFRP 00 hydrofoil was observed at a load of 2.49 kN. As expected, the velocity results show that both the CFRP 00 and CFRP -30 hydrofoils will reach the

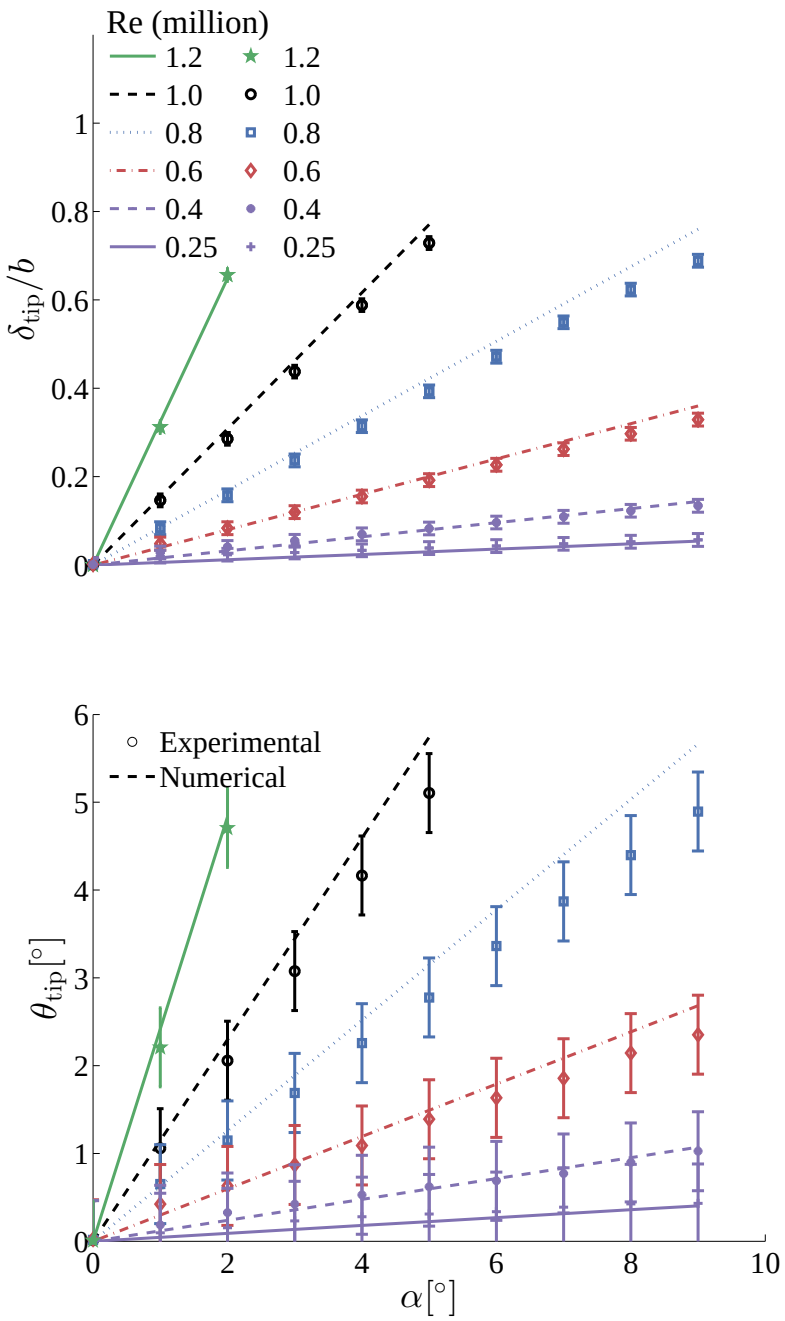

Figure 7.26: Experimental measurements (symbols) and the 2-DOF FSI model prediction (lines) of the CFRP -30 hydrofoil for a range of Re in the linear range. From top to bottom: a) δ_{tip}/b and b) θ_{tip}. The error bars represent the maximum measurement uncertainty of 0.65 mm in δ_{tip} and 0.45° in θ_{tip}.

allowable stress limit before the static divergence limit. The results are consistent with the static divergence studies reported in [39] for plastic hydrofoils, and in [86] for composite

marine propellers.

In Figure 7.27, we observed linear relationship between $\pi\alpha/2\theta_{tip}$ and $q_D/q = U_D^2/U^2$ (as shown in Eq. (7.10)). The symbols represent the experimental data for all Re and α in the linear range, and the line corresponds to the theoretical relationship given by Eq. (7.10). The slope and the intercept of the curve are both one; theoretical static divergence occurs when $U = U_D$, i.e., $\theta_{\text{tip}} \to \infty$ so $\pi\alpha/2\theta_{\text{tip}} = 0$. The discrepancy in the experimental data and the numerical line for the lower Re (or higher U_D^2/U^2) cases is due to the relatively large uncertainty in the measurement when the twist deformation is small.

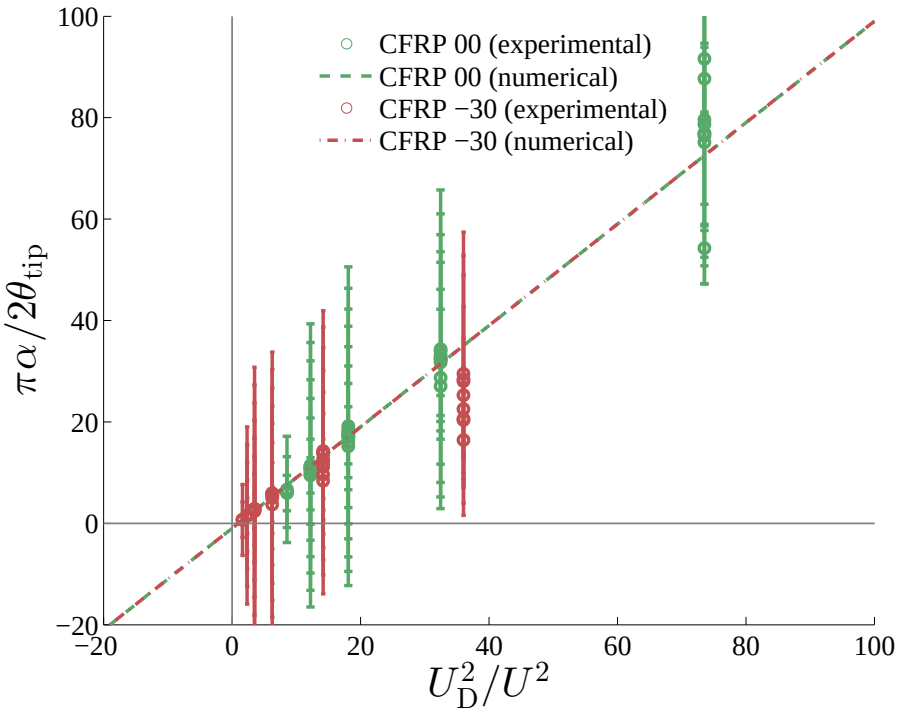

Figure 7.27: Measured versus predicted relationship between the relative twist deformation ($\pi\alpha/2\theta_{\text{tip}}$) and the square of the divergence speed to the inflow speed (U_D^2/U^2) for the CFRP 00 and CFRP -30 hydrofoils. Theoretical static divergence occurs when $U = U_D$, and $\theta_{\text{tip}} \to \infty$ so $\pi\alpha/2\theta_{\text{tip}} = 0$. The error bars represent the maximum measurement uncertainty of 0.45° in θ_{tip}, which is responsible for the greater scatter in the experimental data for the lower Re (or higher U_D^2/U^2) cases.

Table 7.6: Comparison of the static divergence velocity (U_D) computed using using Eqs. (7.9) and (7.12) for the CFRP 00 and CFRP -30 hydrofoils for cases with positive lift or $\alpha > 0$. Also shown are the critical inflow speed, U_{critical}, corresponding to the maximum allowable bending force of 1 kN assuming a maximum lift coefficient of 0.50.

Hydrofoil	U_{D} [m/s]	U_{critical} [m/s] ($C_L = 0.50$)
CFRP 00	33.62	12.18
CFRP -30	14.77	12.18

7.4.4 Cavitation Performance

In addition to modifying the hydrodynamic performance and deformation response, the material bend-twist coupling also impacts the cavity shedding frequency and structural response. Similar to previous results, the type II stainless steel, CFRP +30, and CFRP -30 hydrofoils are used for the investigation. To be consistent, the hydrofoils were tested at a fixed Re of 0.8 $\times 10^6$, a fixed incidence of 6^{o}, and a range of cavitation numbers from inception to supercavitation.

For the results presented in this section, high-speed photography was recorded using a LaVision HighSpeedStar8 camera with a Nikkor f/1.4 lens. The high-speed images were recorded at 3000 Hz and a total of 2048 images were recorded at each flow condition. A field of view encompassing all of the hydrofoil planform was obtained with a spatial resolution of 1024 $\times$ 512 pixels. Similarly to the fully wetted testing of composite hydrofoils, the cavitation testing of the composite hydrofoils was carried out at AMC.

7.4.4.1 Definitions and Numerical Model

As defined in Harwood et al. [54] and Young et al. [151], a fully wetted (FW) flow is a condition when there is no observed cavitation along the hydrofoil surface. While the partial cavitation has a maximum cavity length that does not extend to the hydrofoil trailing edge, supercavitation has a maximum cavity length that extends beyond the hydrofoil trailing edge.

Harwood et al. [54] also presented polynomial equations to approximate the variation

in the maximum cavity length ($L_{c\max}$), cavity shedding frequency (f_c), and slope of lift coefficient curve (a_o) for a rigid 2-D hydrofoil as a function of the effective cavitation number (ψ) based on [5, 6, 8, 16, 134]. The expressions are given as,

$$\frac{L_{c\max}}{c} = \frac{2.67\psi + 96.62}{\psi^3 - 7.1\psi^2 + 49.42\psi + 0.961} \tag{7.14}$$

$$S_c = \frac{f_c\, c}{U} = \kappa\sqrt{(1+\sigma)}\left[\frac{L_{c\max}}{c}\right]^{-1} \tag{7.15}$$

$$a_o = \frac{\frac{\pi}{2}\left(\frac{L_{c\max}}{c}\right)^3 - 2\left(\frac{L_{c\max}}{c}\right)^2 + 4.5\left(\frac{L_{c\max}}{c}\right) + 1}{\left(\frac{L_{c\max}}{c}\right)^3 - \left(\frac{L_{c\max}}{c}\right)^2 + 0.75\left(\frac{L_{c\max}}{c}\right) + \frac{1}{2\pi}}. \tag{7.16}$$

where $\psi = \dfrac{\sigma}{2\alpha_{\text{eff}}}$ is the dimensionless effective cavitation number, $\alpha_{\text{eff}} = \alpha + \dfrac{2}{\pi}\theta_{\text{tip}}$ is the effective incidence, α is the geometric incidence, θ_{tip} is the tip twist angle measured at the elastic axis with the nose-up direction as positive and S_c is the Strouhal number based on the cavity-shedding frequency, f_c, and the mean chord, c. For the results presented in this section, $\kappa = 0.22$.

7.4.4.2 Cavity Length

In this section, the maximum and minimum cavity length (L_c) non-dimensionalized by the mean chord (c) at the mid-span as a function of cavitation number (σ) is presented for the stainless steel, CFRP +30, and CFRP -30 hydrofoils. The cavity length is computed using the high-speed images via processing within the Matlab environment. Experiments are conducted only until a steady supercavity was established, which typically happens when the non-dimensional maximum cavity length ($L_{c\max}/c$) is at (or higher than) 1.4. As defined in Harwood et al. [54], inception is the transition from the fully wetted flow to the partial cavitation flow, and the growth and collapse of the cavity lead to fluctuations in the hydrodynamic load coefficients, as well as flow-induced vibrations. Figure 7.28a) and b)

presents the non-dimensional cavity length against σ and $\sigma/(2\alpha_{\text{eff,wet}})$, respectively. $\alpha_{\text{eff,wet}}$ ($= \alpha + 2\theta_{\text{tip,wet}}/\pi$) correspond to the effective angle of attack for the fully wetted (FW) (or non-cavitating) condition at $\text{Re} = 0.8 \times 10^6$ and $\alpha = 6^\circ$. $\theta_{\text{tip,wet}}$ is used in this section, since θ_{tip} cannot be reliably measured in cavitating conditions using the current method due o the unsteady cavity-induced vibrations. The measured $\theta_{\text{tip,wet}}$ values at $\text{Re} = 0.8 \times 10^6$ and $\alpha = 6^\circ$ for the stainless steel, CFRP +30, and CFRP -30 hydrofoils are 0°, 3.36°, and -1.2°, respectively (as reported in previous sections).

Figure 7.28a) shows that cavitation inception is accelerated, i.e., cavitation onsets at a higher cavitation number and hence at higher free stream static pressure, for the CFRP -30 hydrofoil, and delayed for the CFRP +30 hydrofoil (i.e. lower σ), relative to the rigid stainless steel hydrofoil. Note that there is a difference of $\sigma \approx 1$ between the cavitation inception of the two composite hydrofoils. Additionally, for a given cavitation number, while the cavity length of the CFRP +30 hydrofoil is shorter than the rigid stainless steel hydrofoil, the cavity length of CFRP -30 hydrofoil is longer. A significant increase in cavity length variation occurs when the non-dimensional cavity length is between $0.6 \lessapprox L_{c\max}/c \lessapprox 1.5$ for both the CFRP -30 hydrofoil and the CFRP +30 hydrofoil. Note that the semi-theoretical results presented in Figure 7.28 are for the maximum cavity length and not the mean. The CFRP +30 hydrofoil results in a decrease in effective angle of incidence at the same α (as $\alpha_{BT} > 0$ and thus, $\theta_{\text{tip}} < 0$), resulting in reduction of lift and consequent reduction in cavity length. For the CFRP -30 hydrofoil, there is an increase in effective angle of incidence (as $\alpha_{BT} < 0$ and thus, $\theta_{\text{tip}} > 0$), resulting in increase in both lift and cavity length. The cavitating trends of the two composite hydrofoils can be explained by the difference in the material bend-twist coupling. Thus, to collapse the results, we plot the normalized cavity length against $\sigma/(2\alpha_{\text{eff,wet}})$ in Figure 7.28b). The result show that the semi-theoretical results for the three hydrofoils collapse to one line, as expected. The maximum measured non-dimensional cavity length values also follow the same curve with some scatter. Note that for $1.5 \lessapprox \sigma/(2\alpha_{\text{eff,wet}}) \lessapprox 2.5$, the cavity is very unstable, where L_c/c

varies from 0 to near 1 in each cavity collapse and growth cycle. The variation in the cavity length is responsible for the variation in the C_L values (presented later in Figure 7.29).

7.4.4.3 Forces

To complement the cavity length measurement, the maximum, minimum, and mean values of force coefficients (i.e., $C_L/C_{L\text{wet}}$ and $C_D/C_{D\text{wet}}$) are plotted against cavitation number (σ and $\sigma/(2\alpha_{\text{eff,wet}})$) for the stainless steel, CFRP +30, and CFRP -30 hydrofoils. In Figures 7.29 and 7.30, the $C_{L\text{wet}}$ and $C_{D\text{wet}}$ correspond to the measured force coefficient values for the fully wetted (FW) (or non-cavitating) condition at $\text{Re} = 0.8\times10^6$ and $\alpha = 6°$. The fluctuations in the load coefficients (which occurs due to the unsteady cavity shedding) increases as the cavity length increases, i.e., as σ decreases, until stable supercavitation is achieved. The most significant fluctuations typically occur at $0.6 \lessapprox L_c/c \lessapprox 1.5$, as shown in Figure 7.28. As shown in the previous literature [54], the mean C_L increases marginally with the onset of cavitation, and then eventually reduces significantly with the further reduction in σ and a corresponding increase in the cavity length. Note that when $C_L/C_{L\text{wet}}$ is plotted against the $\sigma/(2\alpha_{\text{eff,wet}})$, the results collapse for all three hydrofoils, especially the mean values, as shown in Figure 7.29. C_D also follows the similar trend as C_L (due to the induced drag), i.e., increasing upon the cavitation inception and then reducing corresponding to the reduction in lift. Results also show that C_D is always higher in cavitating conditions (due to the additional energy dissipation through cavity growth and collapse), as compared to fully wetted conditions. Note that the fluctuations in lift and drag are generally much higher for the CFRP -30 hydrofoil than for the CFRP +30 hydrofoil, and the fluctuations can be higher than the mean values.

Figure 7.31 shows the ratio of the measured standard deviation of the unsteady lift coefficient, i.e., σ_{C_L}, to the respective mean values, C_L, along with the semi-theoretical maximum normalized cavity length (using Eq. (7.14)). The result show that the increase in non-dimensional cavity length beyond 0.6 yields sudden increase in the variation in the

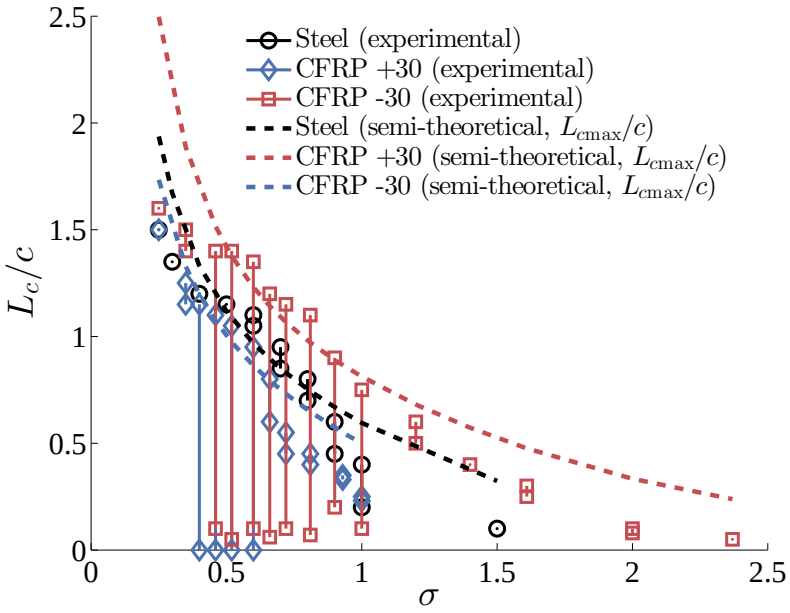

(a) Cavity length against σ.

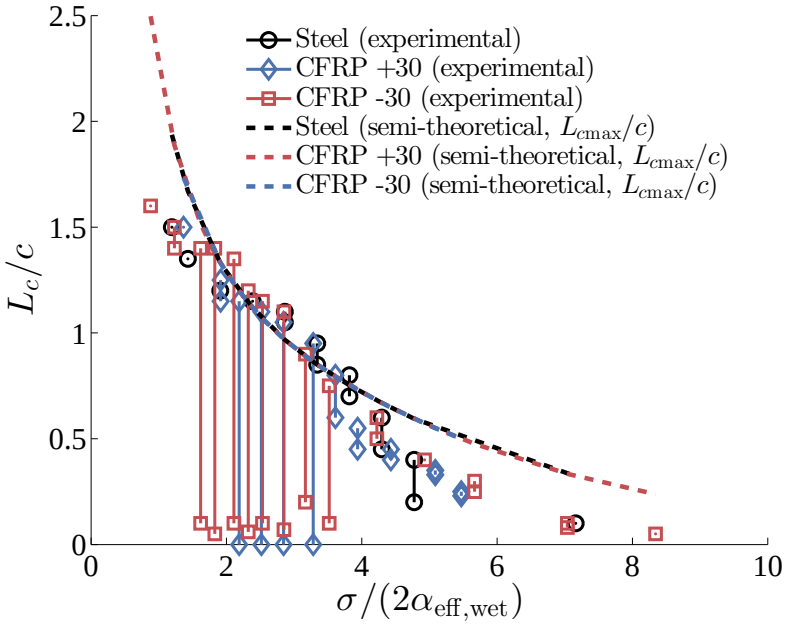

(b) Cavity length against $\sigma/(2\alpha_{\text{eff,wet}})$.

Figure 7.28: The maximum and minimum non-dimensional cavity length at the mid-span against the effective cavitation number for the rigid stainless steel, CFRP+30, and CFRP -30 hydrofoil. The semi-theoretical prediction from Eq. (7.14) are shown as dashed lines. Note that the semi-theoretical prediction is for the maximum cavity length. The results are for $\alpha = 6°$, $\text{Re} = 0.8 \times 10^6$, and $z/s = 0.50$.

cavity length, is also accompanied by the drastic increase in force fluctuations, i.e., the standard deviation of C_L. The load fluctuations subside when $L_{c\max} \gtrapprox 1.5$.

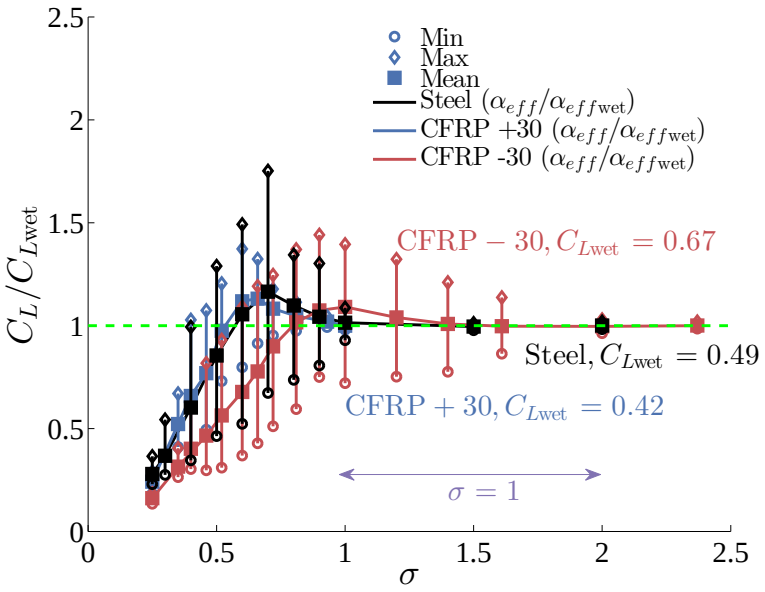

(a) C_L against σ. The horizontal dashed line are the non-cavitating or fully-wetted C_L values. The solid lines represent the ratio of effective angle of attack to the fully wetted effective angle of attack.

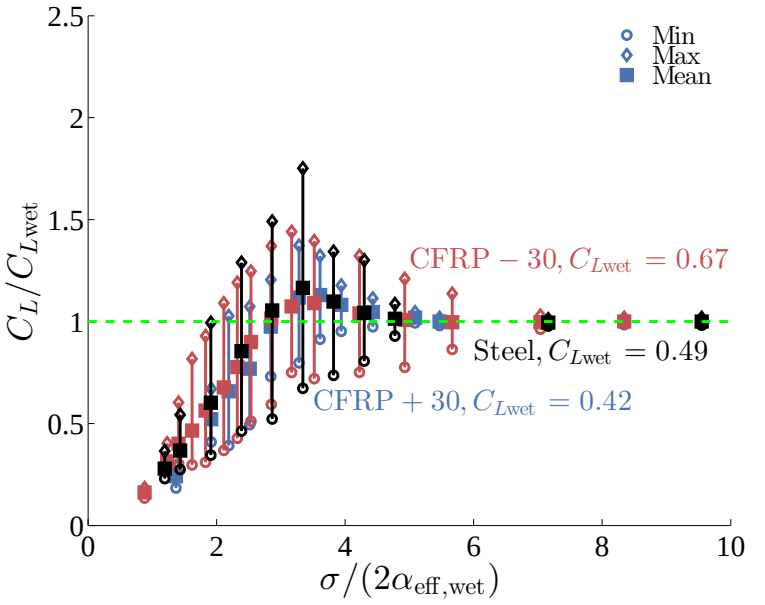

(b) C_L against $\sigma/(2\alpha_{\text{eff,wet}})$. The horizontal dashed line are the non-cavitating or fully-wetted C_L values.

Figure 7.29: Experimental measurements of C_L for the stainless steel, CFRP +30, and CFRP -30 hydrofoils against the effective cavitation number. The results are for $\alpha = 6^\circ$, $\text{Re} = 0.8 \times 10^6$, and $z/s = 0.50$.

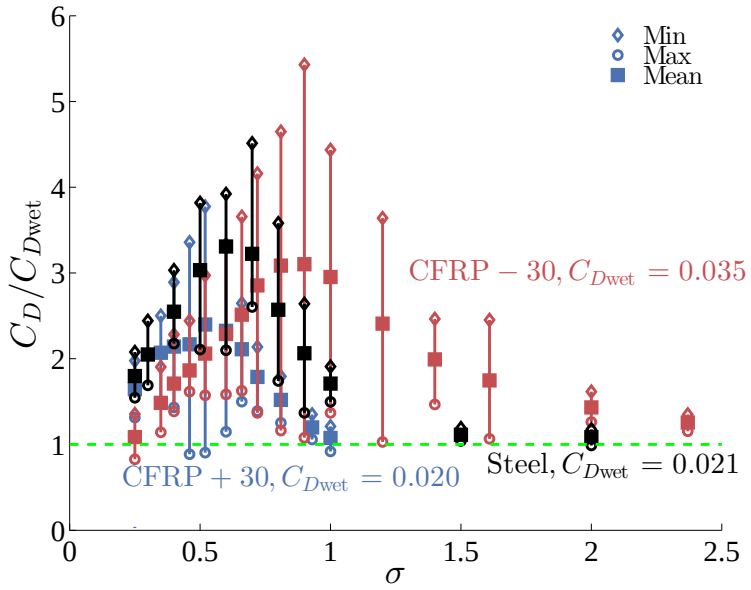

(a) C_D against σ. The horizontal dashed line are the non-cavitating or fully-wetted C_D values.

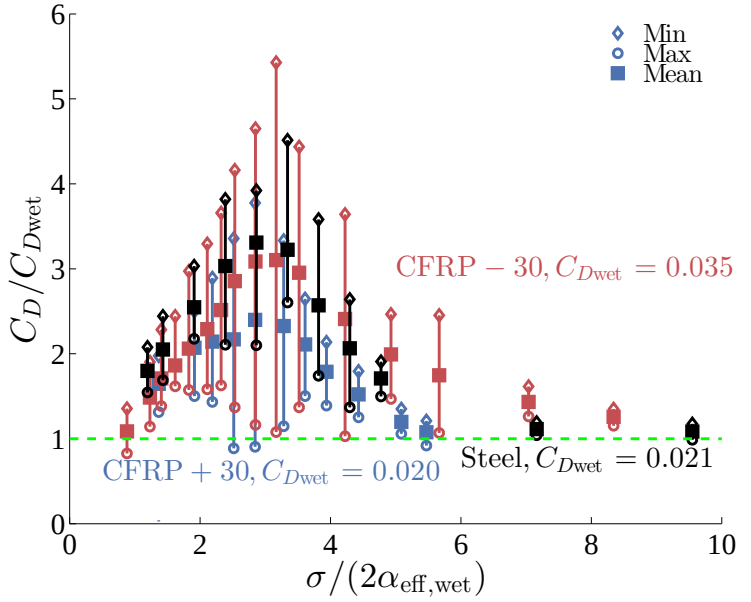

(b) C_D against $\sigma/(2\alpha_{\text{eff,wet}})$. The horizontal dashed line are the non-cavitating or fully-wetted C_D values.

Figure 7.30: Experimental measurements of C_D for the stainless steel, CFRP +30, and CFRP -30 hydrofoils against the effective cavitation number. The results are for $\alpha = 6^\circ$, $\text{Re} = 0.8 \times 10^6$, and $z/s = 0.50$.

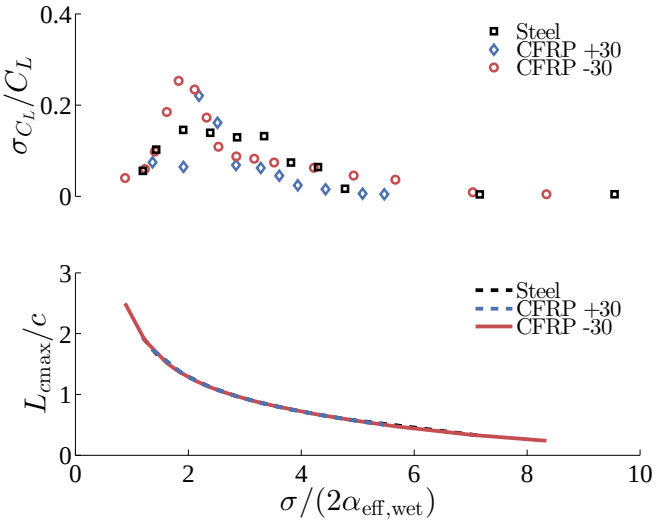

Figure 7.31: The ratio of the standard deviation of the unsteady lift coefficient, i.e. σ_{C_L}, to the respective mean values, C_L, along with the semi-theoretical maximum normalized cavity length against $\sigma/(2\alpha_{\text{eff,wet}})$ for the stainless steel, CFRP +30, and CFRP -30 hydrofoil. Note the increase in standard deviation (or fluctuations) with increase in maximum non-dimensional cavity length beyond 0.6, and drop in fluctuations for $L_{c\max} \gtrapprox 1.5$. The results are for $\alpha = 6°$, and $\text{Re} = 0.8 \times 10^6$.

7.4.4.4 Lift Spectra

In this section, the power spectrograms (power spectral density) of the lift data as a function of cavitation number and effective cavitation number are shown for the three hydrofoils (i.e., stainless steel, CFRP+30, and CFRP -30) in Figures 7.32 and 7.33, respectively. The cavity shedding frequency (f_c) obtained using Eq. (7.14) for each hydrofoil is also presented in Figure 7.32 for comparison. The stainless steel hydrofoil results show a good agreement with theory except at the very low σ values, where the $L_{c\max}/c \geq 1.2$. The difference in the predicted cavity shedding frequencies for the composite hydrofoils is due to the material-based bend-twist coupling. As explained before, for CFRP +30 hydrofoil, θ_{tip} or α_{eff} reduces, resulting in shorter cavity length and thus, higher cavity shedding frequency than the stainless steel hydrofoil for a given σ. The opposite is true for CFRP -30 hydrofoil, i.e., it experiences longer cavity length and lower cavity shedding frequency

than the stainless steel hydrofoil for a given σ.

The in-water experimental first structural natural frequency f_1^* of the CFRP +30 hydrofoil in fully wetted condition is measured to be 22 Hz. Due to the limitation in time, in-water natural frequency for CFRP -30 hydrofoil was not calculated. However, since the bending stiffness, first in-air natural frequency, and the mass of two composite hydrofoils is similar, it is safe to assume that the in-water structural natural frequency of the CFRP +30 hydrofoil will also be similar. The energy content of the cavity shedding frequency for the stainless steel hydrofoil is almost half to that of composite hydrofoils at $\approx$ 11 Hz. The most energetic cavity shedding for the stainless steel hydrofoil occurs at σ of 0.35 – 0.55, or $\sigma/(2\alpha_{\text{eff,wet}})$ between 1.6 and 2.6 (as shown in Figure 7.33), and $L_{c\max}/c \geq 1.2$. According to Ganesh et al. [42], for $L_{c\max}/c \geq 1.1$, the cavity shedding cycle is identified as the intermittent type 1 shedding. The detailed features of each type of cavity shedding cycle can be found in Ganesh et al. [42]. The CFRP +30 hydrofoil exhibits the energetic lock-in behavior at two distinct frequencies, depending on the cavitation number range. For σ of about 0.35 – 0.55 (i.e., $L_{c\max}/c \geq 1.2$), the lock-in occurs at a frequency corresponding to the subharmonic of the structural natural frequency ($f_1^*/2 \approx 10.5$Hz). However, for σ from 0.55 to 0.7 (i.e., $0.8 \leq L_{c\max}/c \leq 1.2$), the lock-in occur at a frequency of about 33 Hz ($\approx 3f_1^*/2$). The higher cavity shedding frequency (i.e., 33 Hz) correspond to the unstable partial shedding behavior (and thus, have lesser energy), as also evident from reduced maximum cavity length ($L_{c\max}/c$) in Figure 7.28, while the lower frequency (i.e., 10.5 Hz) correspond to the periodic large sheet-cloud type shedding behavior (and thus, have higher energy), as also evident from higher maximum cavity length ($L_{c\max}/c$). As per the cavity shedding cycle defined in Ganesh et al. [42], the lower frequency behavior yields the intermittent type 1 shedding (same as the stainless steel hydrofoil) and the higher frequency corresponds to type 2 partial cavity shedding dominated by re-entrant jet dynamics. For the CFRP -30 hydrofoil, the most energetic lock-in occurs at the first subharmonic frequency ($f_1^*/2 \approx 11$Hz) for $0.45 < \sigma < 0.8$ (i.e., $L_{c\max}/c \geq 1.2$), which also corresponds to the in-

termittent type 1 cavity shedding (same as the lower frequency regime of CFRP +30 and stainless steel hydrofoils). The most dominant energy for the three hydrofoils tends to be around 11 Hz, illustrating that the global shedding dynamics is dominant over the FSI effect in determining the resultant structural behavior. The frequency behavior observed in the results is also similar to the trend presented in the previous literature [6, 8].

An overview of a typical shedding cycle for the three hydrofoils is shown in Figure 7.34 for $\sigma = 0.6$ and in Figure 7.35 for $\sigma/(2\alpha_{\text{eff,wet}}) = 2.86$ (i.e., with different σ for each hydrofoil). As shown in Figure 7.28a), for a given σ, the CFRP +30 has a shorter cavity, and the CFRP -30 a longer cavity than the nominally rigid stainless steel hydrofoil, due to the effect of material bend-twist coupling present in the composite models. Figure 7.34 and 7.35 are originally presented in Pearce et al. [122]. Figure 7.35 shows that for a given $\sigma/(2\alpha_{\text{eff,wet}})$, the maximum cavity length of the three hydrofoils is almost the same. Note the difference in cavity pattern at the tip due to the different twist directions of the hydrofoils. The fingering cavitating structure observed for CFRP +30 hydrofoil can be attributed to the variations in surface finish of the hydrofoils, which will be investigated further with more experiments in future.

7.5 Conclusions

In the current chapter, combined experimental and numerical studies are presented to study the impact of load-dependent material-induced bend-twist coupling effects on the steady-state hydroelastic response of the three composite hydrofoils. Additionally, results are presented for a stainless steel hydrofoil, which served as the rigid reference. The four hydrofoils have identical unloaded geometry, with a tapered profile and a modified NACA 0009 cross section. The three composite hydrofoils are all made of epoxy resin reinforced with the same nominal layup of carbon fiber reinforced polymers (CFRP) and glass fiber reinforced polymers (GFRP) layers. The three composite hydrofoils only differ

in the orientation of the structural CFRP layers, i.e., 0°, +30°, and -30° relative to the span-wise axis of the hydrofoils. The different orientations lead to significantly different material bend-twist coupling of the three composite hydrofoils. Experiments are conducted in the variable pressure water tunnel at the Australian Maritime College (AMC). The experimental studies are complemented by a simplified two-degrees of freedom (2-DOF) FSI model, and the predictions are compared against experimental measurements.

The results show that there are significant differences in the modal frequencies for the CFRP 00, and CFRP +30 and CFRP -30 hydrofoils, in addition to the mode shapes. The CFRP 00 hydrofoil, due to zero bend-twist coupling, experiences mostly pure bending and pure twisting for first and second mode, respectively. The CFRP +30 and CFRP -30 hydrofoils, due to significant bend-twist coupling (α_{BT}), experience combined bending and twisting for both the first and second modes. The twisting directions of the CFRP +30 and CFRP -30 are opposite because of the opposite sign of α_{BT}. The results show that the material-based bend-twist coupling significantly affects the modal characteristics of three composite hydrofoils, which governs the hydrofoil deformation and thus the hydrodynamic performance.

The mean non-dimensional hydrodynamic lift, drag, and moment coefficients, and the hydrofoil tip bending and twisting deformations are presented for all four hydrofoils for incidence angles (α) ranging from 0° to 20° and for Reynolds number (based on the mean chord), Re, ranging from 0.25×10^6 to 1.2×10^6. The results show that the hydrodynamic lift induces bending deformation towards the suction side. While the stainless steel and the CFRP 00 hydrofoils have no apparent material bend-twist coupling, there is still bend-twist coupling caused by the hydrodynamic loads. As the CP is upstream of the EA, the hydrodynamic moment results in hydrofoils having a nose-up twist. The CFRP +30 hydrofoil and the CFRP -30 hydrofoil undergo a nose-down and a nose-up twist, respectively, because of opposite material bend-twist coupling effects. Due to the negative or nose-down twist, the CFRP +30 hydrofoil experiences reduction in lift and moment coefficients, and delayed

stall, with an increase in Re and α. Due to the positive twist, the CFRP -30 hydrofoil experiences increase in lift and moment coefficients, and accelerated stall with an increase in Re and α. The results also show that the performance of the rigid and the adaptive composite hydrofoils should only be compared at same lift capacity at each speed, instead of same Re and α.

The simplified 2-DOF FSI model presented in this chapter is able to predict the load-dependent bend-twist coupling behavior and hydroelastic performance of the three composite hydrofoils. The stiffness values required for the 2-DOF FSI model are computed using the experimental measurements. The results show that if the stiffness values of the hydrofoil are readily available, the bend-twist coupling behavior can be easily predicted using the simplified 2-DOF FSI model. The mean error between the predicted and measured tip bending deflection for CFRP 00, CFRP +30, and CFRP -30 hydrofoils is 0.01%. The mean error between the predicted and measured twist deflection for CFRP 00, CFRP +30, and CFRP -30 hydrofoils is 19.67%, 25.53%, and 23.19%, respectively. The error in the predicted bending and twist deformations are generally within the worst case uncertainty of the measurements. The static divergence speed, i.e., the critical speed when the fluid disturbing moment is equal to the hydrofoil elastic restoring moment, of the three composite hydrofoils is also investigated. The 2-DOF model predicts accelerated static divergence for hydrofoils with nose-up twist (CFRP -30, $\alpha_{BT} < 0$) and delayed static divergence for hydrofoils with nose-down twist (CFRP +30, $\alpha_{BT} > 0$) for positive lift condition. However, the comparison between the predicted divergence velocity and the critical inflow speed (based on the maximum allowable load) show that the hydrofoils will experience material failure before reaching the static divergence limit.

Preliminary results are also presented to study the influence of bend-twist coupling on the dynamic cavitating response of composite hydrofoils. The results show that the cavitation incepts earlier for the CFRP -30 hydrofoil, and later for the CFRP +30 hydrofoil, as compared to rigid stainless steel hydrofoil. Similarly, relative to the stainless steel hydro-

foil, the CFRP -30 experiences longer maximum cavity length, and CFRP +30 experiences shorter maximum cavity length. The results show that the cavity length or the force variation for the three hydrofoils in the linear range can be collapsed into a single line by using the effective angle of attack (or the effective cavitation number). Additionally, the stainless steel, CFRP +30, and CFRP -30 hydrofoils display the most energetic lock-in behavior at the similar low effective cavitation number and frequency, illustrating the dominance of global shedding dynamics over bend-twist coupling effects.

In summary, this chapter improves the understanding of the impact of load-dependent bend-twist coupling on the steady-state hydroelastic performance, stall behavior, modal characteristics, static divergence boundary, and cavitation response of adaptive composite hydrofoils. This chapter also presents a high-quality data set that serves as a baseline for future testing of adaptive composite marine propulsors in sub-cavitating and cavitating flows, and provides a rich dataset for validation of high-fidelity numerical models. The results demonstrate that the intrinsic material bend-twist coupling of anisotropic composites can be used to increase the efficiency, delay stall, or delay cavitation of hydrodynamic lifting bodies, but care is needed to account for load-dependent deformations.

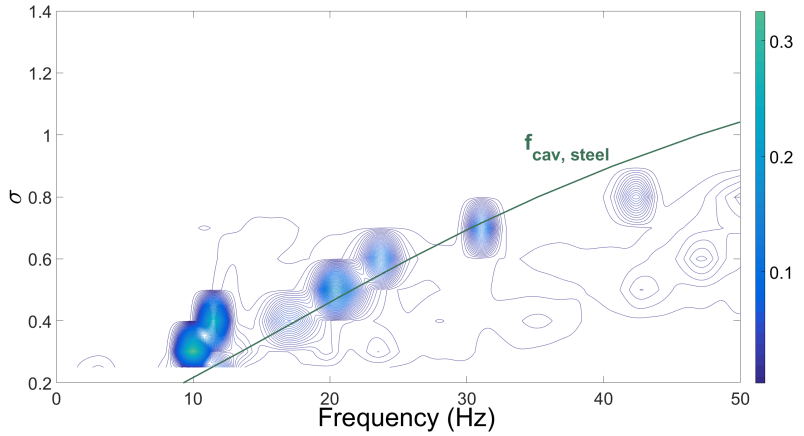

(a) Stainless steel hydrofoil.

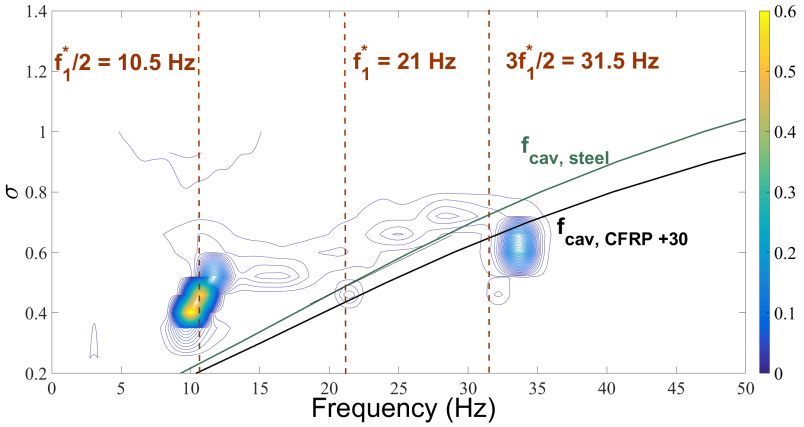

(b) CFRP +30 hydrofoil.

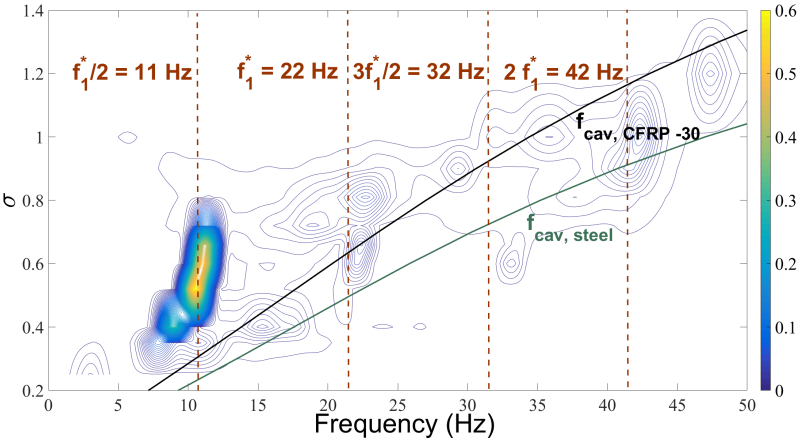

(c) CFRP -30 hydrofoil.

Figure 7.32: The lift power spectrogram for the hydrofoils illustrating the frequency content for the range of cavitating conditions. The solid lines represent the semi-theoretical cavity shedding frequency (Eq. (7.15)). The green solid line in the two composite hydrofoil plots is the semi-theoretical line for the rigid stainless steel hydrofoil for comparison. $\alpha = 6^\circ$ and Re$= 0.8 \times 10^6$.

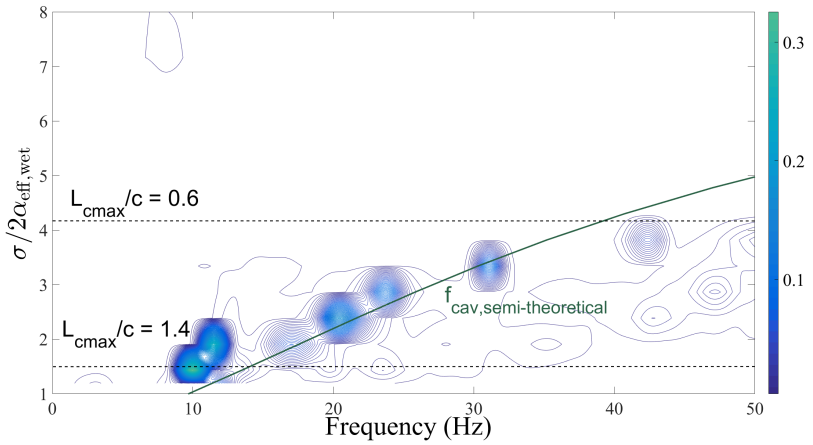

(a) Stainless steel hydrofoil.

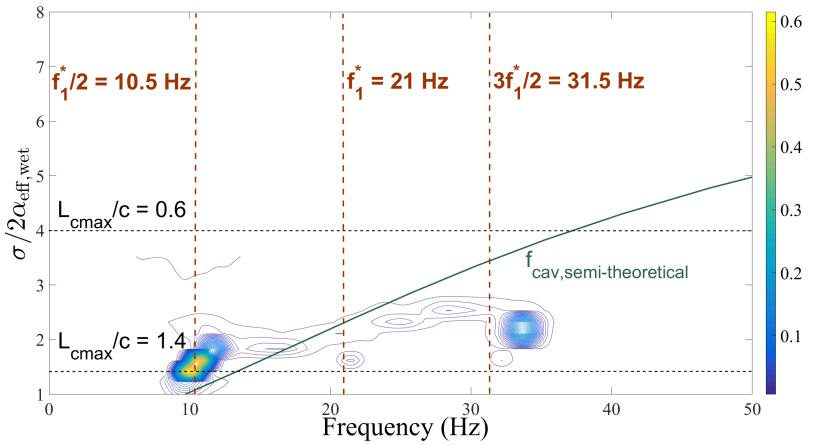

(b) CFRP +30 hydrofoil.

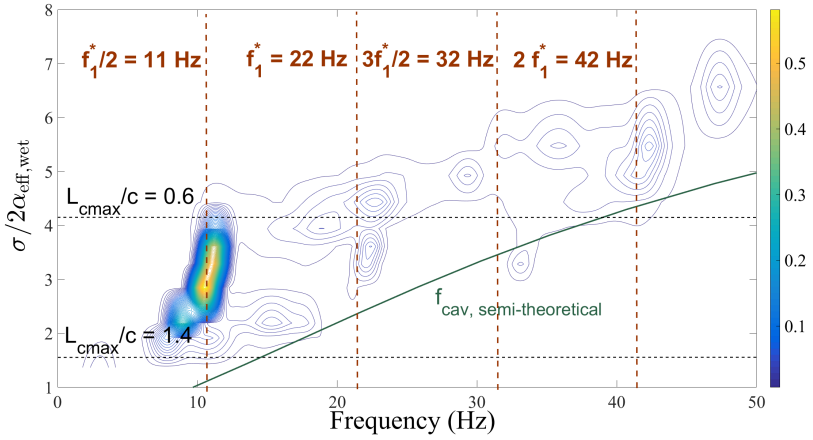

(c) CFRP -30 hydrofoil.

Figure 7.33: The lift power spectrogram for the hydrofoils illustrating the frequency content for the effective cavitation number. The solid line represents the semi-theoretical cavity shedding frequency (Eq. (7.15)). $\alpha = 6^\circ$ and Re$= 0.8 \times 10^6$.

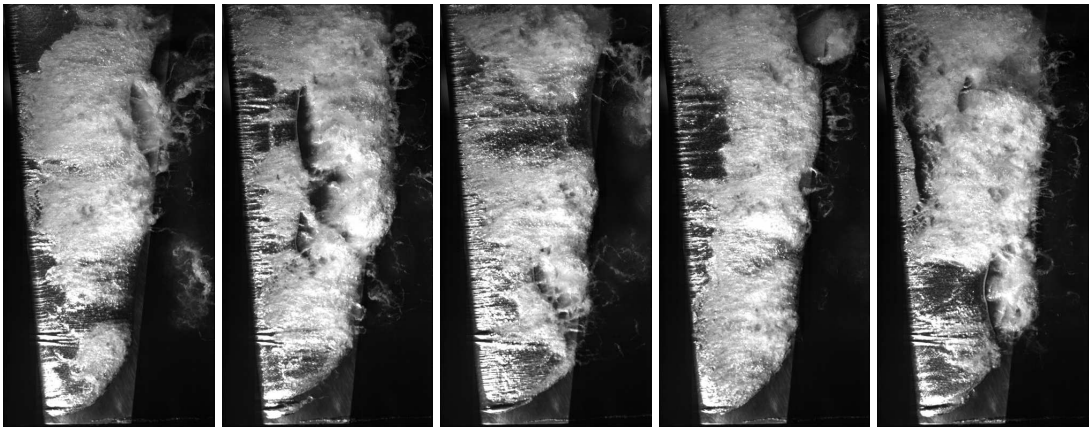

(a) Stainless steel hydrofoil.

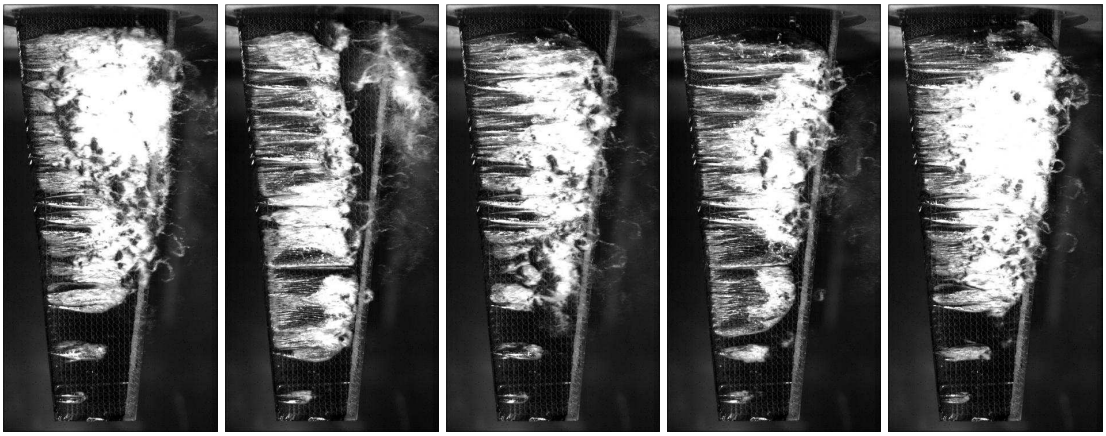

(b) CFRP +30 hydrofoil.

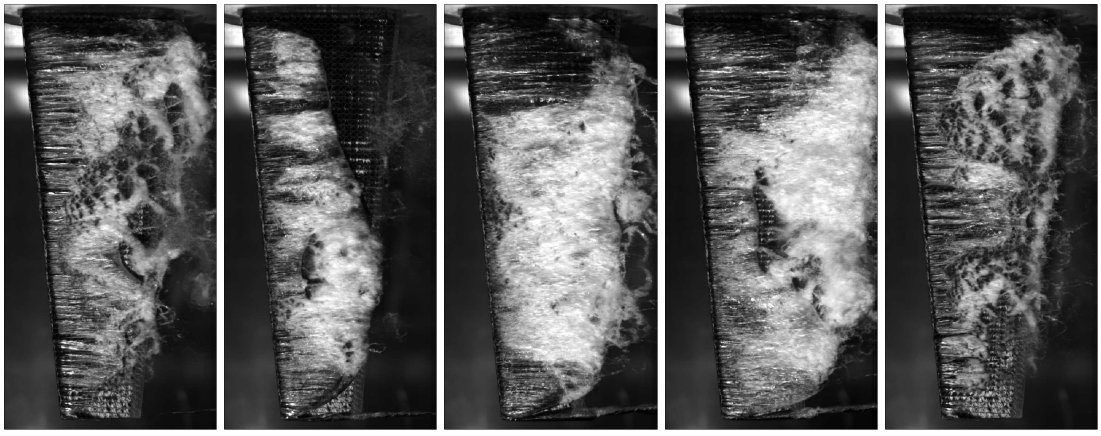

(c) CFRP -30 hydrofoil.

Figure 7.34: Image sequence of one cavity shedding cycle for the three hydrofoils showing cavity growth ($\sigma = 0.6$, $\alpha = 6^\circ$, and $\mathrm{Re} = 0.8 \times 10^6$). The figure is originally presented in Pearce et al. [122].

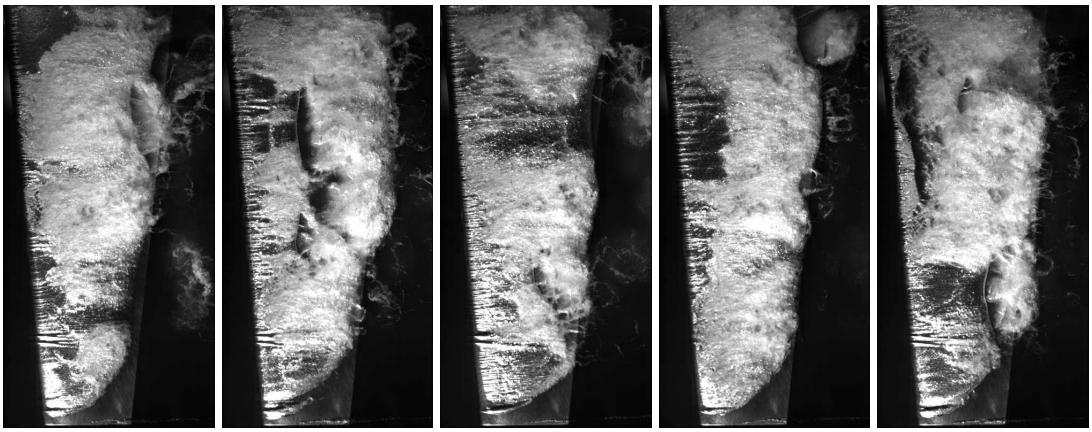

(a) Stainless steel hydrofoil, $\sigma = 0.60$.

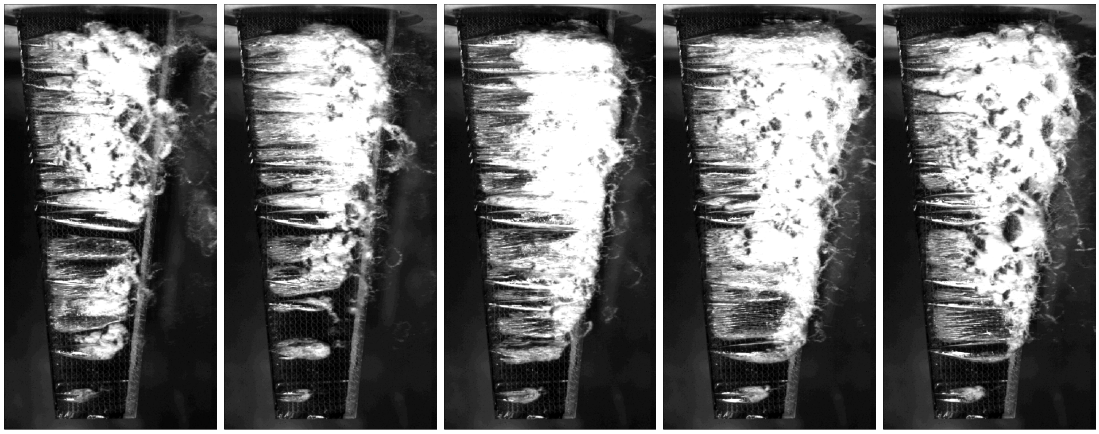

(b) CFRP +30 hydrofoil, $\sigma = 0.52$.

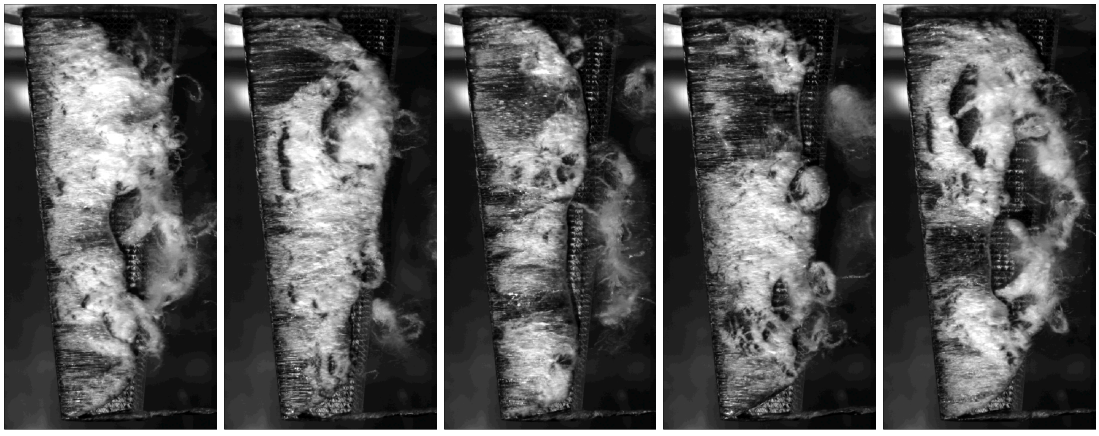

(c) CFRP -30 hydrofoil, $\sigma = 0.81$.

Figure 7.35: Image sequence of one shedding cycle for the three hydrofoils showing cavity growth for same $\sigma/(2\alpha_{\text{eff,wet}})$ of 2.86, i.e., different σ for each hydrofoil ($\alpha = 6^\circ$, and Re $= 0.8 \times 10^6$). The figure is originally presented in Pearce et al. [122].

CHAPTER 8

Towards Hydrostructural Optimization of Composite Hydrofoils

In this chapter, we take the first step towards the development of a hydrostructural design optimization tool that optimizes both the shape and the material configurations of composite hydrofoils. To achieve this, we extend our structural solver, TACS, to solve for anisotropic material response of composites and verify the solver against the commercial FEA solver, Abaqus.

8.1 Anisotropic Solid Element Formulation

In Chapter 5, the structural solver (TACS) primarily meant for solving thin-walled structure encountered in aerospace applications is extended to solve for solid isotropic elements. The hollow and rib-spar structure typical of aircraft wings, helicopter blades, and wind turbines allows the use of shell elements for structure modeling. On the other hand, most marine hydrofoils and propulsors have either solid interior structure or thick cross sections (due to the need to withstand higher hydrodynamic loads), necessitating the use of solid elements for structural modeling.

Isotropic materials (e.g., metals) have identical properties in all directions, and their stress-strain relations can be defined with only two independent constants. Anisotropic materials (e.g., composites) have different properties in different directions and have 21

independent constants to completely define the stress-strain relationship. Orthotropic materials (e.g., wood) are a subset of anisotropic materials, with different properties along the three mutually orthogonal axes of rotational symmetry. Orthotropic materials require nine independent constants for their stress-strain relationship. The stress-strain relationship of orthotropic material is equivalent to anisotropic materials, when the orthotropic materials are loaded in an arbitrary orientation instead of principal material coordinates. In this chapter, the structural solver is further extended to solve for unidirectional solid anisotropic elements. Since the fundamental capability of the unidirectional anisotropic material is to carry stresses in the plane of its fibers. Thus, by considering only the in-plane stresses, the constitutive properties of the anisotropic materials can be specified with only 13 independent constants. The general constitutive equation, i.e., the relationship between the stress and strain, in principal material or local coordinates (where the 1-axis is aligned with the fiber direction, as presented in Figure 8.1) is given as,

$$\{\sigma\}_i = \{C\}_{ij}\{\epsilon\}_i \tag{8.1}$$

where $i, j = \{1,2,3,4,5,6\}$, $\{\sigma\}_i$ $(= [\sigma_{11}, \sigma_{22}, \sigma_{33}, \sigma_{23}, \sigma_{13}, \sigma_{12}]^T)$ represent stress components in the local coordinates, and $\{\epsilon\}_i$ $(= [\epsilon_{11}, \epsilon_{22}, \epsilon_{33}, \epsilon_{23}, \epsilon_{13}, \epsilon_{12}]^T)$ represents strain components in the local coordinates, and $\{C\}_{ij}$ are the stiffness components.

The constitutive equation for the orthotropic material loaded in principal material coordinates can be expressed as,

$$\begin{bmatrix} \sigma_{11} \\ \sigma_{22} \\ \sigma_{33} \\ \sigma_{23} \\ \sigma_{13} \\ \sigma_{12} \end{bmatrix} = \begin{bmatrix} C_{11} & C_{12} & C_{13} & 0 & 0 & 0 \\ C_{12} & C_{22} & C_{23} & 0 & 0 & 0 \\ C_{13} & C_{23} & C_{33} & 0 & 0 & 0 \\ 0 & 0 & 0 & C_{44} & 0 & 0 \\ 0 & 0 & 0 & 0 & C_{55} & 0 \\ 0 & 0 & 0 & 0 & 0 & C_{66} \end{bmatrix} \begin{bmatrix} \epsilon_{11} \\ \epsilon_{22} \\ \epsilon_{33} \\ \epsilon_{23} \\ \epsilon_{13} \\ \epsilon_{12} \end{bmatrix} \tag{8.2}$$

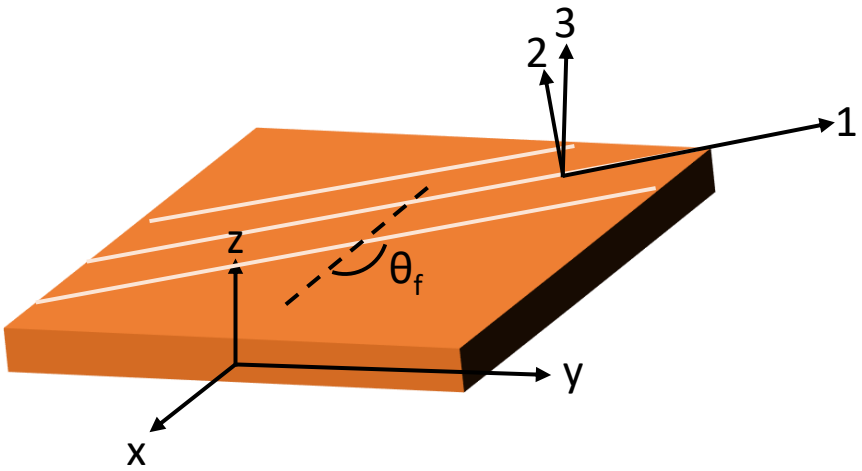

Figure 8.1: Unidirectional anisotropic plate with global $x-y-z$ coordinates and 1-2-3 principal (or local) material coordinates.

The individual components of the stiffness matrix can be expressed using the material properties and are defined as,

$$
\begin{aligned}
C_{11} &= \frac{1-\nu_{23}\nu_{32}}{E_2E_3D} \\
C_{12} &= \frac{\nu_{21}+\nu_{23}\nu_{31}}{E_2E_3D} \\
C_{13} &= \frac{\nu_{31}+\nu_{21}\nu_{32}}{E_2E_3D} \\
C_{22} &= \frac{1-\nu_{13}\nu_{31}}{E_2E_3D} \\
C_{23} &= \frac{\nu_{32}+\nu_{12}\nu_{31}}{E_1E_3D} \\
C_{33} &= \frac{1-\nu_{12}\nu_{21}}{E_1E_2D} \\
C_{44} &= G_{23} \\
C_{55} &= G_{13} \\
C_{66} &= G_{12} \\
D &= \frac{1-\nu_{12}\nu_{21}-\nu_{23}\nu_{32}-\nu_{13}\nu_{31}-2\nu_{21}\nu_{32}\nu_{13}}{E_1E_2E_3}
\end{aligned}
\tag{8.3}
$$

where E_1, E_2, and E_3 are the Young's moduli in 1, 2, and 3 directions, respectively, G_{ij}

represents the shear moduli, and ν_{ij} are the Poisson's ratio. Note that since there is no material bend-twist coupling experienced in the orthotropic material if the lamina is aligned with the global coordinates, the C_{16}, C_{26}, and C_{36} terms are zero.

However, if the fibers in a lamina are not oriented along the x-axis, then the stress and strain components needs to be transformed from principal material coordinates 1-2-3 to global $x-y-z$ coordinates (as shown in Figure 8.1). The transformed stiffness matrix is represented as $\left[\overline{C}\right]$. The constitutive equation for anisotropic elements in global coordinates is written as,

$$\begin{bmatrix} \sigma_{xx} \\ \sigma_{yy} \\ \sigma_{zz} \\ \sigma_{yz} \\ \sigma_{xz} \\ \sigma_{xy} \end{bmatrix} = \begin{bmatrix} \overline{C}_{11} & \overline{C}_{12} & \overline{C}_{13} & 0 & 0 & \overline{C}_{16} \\ \overline{C}_{12} & \overline{C}_{22} & \overline{C}_{23} & 0 & 0 & \overline{C}_{26} \\ \overline{C}_{13} & \overline{C}_{23} & \overline{C}_{33} & 0 & 0 & \overline{C}_{36} \\ 0 & 0 & 0 & \overline{C}_{44} & \overline{C}_{45} & 0 \\ 0 & 0 & 0 & \overline{C}_{45} & \overline{C}_{55} & 0 \\ \overline{C}_{16} & \overline{C}_{26} & \overline{C}_{36} & 0 & 0 & \overline{C}_{66} \end{bmatrix} \begin{bmatrix} \epsilon_{xx} \\ \epsilon_{yy} \\ \epsilon_{zz} \\ \epsilon_{yz} \\ \epsilon_{xz} \\ \epsilon_{xy} \end{bmatrix} \tag{8.4}$$

Using the fiber angle (θ_{f}) defined relative to the x-axis, the individual components of

the $[\overline{C}]$ can be described as,

$$
\begin{aligned}
\overline{C}_{11} &= m^4 C_{11} + 2m^2 n^2 (C_{12} + 2C_{66}) + n^4 C_{22} \\
\overline{C}_{12} &= n^2 m^2 (C_{11} + C_{22} - 4C_{66}) + \left(n^4 + m^4\right) C_{12} \\
\overline{C}_{13} &= m^2 C_{13} + n^2 C_{23} \\
\overline{C}_{16} &= nm\left[m^2 (C_{11} - C_{12} - 2C_{66}) + n^2 (C_{12} - C_{22} + 2C_{66})\right] \\
\overline{C}_{22} &= n^4 C_{11} + 2m^2 n^2 (C_{12} + 2C_{66}) + m^4 C_{22} \\
\overline{C}_{23} &= n^2 C_{13} + m^2 C_{23} \\
\overline{C}_{26} &= nm\left[n^2 (C_{11} - C_{12} - 2C_{66}) + m^2 (C_{12} - C_{22} + 2C_{66})\right] \\
\overline{C}_{33} &= C_{33} \\
\overline{C}_{36} &= mn (C_{13} - C_{23}) \\
\overline{C}_{44} &= m^2 C_{44} + n^2 C_{55} \\
\overline{C}_{45} &= mn (C_{55} - C_{44}) \\
\overline{C}_{55} &= n^2 C_{44} + m^2 C_{55} \\
\overline{C}_{66} &= n^2 m^2 (C_{11} - 2C_{12} + C_{22}) + \left(n^2 - m^2\right)^2 C_{66}
\end{aligned}
\tag{8.5}
$$

where $m = \cos\theta_{\mathrm{f}}$, $n = \sin\theta_{\mathrm{f}}$, θ_{f} is the fiber angle in radians, and C_{ij} are as defined in Eq. (8.3). The angle θ_{f} is the angle between the fiber orientation and x-axis, as shown in Figure 8.1.

Nonzero $\overline{C}_{16}$, $\overline{C}_{26}$, and $\overline{C}_{36}$ reflect the existence of bend-twist coupling in the anisotropic materials, as shown later in Figures 8.3 and 8.10. Note that the terms $\overline{C}_{16}$, $\overline{C}_{26}$, and $\overline{C}_{36}$ are zero for isotropic and orthotropic materials. In the next section, we verify the behavior of anisotropic solid elements in the TACS solver with Abaqus as a reference.

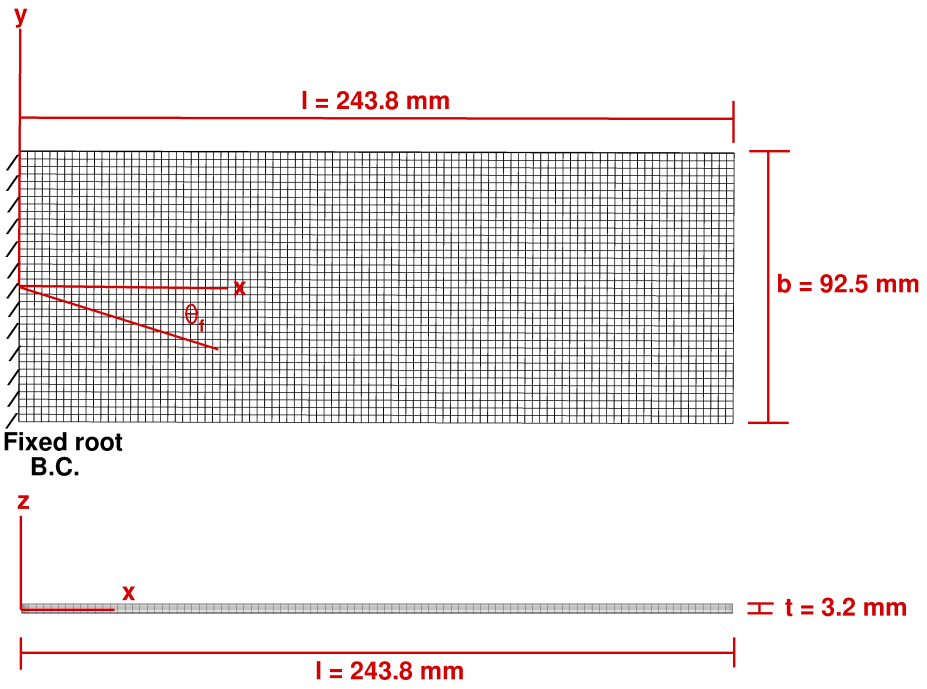

Figure 8.2: Cantilevered plate (with the fine mesh and dimensions) for the anisotropic solid element verification study. Note the fixed root boundary condition on the left side.

8.2 Validation Study

8.2.1 Structural Model

The structural model used for the modal characteristics and the static stress and deformation verification study is presented in Figure 8.2. The fixed root boundary conditions are implemented on the left side, while the right end of the plate is free, as shown in Figure 8.2. The assumed material properties for the composite plate are listed in Table 8.1, which are same as the assumed values used in a similar study by Kramer et al. [75].

8.2.2 Grid Convergence Study

The structural grid convergence study is performed using four different structural meshes. The different structural meshes are obtained by systematically varying the three mesh parameters: n_x, n_y, and n_z, i.e., the number of elements in x, y, and z coordinates. The n_x

Table 8.1: Assumed material properties of composite plate.

Symbol	Description	Value	Units
ρ_s	Solid density	1500.00	Kg/m^3
E_1	Young's modulus	171.42	GPa
E_2, E_3	Young's modulus	9.08	GPa
G_{12}, G_{13}	Shear modulus	5.29	GPa
G_{23}	Shear modulus	0.28	GPa
ν_{12}, ν_{13}	Poisson's ratio	0.32	–
ν_{23}	Poisson's ratio	0.29	–

and n_y are chosen to keep the element faces as close to square as possible, i.e., $n_x/n_y \approx AR$, where $AR = l/b$. 8-noded linear brick elements, and a Gaussian second order integration scheme, are used in both TACS and Abaqus [4].

The first and second in-air natural frequencies for various structural mesh predicted using TACS and Abaqus [2] for $\theta_f = 30^\circ$ are shown in Table 8.2. The first and second in-air analytical natural frequencies presented in Kramer et al. [75] are 42.4 Hz and 212.20 Hz, respectively. The fine mesh (presented in Figure 8.2) is used for validation studies (presented in next section) with both Abaqus and TACS.

Table 8.2: Convergence study of the in-air natural frequencies for various structural mesh resolution for a cantilevered plate at $\theta_f = 30^\circ$ obtained using Abaqus and TACS, along with the analytical values from Kramer et al. [75].

Mesh	n_x	n_y	n_z	Mode 1 [Hz]		Mode 2 [Hz]	
				Abaqus	TACS	Abaqus	TACS
Coarse	48	18	5	45.6	46.5	242.1	245.1
Medium	72	27	7	43.7	45.2	225.6	227.4
Fine	96	36	9	42.9	44.2	220.1	221.1
Finest	120	48	12	42.7	44.0	218.0	219.9
Analytical [75]				42.4		212.2	

8.2.3 Validation of the Natural Frequency Predictions

A cantilevered plate (presented in Section 8.2.1) is studied with both TACS and Abaqus for the natural frequency validation study. The fine mesh is used for both TACS and Abaqus.

As mentioned earlier, $\overline{C}_{16}$, $\overline{C}_{26}$, and $\overline{C}_{36}$ represent the material bend-twist coupling of anisotropic materials. Thus, to understand the variation of bend-twist coupling with fiber angle, the ratio of $\overline{C}_{16}$ to $\overline{C}_{11}$ for a range of fiber angle is plotted in Figure 8.3. As expected, bend-twist coupling is zero for $\theta_f = 0^\circ$ and $\theta_f = 90^\circ$. Note that the highest bend-twist coupling is predicted for $\theta_f = 60^\circ$.

Figure 8.4 presents the comparison of the predicted natural frequency for first three in-air modes for a range of fiber angles obtained using Abaqus and TACS. The results indicate the maximum discrepancy in frequency for the first three in-air modes is 5.0%. Figure 8.4 also show the analytical values for the first two in-air modes, as presented in Kramer et al. [75]. Except for the second mode of the $\theta_f = 0^\circ$ plate, the analytical values match very well between both structural solvers. The mean error between TACS and analytical values for the first two in-air modes is 5.6%. The first two in-air mode shapes obtained using Abaqus and TACS are shown in Figure 8.5. The mode shapes from both the structural solvers look similar. Note the difference in mode shapes with changes in the fiber angle. For example, the first in-air mode for $\theta_f = 0^\circ$ and $\theta_f = 90^\circ$ is pure bending, and the first in-air mode for any other fiber angle is combined bending and twisting, due to the inherent material bend-twist coupling, as observed previously for the composite hydrofoils in Section 7.2 and in Figure 8.3.

8.2.4 Static Deformation and Stress Verification Study

For the purpose of static deformation and stress verification, we use the same structural model (as presented in Section 8.2.1 and Figure 8.2) and the fine mesh for both Abaqus and TACS. In Figure 8.6, we compare the tip bending and twist deflection at the elastic axis,

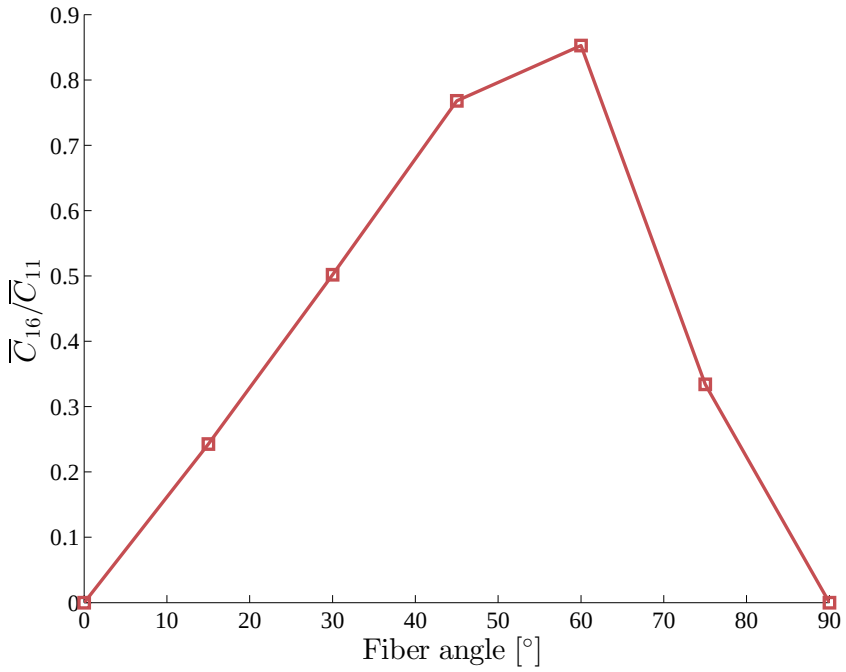

Figure 8.3: Comparison of the effective material bend-twist coupling, $\overline{C}_{16}/\overline{C}_{11}$, for a cantilevered plate for range of unidirectional fiber angles.

for a range of fiber angles. The elastic axis for a rectangular section is at the mid-chord, or mid-breadth. A uniform pressure of 443.5 Pa (i.e., uniform load of 10 N) is applied on one side of the cantilevered plate. The results show that the bending deformation increases with increasing fiber angle, as the effective bending stiffness decreases. The maximum twist is observed for $\theta_f = 45^\circ$ and the twist is zero for $\theta_f = 0^\circ$ and $\theta_f = 90^\circ$, where the material bend-twist coupling is zero. The maximum discrepancy in the bending deformation and the twist deformation is 8.8% for $\theta_f = 60^\circ$, and 5.0% for $\theta_f = 45^\circ$, respectively. Figure 8.7 compares the different deformation pattern for the different fiber angles. Similar to the first in-air mode and consistent with the deformation results presented in Chapter 7, while the deformation pattern for the $\theta_f = 0^\circ$ and $\theta_f = 90^\circ$ is predominantly bending, all the other fiber angles experience combined bending and twisting.

Figure 8.8 compares the in-plane non-dimensionalized bending and shear stresses from Abaqus and TACS. The stress is non-dimensionalized by Plb/t^2, where P (= plb) is the

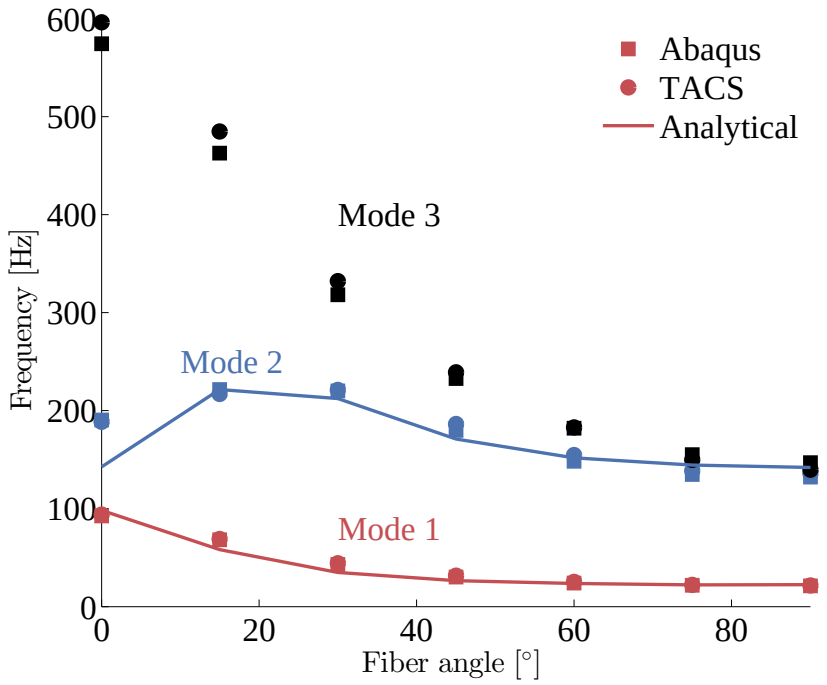

Figure 8.4: Comparison of the first three predicted in-air natural frequencies from Abaqus and TACS for a cantilevered plate (shown in Figure 8.2) for a range of unidirectional fiber angles. The analytical results from Kramer et al. [75] are shown as lines. The maximum discrepancy in frequency is 5.0% between two structural solvers. The mean error between TACS and the analytical results for first two in-air modes from Kramer et al. [75] is 5.6%.

uniform load, and p is the uniform pressure; l, b, and t are the dimensions of the plate, as shown in Figure 8.2. The stresses are compared at the center of the top surface of the cantilevered plate. The results show good agreement between the predicted bending and shear stresses from both Abaqus and TACS. The maximum difference in the stress values is 13.5%, i.e., for $\theta_f = 15^\circ$ and S_{yy}.

8.3 Comparison of Predicted and Measured Modal Characteristics of Composite Hydrofoils

In this section, we compare the predicted in-air natural frequencies of a canonical type II NACA 0009 hydrofoil composed purely of unidirectional carbon (carbon-UD). The ma-

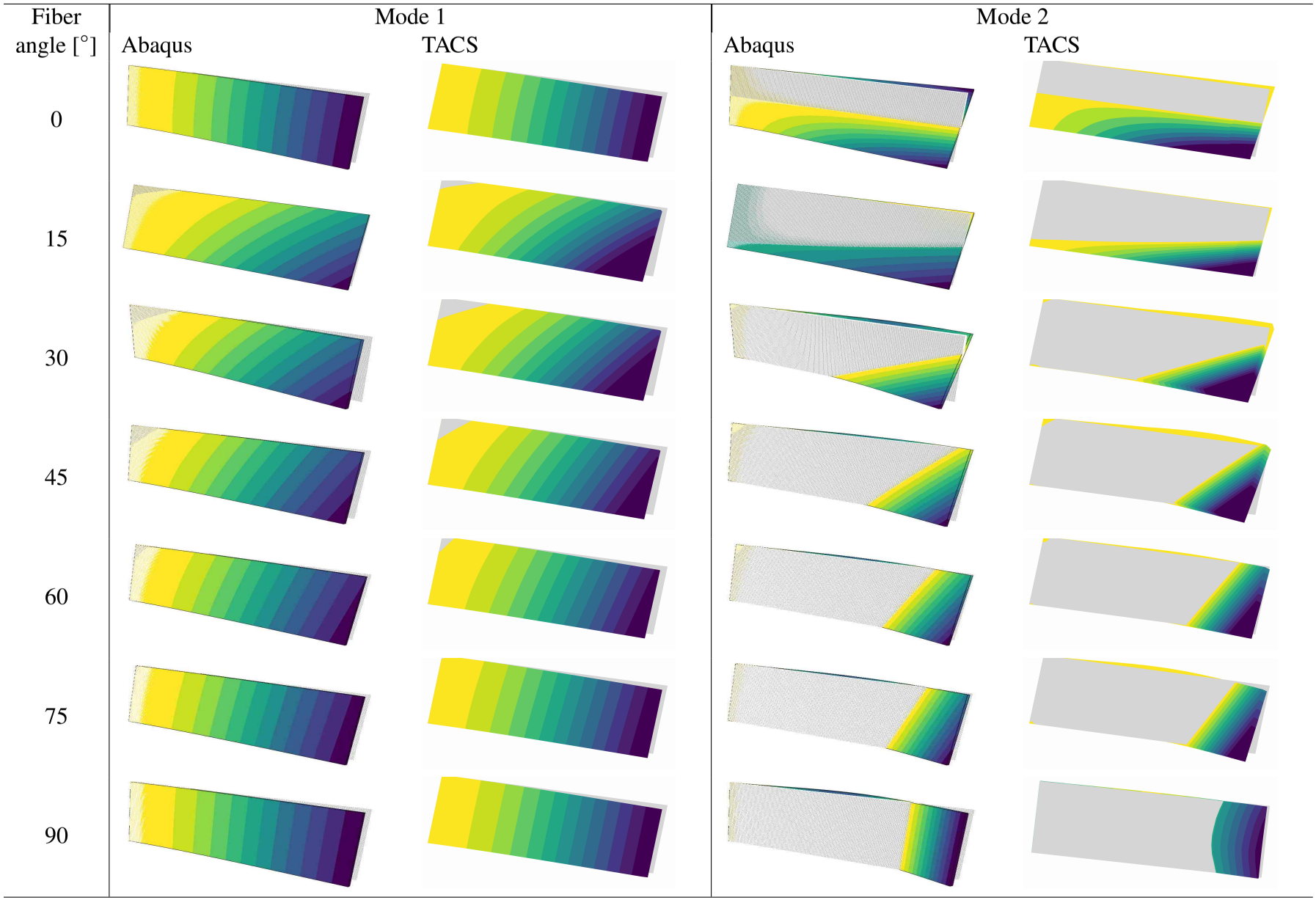

Figure 8.5: The first two predicted in-air mode shapes of a cantilevered plate for a range of unidirectional fiber angles obtained using Abaqus and TACS. The contours represent the deflection in z direction. Note the good agreement between the mode shapes predicted using the two structural solvers.

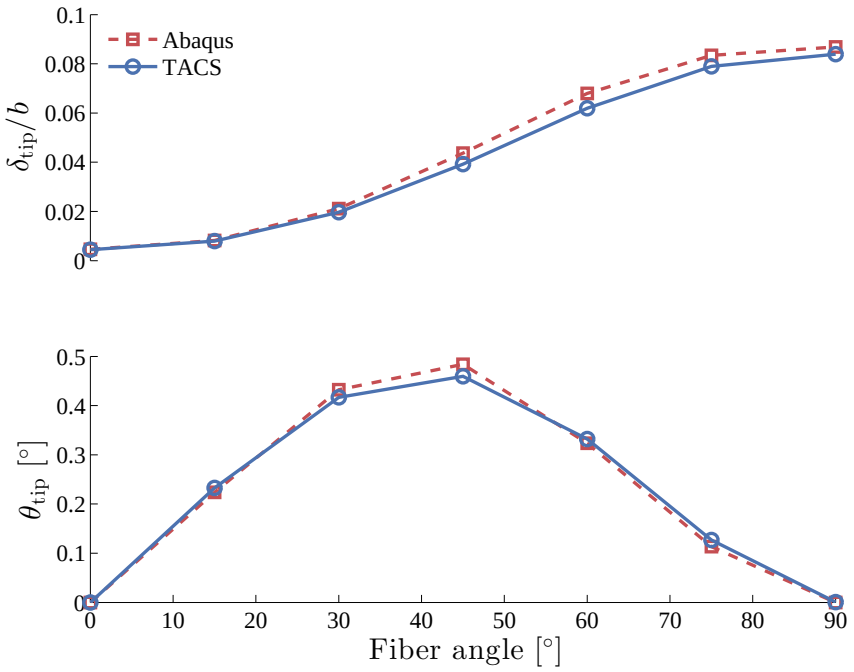

Figure 8.6: Comparison of the predicted bending and twist deformations from Abaqus and TACS for a cantilevered plate under uniform pressure of 443.5 Pa for a range of fiber angles. The deflections are measured at the elastic axis (i.e., the mid-breadth). The results show maximum discrepancy of 8.8% in the bending deformation, and 5.0% in the twist deformation.

terial properties of the carbon-UD are listed in Table 8.3. The geometry of the NACA 0009 hydrofoil is same as presented in the previous chapters. The intention of the current section is to show the frequency verification for a realistic geometry, as opposed to a simple cantilevered plate. As shown earlier in the grid convergence study in Section 8.2.2, we need at least 9 elements in the thickness direction to capture the anisotropic effects. Thus, for this study, we use 120, 36, and 9 elements in the spanwise, chordwise, and the thickness directions, respectively, as shown in Figure 8.9. Fixed boundary conditions are enforced at the root. Figure 8.10 presents the computed material bend-twist coupling for a cantilevered NACA 0009 hydrofoil with 00°, +30°, and -30° unidirectional fiber angles, using Eq. (8.4). As expected, material bend-twist coupling is zero for 00° and non-zero for +30° and -30° hydrofoils, with equal magnitude and opposite signs.

Figure 8.11 compares the first three predicted in-air natural frequencies from Abaqus

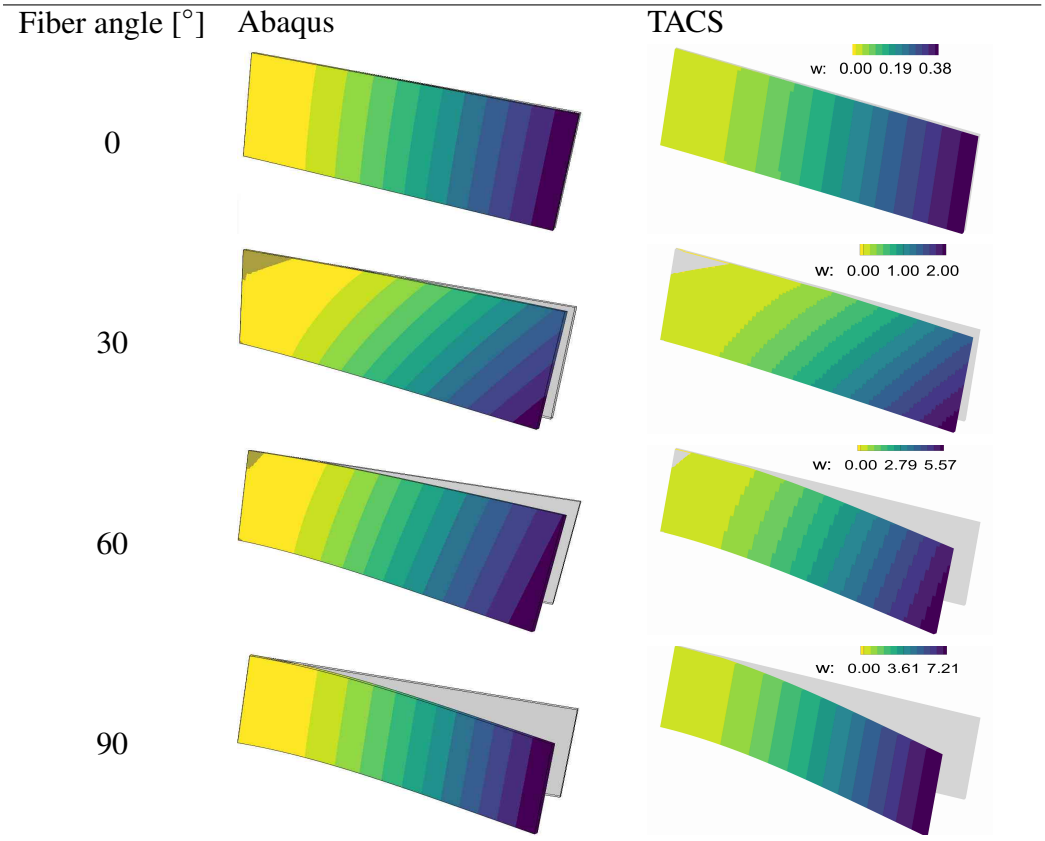

Figure 8.7: Predicted deformation pattern of a cantilevered plate under uniform pressure of 443.5 Pa for a range of fiber angle obtained using Abaqus and TACS. The contours represent the deflection in z-axis. To clearly demonstrate the differences, the deformations are scaled 10 times the actual deformations. Note the pure bending deformation for $\theta_f = 0^\circ$ and $\theta_f = 90^\circ$ and the combined bend-twist for $\theta_f = 30^\circ$ and $\theta_f = 60^\circ$. The deflections are in mm.

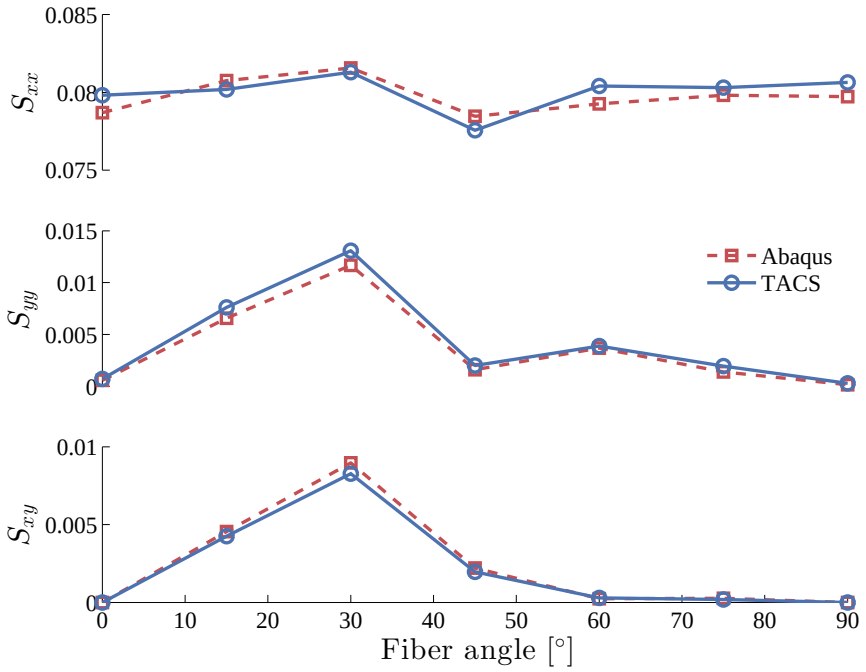

Figure 8.8: Comparison of the predicted non-dimensionalized bending (S_{xx} and S_{yy}) and shear stresses (S_{xy}) in the global coordinates obtained using Abaqus and TACS for a cantilevered plate under uniform pressure for a range of fiber angles. The stresses are compared at the center (mid-chord) of the top surface of the cantilevered plate.

and TACS for a cantilevered NACA 0009 hydrofoil with 00°, +30°, and -30° unidirectional fiber angle. The results show that there is a maximum discrepancy of 4.7%, i.e., for the second in-air mode of the UD 00° hydrofoil, between the two structural solvers. Figure 8.12 shows the predicted mode shapes for first two in-air modes from Abaqus and TACS. Note the similarities between the modes shapes from two structural solvers. Additionally, as presented in Chapter 7, while the 00° hydrofoil experiences primarily bending and twisting for the first and second mode, respectively; the +30° and -30° hydrofoils experience first bending mode as first mode and second bending mode as the second mode, with some twisting. The +30° and -30° hydrofoils also experience opposite twist direction, due to opposite orientation of the unidirectional fibers and the opposite signs of material bend-twist coupling (as shown in Figure 8.10).

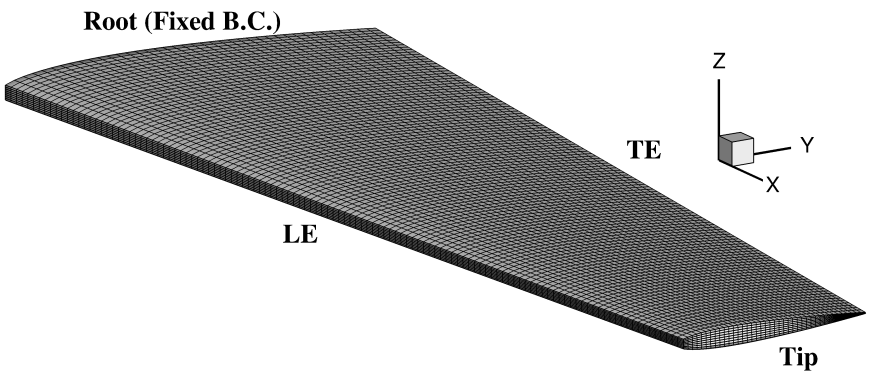

Figure 8.9: Structural mesh for the cantilevered NACA 0009 hydrofoil with 38,880 8-noded linear brick elements (120, 36, and 9 elements in the spanwise, chordwise, and the thickness direction, respectively).

Table 8.3: Material properties of composite hydrofoil made of unidirectional carbon.

Symbol	Description	Value	Units
ρ_s	Solid density	1540.00	Kg/m^3
E_1	Young's modulus	117.80	GPa
E_2	Young's modulus	13.40	GPa
E_3	Young's modulus	9.40	GPa
G_{12}, G_{13}	Shear modulus	3.90	GPa
G_{23}	Shear modulus	3.30	GPa
ν_{12}, ν_{13}	Poisson's ratio	0.25	–
ν_{23}	Poisson's ratio	0.45	–

8.4 Hydrostructural Analysis of Composite Hydrofoils

In this section, we present the preliminary hydrostructural analysis of the composite hydrofoils with 00°, +30°, and -30° unidirectional fiber angles. The properties of the unidirectional carbon material is already listed in Table 8.3. Figure 8.13 compares the mean lift, drag, moment coefficients, non-dimensional tip bending (δ_{tip}/b), and the twist (θ_{tip}) of the three composite hydrofoils (i.e., UD 00, UD +30, and UD -30) as a function of the angle of attack (α) for Re = 1.0×10^6. Due to the difference in material bend-twist coupling of the three composite hydrofoils, while the UD 00 and UD -30 hydrofoils experience positive twist, the UD +30 hydrofoil experiences negative twist, similar to the results presented in

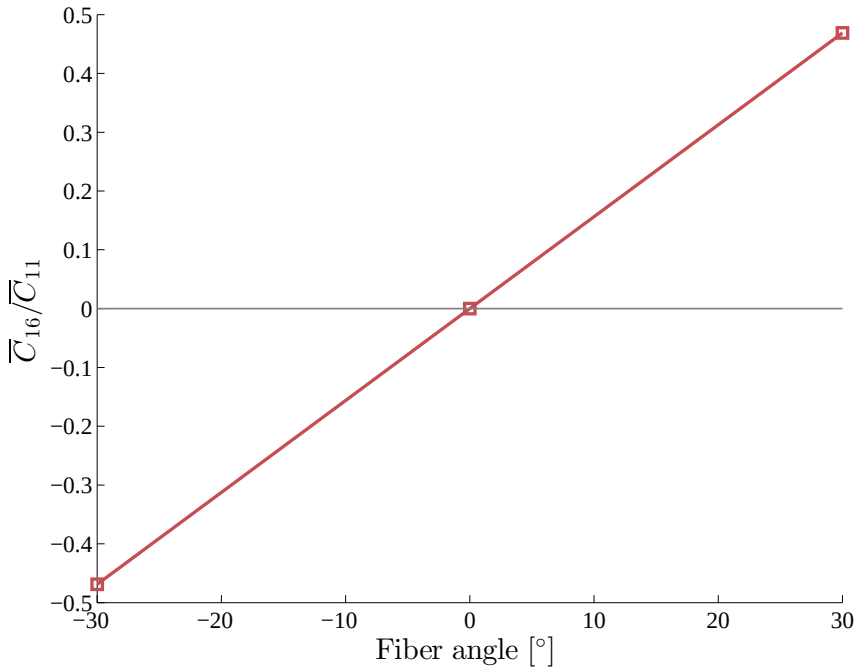

Figure 8.10: Comparison of the effective material bend-twist coupling, $\overline{C}_{16}/\overline{C}_{11}$, for a cantilevered NACA 0009 hydrofoil with 00°, +30°, and -30° unidirectional fiber angle.

Chapter 7. The negative twist results in decrease in lift, moment, and drag for the UD +30 hydrofoil, compared to the UD 00 hydrofoil. The positive twist results in increase in lift, moment, and drag for the UD -30 hydrofoil, compared to the UD 00 hydrofoil. The results confirm that the high-fidelity FSI solver was able to capture the bend-twist coupling effects of composite hydrofoils effectively.

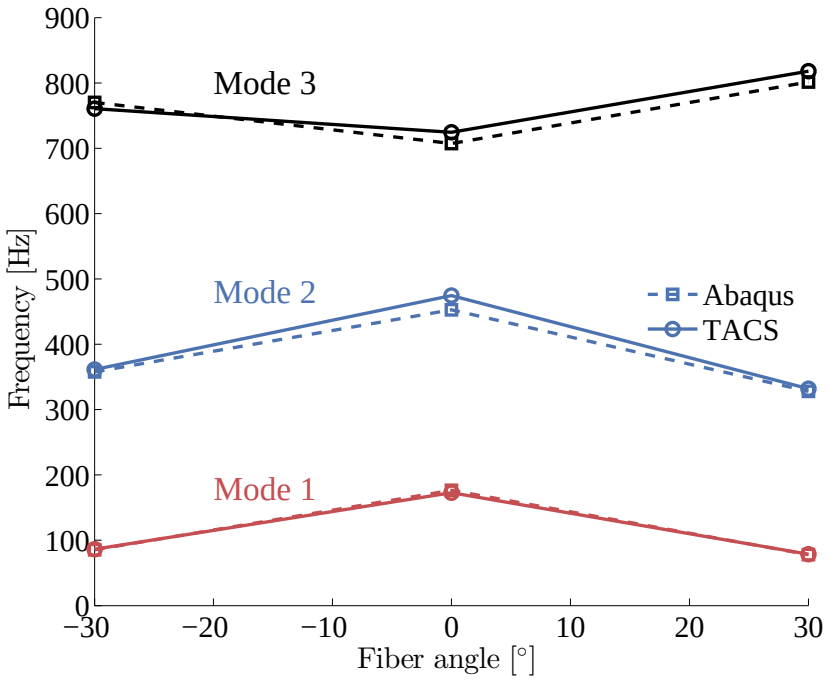

Figure 8.11: Comparison of the first three predicted in-air natural frequencies from Abaqus and TACS for the cantilevered NACA 0009 hydrofoil for the 00°, +30°, and -30° UD hydrofoils. Note the maximum discrepancy of 4.7% in the predicted natural frequencies between Abaqus and TACS.

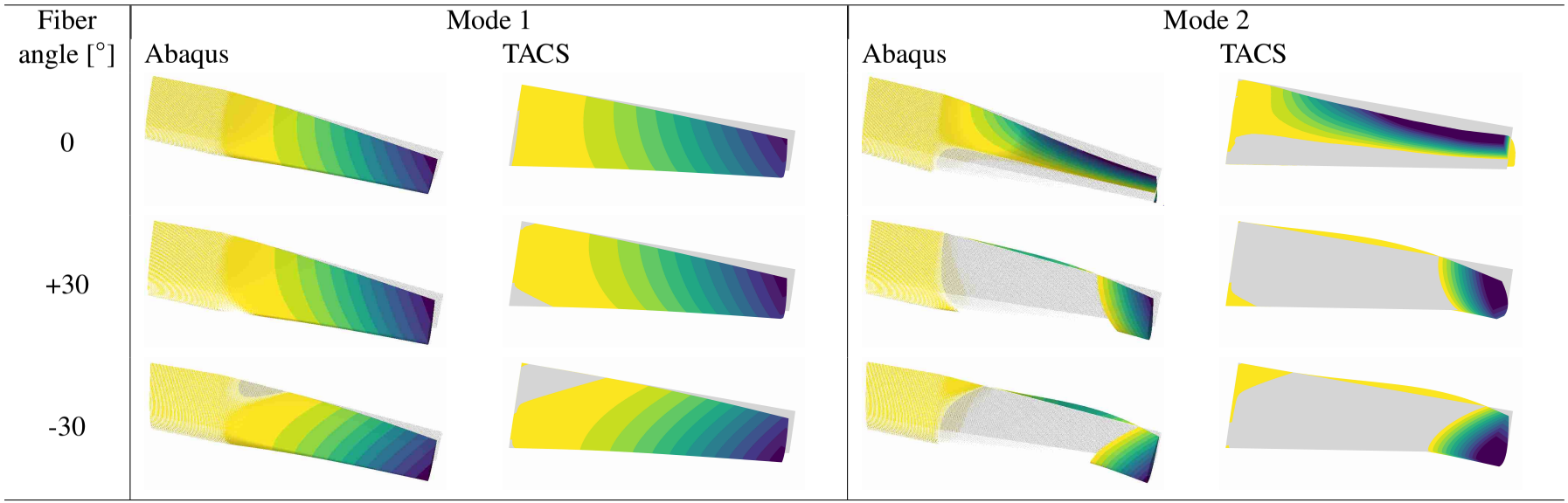

Figure 8.12: The first two predicted in-air mode shapes of the cantilevered NACA 0009 hydrofoil for 00°, +30°, and -30° unidirectional fiber angle obtained using Abaqus and TACS. The contours represent the deflection in z-axis. Note the good agreement between the mode shapes predicted from the two structural solvers.

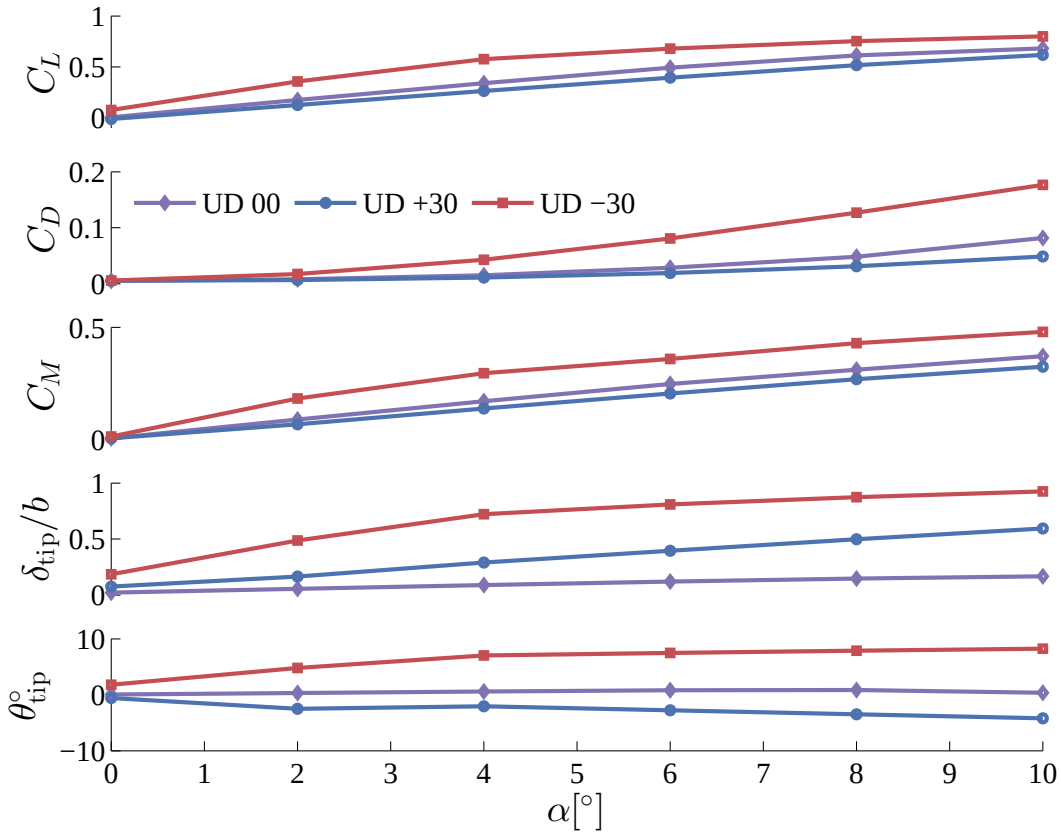

Figure 8.13: Top to bottom: Predicted values of mean lift coefficient (C_L), drag coefficient (C_D), pitch moment coefficient (C_M), non-dimensional tip bending deflection, and tip twisting deformations with angle of incidence for the three composite hydrofoils made of unidirectional fiber angles. While the UD -30 experiences an increase in lift, drag, and moment, UD +30 experiences a reduction in lift, drag, and moment, as compared to the UD 00 hydrofoil due to the opposite material based bend-twist coupling. Note the negative twist deformation for UD +30 hydrofoil, as compared to positive twist for UD 00 and UD -30 hydrofoils (similar to the results presented in Chapter 7).

8.5 Conclusions

In this chapter, the previously developed structural solver (TACS) was extended to solve for unidirectional anisotropic solid elements. We verified the modal behavior (i.e., mode shapes and modal frequencies) of TACS against the commercial structural solver, Abaqus. The results show that the maximum discrepancy in the frequency predictions for the first three in-air modes between the two solvers is 5.0%. The predicted mode shapes from TACS and Abaqus also look similar for a range of fiber angles. Additionally, the static stress and deformation verification of the cantilevered plate was conducted. The results show similar deformation trends predicted by Abaqus and TACS over a range of fiber angles, with a maximum discrepancy of 8.8% in the tip bending deformations.

We also verified the modal behavior for a cantilevered NACA 0009 hydrofoil with 00°, +30°, and -30° unidirectional carbon fiber angles. The results show a maximum discrepancy of 4.7% between the Abaqus and TACS predictions for the first three in-air natural frequencies. The predicted mode shapes for first two in-air modes are also very similar between Abaqus and TACS. The preliminary hydrostructural analysis of the composite hydrofoils show that while the +30° ($\alpha_{BT} > 0$) hydrofoil experiences negative twist, the -30° ($\alpha_{BT} < 0$) hydrofoil experiences positive twist. Thus, this chapter showed that the solid anisotropic elements implemented in TACS is able to accurately capture the bend-twist coupling effects of a composite hydrofoil.

To summarize, in this chapter, we laid the foundation work necessary to carry out high-fidelity hydrostructural optimization of the shape and material configurations of composite hydrofoils by implementing the solid anisotropic elements in our high-fidelity structural solver. We also validated the predictions with analytical and a commercial FEA solver, Abaqus.

CHAPTER 9

Final Remarks

This chapter presents the overall conclusions of this thesis, the main contributions, and the recommendations for future research directions.

9.1 Overall Conclusions

With recent improvements in the computational capability and the efficiency of the numerical solvers, marine propulsor design has been increasingly reliant on high-fidelity computational fluid dynamics (CFD) and computational structural dynamics (CSD) solvers. However, high-fidelity coupled hydrostructural optimization still remains challenging due to its high computational cost, especially for a large number of design variables.

In Chapter 4, we demonstrated that even for a simple unswept tapered hydrofoil, a minimum of 200 design variables is required to achieve an optimum design. We also validated our hydrodynamic solver with experimental measurements. The results show that high-fidelity (i.e., RANS-based) optimization is required to achieve an acceptable optimum solution, especially for off-design conditions. The RANS-based hydrodynamic shape optimization of a hydrofoil was presented with 210 design variables and a constraint to avoid cavitation inception. We concluded that the multipoint optimization is necessary to obtain a design capable of performing well over the entire range of operating conditions. The results show that there is an overall increase in the lift-to-drag ratio of 14.4% for the multipoint hydrodynamic optimized hydrofoil.

Chapter 5 presents a state-of-the-art coupled hydrostructural design optimization tool capable of handling a large number of design variables and operating conditions, with constraints on cavitation inception, fatigue stress, and the manufacturing tolerances. The hydrostructural solver was validated against experimental measurements for a cantilevered aluminum NACA 0009 hydrofoil. Similar to the hydrodynamic shape optimization results presented in Chapter 4, the results show that the multipoint optimization is necessary to obtain a design capable of performing well over the entire range of operating conditions. The multipoint hydrostructural optimization yields a weighted average increase in the lift-to-drag ratio of 8.5%, and an increased cavitation inception speed of 38%. The hydrostructural optimal result is also compared to an equivalent hydrodynamic-only optimization, and results show that hydrostructural optimization leads to a completely different geometry. Only the hydrostructural optimized design satisfies the stress constraint up to the highest expected loading condition, highlighting the need for coupled hydrostructural optimization. In Chapter 6, the improvement in the hydroelastic performance and the cavitation performance of the multipoint optimized hydrofoil was validated experimentally. The experimental and numerical results show that the multipoint optimization leads to an overall increase in the lift-to-drag ratio of 29%, with improved cavitation performance.

In Chapter 7, we presented numerical and experimental studies to understand the effects of load-dependent bend-twist coupling on the steady-state hydroelastic and cavitation response of three composite hydrofoils. The results show that the material bend-twist coupling, caused by the structural CFRP layers oriented away from the spanwise axis of the hydrofoil, significantly affected the mode shapes and modal frequencies, as well as the hydroelastic response of the hydrofoils. For the stainless steel and the CFRP 00 hydrofoils without material bend-twist coupling, the hydrodynamic moment caused the hydrofoils to undergo a nose up twist because the center of pressure was upstream of the elastic axis. The CFRP +30 hydrofoil with $\alpha_{BT} > 0$ (negative twist) experiences reduced hydrodynamic load coefficients and delayed stall compared to the stainless steel hydrofoil, and the relative

reduction in lift and moment coefficients increased with an increasing in Re and angle of attack. The CFRP -30 hydrofoil with $\alpha_{BT} < 0$ (positive twist) experiences increased hydrodynamic load coefficients and accelerated stall compared to the stainless steel hydrofoil, and the relative increase in lift and moment coefficients increased with increasing Re and angle of attack. The two degree-of-freedom (2-DOF) fluid structure interaction model was able to predict the steady-state load-dependent bend-twist coupling behavior and hydroelastic performance of all three composite hydrofoils. The 2-DOF model predicts accelerated stall for hydrofoils with nose up twist (CFRP -30, $\alpha_{BT} < 0$) and delayed static divergence for hydrofoils with nose down twist (CFRP +30, $\alpha_{BT} > 0$) for positive lift condition. The preliminary cavitation results show that the cavitation inception for the CFRP -30 hydrofoil occurs at a higher cavitation number (i.e., lower cavitation inception speed), and for the CFRP +30 hydrofoil at a lower cavitation number (i.e., higher cavitation inception speed), as compared to the rigid stainless steel hydrofoil. Similarly, relative to the stainless steel hydrofoil, CFRP -30 experiences longer cavity length, and CFRP +30 experiences shorter cavity length. The cavity length or the hydrodynamic load variation for the three hydrofoils can be collapsed into a single line by using the effective angle of attack (or the effective cavitation number). The results also show that the stainless steel, CFRP +30, and CFRP -30 hydrofoils display the most energetic lock-in behavior at the similar range of low cavitation number and frequency, illustrating the dominance of global shedding dynamics over bend-twist coupling effects.

In Chapter 8, we take the first step towards the high-fidelity hydrostructural optimization of composite hydrofoils by extending our high-fidelity structural solver to simulate the performance of anisotropic composite hydrofoils. We verified our structural solver for a range of unidirectional fiber angles for modal characteristics (i.e., frequency and mode shapes), static stresses and deformations, using a commercial structural solver, Abaqus. We also verified the modal characteristics and influence of material-based bend-twist coupling on the load-dependent deformation response of the NACA 0009 hydrofoil presented in the

previous chapter.

In summary, this thesis developed a state-of-the-art hydrostructural design optimization methodology capable of handling a large number of design variables. The design optimization methodology is capable of performing coupled multipoint hydrostructural optimizations with around 200 design variables overnight using 1,000 processors. With such a short design cycle, the proposed approach has the potential to revolutionize the design of the next generation of advanced hydrofoils and marine propulsors. The improvements in the optimized design were also confirmed experimentally. Additionally, we helped advance the understanding of the impact of load-dependent bend-twist coupling and on the steady-state hydroelastic performance, stall behavior, modal characteristics, static divergence boundary, and the cavitation response of adaptive composite hydrofoils. Lastly, we extended our high-fidelity FSI solver to solve for unidirectional anisotropic solid elements as the first step to develop a high-fidelity hydrostructural solver to analyze, design, and optimize the next generation adaptive composite marine propulsors.

9.2 Thesis Contributions

The results and the optimization approach presented in this thesis represent the current state-of-the-art in high-fidelity gradient based multipoint hydrostructural shape optimization. The main contributions of the thesis are as follows:

1. Adapted a state-of-the-art coupled high-fidelity aerostructural design optimization tool to solve for coupled hydrostructural applications, with a large number of design variables and constraints on cavitation inception, aggregated von Mises stress, and manufacturing tolerances, over a wide range of operating conditions.

2. Developed a constraint on the cavitation inception.

3. Extended structural solver (TACS) to include solid elements, instead of just shell

elements.

4. Validated the hydroelastic and cavitation performance improvement of an optimized hydrofoil with experimental measurements via collaborations with Australian Maritime College, Tasmania and Defense Science and Technology Group, Australia.

5. Presented a combined experimental and numerical study to improve the understanding of the governing physics behind load-dependent bend-twist coupling of adaptive composite hydrofoils.

6. Extended the high-fidelity FSI solver to simulate the performance of unidirectional anisotropic composite hydrofoils.

The above-mentioned contributions enable multipoint optimization of hydrodynamic performance for hydrofoils and marine propulsors with respect to shape and material configuration while enforcing design constraints on cavitation inception, fatigue stress, and manufacturing tolerances. The state-of-the-art efficient high-fidelity hydrostructural design optimization tool can be used for improving the performance of existing designs, and exploring new concepts. The thesis also presents the first experimental validation of the numerically optimized hydrofoil and thus, validates the effectiveness of the numerical optimization for future applications.

The thesis helps in advancing the understanding of the impact of load-dependent bend-twist coupling on the performance of adaptive composite hydrofoils. With the extension of the solver to predict the performance of the unidirectional anisotropic composite hydrofoils, the high-fidelity hydrostructural solver has the potential to play an important role in exploring and designing the next generation adaptive composite marine propulsors.

9.3 Recommendations

Throughout the thesis, several research directions have been identified to further improve the state-of-the-art of high-fidelity hydrostructural shape optimization of metallic and composite marine propulsors.

1. Preliminary experimental investigation showed improved cavitation performance for the optimized hydrofoil. However, further experiments are needed to quantify the improvement in cavitation performance of the optimized hydrofoil.

2. Further experiments should be carried out to improve the understanding of the impact of bend-twist coupling on the cavitating performance of adaptive composite hydrofoils.

3. In terms of the applications of the state-of-the-art hydrostructural design optimization tool, further improvements can be made to include more realistic operational profiles.

4. After understanding the impact of inherent material bend-twist coupling on the hydroelastic and cavitation performance, next step will be to conduct the high-fidelity hydrostructural optimization of a composite hydrofoil. For hydrostructural optimization of adaptive composite hydrofoils, design variables need to be developed for fiber angle and material failure criterion.

5. The hydrofoils for Moth class sailing boats can be designed using the new high-fidelity hydrostructural optimization tool for the composite hydrofoils. Optimizing the hydrofoil for these boats will provide a real-world multipoint optimization problem.

6. Finally, a state-of-the-art hydrostructural design optimization tool presented in this thesis can be used to conduct high-fidelity optimization for rotating marine propellers.

BIBLIOGRAPHY

[1] MSC Nastran Quick reference guide. MSC. SOFTWARE (2004), volume: 1, 2004.

[2] Abaqus 6.14 - Abaqus Analysis User's Guide. Dassault Systems Simulia, 2014.

[3] I. H. Abbott, A. E. Von Doenhoff, and L. Stivers Jr. Summary of airfoil data. NACA Technical Report 824, 1945, 1945.

[4] M. Abramowitz and I. A. Stegun. Handbook of mathematical functions: with formulas, graphs, and mathematical tables, volume 55. Courier Corporation, 1964.

[5] A. J. Acosta. A note on partial cavitation of flat plate hydrofoils. California Institute of Technology, 1955.

[6] D. T. Akcabay, E. J. Chae, Y. L. Young, A. Ducoin, and J. A. Astolfi. Cavity induced vibration of flexible hydrofoils. Journal of Fluids and Structures, 49:463–484, 2014.

[7] D. T. Akcabay and Y. L. Young. Influence of cavitation on the hydroelastic stability of hydrofoils. Journal of Fluids and Structures, 49:170–185, 2014.

[8] D. T. Akcabay and Y. L. Young. Parametric excitations and lock-in of flexible hydrofoils in two-phase flows. Journal of Fluids and Structures, 57:344–356, 2015.

[9] V. D. Azzi and S. W. Tsai. Anisotropic strength of composites. Experimental Mechanics, 5:283–288, 1965.

[10] B. Bak, C. Sarrado, A. Turon, and J. Costa. Delamination under fatigue loads in composite laminates: a review on the observed phenomenology and computational methods. Applied Mechanics Reviews, 66(6):060806, 2014.

[11] R. B. Barber and M. R. Motley. Cavitating response of passively controlled tidal turbines. Journal of Fluids and Structures, 66:462–475, 2016.

[12] J.-M. Berthelot. Transverse cracking and delamination in cross-ply glass-fiber and carbon-fiber reinforced plastic laminates: static and fatigue loading. Applied Mechanics Reviews, 56:111–147, 2003.

[13] S. Black. Composite propeller for royal navy minehunter. Composites World, Setember 2011.

[14] J. P. Blasques, C. Berggreen, and P. Andersen. Hydro-elastic analysis and optimization of a composite marine propeller. Marine Structures, 23(1):22–38, 2010.

[15] P. A. Brandner, Y. Lecoffre, and G. J. Walker. Design considerations in the development of a modern cavitation tunnel. In: Proceedings of the 18th Australian Fluid Mechanics Conference, pages 630–637, December 2007.

[16] C. E. Brennen. Cavitation and Bubble Dynamics. Oxford University Press, 1995.

[17] M. Breuer and D. Hänel. A dual time-stepping method for 3-d, viscous, incompressible vortex flows. Computers & fluids, 22(4-5):467–484, 1993.

[18] R. Brincker, L. Zhang, and P. Andersen. Modal identification of output-only systems using frequency domain decomposition. Smart Materials and Structures, 10(3):441, 2001.

[19] T. Brockett. Minimum pressure envelopes for modified NACA-66 sections with NACA A= 0.8 camber and buships type 1 and type 2 sections. DTIC Document (1996), (No. DTMB–1780), 1966.

[20] S. A. Brown. Displacement extrapolation for CFD + CSM aeroelastic analysis. AIAA paper, 1090 (1997), 1997.

[21] D. A. Burdette, G. K. Kenway, and J. R. R. A. Martins. Performance evaluation of a morphing trailing edge using multipoint aerostructural design optimization. In 57th AIAA/ASCE/AHS/ASC Structures, Structural Dynamics, and Materials Conference. American Institute of Aeronautics and Astronautics, January 2016.

[22] J. C. Ward C. M. Harwood, Y. L. Young, and S. L. Ceccio. Experimental investigation of the hydro-elastic response of a surface-piercing hydrofoil in multi-phase flow. In Proceedings of the 31st symposium on naval hydrodynamics, 2016.

[23] W. J. Calclough and J. G. Russell. Development of a composite propeller blade with a carbon fibre reinforced plastics spar. Aeronautical Journal, 76(733), 1972.

[24] E.F. Campana, D. Peri, Y. Tahara, M. Kandasamy, F. Stern, C.Cary, R. Hoffman, J. Gorski, and C. Kennell. Simulation-based design of fast multihull ships. 26th Symposium on Naval Hydrodynamics (2006), 2006.

[25] E. J. Chae, D. T. Akcabay, and Y. L. Young. Influence of flow-induced bend–twist coupling on the natural vibration responses of flexible hydrofoils. Journal of Fluids and Structures, 69:323–340, 2017.

[26] E.J. Chae, D.T. Akcabay, A. Lelong, J.A. Astolfi, and Y.L. Young. Numerical and experimental investigation of natural flow-induced vibrations of flexible hydrofoils. Physics of Fluids, 28:075102, 2016.

[27] B. Chen, S. Neely, T. Michael, S. Gowing, R. Szwerc, D. Buchler, and R. Schult. Design, fabrication and testing of pitch-adapting (flexible) composite propellers. In The SNAME Propellers/Shafting Symposium, volume 6, pages 12–13, 2006.

[28] S. Chen, Z. Lyu, G. K. W. Kenway, and J. R. R. A. Martins. Aerodynamic shape optimization of the Common Research Model wing-body-tail configuration. Journal of Aircraft, 53(1):276–293, January 2016.

[29] J. Cho and S. Lee. Propeller blade shape optimization for efficiency improvement. Computers & Fluids, 27(3):407–419, 1998.

[30] Y. H. Choi and C. L. Merkle. The application of preconditioning in viscous flows. Journal of Computational Physics, 105(2):207–223, 1993.

[31] D. B. Clarke, D. Butler, B. Crowley, and P. A. Brandner. High-speed full-field deflection measurements on a hydrofoil using digital image correlation. In 30th Symposium on Naval Hydrodynamics, Hobart, Tasmania, November 2014.

[32] J. J. Corbett and H. W. Koehler. Updated emissions from ocean shipping. Journal of Geophysical Research: Atmospheres, 108(D20):1984–2012, 2003.

[33] R. Courant, K. Friedrichs, and H. Lewy. On the partial difference equations of mathematical physics. IBM journal, 11(2):215–234, 1967.

[34] K. Dems and Z. Mróz. Variational approach by means of adjoint systems to structural optimization and sensitivity analysis—i: Variation of material parameters within fixed domain. International Journal of Solids and Structures, 19(8):677—692, 1983.

[35] K. Dems and Z. Mróz. Variational approach by means of adjoint systems to structural optimization and sensitivity analysis—ii: Structure shape variation. International Journal of Solids and Structures, 20(6):527–552, 1983.

[36] C. Doolan, P. Brandner, D. Butler, B. Pearce, D. Moreau, and L. Brooks. Hydroacoustic characterisation of the AMC cavitation tunnel. In Proceedings of Acoustics, 2013.

[37] A. Ducoin, J. A. Astolfi, and J. Sigrist. An experimental analysis of fluid structure interaction on a flexible hydrofoil in various flow regimes including cavitating flow. European Journal of Mechanics-B/Fluids, 36:63–74, 2012.

[38] A. Ducoin, F. Deniset, J. A. Astolfi, and J. Sigrist. Numerical and experimental investigation of hydrodynamic characteristics of deformable hydrofoils. Journal of Ship Research, 53(4):214–226, 2009.

[39] A. Ducoin and Y. L. Young. Hydroelastic response and stability of a hydrofoil in viscous flow. Journal of Fluids and Structures, 38:40–57, 2013.

[40] R. Eppler and Y. T. Shen. Wing sections for hydrofoils–Part 1: Symmetrical profiles. Journal of ship research (1979), 23(3), 1979.

[41] J. Faber, M. Hoen, M. Koopman, D. Nelissen, and S. Ahdour. Estimated index values of new ships. CE Delft Technical Report, 2015.

[42] H. Ganesh, J. Wu, and S. Ceccio. Investigation of cavity shedding dynamics on a naca0015 hydrofoil using time resolved x-ray densitometry. In 31st Symposium on Naval Hydrodynamics, CA, USA, September 2016.

[43] N. Garg, G. K. W. Kenway, Z. Lyu, J. R. R. A. Martins, and Y. L. Young. High-fidelity hydrodynamic shape optimization of a 3-D hydrofoil. Journal of Ship Research, 59(4):209–226, December 2015.

[44] N. Garg, G. K. W. Kenway, J. R. R. A. Martins, and Y. L. Young. High-fidelity multipoint hydrostructural optimization of a 3-d hydrofoil. Journal of Fluids and Structures, 71:15–39, 2017.

[45] N. Garg, Z. Lyu, T. Dhert, J. R. R. A. Martins, and Y. L. Young. High-fidelity hydrodynamic shape optimization of a 3-D morphing hydrofoil. In Fourth International Symposium on Marine Propulsors, Houston, USA, June 2015.

[46] H. C. Garner, E. W. Rogers, W. E. Acum, and E. C. Maskell. Subsonic wind tunnel wall corrections. Technical report, DTIC Document, 1966.

[47] M. R. Garnich and V. M. K. Akula. Review of degradation models for progressive failure analysis of fiber reinforced polymer composites. Applied Mechanics Reviews, 62:1–33, 2009.

[48] P. E. Gill, W. Murray, and M. A. Saunders. SNOPT: An SQP algorithm for large-scale constrained optimization. SIAM Journal of Optimization, 12(4):979–1006, 2002.

[49] S Gowing, P Coffin, and C Dai. Hydrofoil cavitation improvements with elastically coupled composite materials. In Proceedings of the 25th American Towing Tank Conference, 1998.

[50] J. A. Green. Aeroelastic tailoring of aft-swept high-aspect-ratio composite wings. Journal of Aircraft, 24(11):812–819, 1987.

[51] D. Griffin. Evaluation of design concepts for adaptive wind turbines, SAND report 2002-2424. Technical report, Sandia National Laboratories, USA, 2002.

[52] G. Grunditz. Quieter, more efficient propellers. Ingenia, 65, December 2015.

[53] JE Hackett, KR Cooper, and ML Perry. Drag, lift and pitching moment increments due to wind tunnel wall constraint- extension to three dimensions. In International Congress of Aeronautical Sciences, 22nd, Harrogate, United Kingdom, 2000.

[54] C.M. Harwood, Y.L. Young, and S.L. Ceccio. Ventilated cavities on a surface-piercing hydrofoil at moderate froude numbers: cavity formation, elimination, and stability. Journal of Fluid Mechanics, 800:5–56, 2016.

[55] M.T. Herath. Optimization of Composite Marine Propeller Blades and Hydrofoils. PhD thesis, School of Mechanical and Manufacturing Engineering, University of New South Wales, Australia, 2015.

[56] R. Hill. The Mathematical Theory of Plasticity. Oxford University Press, London, 1950.

[57] C. Y. Hsin. Application of the panel method to the design of two-dimensional foil sections. Journal of Chinese society of Naval Architects and Marine Engineers, 13(2pp):1–11, 1994.

[58] M. E. Ibrahim, A. W. Phillips, R. J. Ditchburn, and C. H. Wang. Nondestructive evaluation of mechanically loaded advanced marine composite structures. In Advanced Materials Research, volume 891, pages 594–599. Trans Tech Publ, 2014.

[59] U. Icardi, S. Locatto, and A. Longo. Assessment of recent theories for predicting failure of composite laminates. Applied Mechanics Review, 60:76–86, 2007.

[60] E. N. Jacobs and A. Sherman. Airfoil section characteristics as affected by variations of the reynolds number. NACA Report 586. National Advisory Committee for Aeronautics, 1937.

[61] A. Jameson. Aerodynamic design via control theory. Journal of Scientific Computing, 3(3):233–260, September 1988.

[62] A. Jameson, W. Schmidt, and E. Turkel. Numerical solutions of the euler equations by finite volume methods using Runge–Kutta time-stepping schemes. AIAA paper (1981), 1259, 1981.

[63] N.M. Karaolis, P.J. Mussgrove, and G. Jeronimidis. Active and passive aeroelastic power control using asymmetric fibre reinforced laminates for wind turbine blades. In 10th British Wind Energy Conference, pages 446–458, London, 1988.

[64] G. J. Kennedy and J. R. R. A. Martins. A parallel finite-element framework for large-scale gradient-based design optimization of high-performance structures. Finite Elements in Analysis and Design, 87:56–73, September 2014.

[65] G. K. W. Kenway, G. J. Kennedy, and J. R. R. A. Martins. Aerostructural optimization of the Common Research Model configuration. In 15th AIAA/ISSMO Multidisciplinary Analysis and Optimization Conference, Atlanta, GA, June 2014. AIAA 2014-3274.

[66] G. K. W. Kenway, G. J. Kennedy, and J. R. R. A. Martins. Scalable parallel approach for high-fidelity steady-state aeroelastic analysis and derivative computations. AIAA Journal, 52(5):935–951, May 2014.

[67] G. K. W. Kenway and J. R. R. A. Martins. Multipoint high-fidelity aerostructural optimization of a transport aircraft configuration. Journal of Aircraft, 51(1):144–160, January 2014.

[68] G. K. W. Kenway and J. R. R. A. Martins. Multipoint aerodynamic shape optimization investigations of the Common Research Model wing. AIAA Journal, 54(1):113–128, January 2016.

[69] G. K. W. Kenway and J. R. R. A. Martins. Buffet onset constraint formulation for aerodynamic shape optimization. AIAA Journal, 2017. (In press).

[70] M. Khan, Daniel O. Adams, Vinay Dayal, Jerald M. Vogel, and Abdul. Effects of bend–twist coupling on composite propeller performance. Mechanics of Composite Materials and Structures, 7(4):383–401, 2000.

[71] N. S. Khot and J. V. Zweber. Design of flutter characteristics of composite wings using frequency constraint optimization. Journal of Aerospace Engineering, 16(1):19–30, 2003.

[72] S. A. Kinnas and N. E. Fine. Non-linear analysis of the flow around partially or super-cavitating hydrofoils by a potential based panel method. In Boundary Integral Methods, pages 289–300. Springer, 1991.

[73] S. A. Kinnas, S. Mishima, and W. H. Brewer. Nonlinear analysis of viscous flow around cavitating hydrofoils. In 20th Symposium on Naval Hydrodynamics, pages 21–26, 1994.

[74] M. R. Kramer, M. R. Motley, and Y. L. Young. An integrated probability-based propulsor-hull matching methodology. Journal of Offshore Mechanics and Arctic Engineering, 135(1):011801, 2013.

[75] M.R. Kramer, Z. Liu, and Y.L. Young. Free vibration of cantilevered composite plates in air and in water. Composite Structures, 95:254–263, 2013.

[76] M.A. Lackner and M.A. Rotea. Passive structural control of offshore wind turbines. Wind Energy, 14(3):373–388, 2010.

[77] A. B. Lambe, G. J. Kennedy, and J. R. R. A. Martins. An evaluation of constraint aggregation strategies for wing box mass minimization. Structural and Multidisciplinary Optimization, 55(1):257–277, 2017.

[78] Y. Lee and C. Lin. Regression of the response surface of laminated composite structures. Composite structures, 62(1):91–105, 2003.

[79] Y.J. Lee and C.C. Lin. Optimized design of composite propeller. Mechanics of Advanced Materials and Structures, 11:17–30, 2004.

[80] R. Liem, G. K. W. Kenway, and J. R. R. A. Martins. Multimission aircraft fuel burn minimization via multipoint aerostructural optimization. AIAA Journal, 53(1):104–122, January 2015.

[81] R. P. Liem, J. R. R. A. Martins, and G. K. Kenway. Expected drag minimization for aerodynamic design optimization based on aircraft operational data. Aerospace Science and Technology, 63:344–362, April 2017.

[82] C. Lin, Y. Lee, and C. Hung. Optimization and experiment of composite marine propellers. Composite Structures, 89(2):206–215, 2009.

[83] C.C. Lin and Y.J. Lee. Stacking sequence optimization of laminated composite structures using genetic algorithm with local improvement. Composite Structures, 63:339–345, 2004.

[84] H.J. Lin and J.J. Lin. Effect of stacking sequence on the hydroelastic behavior of composite propeller blades. In Eleventh International Conference on Composite Materials, Gold Coast, Australia, 1997. Australian Composite Structures Society.

[85] Z. Liu and Y. L. Young. Utilization of bend–twist coupling for performance enhancement of composite marine propellers. Journal of Fluids and Structures, 25(6):1102–1116, 2009.

[86] Z. Liu and Y. L. Young. Static divergence of self-twisting composite rotors. Journal of Fluids and Structures, 26(5):841–847, 2010.

[87] D. Lobitz and P. Veers. Aeroelastic behavior of twist-coupled hawt blades. In 1998 ASME Wind Energy Symposium, page 29, 1998.

[88] D.W. Lobitz, P.S. Veers, G.R. Eisler, D.J. Laino, P.G. Migliore, and G. Bir. The use of twist-coupled blades to enhance the performance of horizontal axis wind turbines. Technical report, Sandia National Laboratories, 2001.

[89] Z. Lyu, G. K. Kenway, and J. R. R. A. Martins. Aerodynamic shape optimization investigations of the Common Research Model wing benchmark. AIAA Journal, 53(4):968–985, April 2015.

[90] Z. Lyu, G. K. Kenway, C. Paige, and J. R. R. A. Martins. Automatic differentiation adjoint of the Reynolds-averaged Navier–Stokes equations with a turbulence model. In 21st AIAA Computational Fluid Dynamics Conference, San Diego, CA, Jul. 2013.

[91] Z. Lyu and J. R. R. A. Martins. Aerodynamic design optimization studies of a blended-wing-body aircraft. Journal of Aircraft, 51(5):1604–1617, September 2014.

[92] Z. Lyu, Z. Xu, and J. R. R. A. Martins. Benchmarking optimization algorithms for wing aerodynamic design optimization. In Proceedings of the 8th International Conference on Computational Fluid Dynamics, Chengdu, Sichuan, China, July 2014. ICCFD8-2014-0203.

[93] C. A. Mader, J. R. R. A. Martins, J. J. Alonso, and E. van der Weide. ADjoint: An approach for the rapid development of discrete adjoint solvers. AIAA Journal, 46(4):863–873, April 2008.

[94] A. Maheri and A.T. Isikveren. Performance prediction of wind turbines utilizing passive smart blades: approaches and evaluation. Wind Energy, 13:255–265, 2009.

[95] A. Maheri, S. Noroozi, and J. Vinney. Application of combined analytical/FEA coupled aero-structure simulation in design of wind turbine adaptive blades. Renewable Energy, 32:2011–2018, 2007.

[96] J. R. R. A. Martins, J. J. Alonso, and J. J. Reuther. High-fidelity aerostructural design optimization of a supersonic business jet. Journal of Aircraft, 41(3):523–530, May 2004.

[97] J. R. R. A. Martins, J. J. Alonso, and J. J. Reuther. A coupled-adjoint sensitivity analysis method for high-fidelity aero-structural design. Optimization and Engineering, 6(1):33–62, March 2005.

[98] J. R. R. A. Martins and J. T. Hwang. Review and unification of methods for computing derivatives of multidisciplinary computational models. AIAA Journal, 51(11):2582–2599, November 2013.

[99] J. R. R. A. Martins, P. Sturdza, and J. J. Alonso. The complex-step derivative approximation. ACM Transactions on Mathematical Software, 29(3):245–262, 2003.

[100] MATLAB. R2013b. The MathWorks Inc., Natick, Massachusetts, 2013.

[101] C. Merkle. Time-accurate unsteady incompressible flow algorithms based on artificial compressibility. In 8th Computational Fluid Dynamics Conference, page 1137, 1987.

[102] R. Miller, S.E. Kim, B. Rhee, and Y.L. Young. Unsteady fluid structure interaction response of marine propellers in crashback. In Proceedings of the 29th Symposium on Naval Hydrodynamics, 2012.

[103] S. Mishima and S. A. Kinnas. A numerical optimization technique applied to the design of two-dimensional cavitating hydrofoil sections. Journal of Ship Research, 40(1):28–38, 1996.

[104] M. R. Motley and R. B. Barber. Passive control of marine hydrokinetic turbine blades. Composite Structures, 110:133–139, 2014.

[105] M. R. Motley, M. Nelson, and Y. L. Young. Integrated probabilistic design of marine propulsors to minimize lifetime fuel consumption. Ocean Engineering, 45:1–8, 2012.

[106] M. R. Motley and Y. L. Young. Influence of uncertainties on the response and reliability of self-adaptive composite rotors. Composite Structures, 94(1):114–120, 2011.

[107] M. R. Motley and Y. L. Young. Performance-based design and analysis of flexible composite propulsors. Journal of Fluids and Structures, 27(8):1310–1325, 2011.

[108] M.R. Motley, M.R. Kramer, and Y.L. Young. Free surface and solid boundary effects on the free vibration of cantilevered composite plates. Composite Structures, 95:365–375, 2013.

[109] MR Motley, Z Liu, and YL Young. Utilizing fluid–structure interactions to improve energy efficiency of composite marine propellers in spatially varying wake. Composite Structures, 90(3):304–313, 2009.

[110] A. P. Mouritz, E. Gellert, P. Burchill, and K. Challis. Review of advanced composite structures for naval ships and submarines. Composite Structures, 53(1):21–42, 2001.

[111] T. J. Mueller and S. M. Batil. Experimental studies of separation on a two-dimensional airfoil at low Reynolds numbers. AIAA journal, 20(4):457–463, 1982.

[112] C. Münch, P. Ausoni, O. Braun, M. Farhat, and F. Avellan. Fluid–structure coupling for an oscillating hydrofoil. Journal of Fluids and Structures, 26(6):1018–1033, 2010.

[113] M. Nelson, D. W. Temple, J. T. Hwang, Y. L. Young, J. R. R. A. Martins, and M. Collette. Simultaneous optimization of propeller–hull systems to minimize lifetime fuel consumption. Applied Ocean Research, 43:46–52, 2013.

[114] R. F. Nicholls-Lee, S. R. Turnock, and S. W. Boyd. Performance prediction of a free stream tidal turbine with composite bend-twist coupled blades. In 2nd International Conference on Ocean Energy, October 2008.

[115] R. F. Nicholls-Lee, S. R. Turnock, and S. W. Boyd. Application of bend-twist coupled blades for horizontal axis tidal turbines. Renewable Energy, 50:541–550, 2013.

[116] Eric J. Nielsen and W. Kyle Anderson. Aerodynamic design optimization on unstructured meshes using the Navier–Stokes equations. AIAA Journal, 37(11):1411–1419, 1999.

[117] A. C. Orifici, I. Herszerg, and R. S. Thomson. Review of methodologies for composite material modelling incorporating failure. Composite Structures, 86:194–210, 2008.

[118] Oslash, m. Soykasap, and D. H Hodges. Performance enhancement of a composite tilt-rotor using aeroelastic tailoring. Journal of Aircraft, 37(5):850–858, 2000.

[119] B.G. Paik, G.D. Kim, K.Y. Kim, H.S. Seol, B.S. Hyan, S.G. Lee, and Y.R. Jung. Investigation on the performance characteristics of the flexible propellers. Ocean Engineering, 73:139–148, 2013.

[120] E. M. Papoutsis-Kiachagias, S. A. Kyriacou, and K. C. Giannakoglou. The continuous adjoint method for the design of hydraulic turbomachines. Computer Methods in Applied Mechanics and Engineering, 278:621–639, 2014.

[121] F. Paris. A study of failure criteria of fibrous composite materials. Technical report, NASA/CR-2001-210661, 2001.

[122] B. W. Pearce, P. A. Brandner, N. Garg, Y. L. Young, A. W. Phillips, and D. B. Clarke. The influence of bend-twist coupling on the dynmaic response of cavitating composite hydrofoils. In Fifth International Symposium on Marine Propulsors smpâĂŹ17, Espoo, Finland, June, 2017.

[123] J. E. V. Peter and R. P. Dwight. Numerical sensitivity analysis for aerodynamic optimization: A survey of approaches. Computers and Fluids, 39(3):373–391, March 2010.

[124] A. W. Phillips, R. Cairns, C. Davis, P. Norman, P. A. Brandner, B. W. Pearce, and Y. L. Young. Effect of material design parameters on the forced vibration response of composite hydrofoils in air and in water. In Fifth International Symposium on Marine Propulsors, Espoo, Finland, June 2017.

[125] A. W. Phillips, A. Nanayakkara, R . Cairns, N .St John, M. T. Herath, G. A. Zarruk, and P. A. Brandner. Effect of material anisotropy on the structural response of flexible composite hydrofoils. In SAMPE Baltimore 2015, pages 1–14, 2015.

[126] M. Plucinski, Y. Young, and Z. Liu. Optimization of a self-twisting composite marine propeller using a genetic algorithms. In Proceedings of 16th International Conference on Composite Materials, Kyoto, Japan, 2007.

[127] N. M. K. Poon and J. R. R. A. Martins. An adaptive approach to constraint aggregation using adjoint sensitivity analysis. Structural and Multidisciplinary Optimization, 34(1):61–73, July 2007.

[128] M. S. Selig, J. J. Guglielmo, A. P. Broeren, and P. Giguere. Experiments on airfoils at low Reynolds numbers. AIAA Paper, 62, 1996.

[129] R. D. B. Sevenois and W. Van Paepegem. Faitgue damage modeling techniques for textile composites: Review and comparison with unidirectional composite modeling techniques. Applied Mechanics Reviews, 67:1–12, 2015.

[130] Y. T. Shen and R. Eppler. Wing sections for hydrofoils–Part 2: Nonsymmetrical profiles. Journal of ship research, 25(3):191–200, 1981.

[131] P. Spalart and S. Allmaras. A one-equation turbulence model for aerodynamic flows. In 30th Aerospace Sciences Meeting and Exhibit, 1992.

[132] W. Sutherland. Lii. the viscosity of gases and molecular force. The London, Edinburgh, and Dublin Philosophical Magazine and Journal of Science, 36(223):507–531, 1893.

[133] S.W. Tsai and E.M. Wu. A general theory of strength for anisotropic materials. Journal of Composite Materials, 5:58–80, 1971.

[134] M. P. Tulin. Steady two-dimensional cavity flows about slender bodies. Technical Report 834, David Taylor Model Basin., 1953.

[135] E. Turkel. Preconditioned methods for solving the incompressible and low speed compressible equations. Journal of computational physics, 72(2):277–298, 1987.

[136] E. Turkel, R. Radespiel, and N. Kroll. Assessment of preconditioning methods for multidimensional aerodynamics. Computer and Fluids, 26(6):613–634, 1997.

[137] E. van der Weide, G. Kalitzin, J. Schluter, and J. J. Alonso. Unsteady turbomachinery computations using massively parallel platforms. In Proceedings of the 44th AIAA Aerospace Sciences Meeting and Exhibit, Reno, NV, 2006. AIAA 2006-0421.

[138] B. Van Leer, W. T. Lee, and P. L. Roe. Characteristic time-stepping or local preconditioning of the euler equations. 10th Computational Fluid Dynamics Conference, 1:260–282, 1991.

[139] P. Veers, G. Bir, and D. Lobitz. Aeroelastic tailoring in wind-turbine blade applications. In Windpower '98, American Wind Energy Association Meeting and Exhibition, pages 291–304, Bakersfield, California, 1998.

[140] S. Venkateswaran and C. Merkle. Dual time-stepping and preconditioning for unsteady computations. In 33rd Aerospace Sciences Meeting and Exhibit, page 78, 1995.

[141] W. Wilson, J. Gorski, M. Kandasamy, He Takai, T., F. W., Stern, and Y. Tahara. Hydrodynamic shape optimization for naval vehicles. High Performance Computing Modernization Program Users Group Conference (HPCMP-UGC), pages 161–168, 2010.

[142] G. A. Wrenn. An indirect method for numerical optimization using the Kreisselmeier–Steinhauser function. Technical Report CR-4220, NASA, 1989.

[143] T. Yamane and P. P. Friedmann. Aeroelastic tailoring analysis for preliminary design of advanced propellers with composite blades. Journal of aircraft, 30(1):119–126, 1993.

[144] Y. L. Young. Fluid–structure interaction analysis of flexible composite marine propellers. Journal of Fluids and Structures, 24(6):799–818, 2008.

[145] Y. L. Young, J. W. Baker, and M. R. Motley. Reliability-based design and optimization of adaptive marine structures. Composite structures, 92(2):244–253, 2010.

[146] Y. L. Young, N. Garg, P. A. Brandner, B. W. Pearce, D. B. Butler, D. Clarke, and A. W. Phillips. Load-dependent bend-twist coupling effects on the steady-state hydroelastic response of composite hydrofoils. Composite Structures, Under preparation.

[147] Y. L. Young, M. R. Motley, R. Barber, E. J. Chae, and N. Garg. Adaptive composite marine propulsors and turbines: Progress and challenges. Applied Mechanics Reviews, 68(6):060803, 2016.

[148] Y. L. Young, M. R. Motley, and R. W. Yeung. Three-dimensional numerical modeling of the transient fluid-structural interaction response of tidal turbines. Journal of Offshore Mechanics and Arctic Engineering, 132(1):011101, 2010.

[149] Y.L. Young. Time-dependent hydroelastic analysis of cavitating propulsors. Journal of Fluids and Structures, 23:269–295, 2007.

[150] Y.L. Young. Fluid-structure interaction analysis of flexible composite marine propellers. Journal of Fluids and Structures, 24:799–818, 2008.

[151] Y.L. Young, C.M. Harwood, F.M. Montero, J.C. Ward, and S.L. Ceccio. Ventilation of lifting bodies: Review of the physics and discussion of scaling effects. Applied Mechanics Review, 69(1):010801, 2017.

[152] YL Young, TJ Michael, M Seaver, and ST Trickey. Numerical and experimental investigations of composite marine propellers. In 26th symposium on naval hydrodynamics, 2006.

[153] Y.L. Young and M.R. Motley. Rate-dependent hydroelastic response of self-adaptive composite propellers in fully wetted and cavitating flows. In Proceedings of the 7th International Symposium on Cavitation (CAV2009), 2009.

[154] Y.L. Young, M.R. Motley, and R.W. Yeung. Three-dimensional numerical modeling of the transient fluid-structure interaction response of tidal turbines. Journal of Offshore Mechanics and Arctic Engineering, 132:011101, 2010.

[155] G.A. Zarruk, P.A. Brandner, B.W. Pearce, and A. W. Phillips. Experimental study of the steady fluid-structure interaction of flexible hydrofoils. Journal of Fluids and Structure, 51:326–343, 2014.

[156] Z. B. ZENG and G. Kuiper. Blade section design of marine propellers with maximum cavitation inception speed. Journal of Hydrodynamics, 24(1):65–75, 2011.